



NATIONAL ADVISORY COMMITTEE FOR AERONAUTICS

TECHNICAL NOTE 3492

DETERMINATION OF INFLOW DISTRIBUTIONS FROM EXPERIMENTAL
AERODYNAMIC LOADING AND BLADE-MOTION DATA ON A
MODEL HELICOPTER ROTOR IN HOVERING
AND FORWARD FLIGHT

By Gaetano Falabella, Jr., and John R. Meyer, Jr.

Massachusetts Institute of Technology



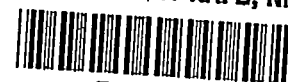
Washington

November 1955

AFMPC

RECEIVED

9775 2 9116
NACA TN 3492



TECHNICAL NOTE 3492

DETERMINATION OF INFLOW DISTRIBUTIONS FROM EXPERIMENTAL
AERODYNAMIC LOADING AND BLADE-MOTION DATA ON A
MODEL HELICOPTER ROTOR IN HOVERING
AND FORWARD FLIGHT

By Gaetano Falabella, Jr., and John R. Meyer, Jr.

SUMMARY

Inflow distributions, azimuth and spanwise, were determined analytically from measured pressure distributions and blade-motion data on a model helicopter rotor blade under hovering and simulated forward-flight conditions. Pressures and corresponding blade flapping were recorded for various rotor conditions at tip-speed ratios of 0.10 to 1.00. Included in this range are one-bladed-rotor operation effects, deliberate blade stall, data on the effects of cyclic pitch, and tests on a rotor with a 13-percent-offset flapping hinge. Since the offset-flapping-hinge rotor was used primarily as a means of alleviating stall in order to obtain inflow data at high tip-speed ratios μ in the vicinity of 1.0, no cyclic pitch was used to balance out the hub moments resulting from the incorporation of offset hinges. It is these moments which are the primary source of the stall alleviation.

Analyses of the data are presented in the form of raw data, spanwise loadings, and plots of inflow ratio against azimuth. For rotor operation at $\mu = 0.30$, zero- and 13-percent offsets, additional plots of loading and inflow ratio contours are presented for comparison.

The inflow plots indicate variations very different from the uniform distributions which are sometimes associated with a rotor disk. An extensive investigation of the $\mu = 0.30$, zero-offset rotor condition shows that larger inflow variations than predicted by theory can exist; however, upflow over the forward portion of the disk and relatively large induced velocity at the trailing edge are verified. The inflow patterns for the zero-offset and 13-percent-offset rotors under the same conditions of operation, except for the presence of hub moments in the offset-hinge case, are found to be very different in general character.

Supplementary information concerning reverse-flow effects on offset-blade motion, measured forces and moments on a typical offset model rotor, and additional recorded pressure data are also included.

INTRODUCTION

There are many instances in helicopter design where much can be gained from a knowledge of the correct induced velocity or inflow distribution throughout the rotor disk. Solutions of the problems of excessive vibration, structural fatigue, roughness of control, and rotor interferences would become more evident if the nature of the rotor disturbances was known. At least, with a reasonable knowledge of inflow variations, it may be possible to design away from these adverse characteristics.

The available current experimental inflow data are not adequate to permit a thorough evaluation of existing theories. With the exception of the hovering condition, therefore, only a limited amount of material has been published about the correlation between inflow theory and experiment. In reference 1, longitudinal inflow variations were determined from flight smoke traces. Each plotted variation represents the average of data obtained between the center of the rotor and halfway to its lateral tip. The agreements with both Coleman's and Mangler's theoretical studies, references 2 and 3, respectively, are shown to be reasonable. It is possible, however, that the agreement between references 1 and 3 may be misleading in that it suggests the use of theory in the prediction of inflow over the entire disk on the basis of limited comparison.

If the smoke technique of reference 1 could have been applied to more of the rotor disk and the tests could have been conducted on the retreating part of the rotor disk, it is possible that the forward and rearward or longitudinal inflow variations would not have agreed so well with the theories of references 2 and 3. It is also believed that the severest inflow variations occur in the outboard annulus of the disk and, therefore, any experimental program should include this region. Further experimental study is warranted and additional comparisons with theory are desirable.

Direct pressure and blade flapping measurements on a rotating blade offer a possible means of obtaining inflow distributions rather conveniently. The present program was concerned primarily with the experimental determination of pressure distributions and corresponding blade-motion data on a model rotor blade and with the possibility of obtaining inflow distributions therefrom. Rotor conditions for the most part were selected as representative of possible full-scale rotor operation.

Since no force and moment data for offset-flapping-hinge rotors were available, it was desirable to obtain some information for correlation with the theory previously developed in reference 4. The program, therefore, has included a brief experimental force and moment study on a typical offset model rotor having no cyclic pitch.

As a matter of refinement, reverse-flow effect has been introduced in the blade flapping analysis of reference 4 and a comparison has been made with the theory excluding reverse-flow effect as well as with experimental results.

This investigation was conducted at Massachusetts Institute of Technology under the sponsorship and with the financial assistance of the National Advisory Committee for Aeronautics.

SYMBOLS

A	total disk area, sq ft
A_0	mean blade pitch angle
a	lift slope, per radian
a_0	rotor coning angle
a_n	coefficient of $\cos n\psi$ in expression for β
B_n	coefficient of $\sin n\psi$ in expression for θ
b	number of blades per rotor
b_n	coefficient of $\sin n\psi$ in expression for β
C_D	drag coefficient, D/qA
C_L	lift coefficient, L/qA
C_l	rolling-moment coefficient, L'/qA
C_m	pitching-moment coefficient, M/qA
C_n	yawing-moment coefficient, N/qA

C_T	thrust coefficient, $T/\rho A \Omega^2 R^2$
C_Y	lateral-force coefficient, Y/qA
c	blade-section chord, ft unless otherwise stated
D	drag, lb
e	flapping-hinge offset, ft unless otherwise stated
I_1	blade mass moment of inertia about flapping hinge, slug-ft ²
i	relative power
L	lift, lb
L'	rolling moment, ft-lb
L_r	blade-element loading at radius r at any azimuth, lb/ft unless otherwise stated
M	pitching moment, ft-lb
m	mass of blade per foot of radius, slugs/ft
m_D	total mass of blade, slugs
N	yawing moment, ft-lb
Q	rotor torque, ft-lb
q	dynamic pressure, $\rho V^2/2$, lb/sq ft
R	blade radius, ft unless otherwise stated
r	radial distance to blade element, ft unless otherwise stated
T	rotor thrust, lb
U_p	component at blade element of resultant velocity perpendicular both to blade-span axis and to U_T , ft/sec
U_T	component at blade element of resultant velocity perpendicular to blade-span axis and to axis of no feathering, ft/sec
V	true airspeed of helicopter along flight path, ft/sec

v	induced inflow velocity at rotor, ft/sec
v_r	induced inflow velocity at span station r at any azimuth, ft/sec
x	ratio of blade-element radius to rotor-blade radius, r/R
x'	chordwise distance, ft unless otherwise stated
α	rotor angle of attack; angle between axis of no feathering and line perpendicular to flight path, positive when axis is pointing rearward, radians unless otherwise stated
α_r	blade-element angle of attack, radians unless otherwise stated
β	blade flapping angle at particular azimuth, $a_0 - a_1 \cos \psi - b_1 \sin \psi - a_2 \cos 2\psi - b_2 \sin 2\psi - \dots$, radians unless otherwise stated
γ	mass constant of rotor blade, $cpaR^4/I_1$
θ	blade-section pitch angle, $A_0 - B_1 \sin \psi - \dots$, radians unless otherwise stated
λ	inflow ratio, $(V \sin \alpha - v)/\Omega R$
λ_r	inflow ratio at span station r at any azimuth
μ	tip-speed ratio, $(V \cos \alpha)/\Omega R$
ξ	flapping-hinge offset ratio, e/R
ρ	mass density of air, slugs/cu ft
σ	rotor solidity, $bc/\pi R$
ψ	blade azimuth angle measured from downwind position in direction of rotation, radians unless otherwise stated
Ω	rotor angular velocity, radians/sec

APPARATUS AND METHODS

For the most part, the apparatus used in the present investigation was the same as that described in reference 5. Test procedure was

similar and the same zero- and 13-percent-offset flapping-hinge rotors were employed. Figures 1 to 4 summarize the blade geometry, wind-tunnel control and recording equipment, rotor installations, and rotor hub details. In brief, the rotor was two bladed with a diameter of 5 feet and had a 3-inch constant-chord blade with an NACA 0015 profile. The steel-spar and balsa-wood blade construction resulted in a section stiffness of 43,000 pound-inches squared and a uniform mass distribution of 0.0178 slug per foot. These blades were used on both the zero- and 13-percent offset rotors.

A more versatile and convenient measuring system replaced the autosyn system of reference 5 in the recording of blade flapping motion. The rotor of a small tuning capacitor was coupled to the flapping-hinge pin through gears which served to amplify the blade motion. The general installation and gearing details can be seen in figure 5. The variable capacitor was used in series with a 1,000-cycle source, amplifier, and rectifier. The resulting signal, recorded on an oscillograph, was a single trace whose amplitude was proportional to the angular displacement of the blade. Simultaneously recorded was a zero reference set relative to the rotor shaft axis which, in all but one test condition, corresponded to the axis of no feathering. The calibration curve of the recording equipment was linear over a $\pm 20^\circ$ range, and the sensitivity was of the order of $10^\circ/\text{inch}$ of galvanometer deflection. Sample records of blade motion are presented in figure 6.

The method of dynamic calibration of the pressure-measuring equipment essentially followed the method outlined in reference 5 with the exception of two changes. The vacuum-tube flush-type pressure standard was replaced by a Statham pressure gage, model P6-5D-350, and different amounts of lead in the electrical circuit were used for each span station. The introduction of variable lead made it possible to control amplitude distortion with frequency. The amplitude dynamic response of the pressure-measuring system appears in figure 8. It can be seen from the figure that the frequency-response characteristics of the pressure-measuring system are not altogether satisfactory at frequencies higher than the second. Small errors in aerodynamic loading are introduced as a result and may be significant in the reverse-flow region of the rotor disk where relatively low values of pressure occur and the higher harmonic components are of the same order of magnitude as the first. Although this consideration might affect the absolute magnitude of the downwash in these areas, it is expected that the overall trends indicated by the data are correct.

The distribution of inflow through a rotor disk from experimental aerodynamic loading and blade-motion data was determined as follows: From the continuous pressure-difference traces obtained at a number of points in the chordwise and spanwise directions, the spanwise aerodynamic loading was found at specific azimuths. The blade was then divided into a number of elements in the spanwise direction. For a given operating condition,

azimuth, and blade radius, an elemental loading L_r was obtained from which the blade-element angle of attack α_r was calculated for an assumed value of lift slope. Thus,

$$\alpha_r = \frac{2L_r}{\rho a c U_T^2}$$

which also had the equivalent form

$$\alpha_r = \theta + \frac{U_P}{U_T}$$

where

$$U_P = \lambda_r \Omega R - (r - e) \dot{\beta} - \mu \Omega R \beta \cos \psi$$

$$U_T = \Omega (r + \mu R \sin \psi)$$

$$\beta = a_0 - a_1 \cos \psi - b_1 \sin \psi - \dots$$

$$\dot{\beta} = a_1 \Omega \sin \psi - b_1 \Omega \cos \psi + \dots$$

$$r = xR$$

$$e = \xi R$$

Substitution of the above quantities into the second relation for blade-element angle of attack yields the following expression for blade-element inflow:

$$\lambda_r = (\theta - \alpha_r)(x + \mu \sin \psi) + (x - \xi)(a_1 \sin \psi - b_1 \cos \psi) + \mu \beta \cos \psi$$

It is evident that the blade-motion data are needed in the final computation of the inflow distribution. The flapping coefficients were determined from a graphical harmonic analysis of the recorded blade-motion data. The results are listed in table I.

The mounting rods of the rotor installation shown in figure 7 were redesigned to accommodate the support system of the M.I.T. Wright Brothers tunnel, which has a $7\frac{1}{2}$ - by 10-foot test section. This tunnel was used for the force and moment measurements on a typical offset rotor.

No corrections were applied to the data to account for the effects of tunnel-wall interference on the mean angle of attack of the rotor or to the angle-of-attack distribution over the rotor. Although such corrections might affect the magnitudes of the resultant downwash to some extent, particularly at the higher lift coefficients, it is expected that they would not significantly influence the overall conclusions that are drawn from the results.

RESULTS AND DISCUSSION

HOVERING

The problem of the determination of induced velocity or inflow distribution in the hovering case has been adequately solved by both theoretical and experimental methods. The solutions in references 6 and 7 are two illustrations. As an additional check on the instrumentation used in the current investigation, hovering inflow distribution was determined from experimental pressure measurements and compared with the theory of reference 6. The results are shown in figure 9. Agreement is reasonable, varying from a maximum discrepancy of 10 percent inboard to 15 percent at the tip. The experimental data used to find the hovering inflow distribution were taken from reference 5, which employed essentially the same measuring equipment. The theory assumes no tip losses. The test condition corresponds to a blade pitch setting of 8° , a tip speed of 209 feet per second, and a C_{Tl}/σ value of 0.061. A two-dimensional value of lift slope of 5.7 per radian was used in the analytical solution for the hovering inflow distribution. In general, inflow is referred to the axis or plane of no feathering and is considered negative downward through this plane.

SIMULATED FORWARD FLIGHT

General Considerations of Blade Flapping Motion

The blade flapping data were used to correct the lag in the pressure-measuring system in the same manner as described in reference 5. In summary, the fact that the azimuth of maximum flapping coincides with the azimuth of maximum aerodynamic moment establishes a boundary condition

which enables lag corrections to be made. It should be noted that these lag corrections agreed closely with those determined by dynamic calibration of the pressure-measuring system and therefore may be considered free from excessive error. The azimuth of maximum flapping was obtained from the blade-flapping results of table I. As previously mentioned, these coefficients were determined from graphical harmonic analyses. The flapping coefficients for the last rotor condition, involving cyclic pitch, were corrected to axis of no feathering. It will be noted that for the zero-offset rotor the change to the one-bladed rotor condition did not appreciably change the first-harmonic flapping coefficients. The b_1 coefficients for the 13-percent-offset rotor are all negative and opposite in sign to those for the zero-offset rotor. This is characteristic of the behavior of an offset rotor. For the two rotor conditions of $\mu = 0.30$ and 0.50 , the reduction in flapping due to offset can readily be seen.

The curves of figure 10 show the variations in blade flapping, lift, and relative power for a rotor with a 10-percent flapping-hinge offset and various values of blade mass constant. The changes in lift and power are seen to be negligible, but the corresponding changes in maximum blade flapping and flapping coefficients are rather severe and therefore may not be neglected. It is well then to note that the selection of blade mass constant for model testing, even when comparatively small offsets are involved, may be of importance in the simulation of full-scale blade flapping. This brief experimental study used the equipment pictured in figure 7.

Zero-Offset Rotor

Consideration of second- and first-harmonic pressure variations.-- Since the current zero-offset pressure data differed from the data recorded in reference 5 in that it contained relatively large second-harmonic variations, it was felt advisable to investigate first one rotor condition thoroughly. The rotor condition $\mu = 0.30$, $\xi = 0$, $A_0 = 8^\circ$, and $\alpha = -5^\circ$ was therefore selected for study and comparison. The results of this investigation appear in figures 11 to 29.

The curves of figures 11 and 12 are plots of the current aerodynamic data after the first graphical integration. The presence of the second-harmonic component is evidenced by the sizable variations in spanwise loading with azimuth. These data result in a loading concentration about the 30° azimuth near the tip. Details of the analysis of the rotor condition $\mu = 0.30$ and $\xi = 0$ recorded in reference 5 are presented in reference 8. Comparison of the loading curves of reference 8 (fig. 15) with those of figure 11 shows that the differences in loading appear at azimuths of 0° , 45° , 270° , and 315° .

A comparison of the resulting inflow distributions at two representative span stations for the two tests under discussion is shown in figure 16. The dashed curves refer to the test results of reference 8 which from a practical viewpoint contained no second-harmonic pressure variation. Inasmuch as the measured values of flapping for the two cases were the same, the curves of figure 16 reflect the change in inflow due to the differences in pressure data only. It is therefore concluded that the absence or presence of second-harmonic pressure variations is not a major factor in the consideration of inflow distribution.

It was expected that the strong second-harmonic pressure variation would appear in the plot of total lift against azimuth. The solid line of figure 18 is the result of the double integration of the pressure data. The predominant second harmonic is evident. The dashed curve was determined from conventional theory using a 3-percent tip loss in loading and a constant value of λ . The theoretical curve substantiates the experimental results.

Since the rotor under discussion had zero-offset hinges, any sizable first-harmonic aerodynamic moment would indicate faulty instrumentation. Therefore, it was necessary to determine the total aerodynamic-moment variation and analyze the result harmonically in order to prove the validity of the recorded data. A semigraphical integration method was used to compute the total aerodynamic-moment variation using the loading data of figure 11. The first-harmonic component was then removed and the remaining moment curve compared with the total. As can be seen from the comparison in figure 13, the first-harmonic contribution is negligible.

Comparison of theory and experiment.- Figure 14 gives the inflow distribution from the experimental loading and blade-motion data previously discussed in this section. It can be seen that the inflow is somewhat unique in distribution and is anything but uniform. In the azimuth range of 45° to 180° note the reversal in the values of inflow over the blade span with a minimum at $x = 0.55$. The dashes indicate local blade stall, stall being defined as $\alpha_r \geq 12^\circ$. Note the upwash (upward) trends at $\psi = 120^\circ$ and 240° . The contour plot of inflow, figure 15, clearly shows these trends. The small heavy-line circle in the center represents the area swept by the model hub and blade shanks. The crescent represents the reverse-flow region. Since the flight component of inflow $\mu \sin \alpha$ is equal to -0.026 , the contour line of -0.025 is the approximate boundary between areas of induced upwash and downwash. The area of upwash is somewhat undefined because of the inboard stall region in the retreating half of the cycle. The occurrence of the inboard stall before tip stall was probably due to the following two reasons: The rotor angle of attack (forward tilt) was about 1° less than the rearward tilt of the tip-path plane and the pressure was not converted to lift but left as normal force.

However, it is not believed that the use of normal force for lift had an appreciable effect on the remaining area of the rotor disk, where the blade angles of attack were relatively small. In all but two cases analyzed (deliberate stall and $\mu = 1.0$), the excessive stall regions were minimized by restricting rotor test conditions and therefore represent small percentages of the total disk area.

Because of the difference in the form of presentation, and the stated or implied rotor conditions, direct comparison of the model inflow data of figures 14 and 15 with the data in references 1, 2, 3, and 9 is not too practical. However, of interest are several similarities and dissimilarities of a general nature. Consider first the forward and rearward inflow variations of the above references. Since reference 1 includes forward and rearward inflow comparisons with references 2, 3, and 9, the immediate discussion will chiefly refer to this one investigation. The rotor condition of figure 10, reference 1, agrees more closely with model testing conditions than the other testing conditions investigated. For $i = 0$, the theory of reference 3 (Mangler curve) yields a variation similar to the experimental curve. The points of interest are the upwash shown for the forward part of the rotor disk and the quite linear variation throughout. The indicated forward and rearward inflow variation of figure 15 of this report differs in the forward part of the rotor disk. The experimental model data show a comparatively large induced downwash at the forward edge of the disk, at $\psi = 180^\circ$, and an upwash which appears fairly abruptly at about the 60-percent radius and remains to the center of the disk. An approximate axis of symmetry appears to exist about the $\psi = 330^\circ$ to 150° line. The variation from the center to the rearward portion of the disk ($\psi = 0^\circ$) is similar to theory in that it is somewhat linear. It is believed that, had the tests of reference 1 been conducted on the left or retreating part of the disk, larger lateral variations of inflow would have resulted and the fairing of one curve through all the experimental data would not have been satisfactory, and consequently the comparison with reference 2 would have been difficult.

The theoretical induced velocity contours for a disk incidence of 0° presented in references 9 and 3 (ref. 9 is a preliminary account of the theoretical development of ref. 3) can be compared with the experimental inflow contour of figure 15 for general differences in features. The most apparent difference is the lack of symmetry in the case of figure 15; the variations of inflow on the advancing part of the cycle differ markedly from those on the retreating part of the cycle. There is no provision for stall in the theory and therefore no stall areas are indicated on its contour. The large upwash at the lateral tips ($\psi = 270^\circ$ and 90°) is not present in the experimental contour, but rather a sizable downwash at $\psi = 270^\circ$ and nearly zero values at $\psi = 90^\circ$ are present. The theory and experiment are in better agreement for the rearward half of the rotor disk. Both show large downwash at about $\psi = 315^\circ$ and 45° and a gradual increase in downwash in the region about $\psi = 0^\circ$. It is apparent that better correlation between theory and experiment is desired.

Check on inflow calculation method.- In order to establish the validity of the proposed method for determining inflow from blade loading, it was considered desirable to compare a full cycle of computations starting with an initially established inflow, determining the corresponding airloads, and comparing the inflow computed from these airloads by this method with the initially assumed value. (A list of trigonometric functions found useful in the present analysis is given in appendix A.) The loading curves of figure 17 are the result based on the same flight conditions of advance ratio, rotor shaft inclination, and pitch setting which were used to obtain the experimental loading curves of figure 11 except that no tip-loss effects have been included in the theoretical analysis. The comparison of figures 17 and 11 shows differences of magnitude and variation although none are very severe except in the region of the blade tip. Figure 19 shows the results of the theoretical calculations of inflow based on the theoretically established airloads, for which the original value of λ had been computed to be -0.036 and has been obtained for the representative span stations of $x = 0.45$, 0.65, and 0.85. Because of small differences in the values of λ_r at a given azimuth, one curve was drawn to represent the azimuth inflow distribution. Slight variations about $\lambda_r = -0.036$ are shown particularly in the vicinity of $\psi = 315^\circ$. The reason for this may be the relatively large angles of attack in this neighborhood and the inadequacy of the method when angles close to stall are experienced by the blade. It can be concluded, however, that a reasonably constant value of inflow was obtained over the major portion of the disk and, therefore, the application of this method to experimental data can be expected to yield good results. The method was put to further test by recomputing the inflow distribution with 30-percent reduction in the second-harmonic aerodynamic loading component. As can be seen in figure 19, no major change in inflow resulted.

Effect of parameters on inflow calculation.- A more intensive investigation of the inflow calculation method was conducted which involved the combinations of experimental-loading-theoretical-blade-motion data and theoretical-loading-experimental-blade-motion data. The net result is presented in figures 20 to 22. The average values of inflow in figure 20 are seen to be about equal to those of the corresponding curves in figures 14 and 19, and the inflow variation is seen to be more severe than that of theory, figure 19. The introduction of experimental blade-motion data into theory necessitated the calculation of new loading curves, since the theoretical expression for loading involves blade-motion data. Figure 21 summarizes the loading distribution. The variation in inflow that resulted from the combination of this loading and experimental blade-motion data is shown in figure 22. From the consideration of figures 19, 20, and 22, it appears that any change from the constant λ assumption of theory, for example, the introduction of experimental loading or flapping data, results in inflow distributions of much larger variations.

An error investigation was conducted in order to establish the sensitivity of the resultant experimental inflow distributions to changes comparable with possible experimental errors. Figure 23 shows changes in inflow ratio $\Delta\lambda_r$ for various changes in flapping coefficients, pitch setting, loading, and lift slope. The span stations shown are those for which the change in inflow was a maximum and a minimum. It can be seen that the maximum inflow change occurs outboard and the minimum inboard, so that the delta inflow values for all the other span stations lie somewhere in between. Listed with each parameter is the percent error used, a positive sign indicating increased values. Figure 24 illustrates in detail the type of loading error ΔL_r taken. A reduced distribution of loading was used, in part, to compensate for the increase in pressure values due to the amplitude distortion. It is assumed that no likely combination of the errors could seriously alter the inflow distributions of figure 14.

One-bladed-rotor operation.— The analyzed one-bladed-rotor data are presented in figures 25 to 27. The rotor test conditions are identical to those of the two-bladed rotor previously discussed throughout this section. Figures 25, 26, and 27, therefore, are directly comparable with figures 11, 18, and 14, respectively. As can be seen from these plots of loading, total lift variation, and inflow distribution, no serious changes resulted from the removal of one blade from the rotor. It is interesting to note that the comparatively large differences in loading at $\psi = 0^\circ$ to $\psi = 90^\circ$, figures 25 and 11, do not result in very large differences in inflow distribution over this azimuth range, figures 27 and 14. The recorded data for the one- and two-bladed rotors are included in figures 28 and 29.

High-tip-speed-ratio operation.— The results of the zero-offset rotor condition $\mu = 0.50$ are presented in figures 30 to 33. There is a marked deviation from symmetrical loading around the disk and a pre-dominant second-harmonic lift variation, figures 30 and 31. In addition, there is a definite positive value of aerodynamic loading in the neighborhood of $r/R = 0.50$ and $\psi = 270^\circ$ (fig. 30) which is not expected at a tip-speed ratio of $\mu = 0.50$. Negative or close-to-zero values would appear more reasonable. It may be possible that these positive values are due to experimental error or the lack of satisfactory high-frequency-response characteristics of the pressure-measuring system. However, it should be noted that the remainder of the data presented in this report do not indicate such a positive loading condition in the region of reverse flow. The inflow variations of figure 32 are very great and a very large upwash is present in the region of $\psi = 90^\circ$ to 225° . The general phenomenon of the distribution is similar to that shown in figure 14.

Offset Rotor

Comparison of zero- and 13-percent-offset rotor operation.-- The rotor conditions corresponding to the $\mu = 0.30$ and $\mu = 0.50$ zero-offset tests were repeated using a 13-percent flapping-hinge offset. Similar to the zero-offset presentation, the analyzed data appear in figures 34 to 43. The expected strong first-harmonic variation in load is evidenced in figures 34 and 35, as well as in figures 40 and 41. Of particular note is the comparatively large forward and rearward hub moment indicated by the peaking of the load curve around $\psi = 150^\circ$ in figures 35 and 41. This is characteristic of all the offset load data obtained. The loading concentration on the disk in the neighborhood of $\psi = 150^\circ$ (fig. 36) and the general appearance of the lines of equal loading are compatible with the previously recorded offset data at $\mu = 0.22$ in reference 5. The inflow distributions of figure 37 are very different from the corresponding zero-offset distributions (fig. 14). There is a definite change from upwash to downwash in the vicinity of $\psi = 90^\circ$, a shift toward $\psi = 180^\circ$ of the inflow peaks, and a noticeable reduction in magnitudes of inflow. An approximate axis of symmetry appears to exist about the $\psi = 60^\circ$ to 240° line. The C_T/σ values of both rotors are the same. The difference in azimuth of maximum inflow can best be seen by comparing figure 38 with figure 15. The $\mu = 0.50$ inflow distributions of figure 42 resemble those of the lower tip-speed ratio ($\mu = 0.30$). The only major change is seen to be in magnitude. It should be realized, of course, that load distributions which were measured for the offset rotor would be quite different if sufficient cyclic pitch were employed to reduce the hub moments to zero. In fact, if the hub moments were canceled by cyclic pitch, the rotor conditions would in effect be equivalent to the zero-offset case and the resulting load distributions therefore would be the same.

High-tip-speed-ratio operation.-- The third offset-rotor condition analyzed ($\mu = 1.0$) is presented as spanwise loading, total lift per blade, and inflow distribution plots, figures 44 to 47. The rotor values of $\alpha = -15^\circ$ and $A_0 = 17^\circ$ were selected for this high-tip-speed-ratio operation. Considerable blade stall resulted in the retreating half of the disk. The plots of figures 44 and 45, therefore, necessarily include stall. Although the inflow distributions of figure 46 are incomplete, some noticeable trends are present. The inflow appears to be comparatively strong and uniform for the advancing part of the disk. Subtracting the flight component $\mu \sin \alpha$ from the inflow, it can be seen that the remaining induced portion of the inflow is quite small in this area; this is expected. The large upwash shown for the other half of the disk is indicative of the negative lift present.

Consideration of excessive stall and cyclic pitch.-- Some interest has been expressed about the effect of excessive stall and cyclic pitch

on loading distributions. The rotor condition of $\mu = 0.30$ and $\xi = 0.13$ was therefore modified to include deliberate stall and cyclic pitch as two of the tests to be analyzed. Figures 48 to 54 include the resulting data from these tests. The values of loading for deliberate stall (fig. 48) are seen to be about twice those corresponding to the rotor condition of $\mu = 0.30$, $\xi = 0.13$, $A_0 = 8^\circ$, and $\alpha = -5^\circ$ (fig. 34). Without direct measurement of either drag, lift, or power, it was difficult to determine the extent of the stall condition.

Figures 51 and 52 show the results of introducing 3° of cyclic pitch into the rotor condition described in figure 34. The effect of the cyclic pitch on pitch setting was to reduce the latter 3° at $\psi = 90^\circ$. The rotor angle of attack is referred to the axis of no feathering which accounts for the change from $\alpha = -5^\circ$ to -8° . As can be seen from figures 51 and 52, the introduction of cyclic pitch caused a reduction in loading and lift, as might be expected from the resulting decrease in blade angle of attack in the advancing part of the disk. The inflow distribution resulting from an introduction of 3° of cyclic pitch (fig. 53) is seen to be similar to that obtained without cyclic pitch (fig. 37). The region of upwash of figure 53 is approximately the same as that of figure 37 when the respective values of $\mu \sin \alpha$ are considered. The character of the inflow curves, in both cases, is chiefly due to the presence of the offset flapping hinge. Supplementary studies of offset-rotor behavior and experimental records of other rotor conditions are included in appendixes B to D. It is hoped that this additional information will aid in the understanding of the change in inflow distribution caused by the introduction of flapping offset hinges.

CONCLUSIONS

Inflow distributions, azimuth and spanwise, were determined from measured pressure distributions and blade-motion data on a model helicopter rotor blade under hovering and simulated forward-flight conditions. Pressure and corresponding blade flapping were recorded for various rotor conditions at tip-speed ratios of 0.10 to 1.00. Both zero- and 13-percent flapping-hinge-offset lifting rotors were tested, with no cyclic pitch used to balance out the hub moments resulting from the use of offset hinges. On the basis of the experimental and theoretical treatments presented, the following conclusions may be drawn:

1. Reasonable agreement was obtained between hovering induced velocity distribution calculated from theory and that derived from rotor blade pressure measurements.
2. Although the pressure data for the forward-flight zero-offset rotor condition show the presence of a second-harmonic component, it is not a major factor in the consideration of inflow distribution.

3. The experimental results of this investigation show larger inflow variations than were predicted by theory; however, previous indications of upflow over the forward portion of the rotor disk and relatively large induced velocity at the trailing edge were verified.

4. The inflow contour plots indicate different distributions on the advancing and retreating sides of the rotor disk. An approximate axis of symmetry appears to exist about the line from azimuth angles 330° to 150° for the zero-offset condition and about the line from azimuth angles 60° to 240° for the 13-percent-offset condition.

5. The zero-offset and 13-percent-offset rotors operating under the same conditions, except for the presence of hub moments in the offset-hinge case, are found to produce inflow patterns which differ appreciably in general character.

6. Results of tests on a model rotor having a 10-percent flapping-hinge offset indicate that at a given tip-speed ratio large variations in blade flapping occur with changes in blade mass constant.

Massachusetts Institute of Technology,
Cambridge, Mass., October 7, 1953.

APPENDIX AEXPANSION OF TRIGONOMETRIC FUNCTIONSENCOUNTERED IN HELICOPTER ANALYSES

The following list of trigonometric relationships which were found useful in the present analysis and which frequently appear in helicopter work are given for convenient reference:

$$\sin^2 \phi = 1/2 (1 - \cos 2\phi)$$

$$\sin \phi \sin 2\phi = 1/2 (\cos \phi - \cos 3\phi)$$

$$\sin \phi \sin 3\phi = 1/2 (\cos 2\phi - \cos 4\phi)$$

$$\sin \phi \sin 4\phi = 1/2 (\cos 3\phi - \cos 5\phi)$$

$$\sin \phi \sin 5\phi = 1/2 (\cos 4\phi - \cos 6\phi)$$

$$\sin \phi \sin 6\phi = 1/2 (\cos 5\phi - \cos 7\phi)$$

$$\sin^3 \phi = 1/4 (3 \sin \phi - \sin 3\phi)$$

$$\sin^4 \phi = \frac{3}{8} - \frac{1}{2} \cos 2\phi + \frac{1}{8} \cos 4\phi$$

$$\sin^5 \phi = \frac{5}{8} \sin \phi - \frac{5}{16} \sin 3\phi + \frac{1}{16} \sin 5\phi$$

$$\sin^2 \phi \sin 2\phi = \frac{1}{2} \sin 2\phi - \frac{1}{4} \sin 4\phi$$

$$\sin^2 \phi \sin 3\phi = \frac{1}{2} \sin 3\phi - \frac{1}{4} \sin \phi - \frac{1}{4} \sin 5\phi$$

$$\sin^3 \phi \sin 2\phi = \frac{1}{4} \cos \phi - \frac{3}{8} \cos 3\phi + \frac{1}{8} \cos 5\phi$$

$$\sin^3 \phi \sin 3\phi = -\frac{1}{8} + \frac{3}{8} \cos 2\phi - \frac{3}{8} \cos 4\phi + \frac{1}{8} \cos 6\phi$$

$$\sin^4 \phi \sin 2\phi = \frac{5}{16} \sin 2\phi - \frac{1}{4} \sin 4\phi + \frac{1}{16} \sin 6\phi$$

$$\sin^4 \phi \sin 3\phi = -\frac{5}{16} \sin \phi + \frac{3}{8} \sin 3\phi - \frac{1}{4} \sin 5\phi + \frac{1}{16} \sin 7\phi$$

$$\cos^2 \phi = 1/2 (1 + \cos 2\phi)$$

$$\cos \phi \cos 2\phi = 1/2 (\cos \phi + \cos 3\phi)$$

$$\cos \phi \cos 3\phi = 1/2 (\cos 2\phi + \cos 4\phi)$$

$$\cos \phi \cos 4\phi = 1/2 (\cos 3\phi + \cos 5\phi)$$

$$\cos \phi \cos 5\phi = 1/2 (\cos 4\phi + \cos 6\phi)$$

$$\cos \phi \cos 6\phi = 1/2 (\cos 5\phi + \cos 7\phi)$$

$$\cos^3 \phi = 1/4 (3 \cos \phi + \cos 3\phi)$$

$$\cos^4 \phi = \frac{3}{8} + \frac{3}{4} \cos 2\phi + \frac{3}{8} \cos 4\phi$$

$$\cos^5 \phi = \frac{3}{4} \cos \phi + \frac{9}{16} \cos 3\phi + \frac{3}{16} \cos 5\phi$$

$$\cos^2 \phi \cos 2\phi = \frac{1}{4} + \frac{1}{2} \cos 2\phi + \frac{1}{4} \cos 4\phi$$

$$\cos^2 \phi \cos 3\phi = \frac{1}{4} \cos \phi + \frac{1}{2} \cos 3\phi + \frac{1}{4} \cos 5\phi$$

$$\cos^3 \phi \cos 2\phi = \frac{1}{2} \cos \phi + \frac{3}{8} \cos 3\phi + \frac{1}{8} \cos 5\phi$$

$$\cos^3 \phi \cos 3\phi = \frac{1}{8} + \frac{3}{8} \cos 2\phi + \frac{3}{8} \cos 4\phi + \frac{1}{8} \cos 6\phi$$

$$\cos^4 \phi \cos 2\phi = \frac{1}{4} + \frac{7}{16} \cos 2\phi + \frac{1}{4} \cos 4\phi + \frac{1}{16} \cos 6\phi$$

$$\cos^4 \phi \cos 3\phi = \frac{5}{16} \cos \phi + \frac{3}{8} \cos 3\phi + \frac{1}{4} \cos 5\phi + \frac{1}{16} \cos 7\phi$$

$$\cos \phi \sin 2\phi = 1/2 (\sin 3\phi + \sin \phi)$$

$$\cos \phi \sin 3\phi = 1/2 (\sin 4\phi + \sin 2\phi)$$

$$\cos \phi \sin 4\phi = 1/2 (\sin 5\phi + \sin 3\phi)$$

$$\cos \phi \sin 5\phi = 1/2 (\sin 6\phi + \sin 4\phi)$$

$$\cos \phi \sin 6\phi = 1/2 (\sin 7\phi + \sin 5\phi)$$

$$\sin \phi \cos \phi = 1/2 \sin 2\phi$$

$$\sin \phi \cos 2\phi = 1/2 (\sin 3\phi - \sin \phi)$$

$$\sin \phi \cos 3\phi = 1/2 (\sin 4\phi - \sin 2\phi)$$

$$\sin \phi \cos 4\phi = 1/2 (\sin 5\phi - \sin 3\phi)$$

$$\sin \phi \cos 5\phi = 1/2 (\sin 6\phi - \sin 4\phi)$$

$$\sin \phi \cos 6\phi = 1/2 (\sin 7\phi - \sin 5\phi)$$

$$\sin^2 \phi \cos \phi = 1/4 (\cos \phi - \cos 3\phi)$$

$$\sin^2 \phi \cos 2\phi = -\frac{1}{4} + \frac{1}{2} \cos 2\phi - \frac{1}{4} \cos 4\phi$$

$$\sin^3 \phi \cos \phi = \frac{1}{4} \sin 2\phi - \frac{1}{8} \sin 4\phi$$

$$\sin^3 \phi \cos 2\phi = -\frac{1}{2} \sin \phi + \frac{3}{8} \sin 3\phi - \frac{1}{8} \sin 5\phi$$

$$\sin^4 \phi \cos \phi = \frac{1}{8} \cos \phi - \frac{3}{16} \cos 3\phi + \frac{1}{16} \cos 5\phi$$

$$\sin^4 \phi \cos 2\phi = -\frac{1}{4} + \frac{7}{16} \cos 2\phi - \frac{1}{4} \cos 4\phi + \frac{1}{16} \cos 6\phi$$

$$\cos^2 \phi \sin \phi = 1/4 (\sin \phi + 3\phi)$$

$$\cos^2 \phi \sin 2\phi = \frac{1}{2} \sin 2\phi + \frac{1}{4} \sin 4\phi$$

$$\cos^3 \phi \sin \phi = \frac{1}{4} \sin 2\phi + \frac{1}{8} \sin 4\phi$$

$$\cos^3 \phi \sin 2\phi = \frac{1}{4} \sin \phi + \frac{3}{8} \sin 3\phi + \frac{1}{8} \sin 5\phi$$

$$\cos^4 \phi \sin \phi = \frac{1}{8} \sin \phi + \frac{3}{16} \sin 3\phi + \frac{1}{16} \sin 5\phi$$

$$\cos^4 \phi \sin 2\phi = \frac{5}{16} \sin 2\phi + \frac{1}{4} \sin 4\phi + \frac{1}{16} \sin 6\phi$$

$$\sin^2 \phi \cos^2 \phi = \frac{1}{8} - \frac{1}{8} \cos 4\phi$$

$$\sin^2\phi \cos^3\phi = \frac{1}{8} \cos \phi - \frac{1}{16} \cos 3\phi - \frac{1}{16} \cos 5\phi$$

$$\sin^3\phi \cos^2\phi = \frac{1}{8} \sin \phi + \frac{1}{16} \sin 3\phi - \frac{1}{16} \sin 5\phi$$

$$\sin^2\phi \cos \phi \sin 2\phi = \frac{1}{4} \sin \phi + \frac{1}{8} \sin 3\phi - \frac{1}{8} \sin 5\phi$$

$$\sin^2\phi \cos \phi \cos 2\phi = \frac{1}{8} \cos 3\phi - \frac{1}{8} \cos 5\phi$$

$$\sin^3\phi \cos \phi \sin 2\phi = \frac{1}{8} - \frac{1}{16} \cos 2\phi - \frac{1}{8} \cos 4\phi + \frac{1}{16} \cos 6\phi$$

$$\sin^3\phi \cos \phi \cos 2\phi = -\frac{1}{16} \sin 2\phi + \frac{1}{8} \sin 4\phi - \frac{1}{16} \sin 6\phi$$

$$\cos \phi \sin \phi \sin 2\phi = \frac{1}{4} - \frac{1}{4} \cos 4\phi = 2 \cos^2\phi \sin^2\phi$$

$$\cos \phi \sin \phi \sin 3\phi = 1/4 (\cos \phi - \cos 5\phi)$$

$$\cos \phi \sin \phi \cos 2\phi = \frac{1}{4} \sin 4\phi$$

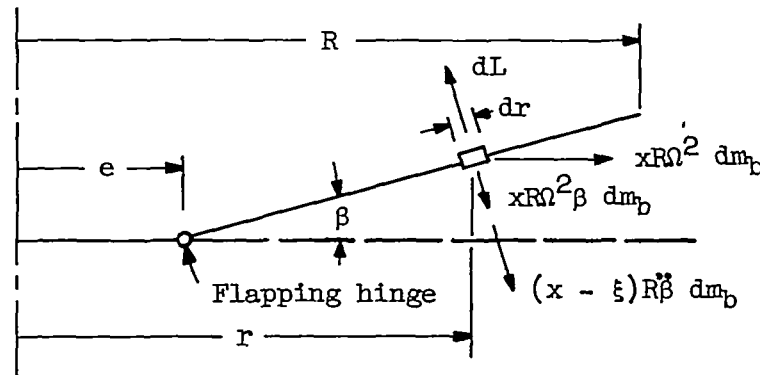
$$\cos \phi \sin \phi \cos 3\phi = 1/4 (\sin 5\phi - \sin \phi)$$

APPENDIX B

ANALYSIS OF AN OFFSET FLAPPING BLADE, INCLUDING REVERSE-FLOW EFFECTS

Since a considerable amount of the work in this report is concerned with offset-rotor operation at high advance ratios, an analysis has been carried out for this condition in order to provide a better basis for comparison. The previous analysis of an offset flapping blade developed in reference 4 neglected the effect of reverse flow. The present analysis includes reverse flow and applies the results to obtain a comparison with the previous analytical study and tests.

Derivation of flapping coefficients.— Consider a rotor blade having a flapping-hinge offset whose distance is e from the center of rotation. The forces acting on such a blade are shown in the following diagram:



The equilibrium of moments about the flapping hinge is expressed by the following equation which includes reverse-flow effects:

$$\int_{\xi}^1 (x - \xi) R dL - 2 \int_{\xi}^{-\mu \sin \psi} (x - \xi) R dL =$$

$$\int_{\xi}^1 \left[x R^2 \Omega^2 (x - \xi) \beta + (x - \xi)^2 R^2 \beta \ddot{\beta} \right] dm_b \quad (1)$$

The method of analysis follows that of reference 4, except that it is necessary here to include the second harmonic in the expression for blade flapping. The right-hand side of equation (1), representing the inertia moment, becomes:

$$\begin{aligned}
M_1 = \Omega^2 R^2 \int_{\xi}^1 & \left[(x - \xi)^2 (a_0 - a_1 \cos \psi - b_1 \sin \psi - a_2 \cos 2\psi - b_2 \sin 2\psi) + \right. \\
& \xi(x - \xi)(a_0 - a_1 \cos \psi - b_1 \sin \psi - a_2 \cos 2\psi - b_2 \sin 2\psi) + \\
& \left. (x - \xi)^2 (a_1 \cos \psi + b_1 \sin \psi + 4a_2 \cos 2\psi + 4b_2 \sin 2\psi) \right] dm_b \quad (2)
\end{aligned}$$

Let

$$I_1 = R^2 \int_{\xi}^1 (x - \xi)^2 dm_b \quad (3)$$

$$\zeta = \frac{\xi R^2}{I_1} \int_{\xi}^1 (x - \xi) dm_b \quad (4)$$

Equation (2) therefore becomes

$$\begin{aligned}
\frac{M_1}{I_1 \Omega^2} = a_0(1 + \zeta) - a_1 \zeta \cos \psi - b_1 \zeta \sin \psi + \\
a_2(3 - \zeta) \cos 2\psi + b_2(3 - \zeta) \sin 2\psi \quad (5)
\end{aligned}$$

In treating the left side of equation (1) an approximation is introduced by changing the lower limit of integration from ξ to 0. This is done to facilitate the process of combining the two Fourier series that are obtained from each of the two aerodynamic moment terms. Let

$$M_a = \int_0^1 (x - \xi) R dL - 2 \int_0^{-\mu \sin \psi} (x - \xi) R dL = M_a' + M_a'' \quad (6)$$

where the series M_a' is applicable in the entire region 0 to 2π , and M_a'' is applicable only from π to 2π . Now

$$dL = \frac{1}{2} \rho a c R \left[\theta U_T^2 + U_P U_T \right] dx \quad (7)$$

where

$$U_P = \lambda \Omega R - (x - \xi) R \dot{\beta} - \mu \Omega R \beta \cos \psi \quad (8)$$

$$U_T = \Omega R [x + \mu \sin \psi] \quad (9)$$

$$\theta = A_0 - B_1 \sin \psi \quad (10)$$

$$\dot{\beta} = a_1 \Omega \sin \psi - b_1 \Omega \cos \psi + 2a_2 \Omega \sin 2\psi - 2b_2 \Omega \cos 2\psi \quad (11)$$

Equation 7 becomes

$$\begin{aligned} dL = \frac{1}{2} \rho a c \Omega^2 R^3 & \left[A_0 (x^2 + 2\mu x \sin \psi + \mu^2 \sin^2 \psi) - B_1 (x^2 \sin \psi + \right. \\ & 2\mu x \sin^2 \psi + \mu^2 \sin^3 \psi) + \lambda (x + \mu \sin \psi) - x(x - \xi) a_1 \sin \psi + \\ & x(x - \xi) b_1 \cos \psi - 2x(x - \xi) a_2 \sin 2\psi + 2x(x - \xi) b_2 \cos 2\psi - \\ & \mu(x - \xi) a_1 \sin^2 \psi + \mu(x - \xi) b_1 \sin \psi \cos \psi - \\ & 2\mu(x - \xi) a_2 \sin \psi \sin 2\psi + 2\mu(x - \xi) b_2 \sin \psi \cos 2\psi - \\ & \mu x a_0 \cos \psi + \mu x a_1 \cos^2 \psi + \mu x b_1 \sin \psi \cos \psi + \mu x a_2 \cos \psi \cos 2\psi + \\ & \mu x b_2 \cos \psi \sin 2\psi - \mu^2 a_0 \cos \psi \sin \psi + \mu^2 a_1 \sin \psi \cos^2 \psi + \\ & \mu^2 b_1 \cos \psi \sin^2 \psi + \mu^2 a_2 \sin \psi \cos \psi \cos 2\psi + \\ & \left. \mu^2 b_2 \sin \psi \cos \psi \sin 2\psi \right] dx \quad (12) \end{aligned}$$

Retaining terms through second harmonic only, equation (12) becomes

$$\begin{aligned}
 dL = \frac{1}{2} \rho a c \Omega^2 R^3 & \left[A_0 \left(x^2 + \frac{\mu^2}{2} + 2\mu x \sin \psi - \frac{\mu^2}{2} \cos 2\psi \right) - B_1 \left(\mu x + \right. \right. \\
 & x^2 \sin \psi + \frac{3}{4} \mu^2 \sin \psi - \mu x \cos 2\psi \left. \right) + \lambda (x + \mu \sin \psi) - \\
 & x(x - \xi) a_1 \sin \psi + x(x - \xi) b_1 \cos \psi - 2x(x - \xi) a_2 \sin 2\psi + \\
 & 2x(x - \xi) b_2 \cos 2\psi + \frac{\mu a_1}{2} \xi + \mu a_2 \xi \cos \psi + \mu b_2 \xi \sin \psi + \\
 & \mu a_1 x \cos 2\psi - \frac{\mu a_1}{2} \xi \cos 2\psi + \mu x b_1 \sin 2\psi - \frac{\mu b_1}{2} \xi \sin 2\psi - \\
 & \mu x a_0 \cos \psi - \frac{\mu x a_2}{2} \cos \psi - \frac{\mu x b_2}{2} \sin \psi + \frac{\mu^2 b_2}{4} + \frac{\mu^2 a_1}{4} \sin \psi + \\
 & \left. \frac{\mu^2 b_1}{4} \cos \psi - \frac{\mu^2 a_0}{2} \sin 2\psi \right] dx \quad (13)
 \end{aligned}$$

If a uniform blade is considered, the following integrals are useful:

Let

$$\left. \begin{aligned}
 A &= \int_0^1 (x - \xi)^2 x \, dx = \frac{1}{4} - \frac{2}{3} \xi + \frac{\xi^2}{2} \\
 B &= \int_0^1 (x - \xi) x^2 \, dx = \frac{1}{4} - \frac{\xi}{3} \\
 C &= \int_0^1 (x - \xi) x \, dx = \frac{1}{3} - \frac{\xi}{2} \\
 D &= \int_0^1 (x - \xi) \xi \, dx = \frac{\xi}{2} - \xi^2 \\
 E &= \int_0^1 (x - \xi) \, dx = \frac{1}{2} - \xi
 \end{aligned} \right\} \quad (14)$$

The expression for M_a' then becomes

$$\begin{aligned}
 \frac{M_a'}{I_1 \Omega^2} &= \frac{1}{I_1 \Omega^2} \int_0^1 (x - \xi) R \, dL \\
 &= \frac{\gamma}{2} \left\{ A_0 \left(B + \frac{\mu^2 E}{2} \right) - \mu B_1 C + \lambda C + \frac{\mu a_1}{2} D + \frac{\mu^2 b_2}{4} E + \right. \\
 &\quad \left[2\mu A_0 C - B_1 \left(B + \frac{3}{4} \mu^2 E \right) + \mu \lambda E - a_1 \left(A - \frac{\mu^2}{4} E \right) + \mu b_2 \left(D - \frac{C}{2} \right) \right] \sin \psi + \\
 &\quad \left[-\mu a_0 C + b_1 \left(A + \frac{\mu^2}{4} E \right) + \mu a_2 \left(D - \frac{C}{2} \right) \right] \cos \psi + \\
 &\quad \left[-\frac{\mu^2 a_0}{2} E + \mu b_1 \left(C - \frac{D}{2} \right) - 2a_2 A \right] \sin 2\psi + \\
 &\quad \left. \left[-A_0 \frac{\mu^2}{2} E + \mu B_1 C + \mu a_1 \left(C - \frac{D}{2} \right) + 2b_2 A \right] \cos 2\psi \right\} \quad (15)
 \end{aligned}$$

The expression for M_a'' is obtained by considering the following integrals, which result from the assumption of a uniform blade:

$$\left. \begin{aligned}
 A' &= \int_0^{-\mu \sin \psi} (x - \xi)^2 x \, dx = \frac{\mu^4}{4} \sin^4 \psi + \frac{2}{3} \mu^3 \xi \sin^3 \psi + \frac{\xi^2}{2} \mu^2 \sin^2 \psi \\
 B' &= \int_0^{-\mu \sin \psi} (x - \xi) x^2 \, dx = \frac{\mu^4}{4} \sin^4 \psi + \frac{\mu^3 \xi}{3} \sin^3 \psi \\
 C' &= \int_0^{-\mu \sin \psi} (x - \xi) x \, dx = -\frac{\mu^3}{3} \sin^3 \psi - \frac{\mu^2 \xi}{2} \sin^2 \psi \\
 D' &= \int_0^{-\mu \sin \psi} (x - \xi) \xi \, dx = \frac{\mu^2 \xi}{2} \sin^2 \psi + \mu \xi^2 \sin \psi \\
 E' &= \int_0^{-\mu \sin \psi} (x - \xi) \, dx = \frac{\mu^2}{2} \sin^2 \psi + \mu \xi \sin \psi
 \end{aligned} \right\} \quad (16)$$

It is necessary to substitute the values of these integrals into the expression for dL since they contain trigonometric functions. Using then equation (12), the expression for M_a'' becomes

$$\begin{aligned}
 \frac{M_a''}{I_1 \Omega^2} = & \frac{-2}{I_1 \Omega^2} \int_0^{-\mu \sin \psi} (x - \xi) R \, dL = -\gamma \left[A_0 \left(\frac{1}{12} \mu^4 \sin^4 \psi + \frac{\mu^3 \xi}{3} \sin^3 \psi \right) - \right. \\
 & B_1 \left(\frac{1}{12} \mu^4 \sin^5 \psi + \frac{\mu^3 \xi}{3} \sin^4 \psi \right) + \lambda \left(\frac{\mu^3}{6} \sin^3 \psi + \frac{\mu^2 \xi}{2} \sin^2 \psi \right) - \\
 & a_0 \left(\frac{\mu^4}{6} \sin^3 \psi \cos \psi + \frac{\mu^3 \xi}{2} \sin^2 \psi \cos \psi \right) - a_1 \left(\frac{\mu^4}{4} \sin^5 \psi + \right. \\
 & \left. \frac{\mu^3 \xi}{6} \sin^4 \psi - \frac{\mu^2 \xi^2}{2} \sin^3 \psi + \frac{\mu^4}{3} \sin^3 \psi \cos 2\psi - \frac{\mu^4}{2} \sin^3 \psi \cos^2 \psi - \right. \\
 & \left. \mu^3 \xi \sin^2 \psi \cos^2 \psi + \frac{\mu^3 \xi}{2} \sin^2 \psi \cos 2\psi \right) + b_1 \left(\frac{3}{4} \mu^4 \sin^4 \psi \cos \psi + \right. \\
 & \left. \frac{5}{3} \mu^3 \xi \sin^3 \psi \cos \psi + \frac{\mu^2 \xi^2}{2} \sin^2 \psi \cos \psi - \frac{\mu^4}{3} \sin^3 \psi \sin 2\psi - \right. \\
 & \left. \frac{3}{4} \mu^3 \xi \sin^2 \psi \sin 2\psi - \frac{\mu^2 \xi^2}{2} \sin \psi \sin 2\psi \right) + a_2 \left(\frac{\mu^4}{6} \sin^4 \psi \sin 2\psi + \right. \\
 & \left. \frac{2}{3} \mu^3 \xi \sin^3 \psi \sin 2\psi + \mu^2 \xi^2 \sin^2 \psi \sin 2\psi + \frac{\mu^4}{6} \sin^3 \psi \cos \psi \cos 2\psi + \right. \\
 & \left. \frac{\mu^3 \xi}{2} \sin^2 \psi \cos \psi \cos 2\psi \right) + b_2 \left(-\frac{\mu^4}{6} \sin^4 \psi \cos 2\psi - \right. \\
 & \left. \frac{2}{3} \mu^3 \xi \sin^3 \psi \cos 2\psi - \mu^2 \xi^2 \sin^2 \psi \cos 2\psi + \frac{\mu^4}{6} \sin^3 \psi \cos \psi \sin 2\psi + \right. \\
 & \left. \frac{\mu^3 \xi}{2} \sin^2 \psi \cos \psi \sin 2\psi \right) \Bigg] \quad (17)
 \end{aligned}$$

Retaining terms through the second harmonic only, equation (17) becomes

$$\begin{aligned}
\frac{M_a''}{I_1 \Omega^2} = & -\gamma \left\{ A_0 \left[\frac{\mu^4}{12} \left(\frac{3}{8} - \frac{\cos 2\psi}{2} \right) + \frac{\mu^3 \xi}{4} \sin \psi \right] - \right. \\
& B_1 \left[\frac{5}{96} \mu^4 \sin \psi + \frac{\mu^3 \xi}{3} \left(\frac{3}{8} - \frac{\cos 2\psi}{2} \right) \right] + \lambda \left[\frac{\mu^3}{8} \sin \psi + \frac{\mu^2 \xi}{4} (1 - \cos 2\psi) \right] - \\
& a_0 \left(\frac{\mu^4}{24} \sin 2\psi + \frac{\mu^3 \xi}{8} \cos \psi \right) - a_1 \left[\frac{5}{32} \mu^4 \sin \psi + \frac{\mu^3 \xi}{6} \left(\frac{3}{8} - \frac{\cos 2\psi}{2} \right) - \right. \\
& \left. \frac{3}{8} \mu^2 \xi^2 \sin \psi - \frac{\mu^4}{6} \sin \psi - \frac{\mu^4}{16} \sin \psi - \frac{\mu^3 \xi}{8} + \frac{\mu^3 \xi}{2} \left(-\frac{1}{4} + \frac{\cos 2\psi}{2} \right) \right] + \\
& b_1 \left(\frac{3}{32} \mu^4 \cos \psi + \frac{5}{12} \mu^3 \xi \sin 2\psi + \frac{\mu^2 \xi^2}{8} \cos \psi - \frac{\mu^4}{12} \cos \psi - \right. \\
& \left. \frac{3}{8} \mu^3 \xi \sin 2\psi - \frac{\mu^2 \xi^2}{4} \cos \psi \right) + a_2 \left(\frac{5}{96} \mu^4 \sin 2\psi + \frac{\mu^3}{6} \xi \cos \psi + \right. \\
& \left. \frac{\mu^2 \xi^2}{2} \sin 2\psi - \frac{\mu^4}{96} \sin 2\psi \right) + b_2 \left(\frac{\mu^4}{24} - \frac{7}{96} \mu^4 \cos 2\psi + \frac{\mu^3}{3} \xi \sin \psi + \right. \\
& \left. \frac{\mu^2 \xi^2}{4} - \frac{\mu^2 \xi^2}{2} \cos 2\psi + \frac{\mu^4}{48} - \frac{\mu^4}{96} \cos 2\psi + \frac{\mu^3 \xi}{8} \sin \psi \right) \left. \right\} \quad (18)
\end{aligned}$$

Collecting terms, the expression for M_a'' finally is obtained as follows:

$$\begin{aligned}
\frac{M_a''}{I_1 \Omega^2} = & -\gamma \left\{ A_0 \frac{\mu^4}{32} - B_1 \frac{\mu^3 \xi}{8} + \lambda \frac{\mu^2 \xi}{4} + \frac{3}{16} a_1 \mu^3 \xi + b_2 \left(\frac{\mu^4}{16} + \frac{\mu^2 \xi^2}{4} \right) + \right. \\
& \left[A_0 \frac{\mu^3 \xi}{4} - B_1 \frac{5}{96} \mu^4 + \lambda \frac{\mu^3}{8} + a_1 \left(\frac{7}{96} \mu^4 + \frac{3}{8} \mu^2 \xi^2 \right) + \frac{11}{24} \mu^3 \xi b_2 \right] \sin \psi + \\
& \left[-a_0 \frac{\mu^3 \xi}{8} + b_1 \left(\frac{\mu^4}{96} - \frac{1}{8} \mu^2 \xi^2 \right) + a_2 \frac{\mu^3}{6} \xi \right] \cos \psi + \left[-a_0 \frac{\mu^4}{24} + b_1 \frac{\mu^3 \xi}{24} + \right. \\
& a_2 \left(\frac{\mu^4}{24} + \frac{\mu^2 \xi^2}{2} \right) \sin 2\psi + \left[A_0 \frac{\mu^4}{24} + B_1 \frac{\mu^3 \xi}{6} - \lambda \frac{\mu^2 \xi}{4} - a_1 \frac{\mu^3 \xi}{6} + \right. \\
& \left. b_2 \left(-\frac{\mu^4}{12} - \frac{\mu^2 \xi^2}{2} \right) \cos 2\psi \right] \left. \right\} \quad (19)
\end{aligned}$$

The two Fourier series given in equations (15) and (19) are combined, in accordance with relationships given in reference 10, to yield a series which is applicable to the entire region of the disk from 0 to 2π . Corresponding terms of this series and that given in equation (5) are equated to obtain the following expressions:

$$\begin{aligned} \frac{2a_0}{\gamma}(1 + \xi) = & A_0 \left(B + \frac{\mu^2}{2} E - \frac{\mu^4}{32} + 0.159\mu^3\xi \right) + B_1 \left(-\mu C + \frac{\mu^3}{8} \xi - 0.0331\mu^4 \right) + \\ & \lambda \left(C - \frac{\mu^2\xi}{4} + 0.08\mu^3 \right) + a_1 \left(\frac{\mu D}{2} - \frac{3}{16} \mu^3\xi + 0.239\mu^2\xi^2 + 0.0464\mu^4 \right) + \\ & b_2 \left(\frac{\mu^2 E}{4} - \frac{\mu^4}{16} - \frac{\mu^2\xi^2}{4} + 0.291\mu^3\xi \right) \end{aligned} \quad (20)$$

$$\begin{aligned} \frac{-2a_1\xi}{\gamma} = & a_0(-\mu C - 0.0354\mu^4) + b_1 \left(A + \frac{\mu^4}{4} E + 0.0354\mu^3\xi \right) + a_2 \left(\mu D - \frac{\mu}{2} C + \right. \\ & \left. 0.0088\mu^4 + 0.424\mu^2\xi^2 \right) \end{aligned} \quad (21)$$

$$\begin{aligned} \frac{-2b_1\xi}{\gamma} = & A_0 \left(2\mu C + 0.0531\mu^4 - \frac{\mu^3\xi}{4} \right) + B_1 \left(-B - \frac{3}{4} \mu^2 E - 0.212\mu^3\xi + \frac{5}{96} \mu^4 \right) + \\ & \lambda \left(\mu E + 0.424\mu^2\xi - \frac{\mu^3}{8} \right) + a_1 \left(-A + \frac{\mu^2 E}{2} + 0.318\mu^3\xi - \frac{3}{8} \mu^2\xi^2 - \right. \\ & \left. \frac{7}{96} \mu^4 \right) + b_2 \left(\mu D - \frac{\mu C}{2} + 0.106\mu^4 + 0.424\mu^2\xi^2 - \frac{11}{24} \mu^3\xi \right) \end{aligned} \quad (22)$$

$$\begin{aligned} \frac{2a_2}{\gamma}(3 - \xi) = & A_0 \left(-\frac{\mu^2}{2} E + \frac{\mu^4}{32} + 0.106\mu^3\xi \right) + B_1 \left(\mu C - \frac{\mu^3\xi}{8} - 0.0221\mu^4 \right) + \\ & \lambda \left(\frac{\mu^2\xi}{4} + 0.053\mu^3 \right) + a_1 \left(\mu C - \frac{\mu D}{2} + \frac{3}{16} \mu^3\xi - 0.0309\mu^4 - \right. \\ & \left. 0.159\mu^2\xi^2 \right) + b_2 \left(2A + \frac{\mu^4}{16} + \frac{\mu^2\xi^2}{4} + 0.194\mu^3\xi \right) \end{aligned} \quad (23)$$

$$\frac{2b_2}{\gamma}(3 - \xi) = a_0 \left(-\frac{\mu^2 \xi}{2} + \frac{\mu^4}{24} \right) + b_1 \left(\mu C - \frac{\mu D}{2} - \frac{\mu^3 \xi}{24} \right) + a_2 \left(-2A - \frac{\mu^4}{96} - \frac{\mu^2 \xi^2}{2} \right) \quad (24)$$

The higher harmonics a_2 and b_2 are now dropped and the analysis continues with the steady-state and first-harmonic terms only. It was necessary to carry the higher harmonics to this point to take account of reverse flow satisfactorily. The equations to be solved are then written

$$\left. \begin{aligned} a_0(1 + \xi) &= S_1 A_0 + T_1 B_1 + U_1 \lambda + W_1 a_1 \\ -a_1 \xi &= V_2 a_0 + X_2 b_1 \\ -b_1 \xi &= S_3 A_0 + T_3 B_1 + U_3 \lambda + W_3 a_1 \end{aligned} \right\} \quad (25)$$

where

$$\left. \begin{aligned} S_1 &= \frac{\gamma}{2} \left(\frac{1}{4} - \frac{\xi}{3} + \frac{\mu^2}{4} - \frac{\mu^2 \xi}{2} - \frac{\mu^4}{32} + 0.159 \mu^3 \xi \right) \\ T_1 &= \frac{\gamma}{2} \left(-\frac{\mu}{3} + \frac{\mu \xi}{2} + \frac{\mu^3 \xi}{8} - 0.0331 \mu^4 \right) \\ U_1 &= \frac{\gamma}{2} \left(\frac{1}{3} - \frac{\xi}{2} - \frac{\mu^2 \xi}{4} + 0.080 \mu^3 \right) \\ W_1 &= \frac{\gamma}{2} \left(\frac{\mu \xi}{4} - \frac{\mu \xi^2}{2} - \frac{3}{16} \mu^3 \xi + 0.239 \mu^2 \xi^2 + 0.0464 \mu^4 \right) \end{aligned} \right\} \quad (26)$$

$$\left. \begin{aligned} V_2 &= \frac{\gamma}{2} \left(-\frac{\mu}{3} + \frac{\mu \xi}{2} - 0.0354 \mu^4 \right) \\ X_2 &= \frac{\gamma}{2} \left(\frac{1}{4} - \frac{2}{3} \xi + \frac{\xi^2}{2} + \frac{\mu^4}{8} - \frac{\mu^4 \xi}{4} + 0.0354 \mu^3 \xi \right) \end{aligned} \right\} \quad (27)$$

$$\left. \begin{aligned} S_3 &= \frac{\gamma}{2} \left(\frac{2}{3} \mu - \mu \xi - \frac{\mu^3 \xi}{4} + 0.0531 \mu^4 \right) \\ T_3 &= \frac{\gamma}{2} \left(-\frac{1}{4} + \frac{\xi}{3} - \frac{3}{8} \mu^2 + \frac{3}{4} \mu^2 \xi - 0.212 \mu^3 \xi + 0.0521 \mu^4 \right) \\ U_3 &= \frac{\gamma}{2} \left(\frac{\mu}{2} - \mu \xi + 0.4245 \mu^2 \xi - \frac{\mu^3}{8} \right) \\ W_3 &= \frac{\gamma}{2} \left(-\frac{1}{4} + \frac{2}{3} \xi - \frac{\xi^2}{2} + \frac{\mu^2}{8} - \frac{\mu^2 \xi}{4} - \frac{3}{8} \mu^2 \xi^2 + 0.3183 \mu^3 \xi - 0.0729 \mu^4 \right) \end{aligned} \right\} \quad (28)$$

The solutions of equations (25) can be written

$$a_0 = \frac{A_0 S_1 + B_1 T_1 + \lambda U_1 + a_1 W_1}{1 + \xi} \quad (29)$$

$$a_1 = \frac{A_0 [V_2 S_1 \xi - X_2 S_3 (1 + \xi)] - B_1 [-V_2 T_1 \xi + X_2 T_3 (1 + \xi)] + \lambda [V_2 U_1 \xi - X_2 U_3 (1 + \xi)]}{X_2 W_3 (1 + \xi) - W_1 V_2 \xi - \xi^2 (1 + \xi)} \quad (30)$$

$$b_1 = \frac{-a_1 \xi - a_0 V_2}{X_2} \quad (31)$$

Application of theory and comparison with experiment.— A calculation of blade flapping coefficients was carried out using the theory developed in reference 4 and the present theory which includes the effects of reverse flow. The parameters chosen for this computation are $\xi = 0.20$, $\gamma = 4$, $C_T/\sigma = 0.10$, $A_0 = 8^\circ$, and $B_1 = 0$. Values of the first-harmonic blade flapping coefficients are plotted in figure 55. The solid line indicates the coefficients resulting from the application of the theory which neglects reverse flow. A calculation, using the modified theory, was made at $\mu = 0.60$ and 0.90 . The results are shown as points plotted in the same figure. Data from experimental tests are also shown in figure 55. Additional blade flapping test data are given in figure 56 for the same rotor but at various blade pitch settings. It is interesting to note the reversal in values of the a_1 coefficient for increasing values of blade pitch. This is not so for the b_1 coefficient; however, the change in b_1 from $A_0 = 12^\circ$ to 16° is less than the change from $A_0 = 8^\circ$ to 12° . Consequently, at a given value of μ , the total flapping $\sqrt{a_1^2 + b_1^2}$ tends to level off with increase in A_0 and the

azimuth of maximum flapping shifts in such a manner that rotor pitch is exchanged for roll at higher values of pitch setting.

A number of conclusions can be drawn from the plot of figure 55. Although the two theories do not show a large difference between the predicted values of a_1 , the theory which takes account of reverse flow tends to be closer to the experimental results. Very little difference in the theoretical values of b_1 is indicated. The differences between the theories are not sufficient to merit the use of the reverse-flow theory so long as the current assumptions and approximations are used. In all cases, less blade flapping motion was obtained experimentally than was predicted by theory. This observation is borne out by previous tests on another model having a low blade mass constant of 1.8 and a 13-percent-offset flapping hinge (ref. 4).

A satisfactory and complete explanation of the discrepancy between theoretical and experimental results is not presented herein. However, the authors feel that tunnel walls may have had some effect upon the rotor blade motion. This, coupled with the assumption in the theory that the inflow is constant and uniform in distribution, may suggest some reasons for the data not being in better agreement.

APPENDIX CEXPERIMENTAL INVESTIGATION OF FORCES AND MOMENTS ON A TYPICAL
OFFSET MODEL ROTOR AND A COMPARISON WITH THEORY

A series of tests were conducted in the Wright Brothers wind tunnel at M.I.T. for the purpose of obtaining force and moment data on a typical lifting offset rotor at high tip-speed ratios. A flapping-hinge offset of 20 percent and a blade mass constant of 4 were selected as representative of possible full-scale application. The additional constant rotor parameters of the test were $R = 2.19$ feet, $\sigma = 0.073$, and $\Omega R = 137$ feet per second.

The wind-on tare readings of the forces and moments obtained included all of the tunnel rotor system except the two blades. The gravity tares for the blades alone were negligible. A blade pitch variation of 8° , 10° , 12° , and 14° was used at each tip-speed ratio of 0.45, 0.60, 0.75, and 0.90. For convenience of testing, thrust and lift were assumed equal, and, for comparison of data, the lift was kept constant. The test procedure involved varying the rotor angle of attack α_r until the predetermined value of lift was obtained corresponding to a C_T/σ value of 0.10. However, because of the unusually large lift tares experienced, the corrected C_T/σ value varied from 0.10 at $\mu = 0.45$ to 0.07 at $\mu = 0.90$. A maximum rotor angle of attack of -13° occurred at $\mu = 0.45$ for $A_0 = 14^\circ$. In general, the rotor angles of attack required for "constant lift" increased with increasing pitch settings and varied slowly over the range of tip-speed ratios.

The data obtained on the six-component balance were reduced to coefficient form and plotted in figures 57 and 58. It should be emphasized that the forces and moments are those produced by the rotor blades alone, since the effects of motor drive, support structure, and hub have been taken into account in the reduction of the data. The moments are those about the center of the rotor hub.

The most significant feature of figure 58 is the difference in character and magnitude between the pitching- and rolling-moment-coefficient curves. The pitching-moment-coefficient values are relatively high and vary more slowly with tip-speed ratio than do the corresponding rolling-moment values. The corresponding variation of moments with tip-speed ratio is shown in figure 59, where the experimental moment values are compared with the theory from reference 4. The signs of the pitching and rolling moments are such that the resultant steady-state hub moment lies in the second quadrant. This is compatible with the offset data of appendix B.

Although better agreement is indicated in the case of pitching moments than in the case of rolling moments, neither shows reasonable agreement. Better agreement probably would have resulted had reverse flow and stall effects been included in the theory.

If the resultant hub moments are considered, it is found that the agreement between theory and experiment is improved. Such a comparison is shown in figure 60 for blade pitch settings of 8° and 12° . In general, wherever there is a sizable difference in moments, the theory appears to be conservative.

APPENDIX DEXPERIMENTAL RECORDS OF OTHER ROTOR CONDITIONS

The raw data included in figures 61 to 71 cover a wide range of tip-speed ratio for various rotor-shaft angle and blade-pitch combinations. It is felt that the values selected are representative of possible full-scale application and, therefore, the data indicate pressure distributions for helicopter forward-flight operation above a tip-speed ratio of 0.10.

A tip-speed-ratio range of 0.10 to 0.40 is included for both the zero- and 13-percent-offset rotors (figs. 61 to 68). Since the operating conditions of these rotors were identical, these data may be compared directly. Examination of figures 61 to 68 shows that the striking difference between these sets of data lies in the predominant harmonic. The zero-offset data show strong second-harmonic pressure variations while the corresponding 13-percent data show strong first-harmonic variations. This difference is present in all the pressure data recorded. That a strong second-harmonic variation is possible in the case of the zero-offset rotor is demonstrated in the section entitled "Results and Discussion." Reference 5 explains the requirement for a large first-harmonic variation in the case of a rotor with offset.

At a tip-speed ratio of 0.60, data are included for two combinations of α and A_0 . The first combination of $\alpha = -10^\circ$ and $A_0 = 12^\circ$ was taken at a rotor speed of 800 rpm; the second combination of $\alpha = -15^\circ$ and $A_0 = 17^\circ$ was taken at 500 rpm. Thrust measurements were not made, but from conventional theory the corresponding values of thrust are 18.3 pounds at 800 rpm and 10.4 pounds at 500 rpm. The resulting C_T/σ values are 0.146 and 0.203, respectively. As a matter of check, both conventional theory and experimental results were used to find the C_T/σ value for the one condition at $\mu = 1.0$, $\alpha = -15^\circ$, $A_0 = 17^\circ$, and 500 rpm. The agreement was very good; a theoretical value of $C_T/\sigma = 0.314$ was obtained against the experimental result of 0.302. This represents a rotor of substantial lift. The remaining high μ rotor condition presented was tested at $\mu = 0.80$, $\alpha = -15^\circ$, and $A_0 = 17^\circ$ and the corresponding theoretical value of C_T/σ is 0.23. The above range of testing was confined to the 13-percent-offset rotor.

It is well known that the blade load for the zero-offset rotor is comparatively constant with azimuth and, consequently, the C_T/σ value for this rotor condition is indicative of the load on a blade at any

azimuth. However, with the offset rotor this is not the case. Because of the large aerodynamic first-harmonic variation in blade load the C_T/σ quantity no longer represents actual blade loads but rather the average blade load. As a consequence, it is possible to have reasonable values of blade angle of attack in the retreating half of the disk even though the value of C_T/σ is unusually high.

REFERENCES

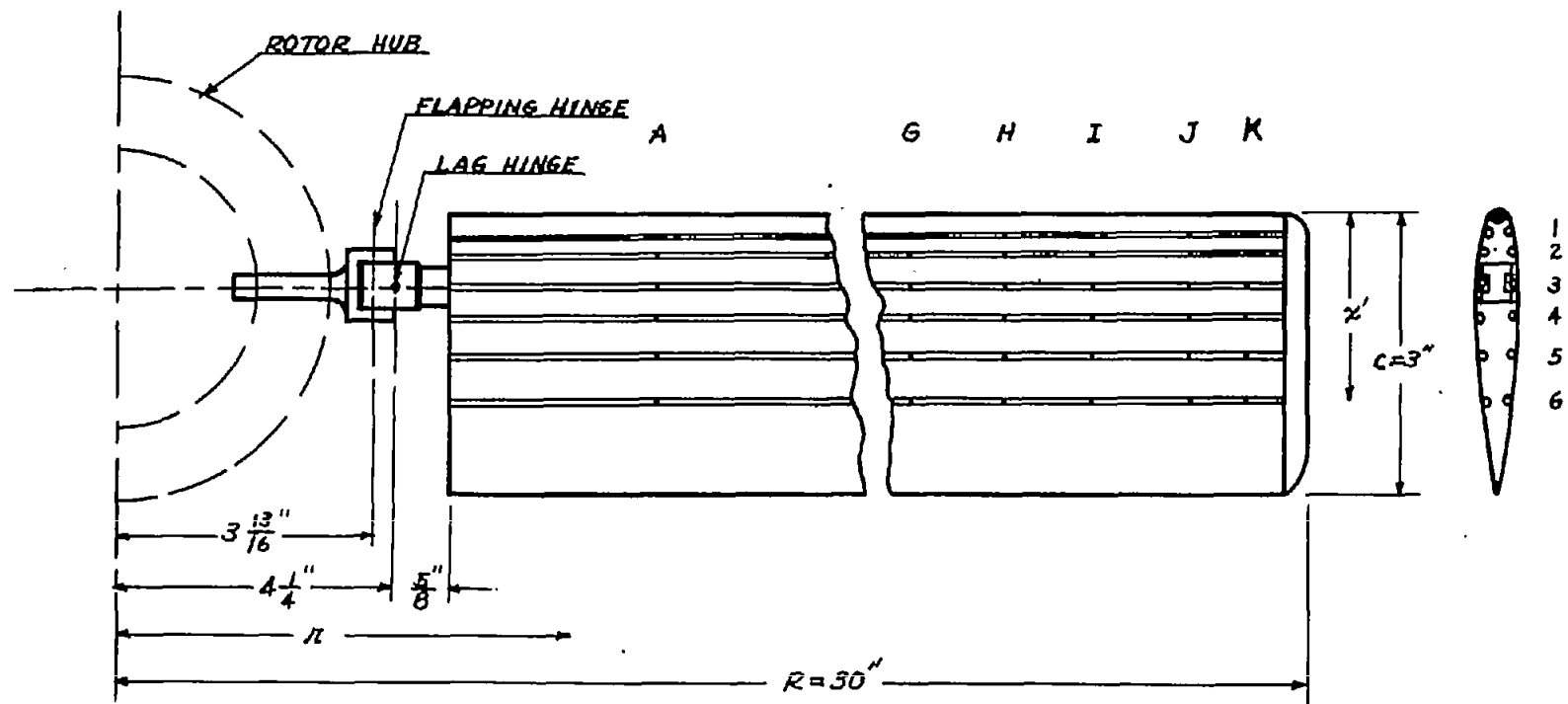
1. Brotherhood, P., and Stewart, W.: An Experimental Investigation of the Flow Through a Helicopter Rotor in Forward Flight. R. & M. No. 2734, British A.R.C., 1949.
2. Coleman, Robert P., Feingold, Arnold M., and Stempin, Carl W.: Evaluation of the Induced-Velocity Field of an Idealized Helicopter Rotor. NACA-WR L-126, 1945. (Formerly NACA ARR L5E10.)
3. Mangler, K. W.: Calculation of the Induced Velocity Field of a Rotor. Rep. No. Aero. 2247, British R.A.E., Feb. 1948.
4. Meyer, John R., Jr., and Falabella, Gaetano, Jr.: The Effect of Blade Mass Constant and Flapping Hinge Offset on Maximum Blade Angles of Attack at High Advance Ratios. Proc. Eighth Annual Forum, Am. Helicopter Soc., Inc., May 15-17, 1952.
5. Meyer, John R., Jr., and Falabella, Gaetano, Jr.: An Investigation of the Experimental Aerodynamic Loading on a Model Helicopter Rotor Blade. NACA TN 2953, 1953.
6. Gessow, Alfred, and Myers, Garry C., Jr.: Aerodynamics of the Helicopter. The Macmillan Co., 1952.
7. Brotherhood, P.: An Investigation in Flight of the Induced Velocity Distribution Under a Helicopter Rotor When Hovering. R. & M. No. 2521, British A.R.C., 1947.
8. Michel, Douglas: Determination of Inflow Through Helicopter Rotor Disc in Forward Flight. M. S. Thesis, M.I.T., June 1952.
9. Squire, H. B.: Some Aerodynamic Problems of the Helicopter. The Jour. Helicopter Assoc. (Great Britain), vol. 1, no. 3, Jan.-Feb.-Mar., 1948, pp. 35-48.
10. Wheatley, John B.: An Aerodynamic Analysis of the Autogiro Rotor With a Comparison Between Calculated and Experimental Results. NACA Rep. 487, 1934.

TABLE I
EXPERIMENTAL FLAPPING COEFFICIENTS FOR
VARIOUS ROTOR CONDITIONS ANALYZED

Rotor condition			$\xi = 0$			$\xi = 0.13$		
μ	α , deg	A_0 , deg	a_0 , deg	a_1 , deg	b_1 , deg	a_0 , deg	a_1 , deg	b_1 , deg
0.30	-5	8	0.5	6.1	2.6	0.5	1.9	-1.3
^a .30	^a -5	^a 8	^a .5	^a 6.2	^a 2.3			
.50	-10	12	.5	12.2	6.2	.5	5.3	-3.0
1.0	-15	17				1.1	10.0	-7.2
.30	0	15				2.0	4.4	-2.8
^b .30	^b -8	^b 8				^b .5	^b 3.6	^b -.3

^aOne-bladed rotor.

^b $B_1 = 3^\circ$.



CHORD STATION	x/c	x , IN.
1	.083	$1/4$
2	.156	$15/32$
3	.271	$13/16$
4	.375	$1 1/8$
5	.500	$1 1/2$
6	.674	$2 1/32$

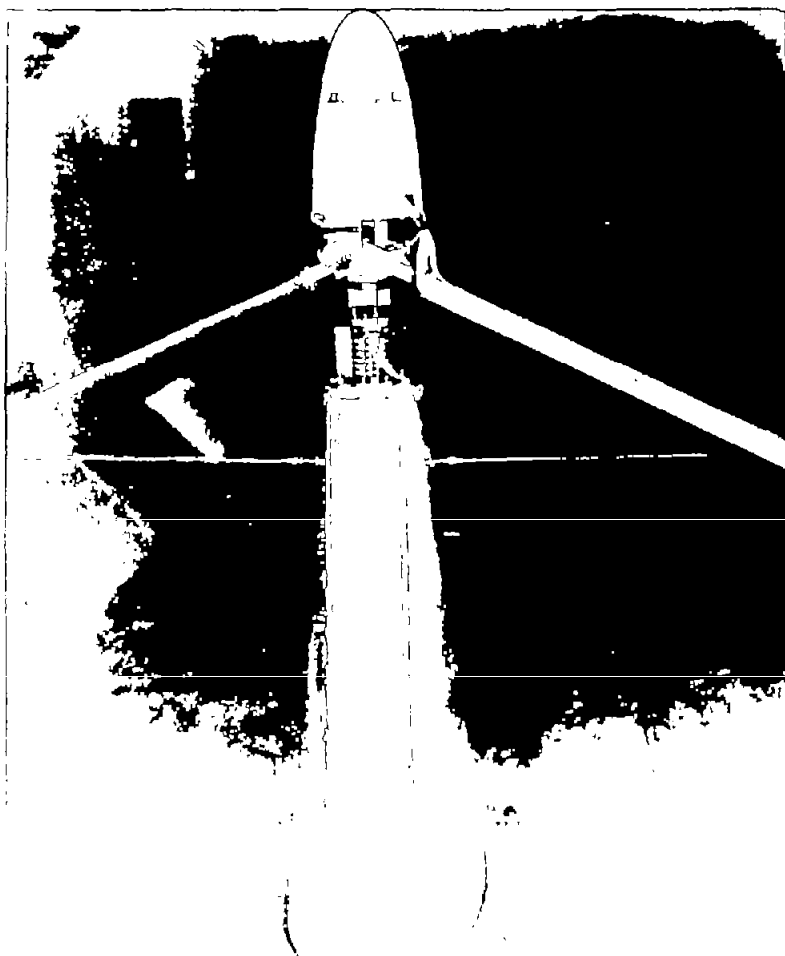
SPAN STATION	r/R	r , IN.	SPAN STATION	r/R	r , IN.
A	.325	9.75	G	.825	24.75
B	.460	13.80	H	.860	25.80
C	.590	17.70	I	.890	26.70
D	.660	19.80	J	.925	27.75
E	.725	21.75	K	.960	28.80
F	.790	23.70	L	.977	29.30

Figure 1.- Location of pressure orifices. NACA 0015 profile.

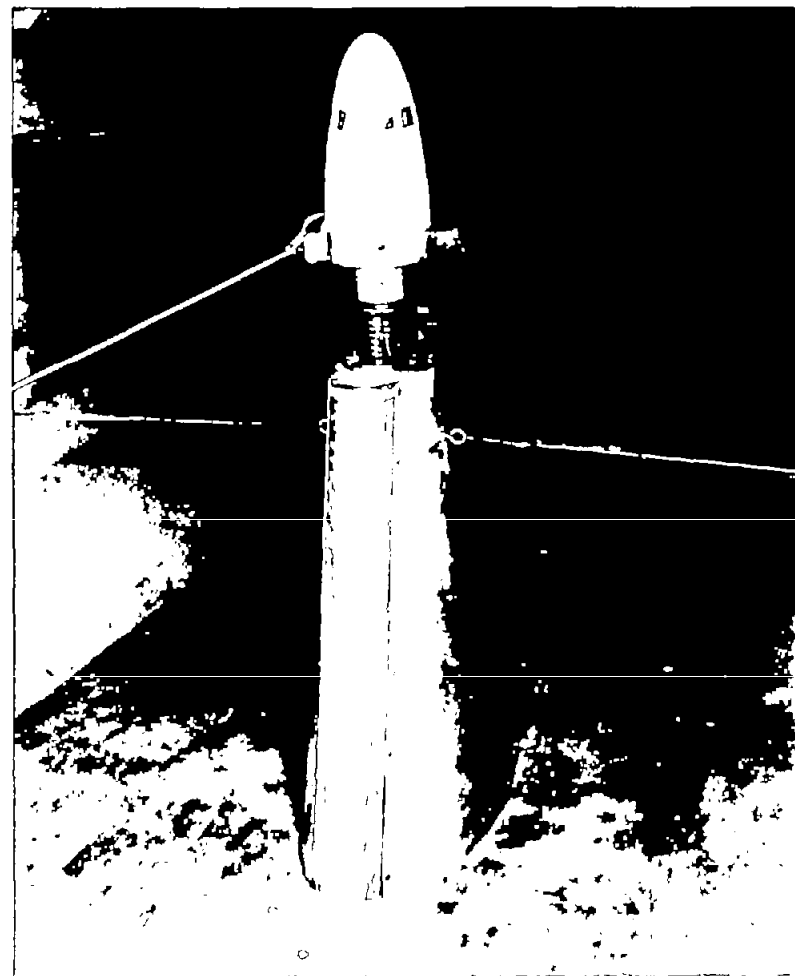


Figure 2.- Wind-tunnel control and recording equipment.

L-89318

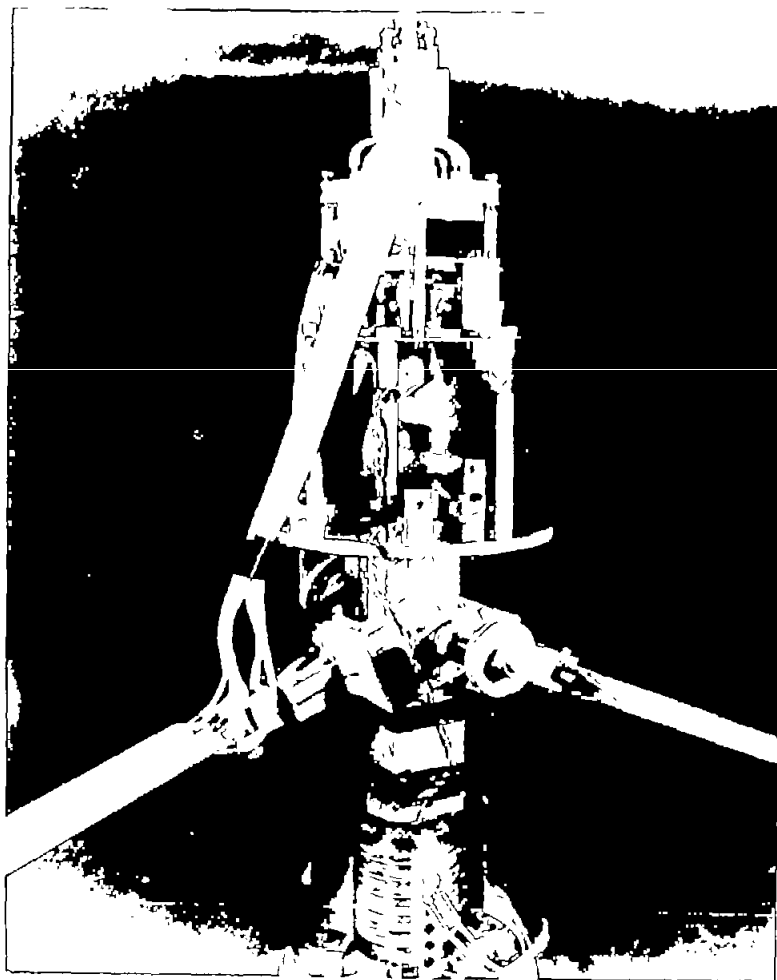


(a) Zero-offset rotor.

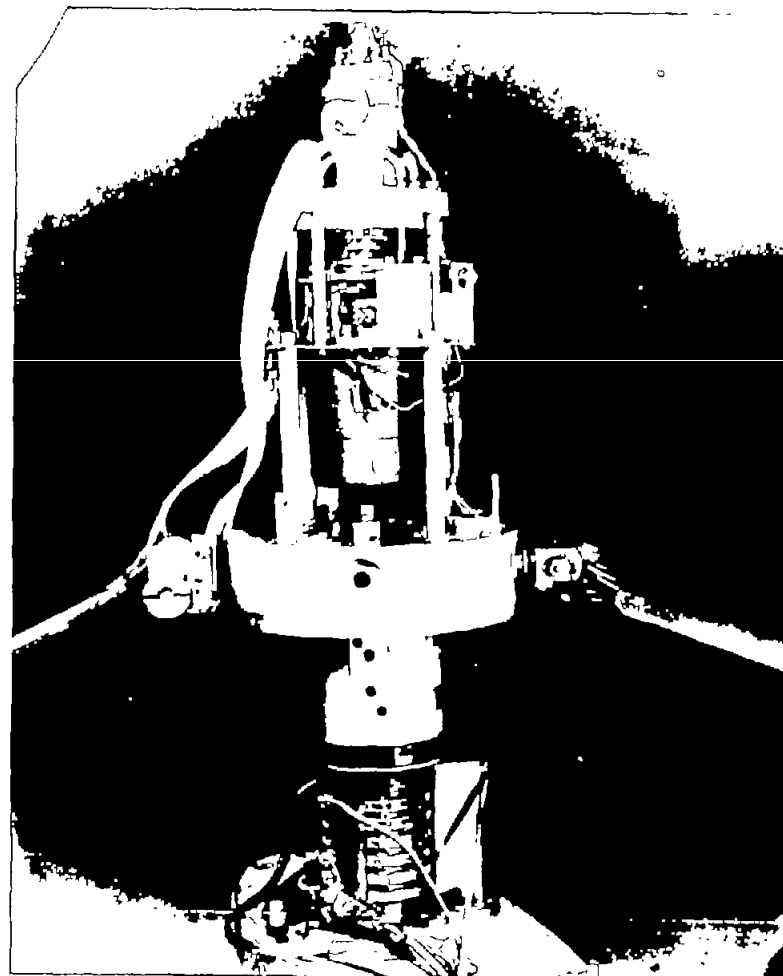


L-89319
(b) Offset rotor.

Figure 3.- Wind-tunnel rotor installations.

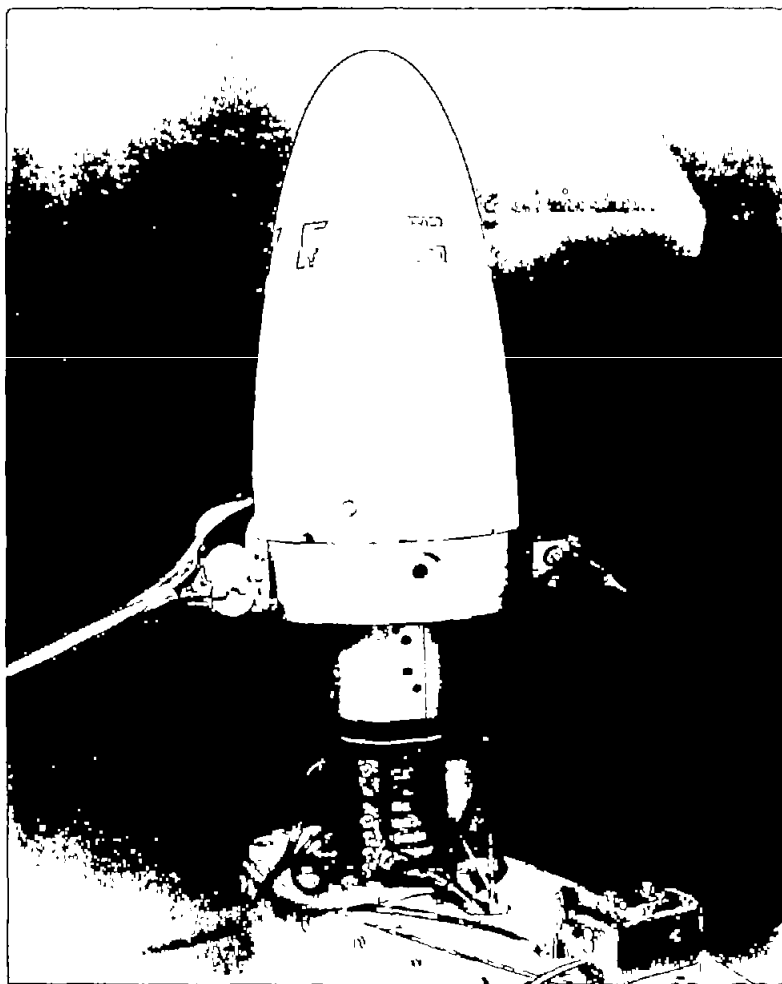


(a) Zero-offset rotor.



L-89320
(b) Offset rotor.

Figure 4.- Rotor hub details.



(a) General installation.



L-89321
(b) Capacitor mounting detail.

Figure 5.- Blade flapping measurement.

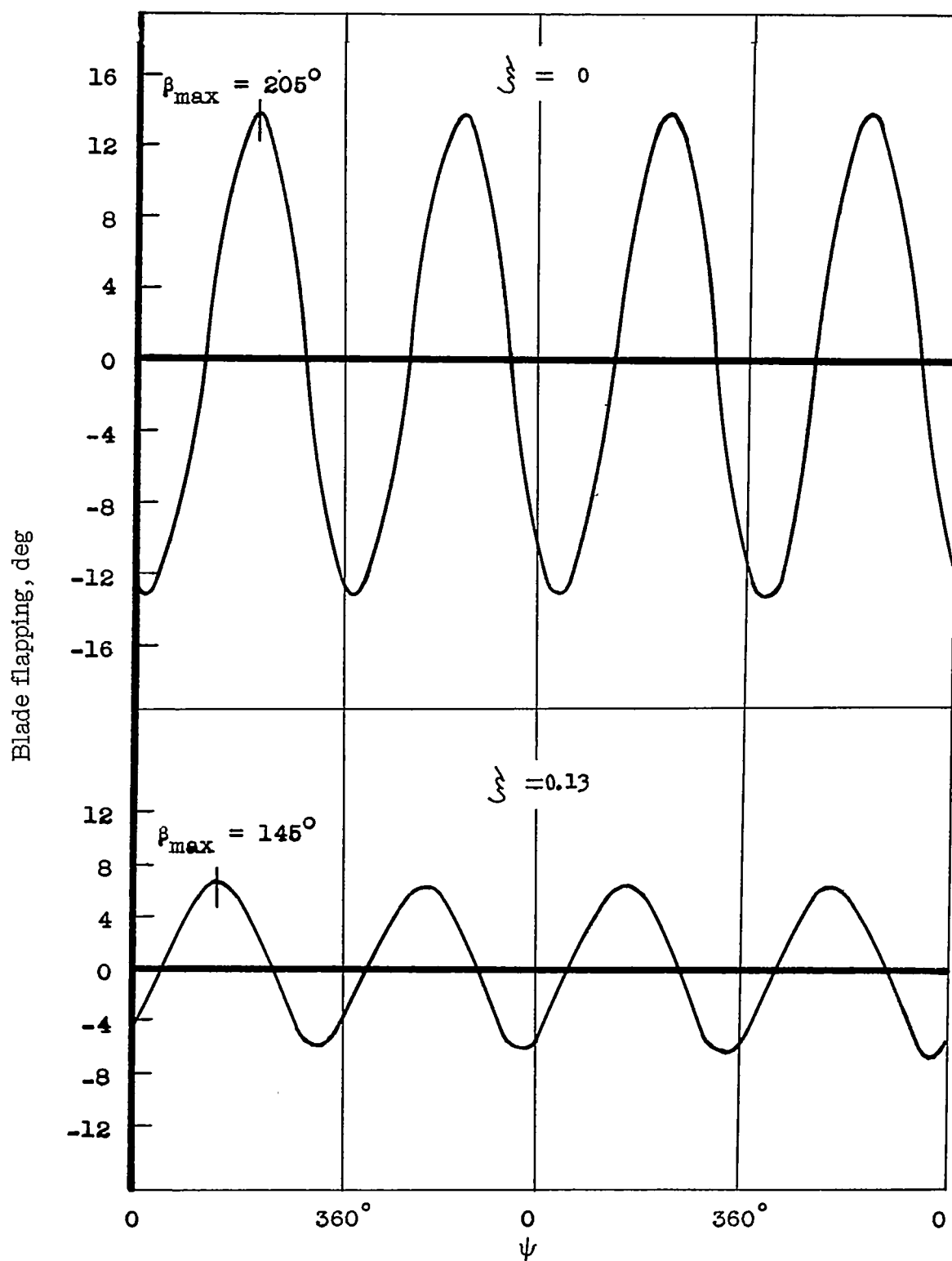


Figure 6.- Sample blade-motion traces (β). Profile, NACA 0015; $\mu = 0.50$;
 $\alpha = -10^\circ$; $A_0 = 12^\circ$.



(a) Rear view.

L-89322
(b) Looking downstream.

Figure 7.- Typical rotor installation used for force and moment measurements.

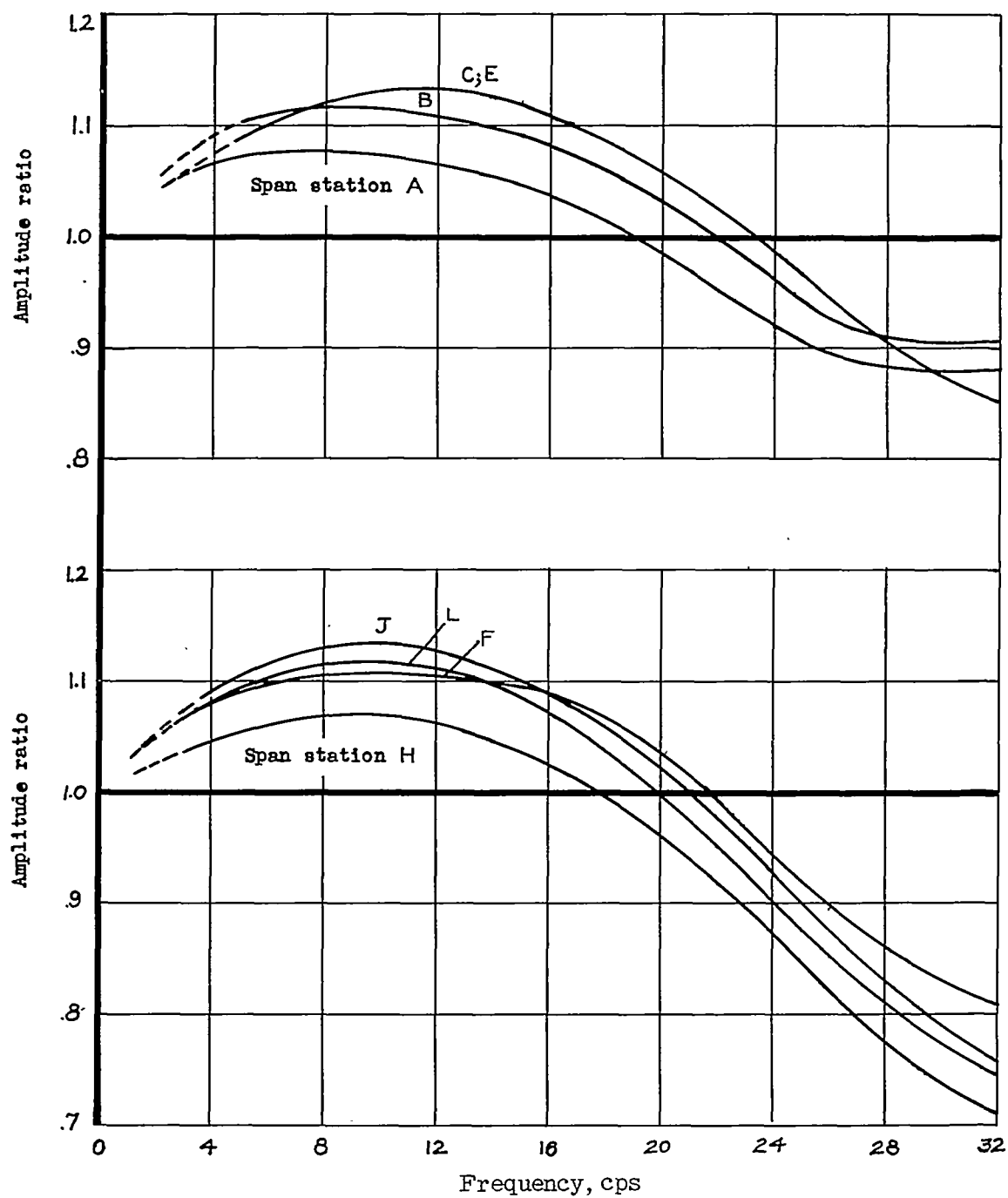


Figure 8.- Amplitude dynamic response of pressure-measuring system.

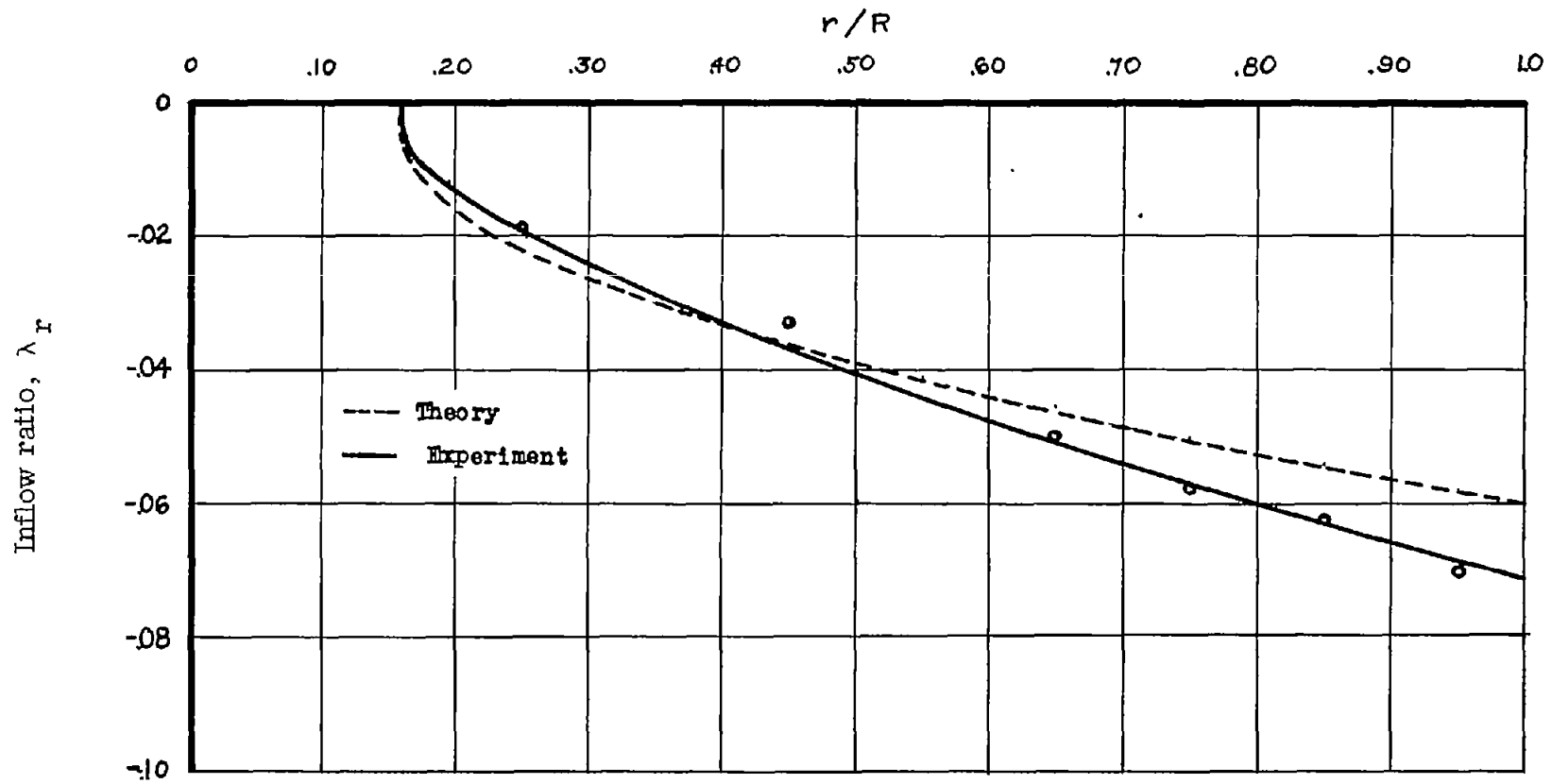


Figure 9.- Comparison of hovering inflow distribution. $A_0 = 8^\circ$; $\Omega R = 209$ feet per second;

$$a = 5.7; C_T/\sigma = 0.061; V_r = \frac{\sigma a \Omega R}{16} \left[-1 + \sqrt{1 + \frac{320X}{\sigma a}} \right]; \lambda_r = -\frac{V_r}{\Omega R}.$$

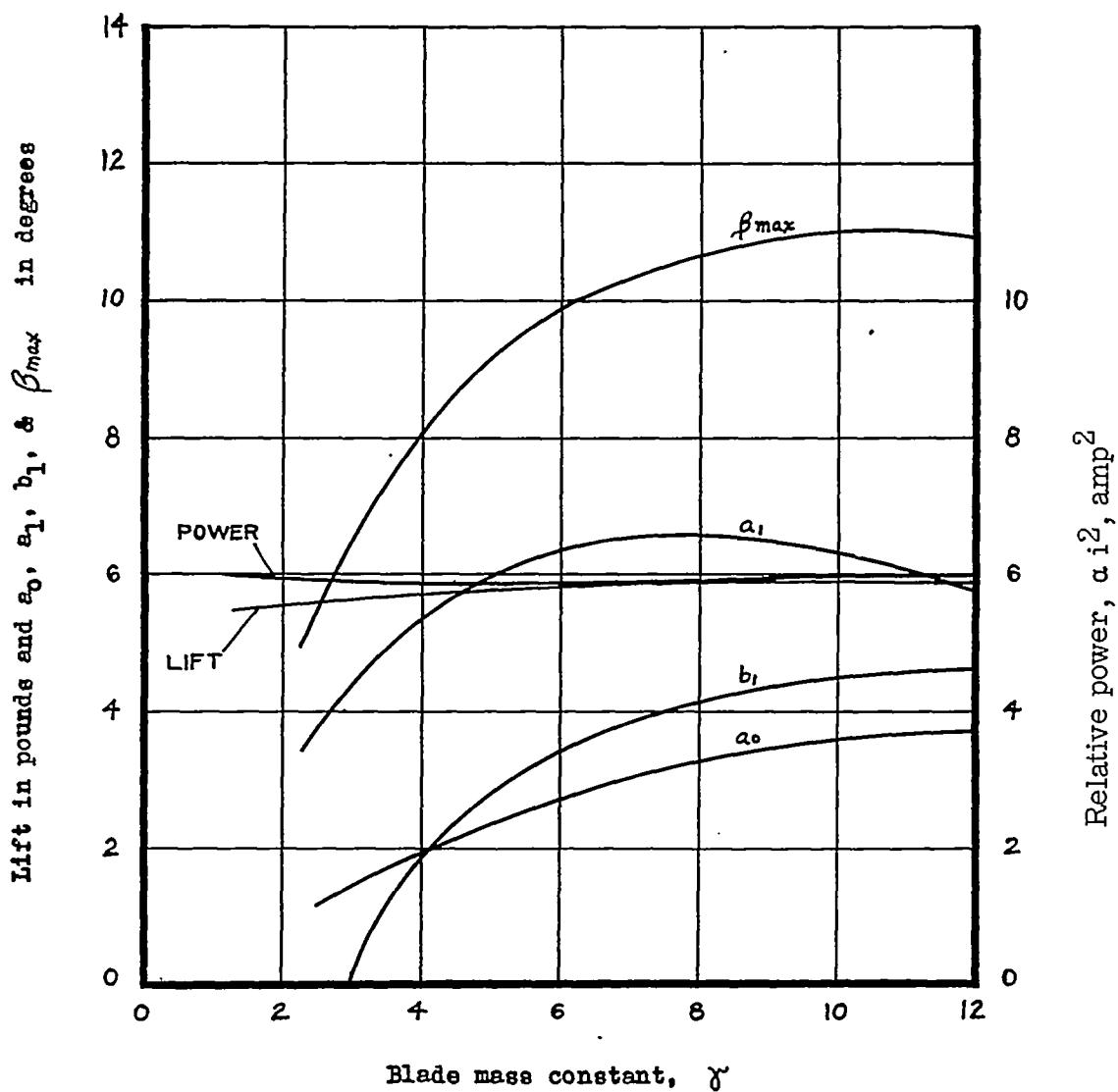
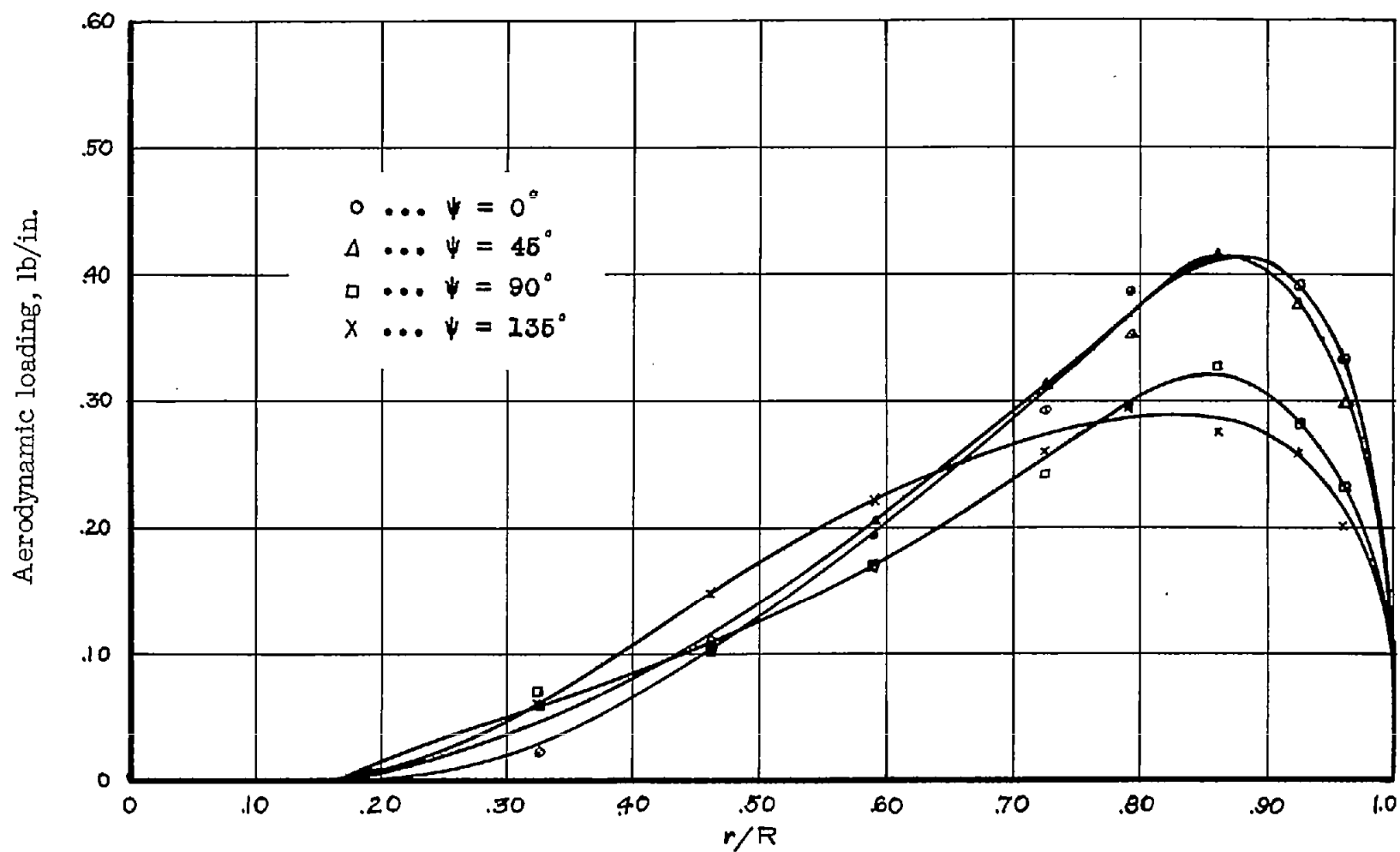
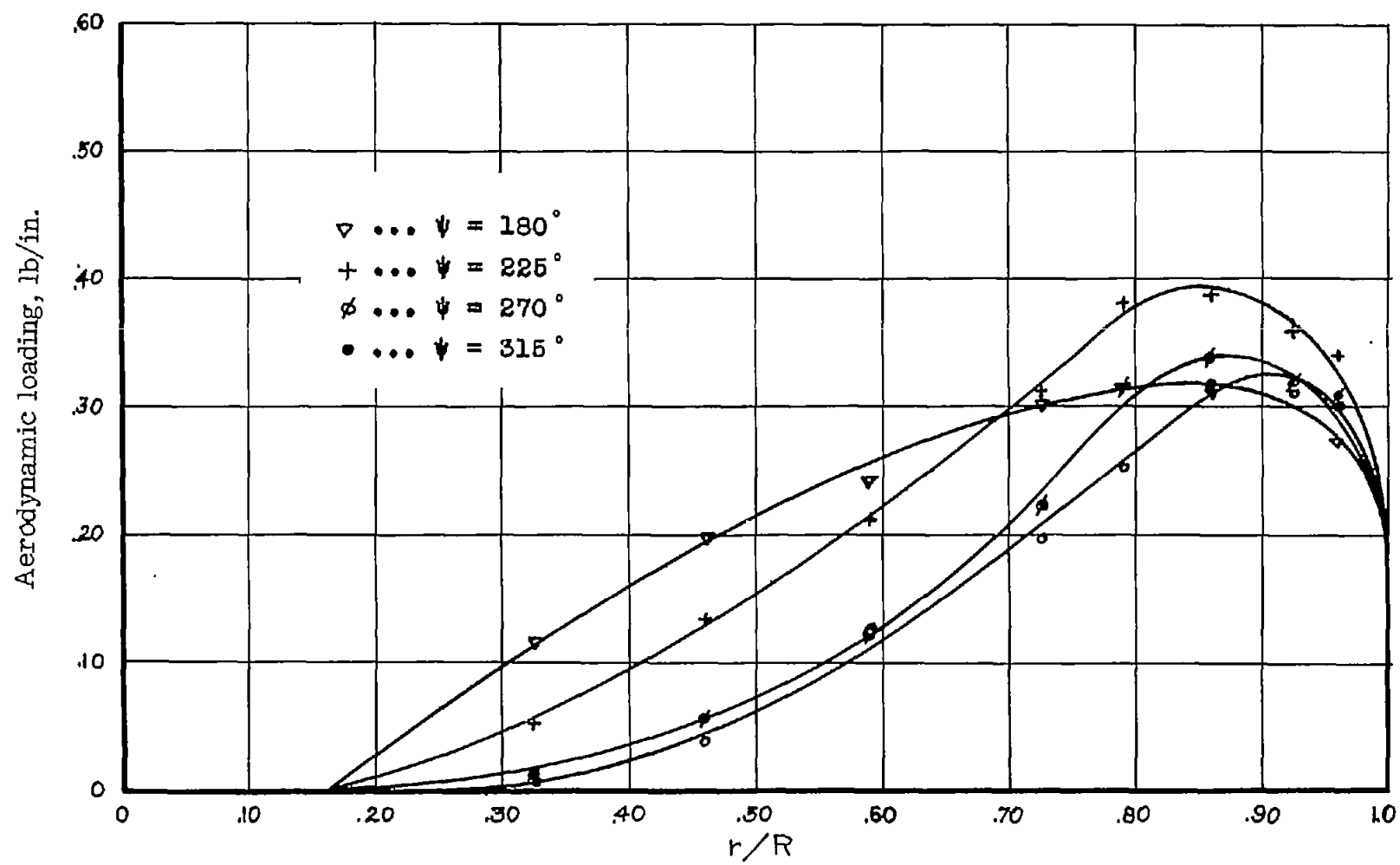


Figure 10.- Measured variations in power, lift, and blade flapping with changes in mass constant. Profile, NACA 0015; $\mu = 0.30$; $\xi = 0.1$; $\alpha = -5^\circ$; $\sigma = 0.08$; $A_0 = 8^\circ$; $R = 1.94$ feet; 800 rpm.



(a) $\psi = 0^\circ$ to 135° .

Figure 11.- Experimental spanwise aerodynamic loading at various azimuths. Profile, NACA 0015;
 $\mu = 0.30$; $\xi = 0$; $A_0 = 8^\circ$; $\alpha = -5^\circ$.



(b) $\psi = 180^\circ$ to 315° .

Figure 11.- Concluded.

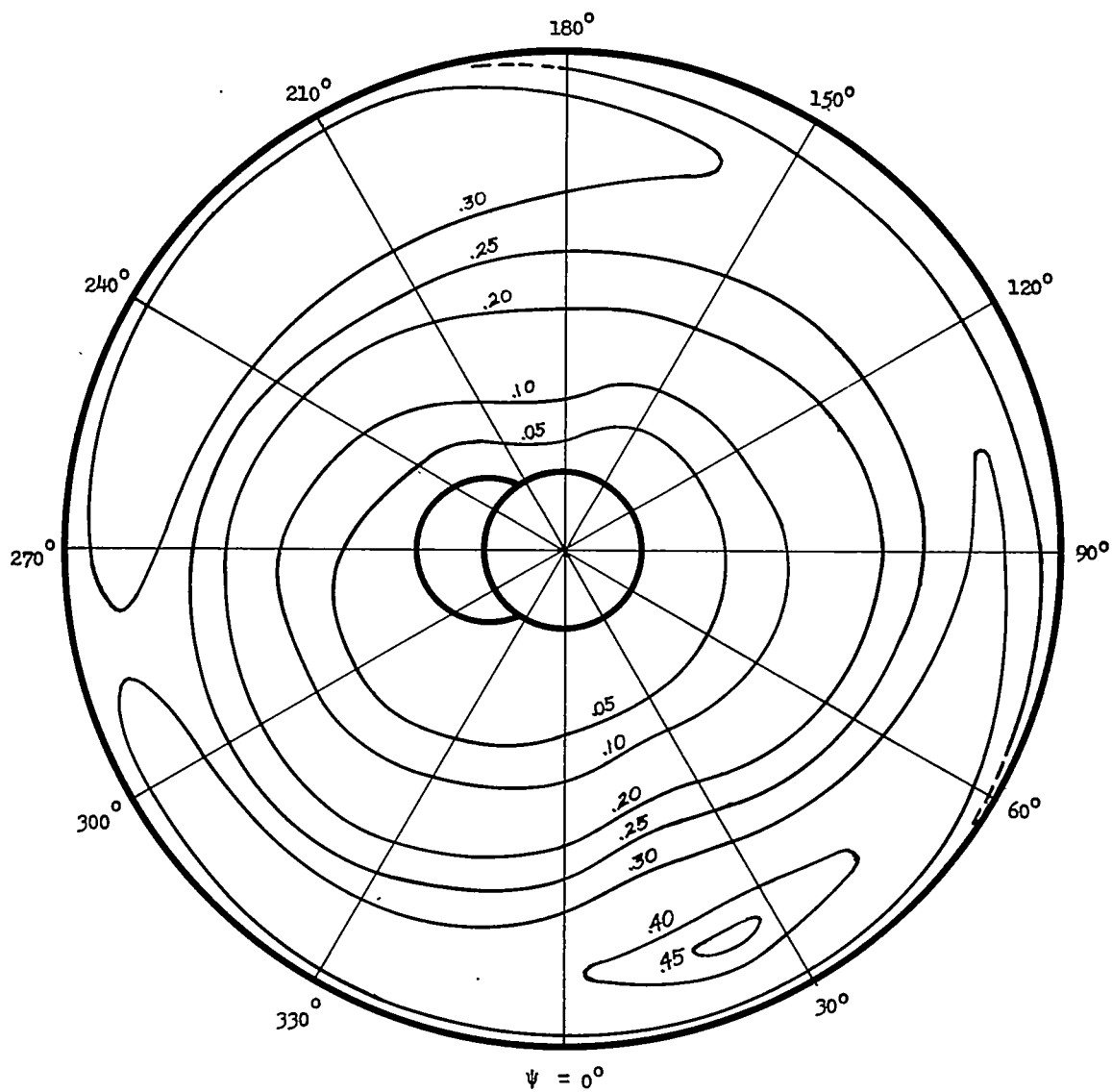


Figure 12.- Curves of constant aerodynamic loading (pounds per inch).
Profile, NACA 0015; $\mu = 0.30$; $\xi = 0$; $A_0 = 8^\circ$; $\alpha = -5^\circ$; $C_T/\sigma = 0.071$.

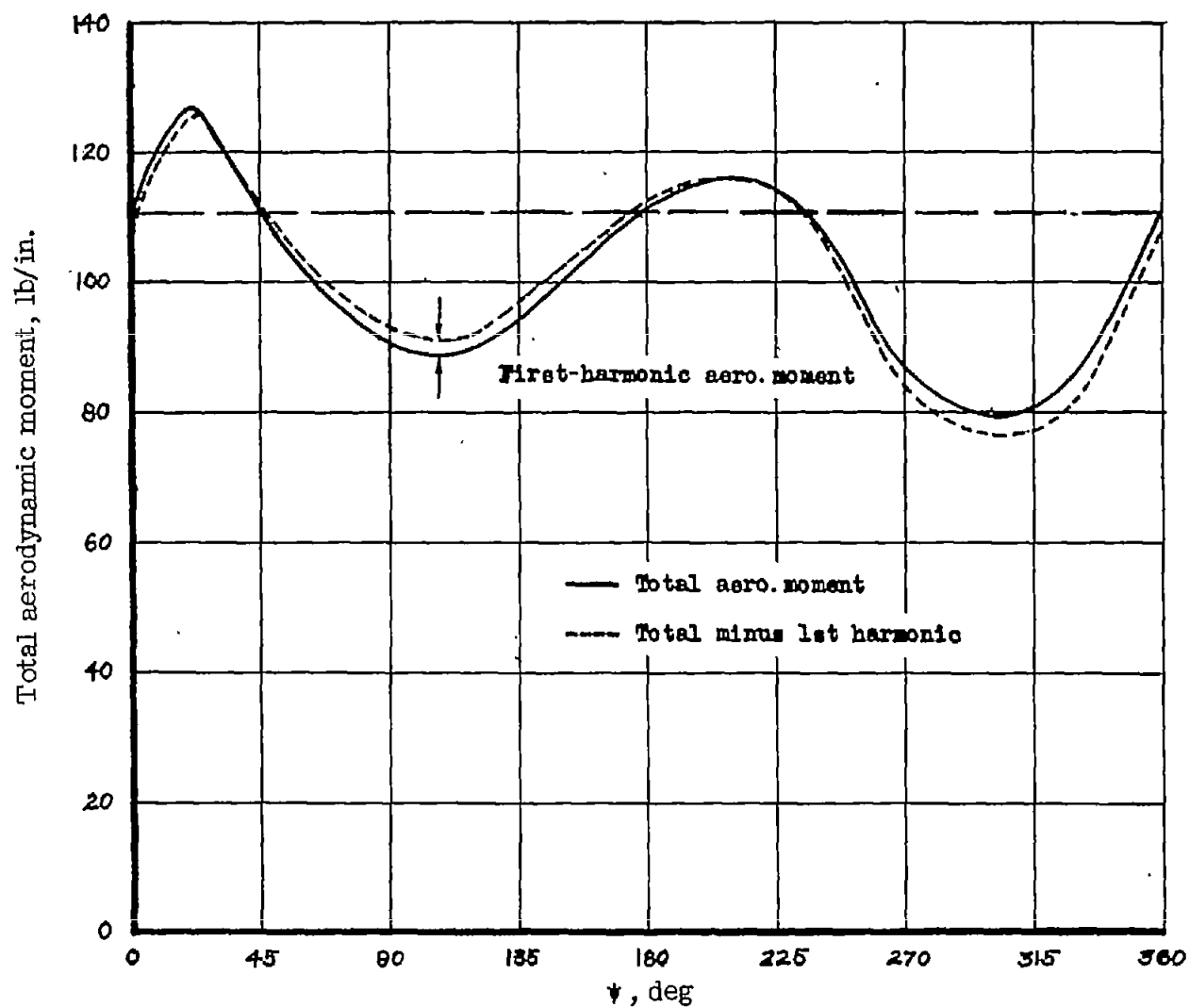


Figure 13.- Total aerodynamic moment variation, showing first-harmonic contribution. $\mu = 0.30$;
 $\xi = 0$; $A_0 = 8^\circ$; $\alpha = -5^\circ$.

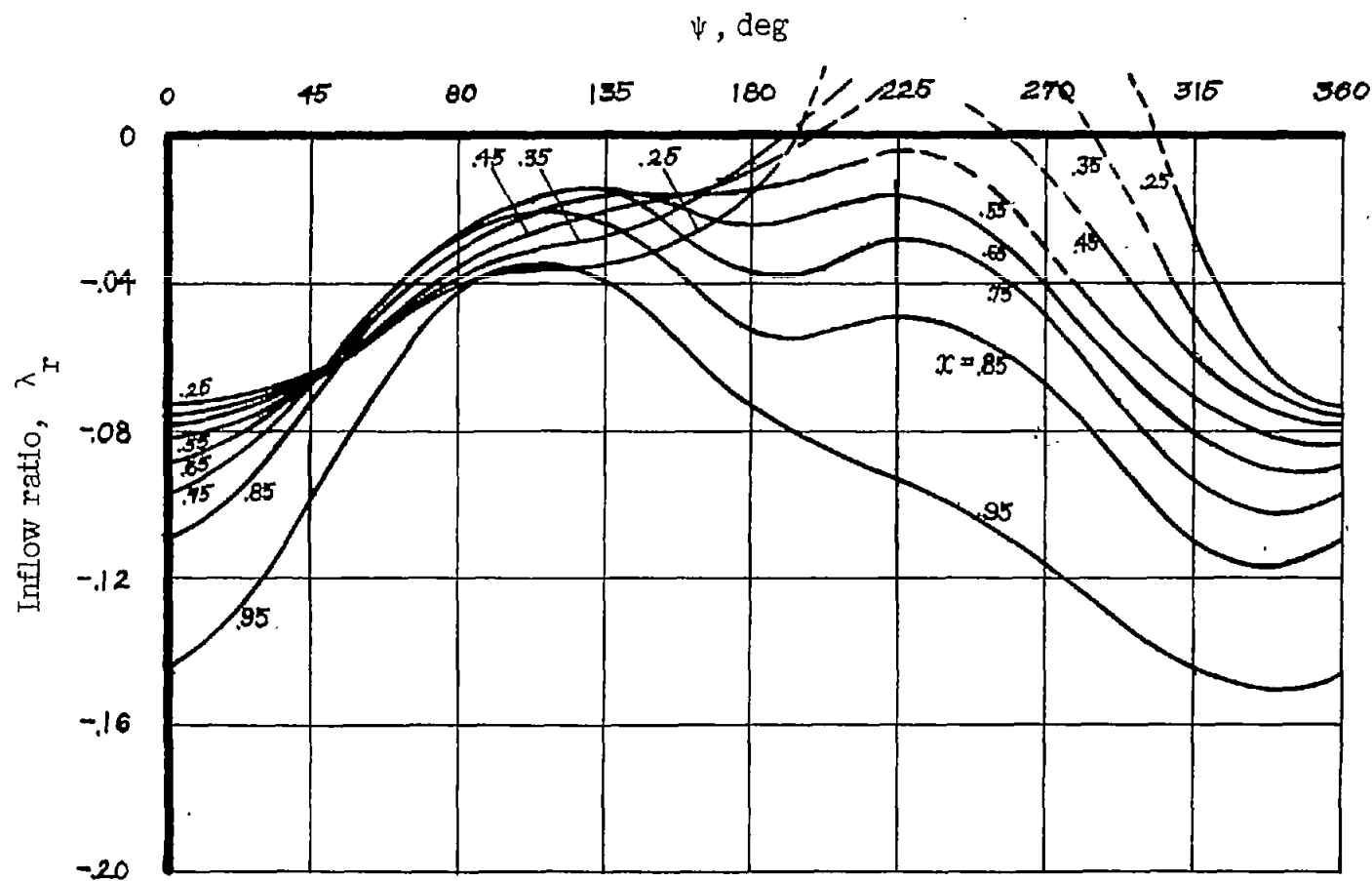


Figure 14.- Inflow distribution from experimental loading and blade-motion data. $\mu = 0.30$; $\xi = 0$; $A_0 = 8^\circ$; $\alpha = -5^\circ$; $a = 5.7$; $\mu \sin \alpha = -0.026$. Dashed lines indicate local blade stall.

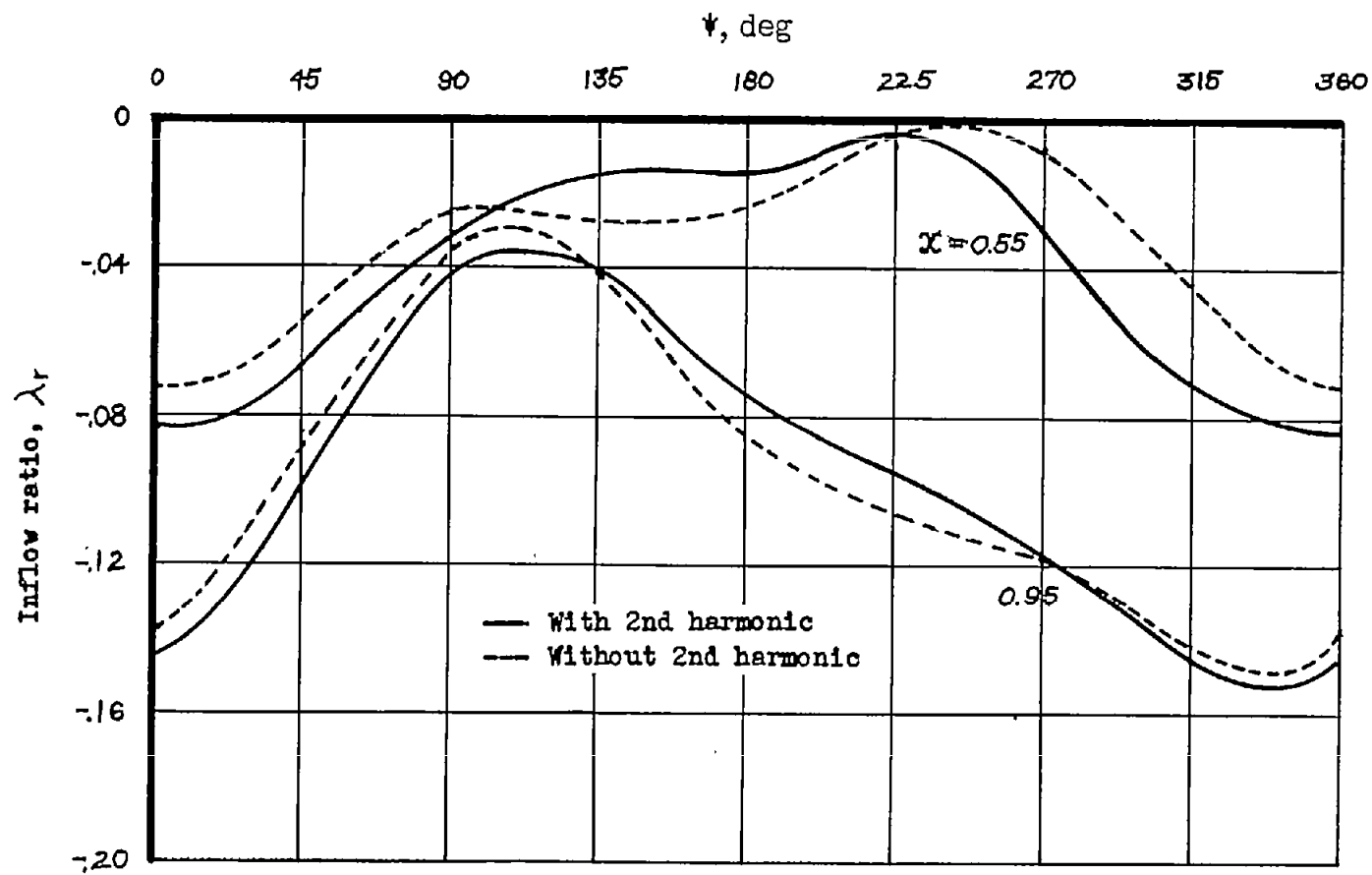
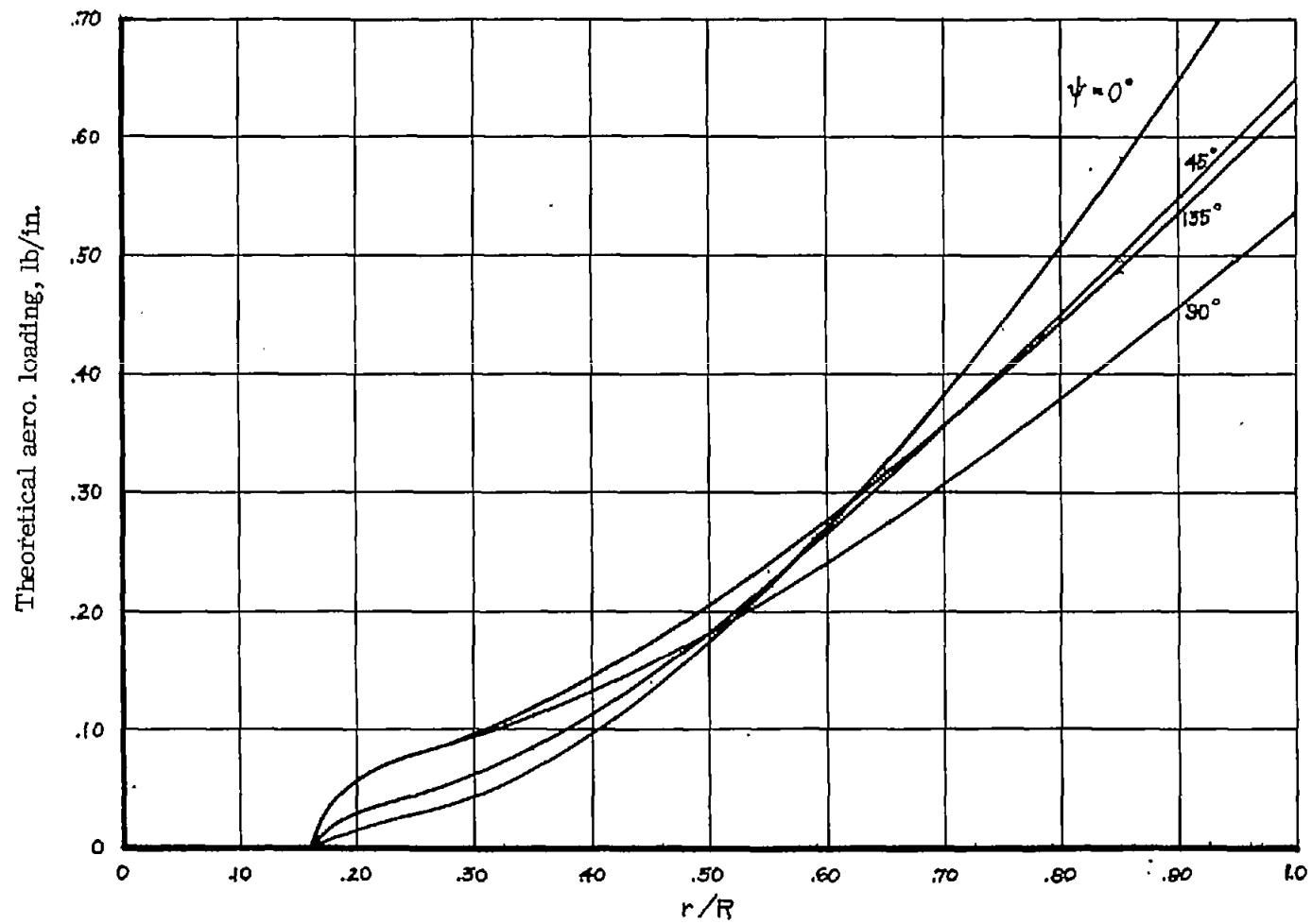
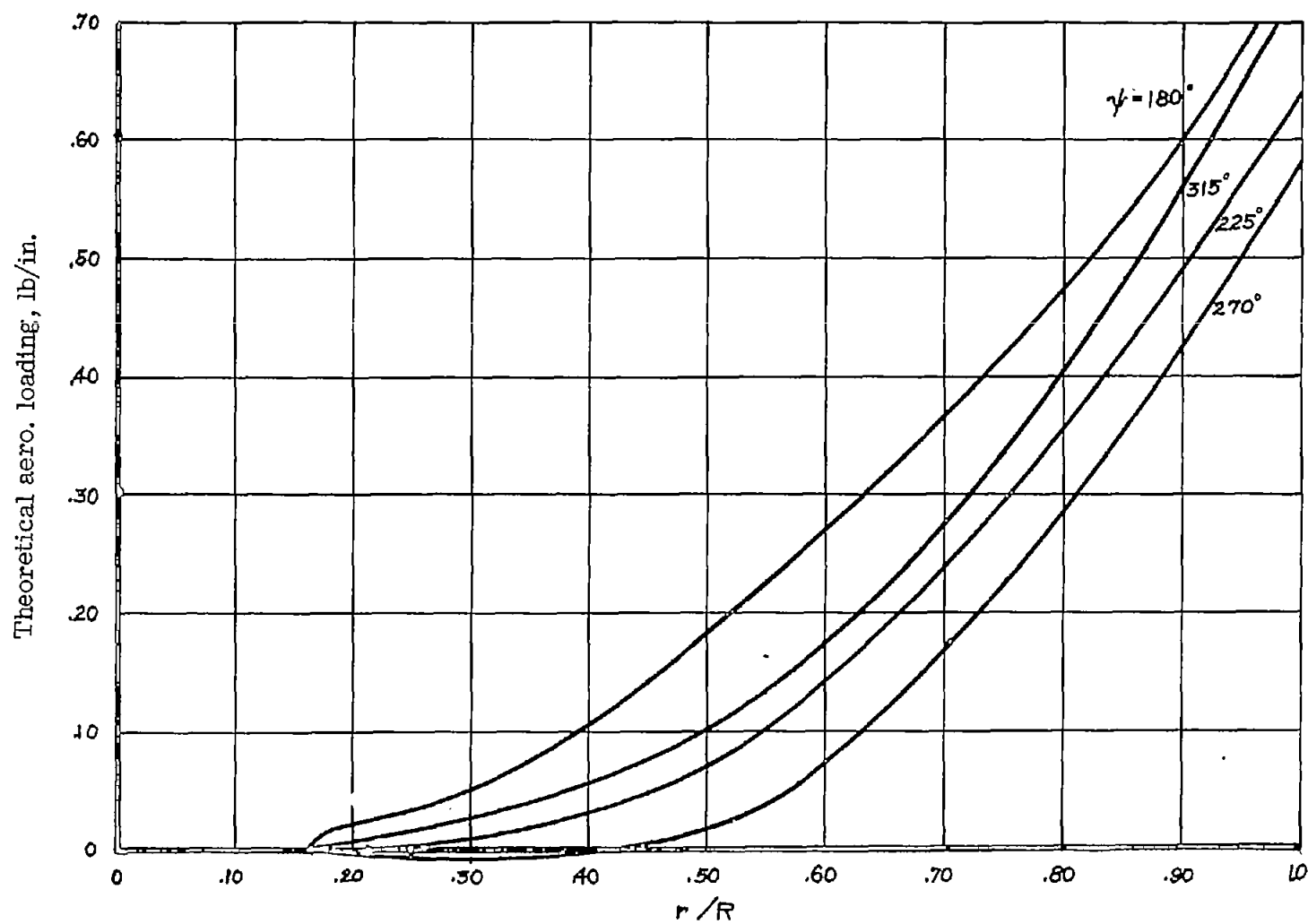


Figure 16.- Comparison of experimental inflow variations with and without second harmonic aerodynamic loading component. $\mu = 0.30$; $\xi = 0$; $A_0 = 8^\circ$; $\alpha = -5^\circ$; $a = 5.7$.



(a) $\psi = 0^\circ$ to 90° .

Figure 17.- Theoretical spanwise aerodynamic loading at various azimuths. $\mu = 0.30$; $\xi = 0$; $A_0 = 8^\circ$; $\alpha = -5^\circ$.



(b) $\psi = 180^\circ$ to 270° .

Figure 17.- Concluded.

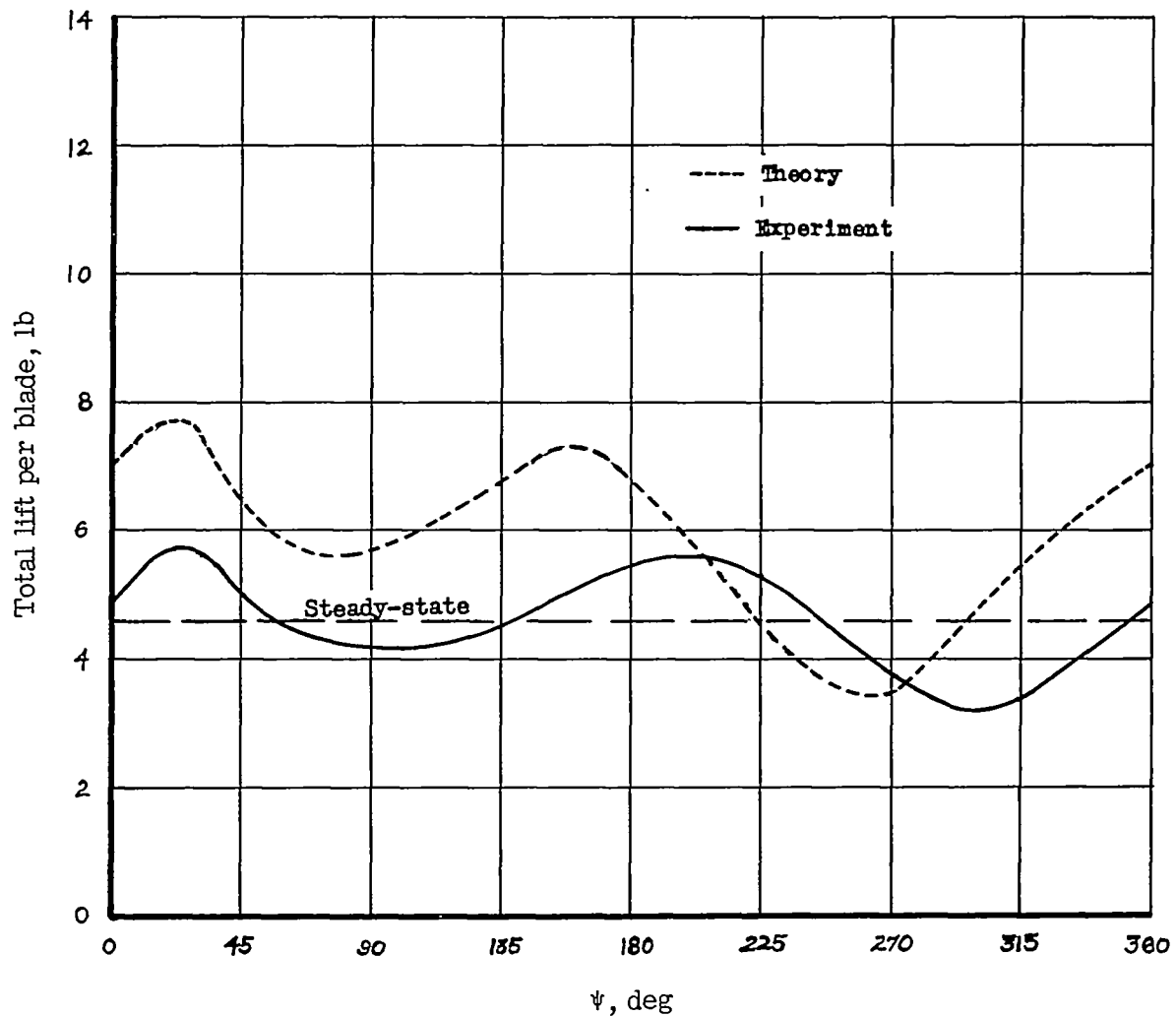


Figure 18.- Comparison of variations in theoretical and experimental total lift per blade. Profile, NACA 0015; $\mu = 0.30$; $\xi = 0$; $A_0 = 8^\circ$; $\alpha = -5^\circ$.

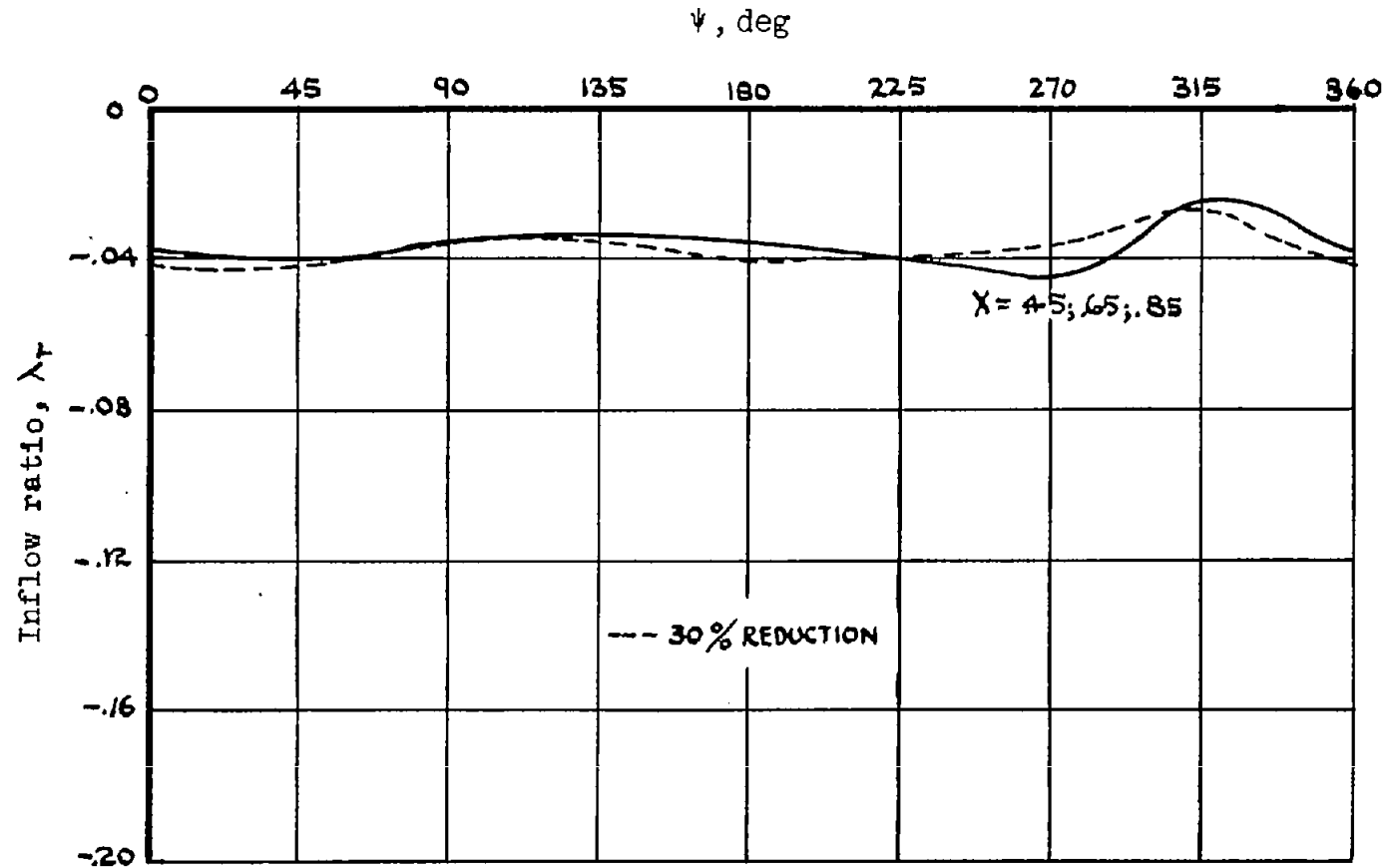


Figure 19.- Theoretical inflow distribution, showing the effect of a 30-percent reduction in the second-harmonic aerodynamic loading component. $\mu = 0.30$; $\xi = 0$; $A_0 = 8^\circ$; $\alpha = 5^\circ$; $a = 5.7$.

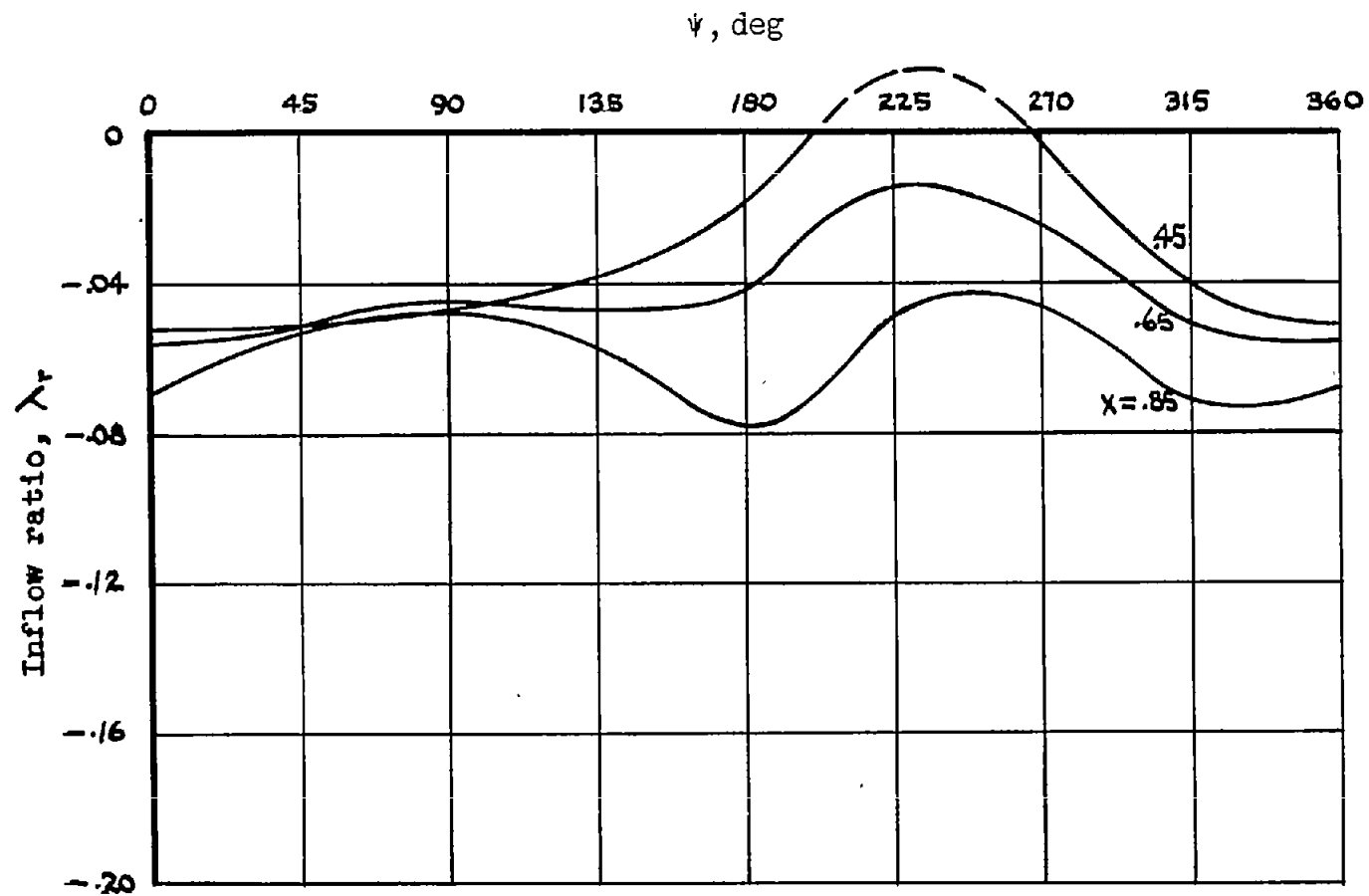


Figure 20.- Inflow distributions using experimental loading and theoretical blade-motion data.
 $\mu = 0.30$; $\xi = 0$; $A_0 = 8^\circ$; $\alpha = -5^\circ$; $a = 5.7$.

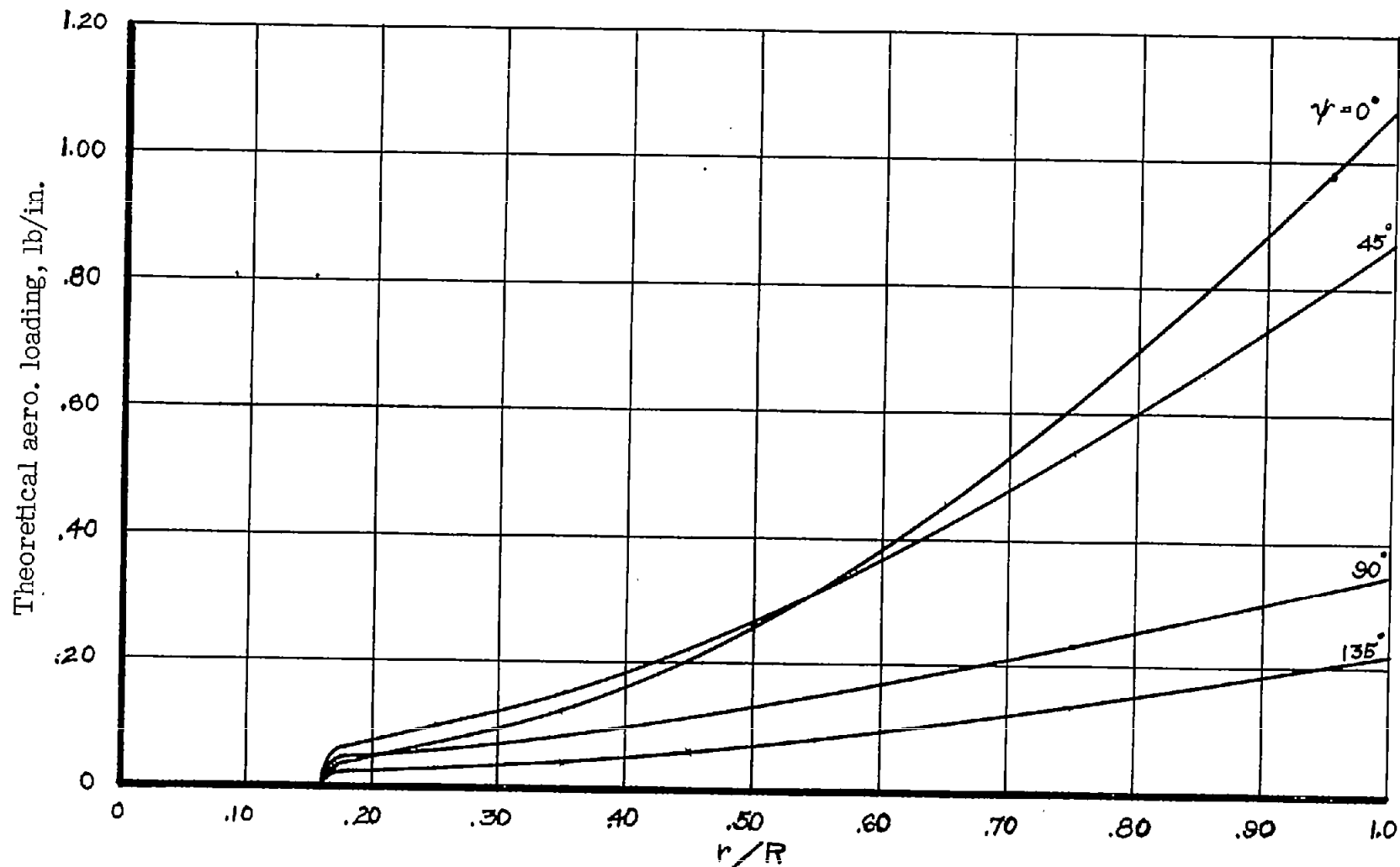
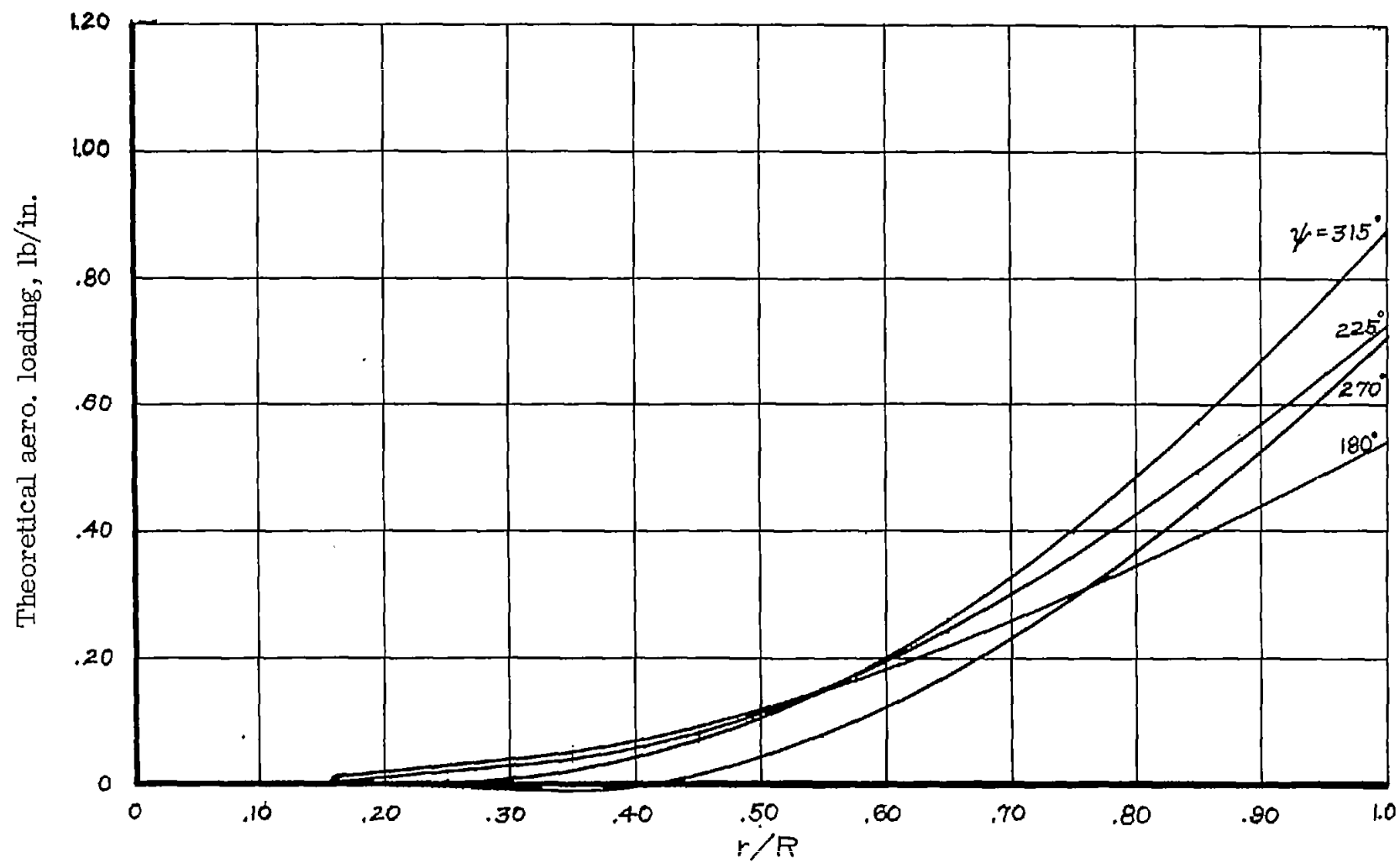
(a) $\psi = 0^\circ$ to 135° .

Figure 21.- Theoretical spanwise aerodynamic loading at various azimuths, using experimental blade-motion data. $\mu = 0.30$; $\xi = 0$; $A_0 = 8^\circ$; $\alpha = -5^\circ$; $a = 5.7$.



(b) $\psi = 180^\circ$ to 315° .

Figure 21.- Concluded.

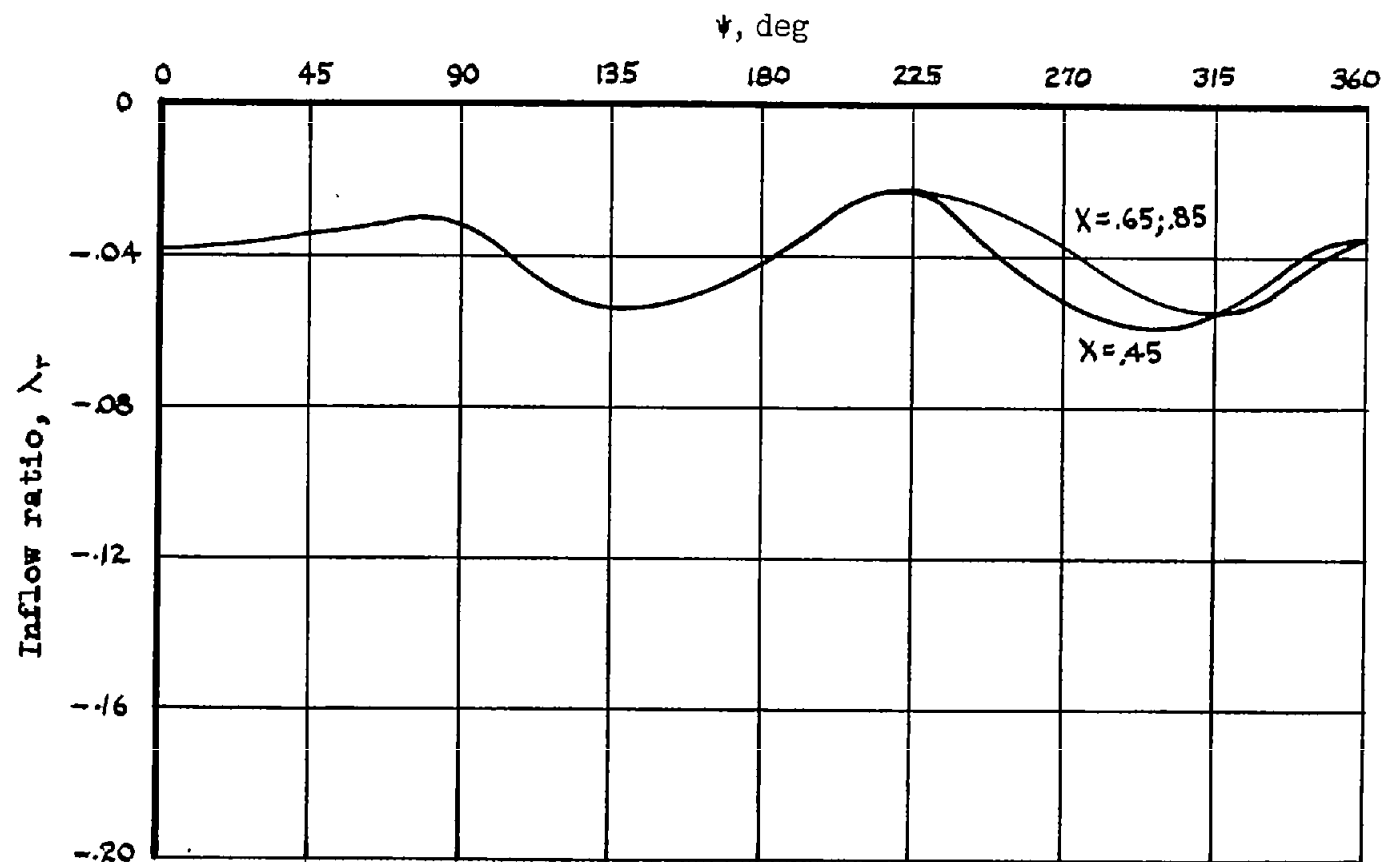


Figure 22.- Inflow distributions using theoretical loading and experimental blade-motion data.
 $\mu = 0.30$; $\xi = 0$; $A_0 = 8^\circ$; $\alpha = -5^\circ$; $a = 5.7$.

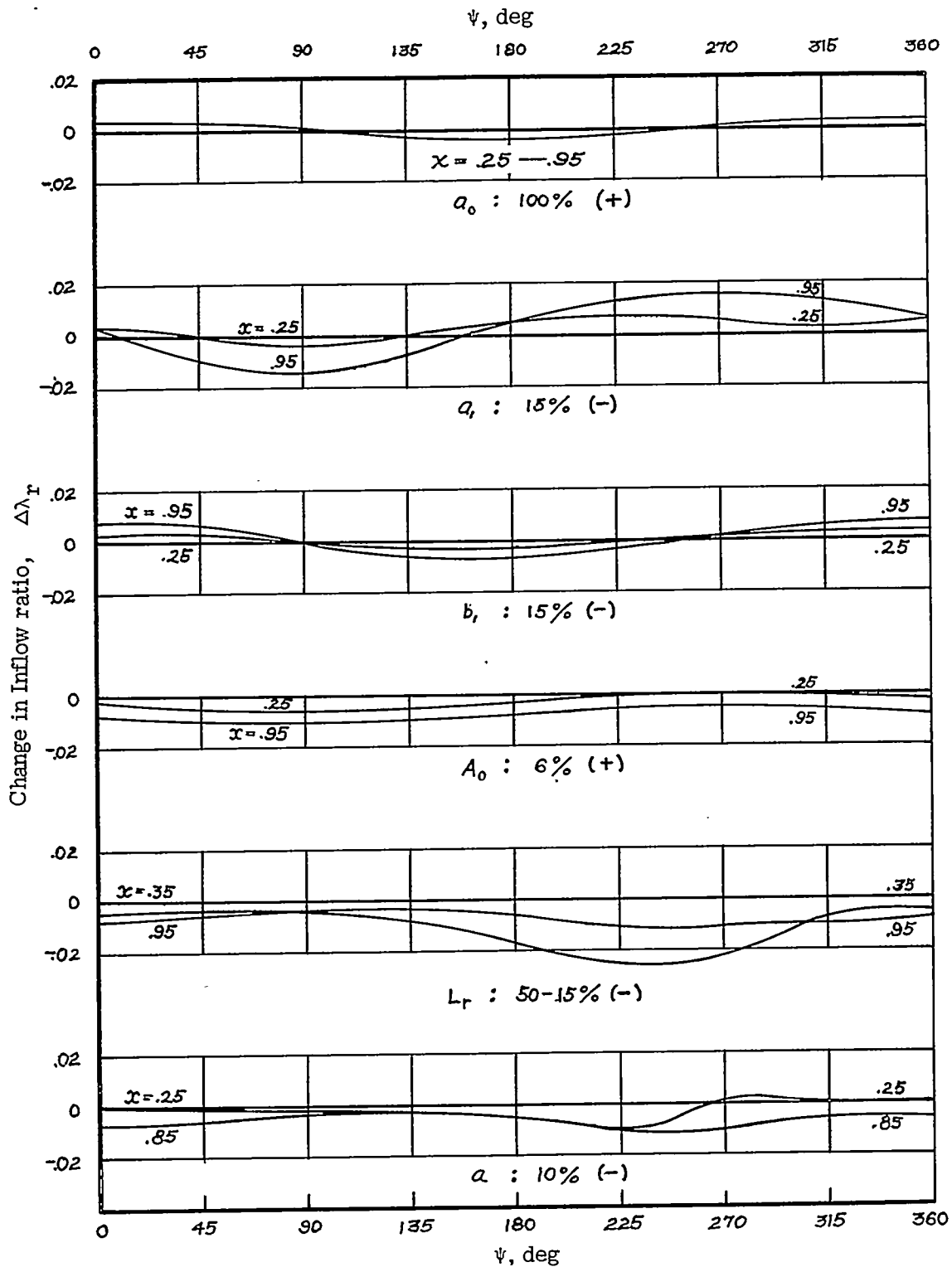


Figure 23.- Changes in experimental inflow ratio for various changes in the involved parameters. $\mu = 0.30$; $\xi = 0$; $A_0 = 8^\circ$; $\alpha = -5^\circ$.

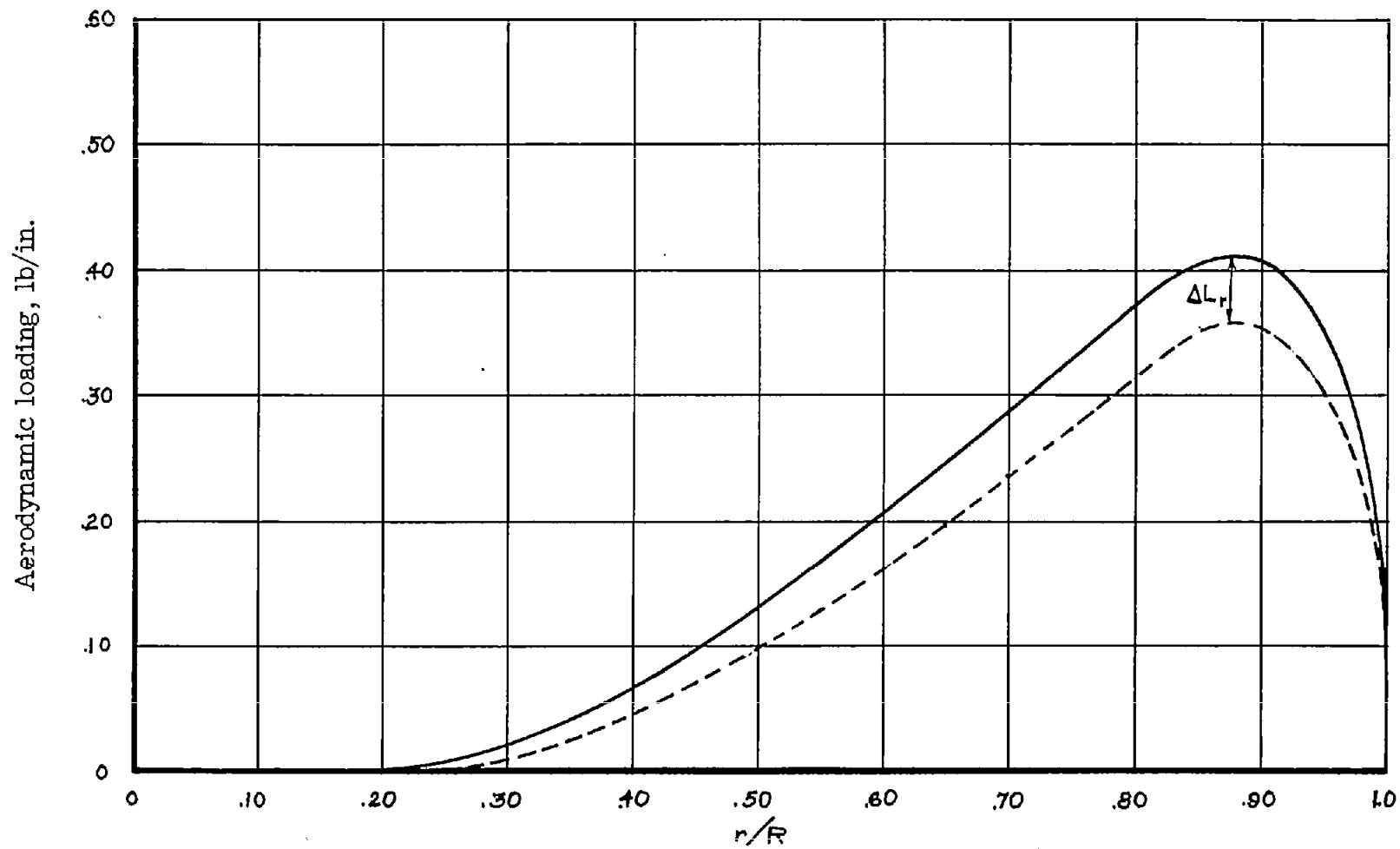
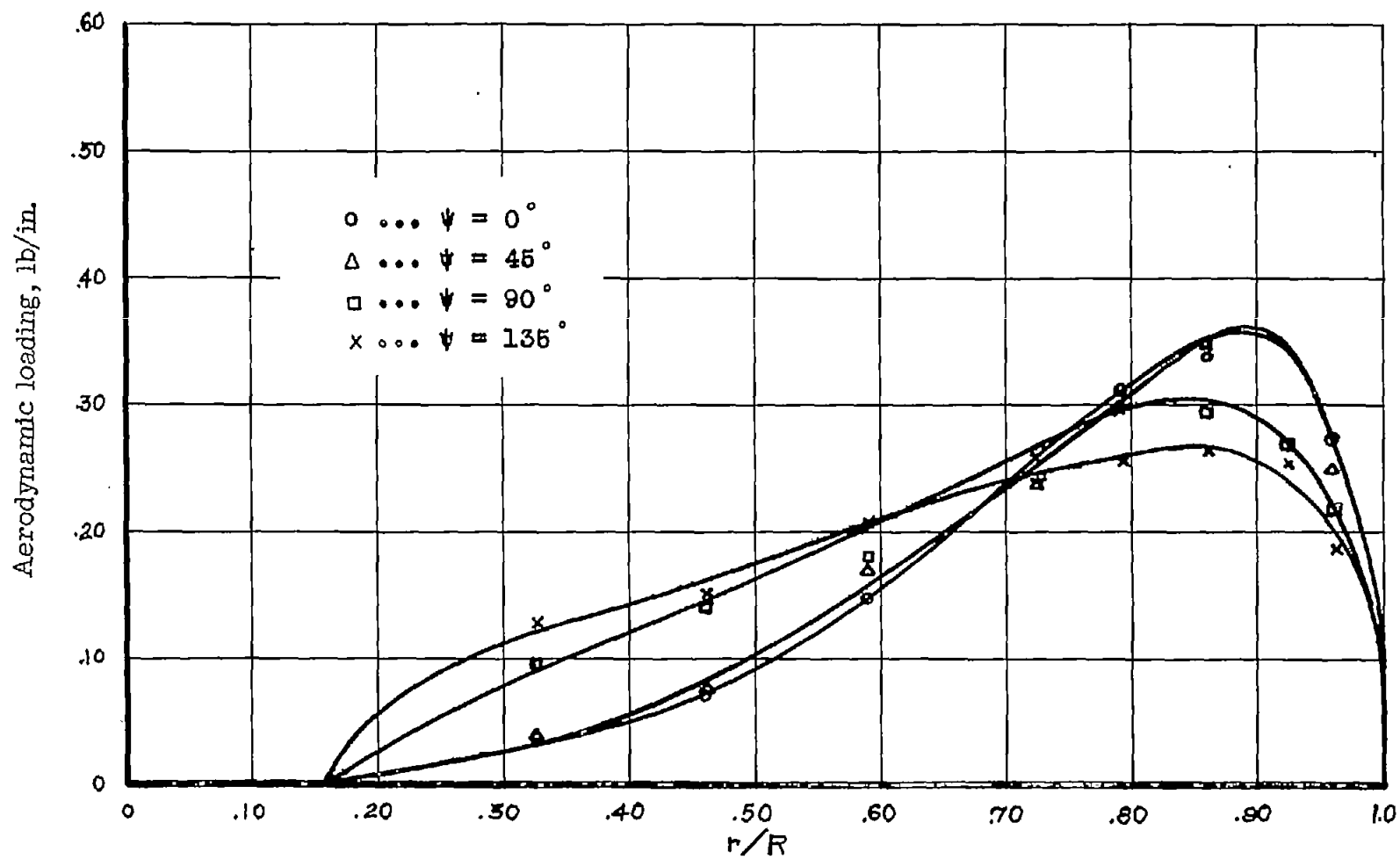
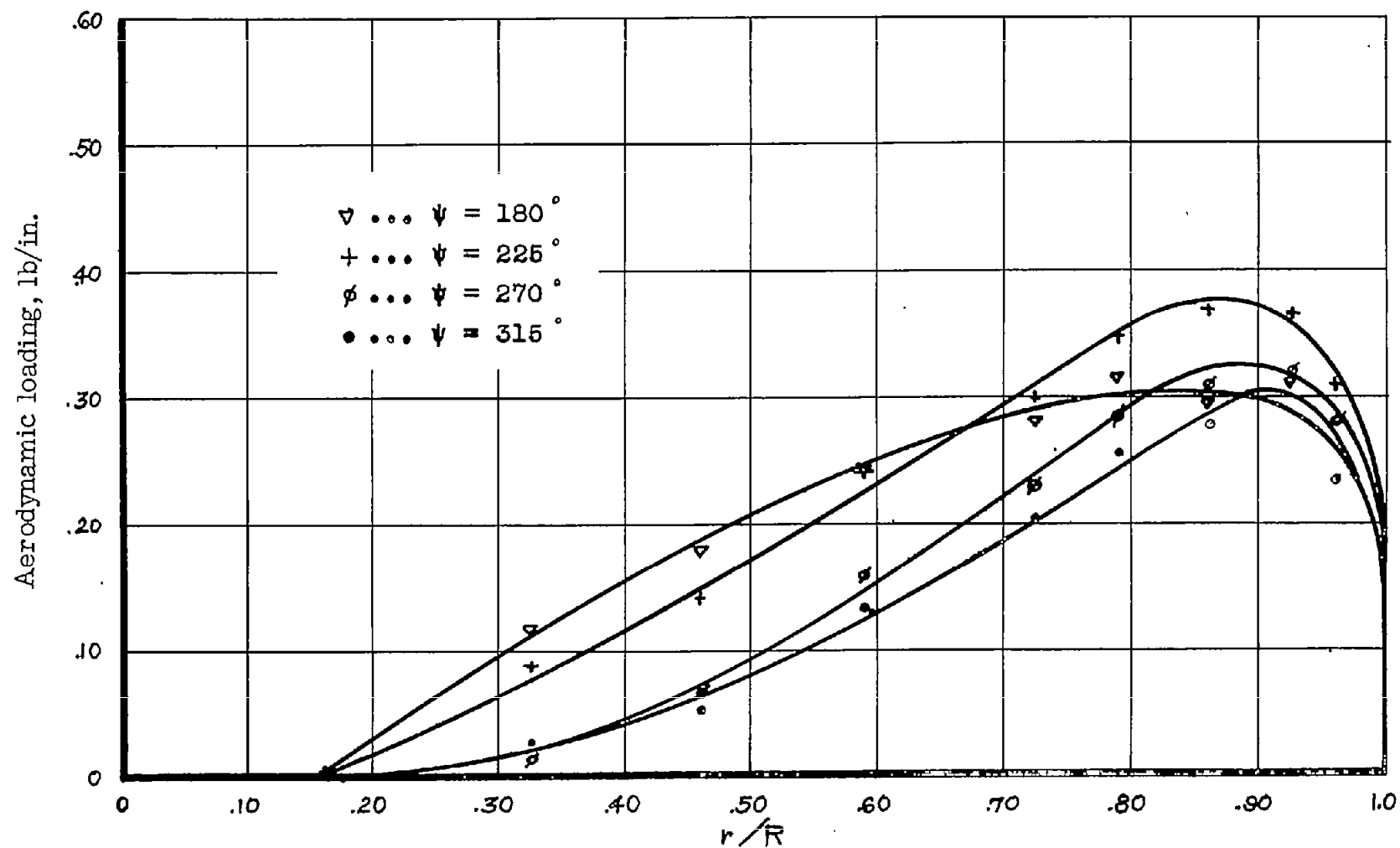


Figure 24.- Experimental spanwise aerodynamic loading at $\psi = 0^\circ$, showing a typical ΔL_r used in the error investigation. $\mu = 0.30$; $\xi = 0$; $A_0 = 8^\circ$; $\alpha = -5^\circ$.



(a) $\psi = 0^\circ$ to 135° .

Figure 25.- Experimental spanwise aerodynamic loading at various azimuths (one-bladed rotor).
 Profile, NACA 0015; $\mu = 0.30$; $\xi = 0$; $A_0 = 8^\circ$; $\alpha = -5^\circ$.



(b) $\psi = 180^\circ$ to 315° .

Figure 25.- Concluded.

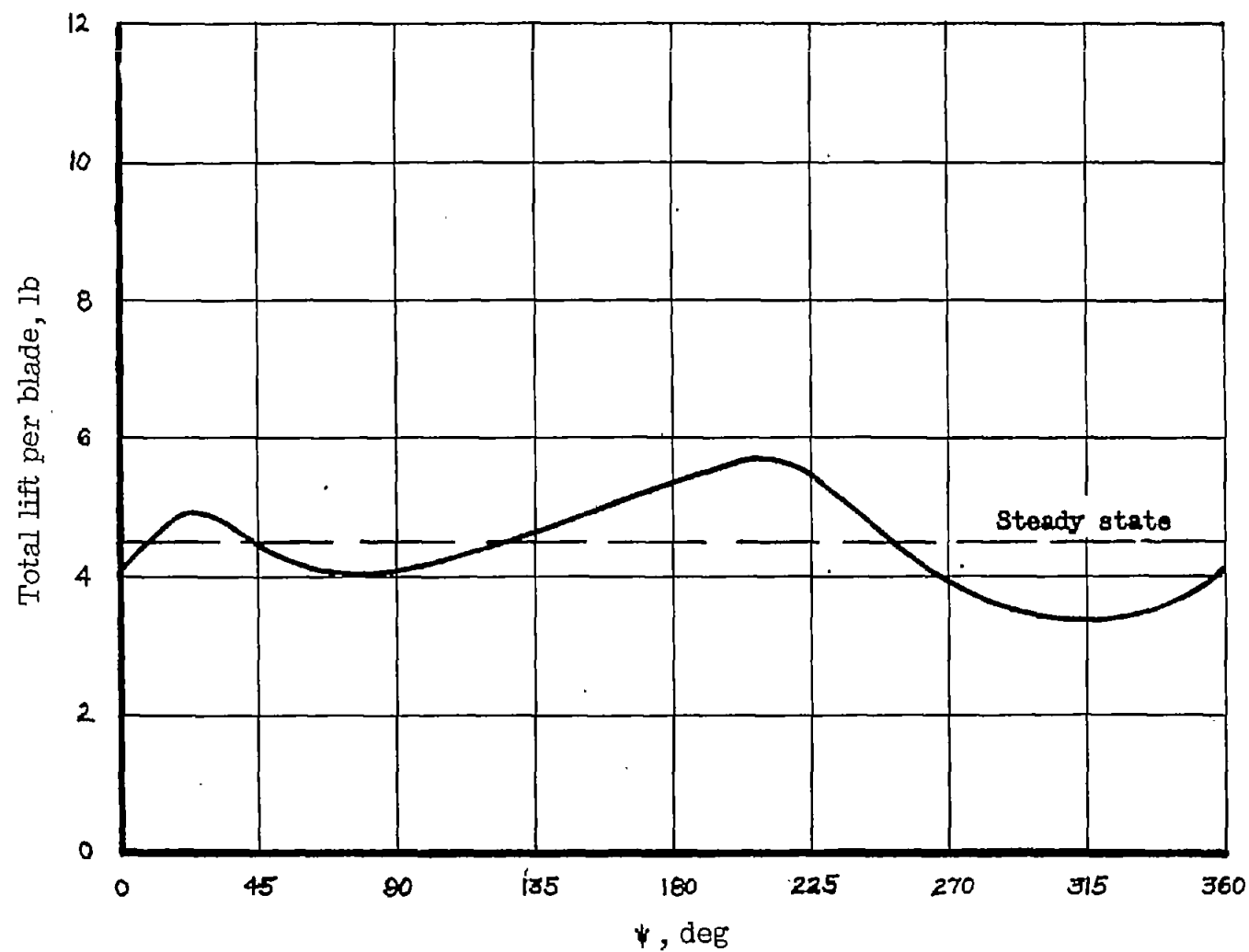


Figure 26.- Total lift per blade variation (one-bladed rotor). Profile, NACA 0015; $\mu = 0.30$; $\xi = 0$; $A_0 = 8^\circ$; $\alpha = -5^\circ$.

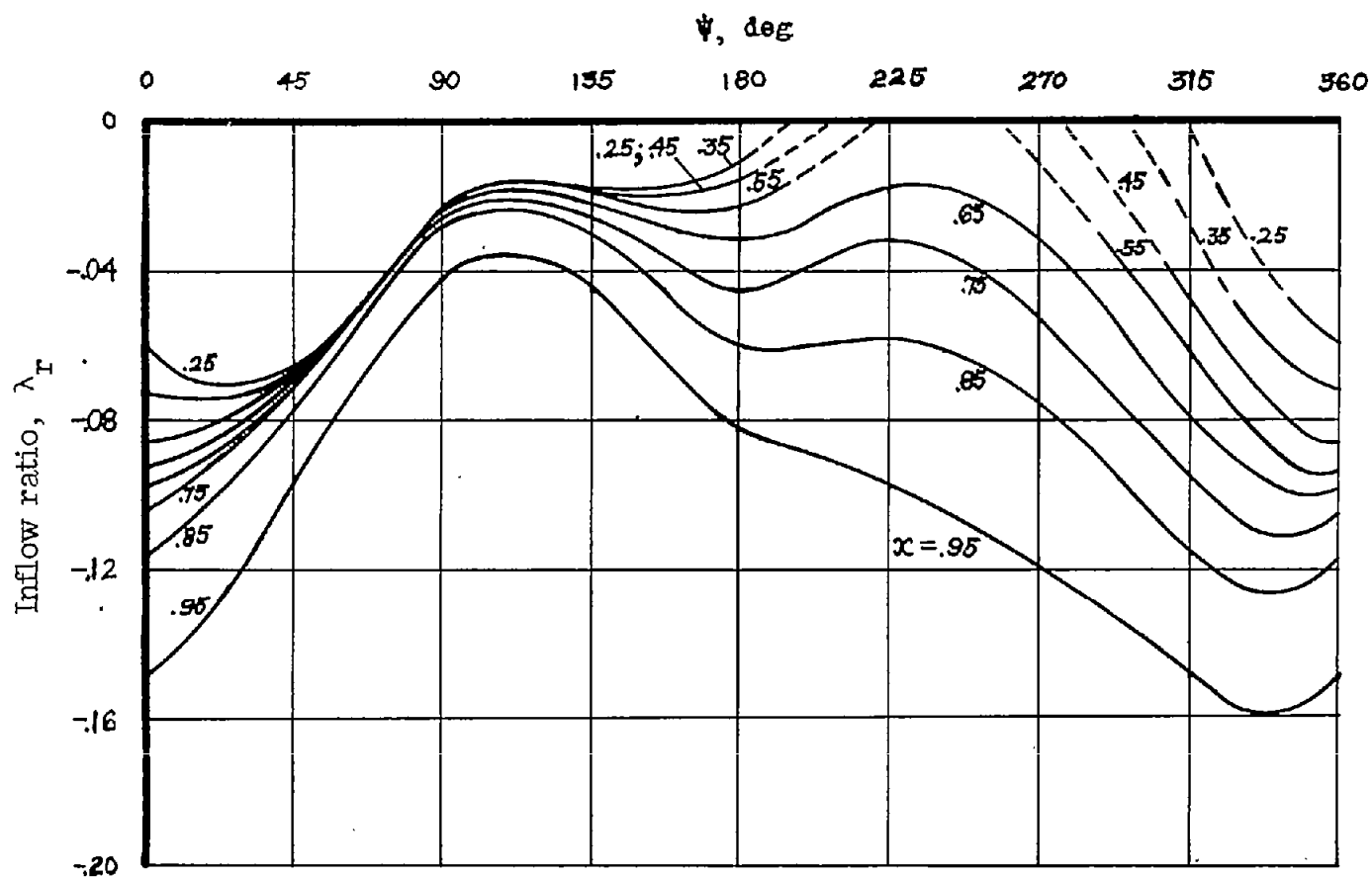
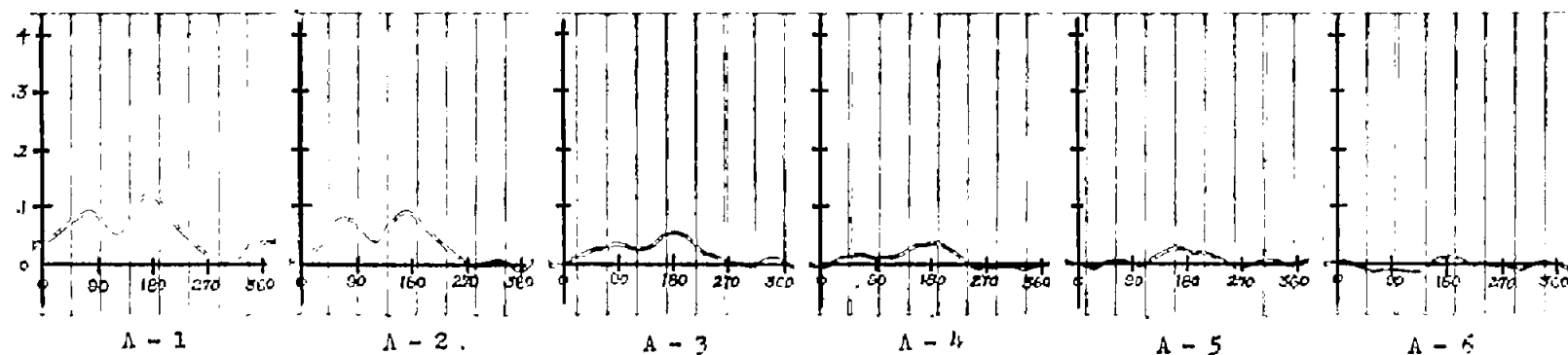
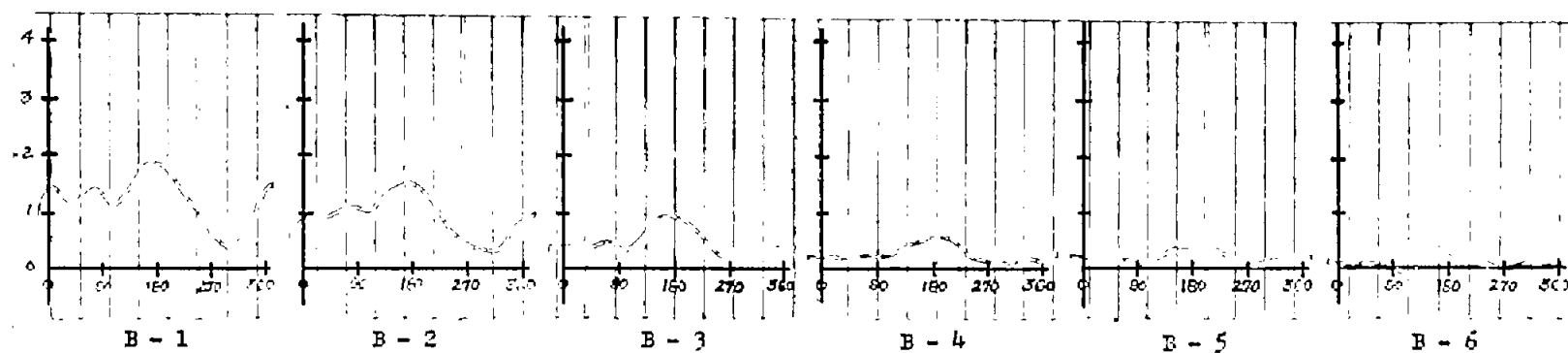


Figure 27.- Inflow distributions from experimental loading and blade-motion data (one-bladed rotor). $\mu = 0.30$; $\xi = 0$; $A_0 = 8^\circ$; $\alpha = -5^\circ$; $a = 5.7$; $\mu \sin \alpha = -0.026$. Dashed lines indicate local blade stall.

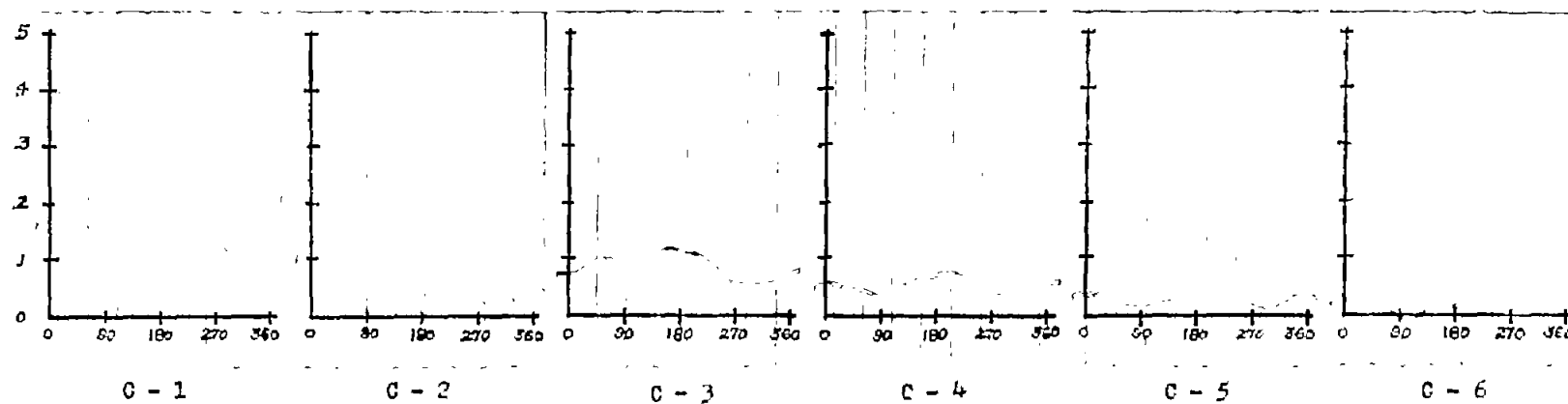


(a) Span station A; $r/R = 0.325$.

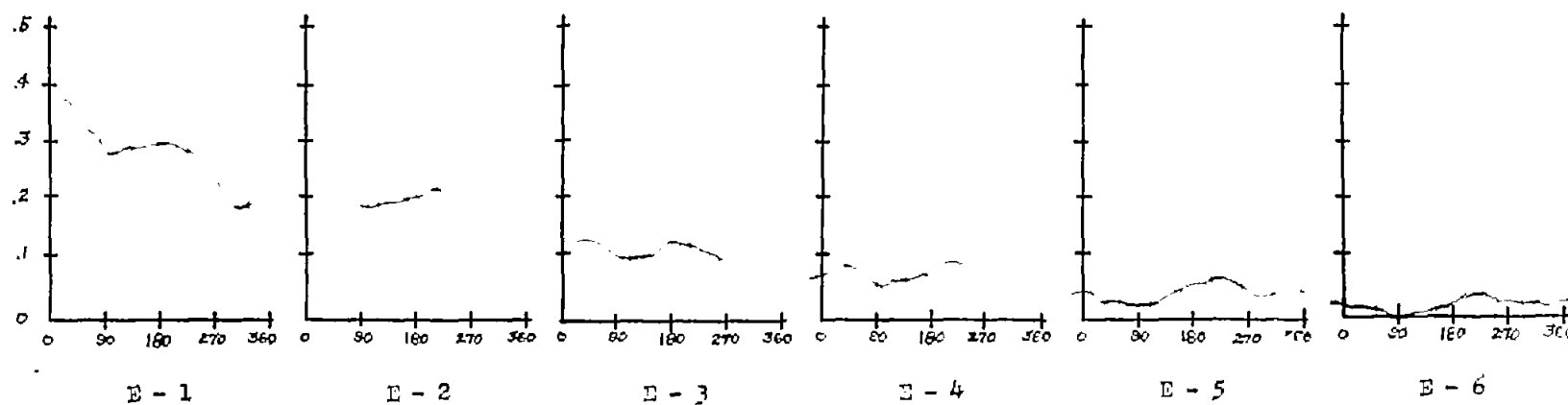


(b) Span station B; $r/R = 0.460$.

Figure 28.- Pressure difference in pounds per square inch against azimuth in degrees. Profile, NACA 0015; speed, 800 rpm; $\xi = 0$; $\mu = 0.30$; $A_0 = 8^\circ$; $\alpha = -5^\circ$.

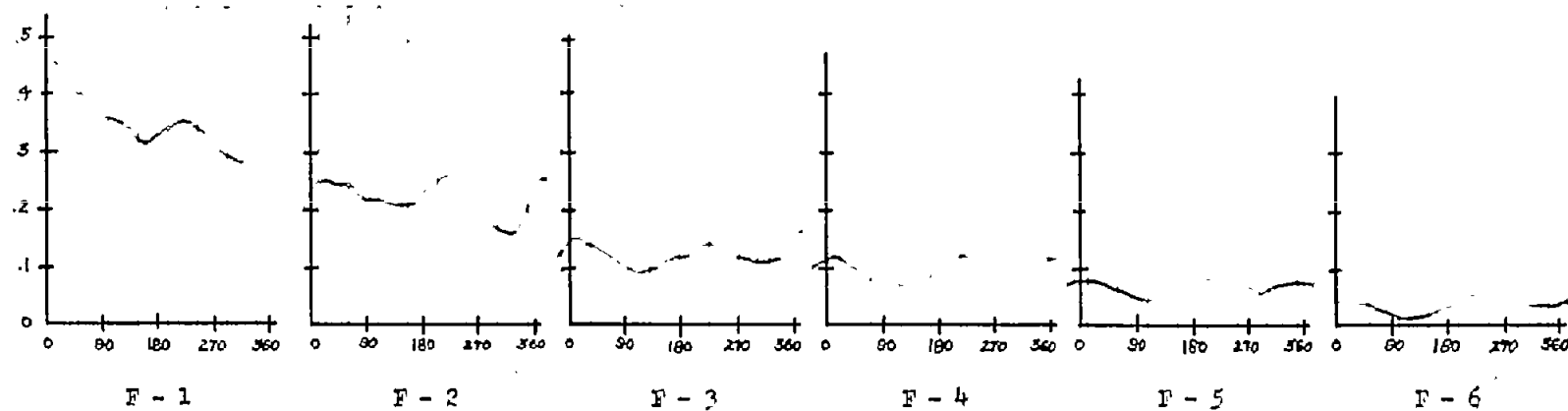


(c) Span station C; $r/R = 0.590$.

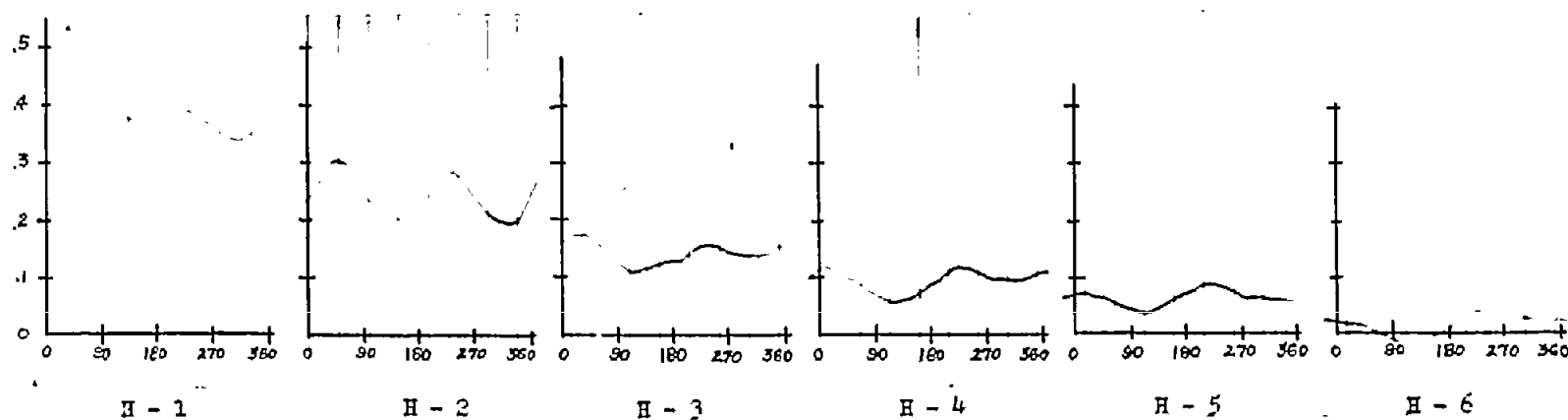


(d) Span station E; $r/R = 0.725$.

Figure 28.- Continued.

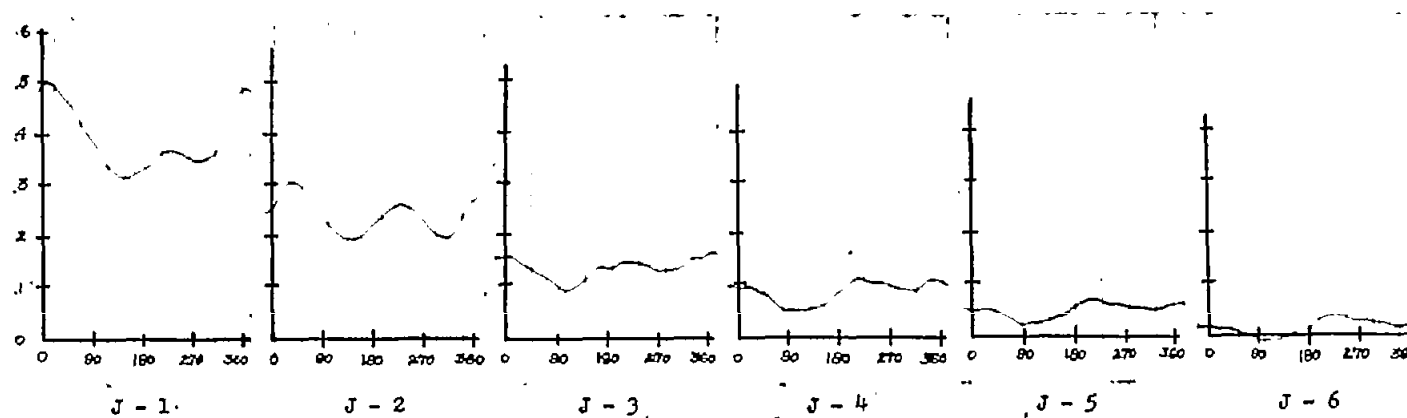


(e) Span station F; $r/R = 0.790$.

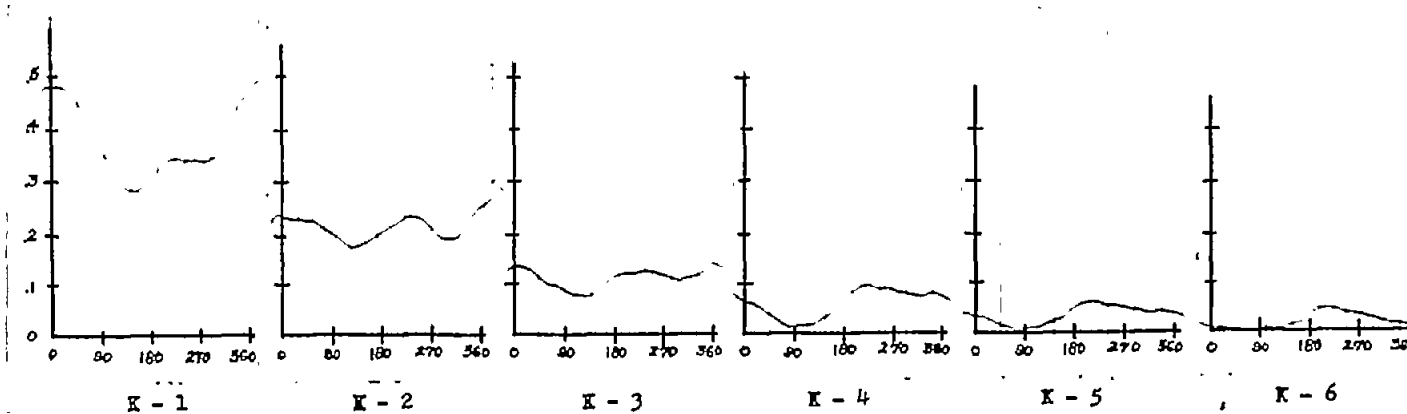


(f) Span station H; $r/R = 0.860$.

Figure 28.- Continued.

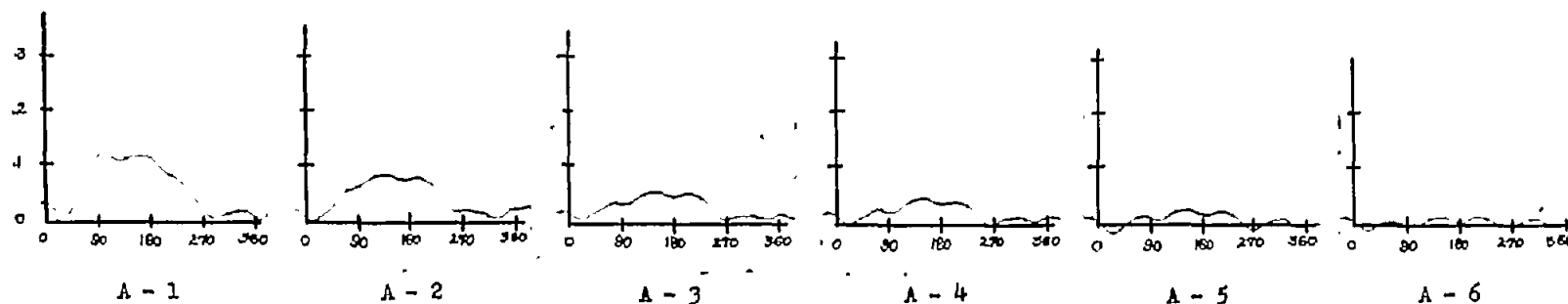


(g) Span station J; $r/R = 0.925$.

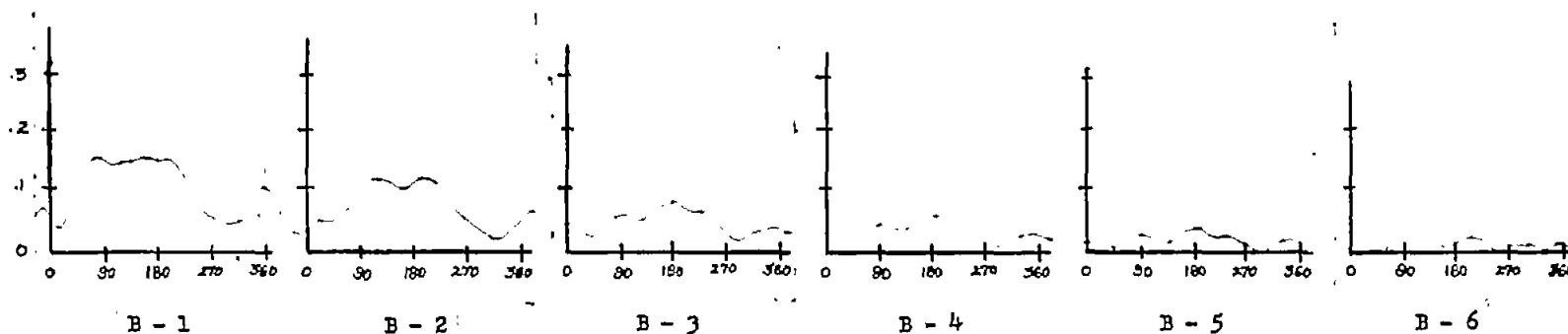


(h) Span station K; $r/R = 0.960$.

Figure 28.- Concluded.

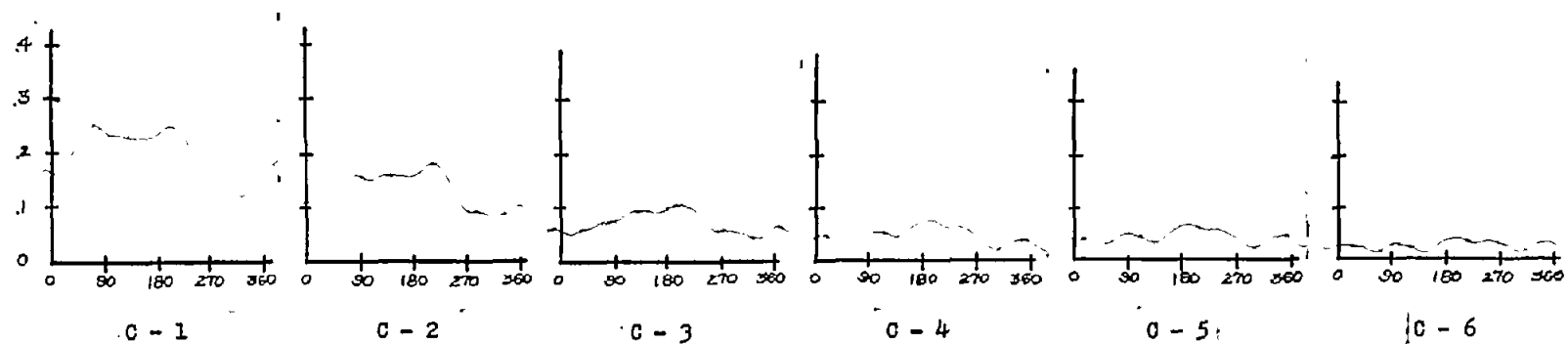


(a) Span station A; $r/R = 0.325$.

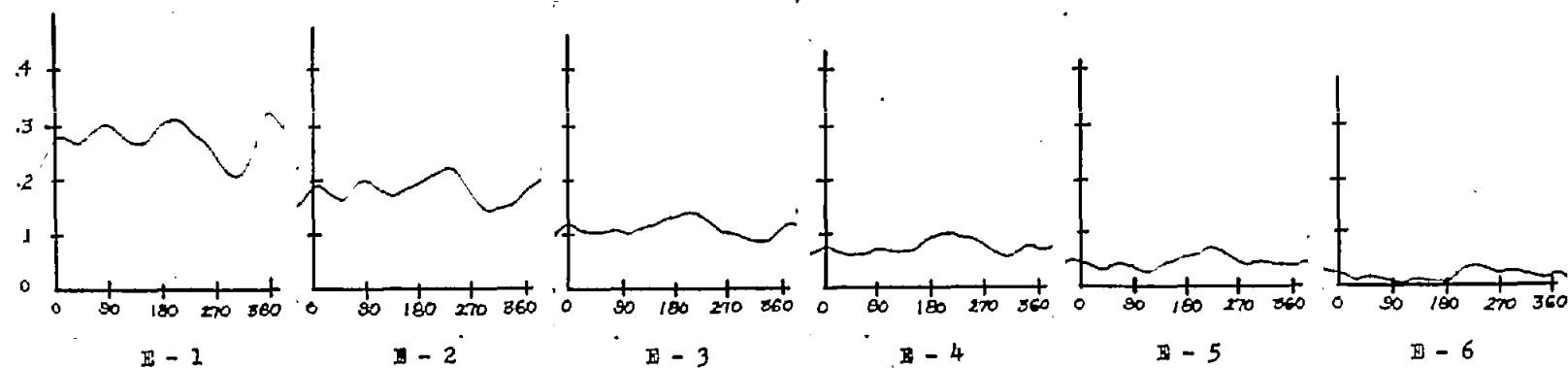


(b) Span station B; $r/R = 0.460$.

Figure 29.- Pressure difference in pounds per square inch against azimuth in degrees (one-bladed rotor). Profile, NACA 0015; speed, 800 rpm; $\xi = 0$; $\mu = 0.30$; $A_0 = 8^\circ$; $\alpha = -5^\circ$.

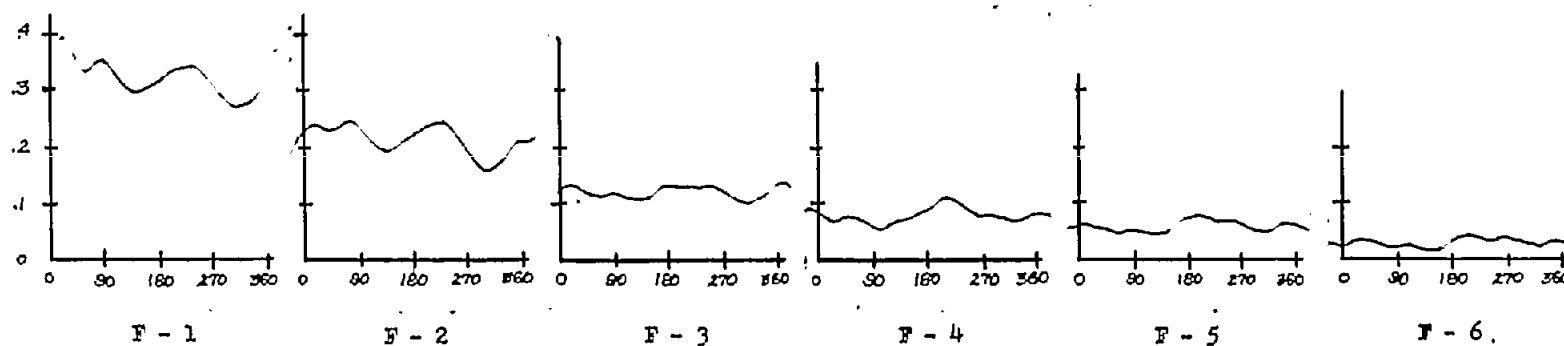


(c) Span station C; $r/R = 0.590$.

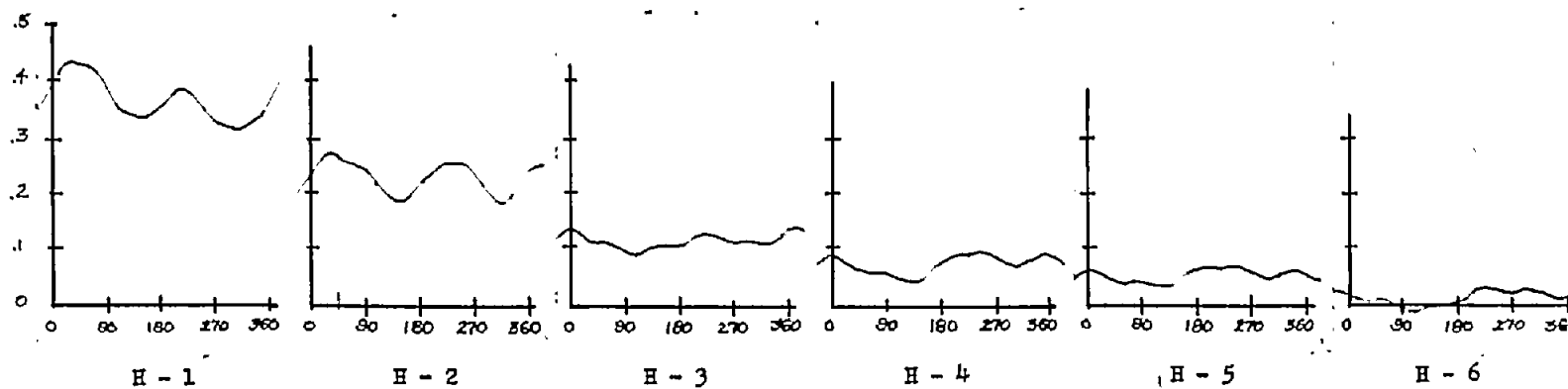


(d) Span station E; $r/R = 0.725$.

Figure 29.- Continued.

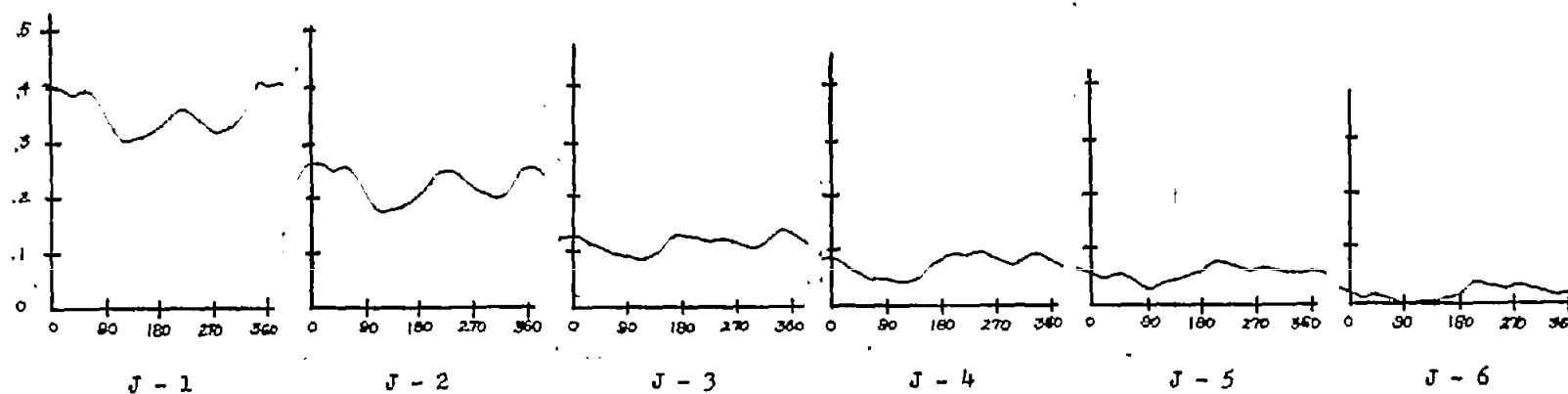


(e) Span station F; $r/R = 0.790$.

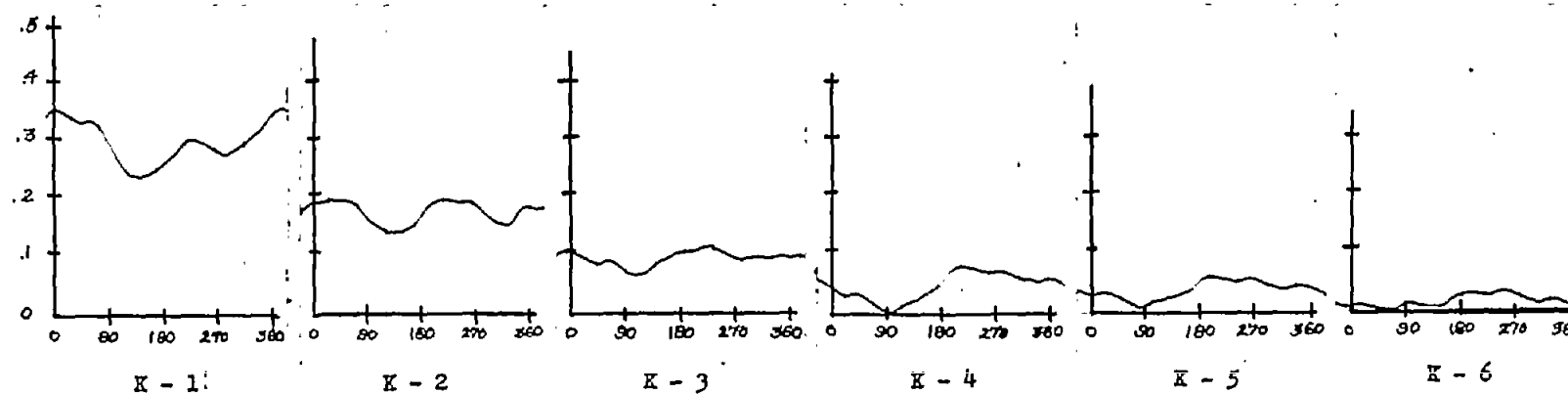


(f) Span station H; $r/R = 0.860$.

Figure 29.- Continued.

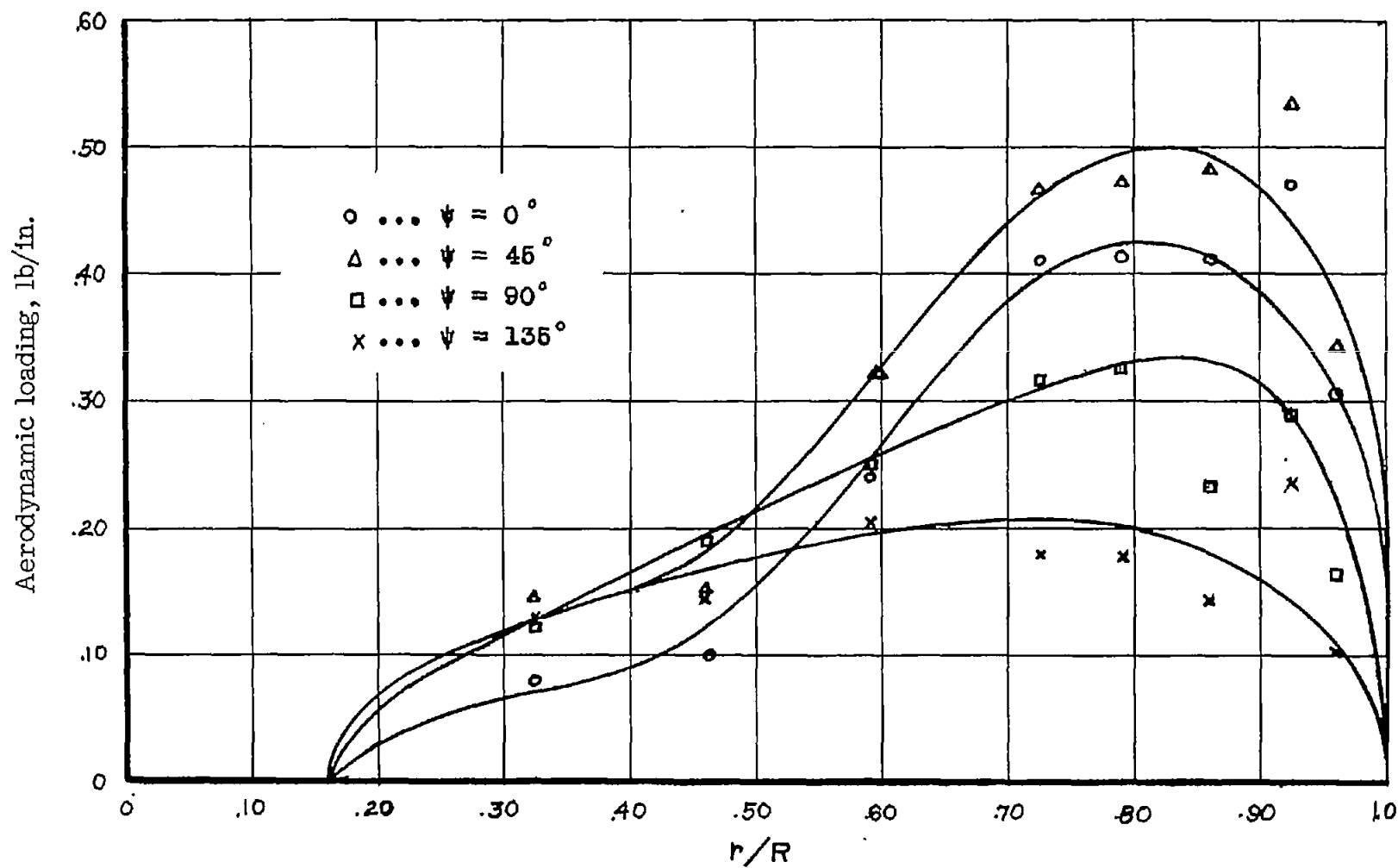


(g) Span station J; $r/R = 0.925$.



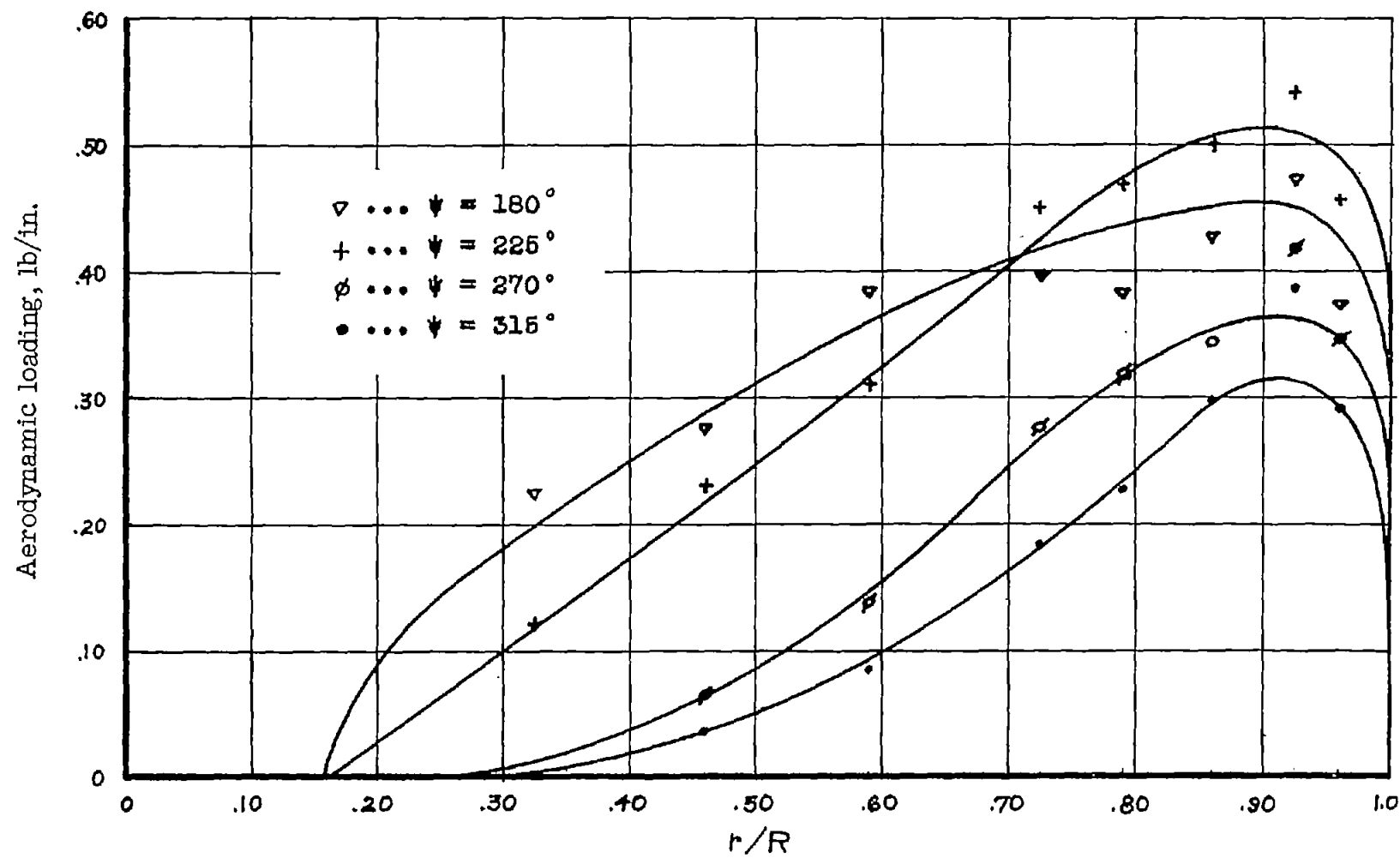
(h) Span station K; $r/R = 0.960$.

Figure 29.- Concluded.



(a) $\psi = 0^\circ$ to 135° .

Figure 30.- Experimental spanwise aerodynamic loading at various azimuths. Profile, NACA 0015;
 $\mu = 0.50$; $\xi = 0$; $A_0 = 12^\circ$; $\alpha = -10^\circ$.



(b) $\psi = 180^\circ$ to 315° .

Figure 30.- Concluded.

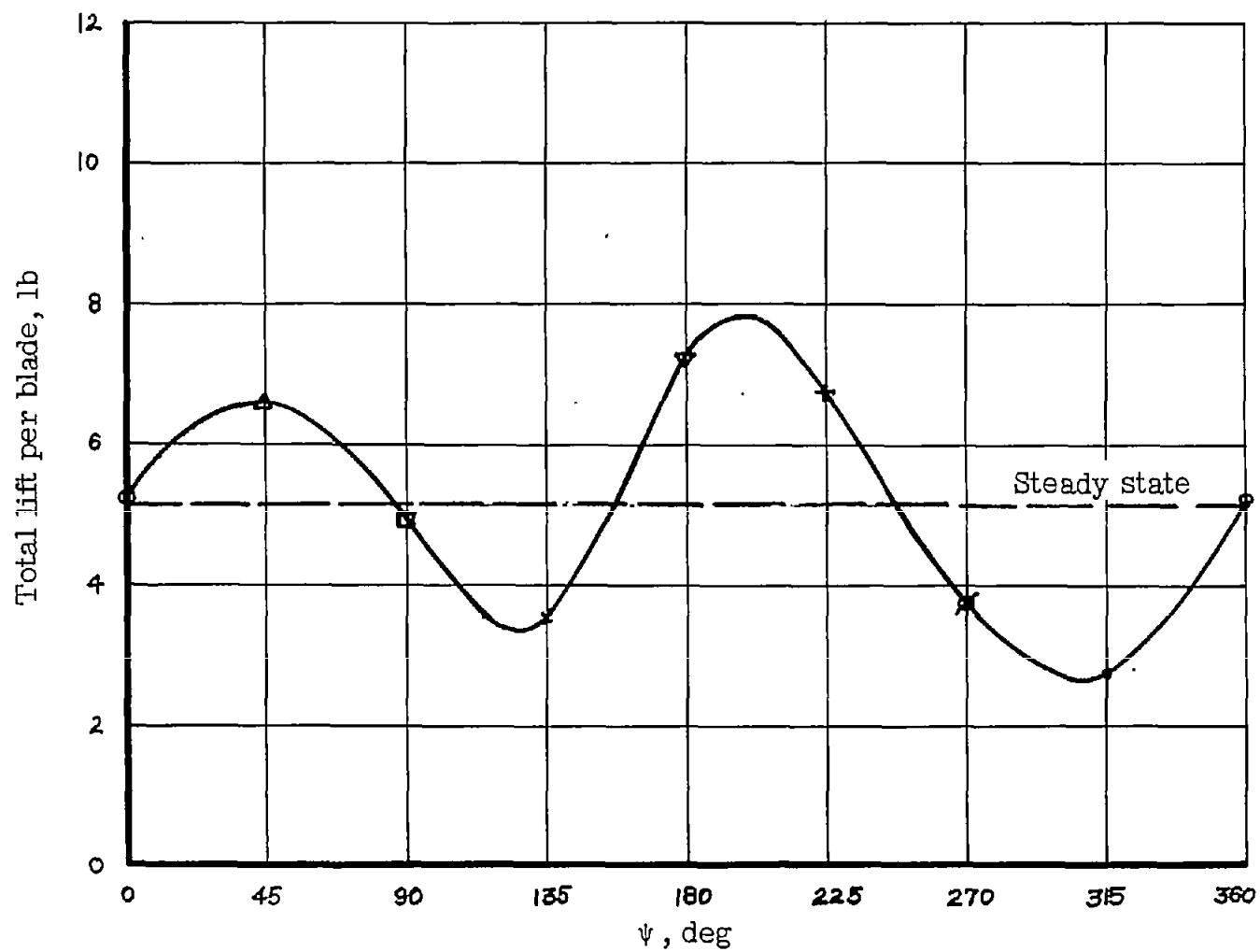


Figure 31.- Variation in total lift per blade. Profile, NACA 0015; $\mu = 0.50$;
 $\xi = 0$; $A_0 = 12^\circ$; $\alpha = -10^\circ$.

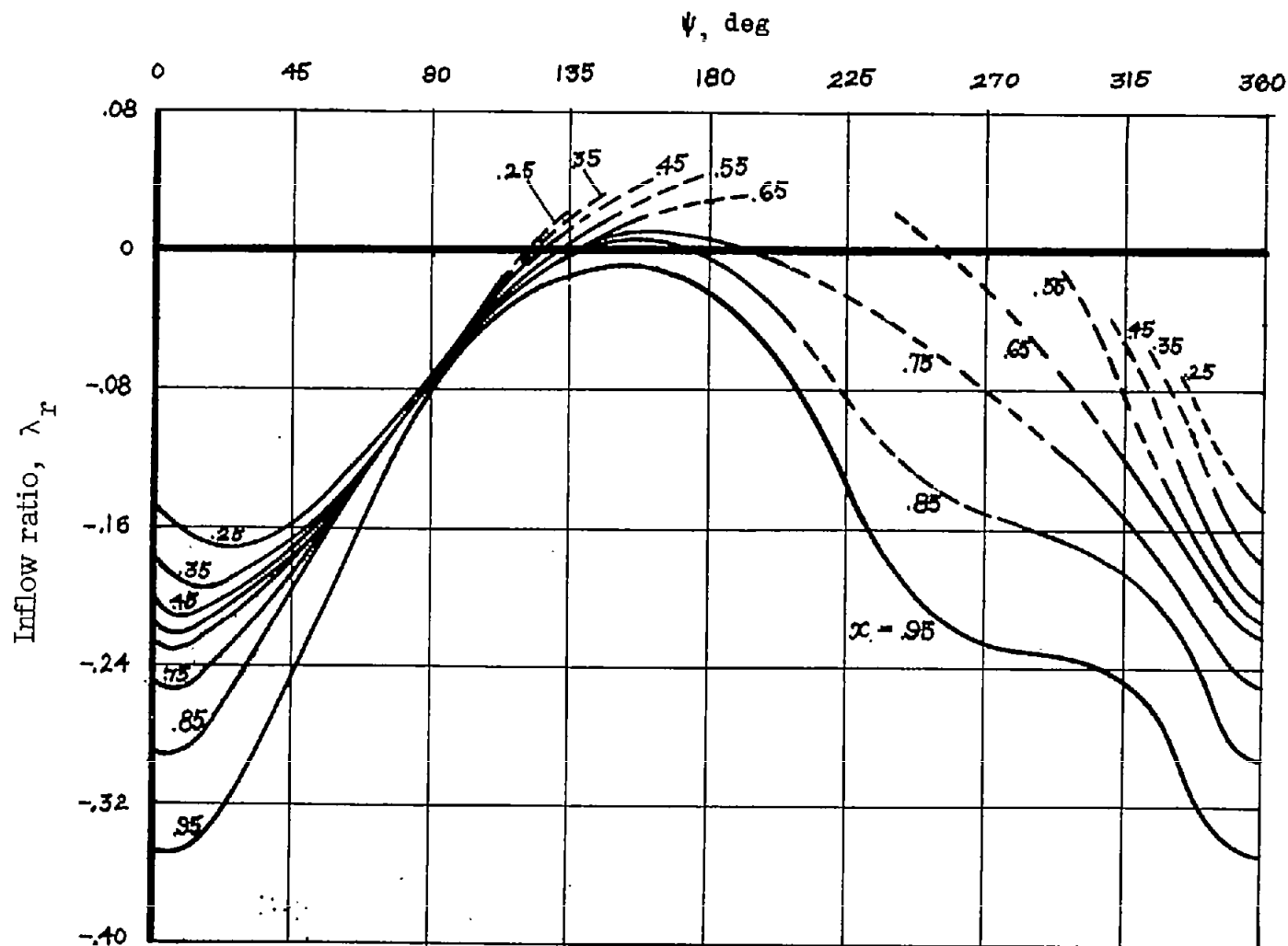
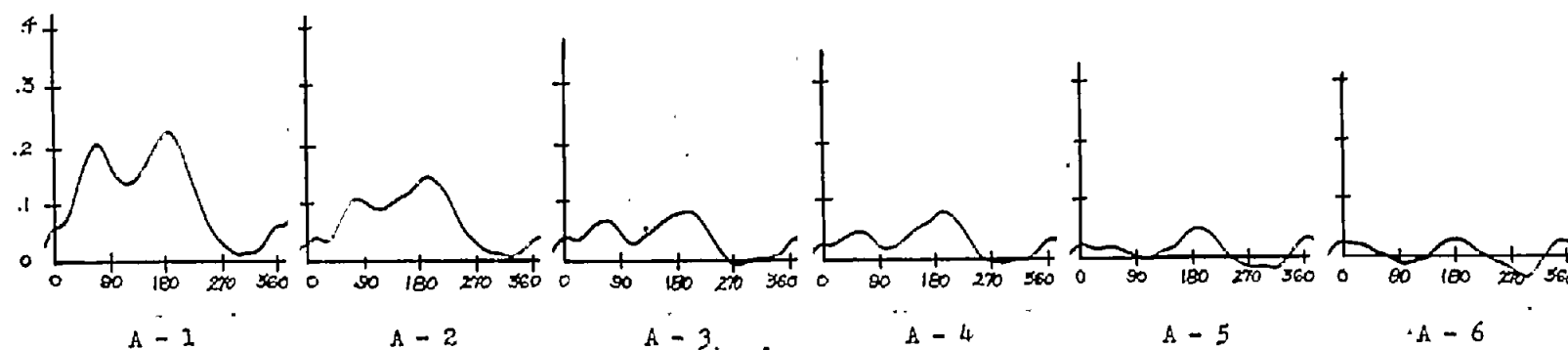
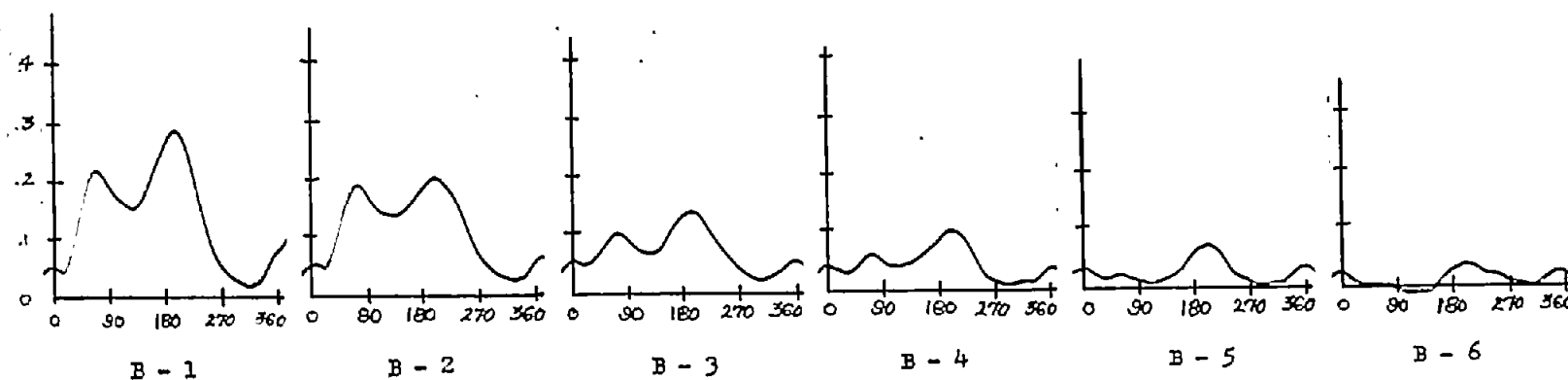


Figure 32.- Inflow distributions from experimental loading and blade-motion data. $\mu = 0.50$; $\xi = 0$; $A_0 = 12^\circ$; $\alpha = -10^\circ$; $a = 5.7$; $\mu \sin \alpha = -0.087$. Dashed lines indicate local blade stall.

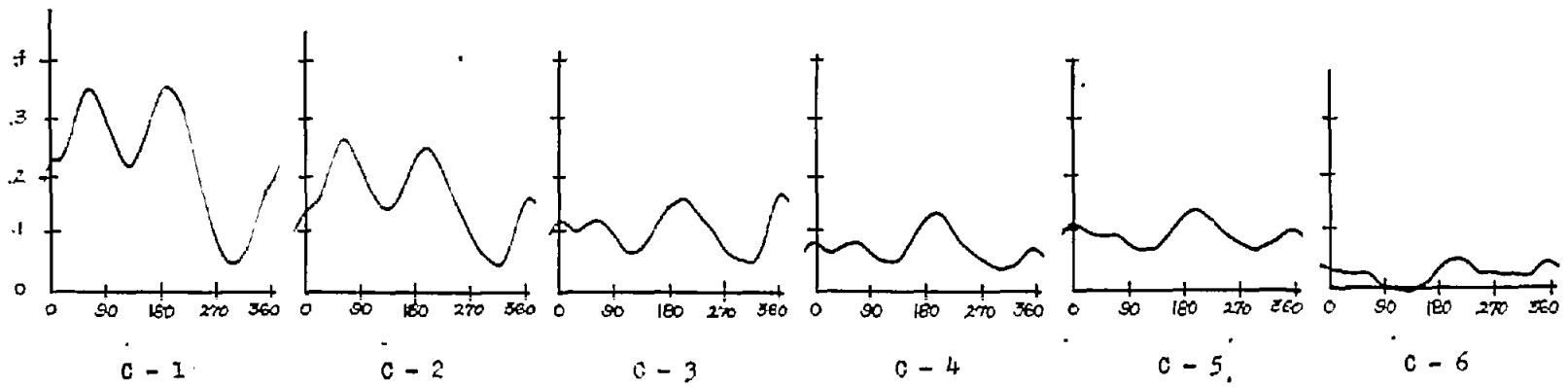


(a) Span station A; $r/R = 0.325$.

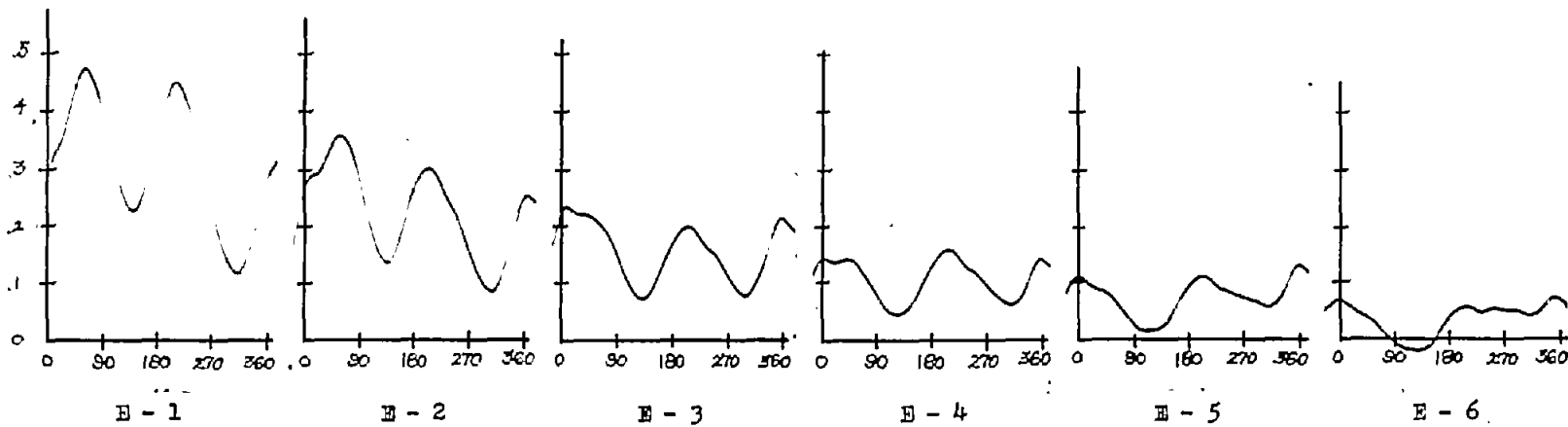


(b) Span station B; $r/R = 0.460$.

Figure 33.- Pressure difference in pounds per square inch against azimuth in degrees. Profile, NACA 0015; speed, 800 rpm; $\xi = 0$; $\mu = 0.50$; $A_0 = 12^\circ$; $\alpha = -10^\circ$.

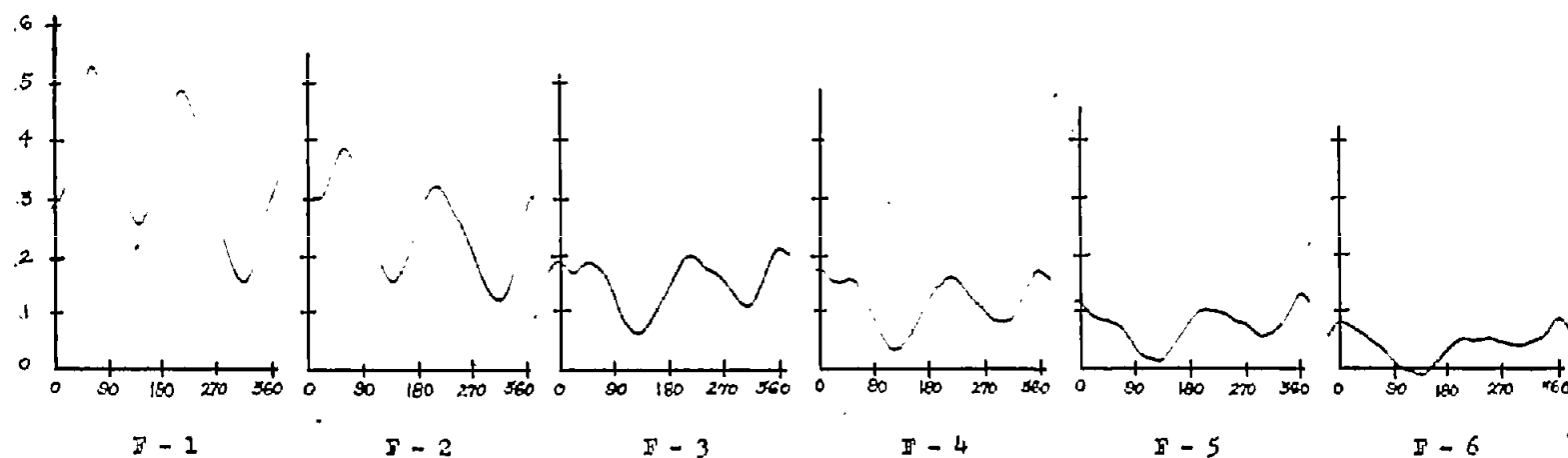


(c) Span station C; $r/R = 0.590$.

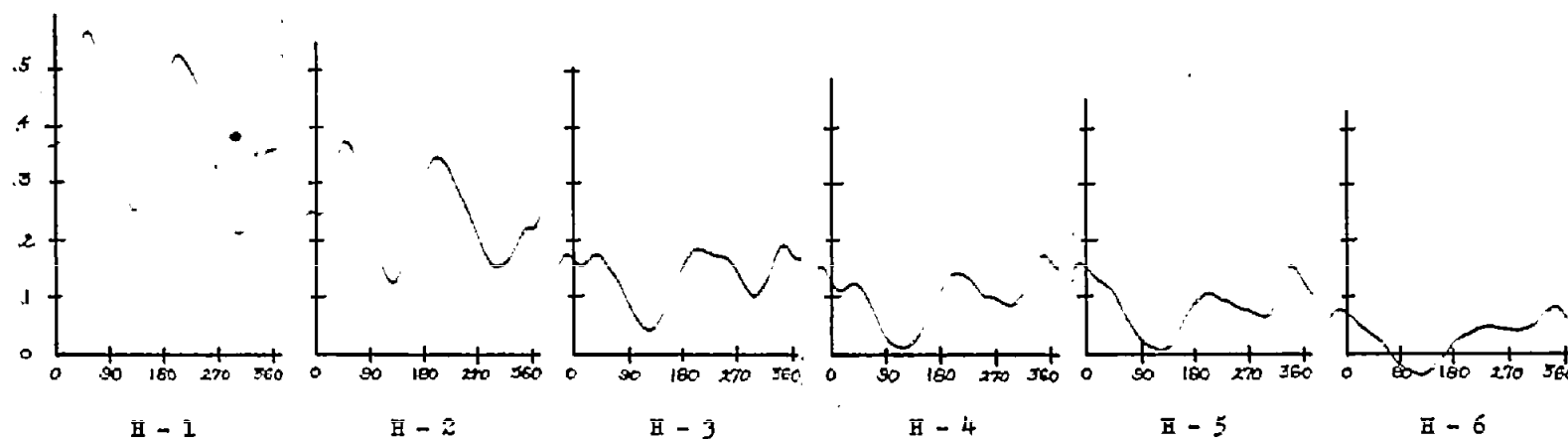


(d) Span station E; $r/R = 0.725$.

Figure 33.- Continued.

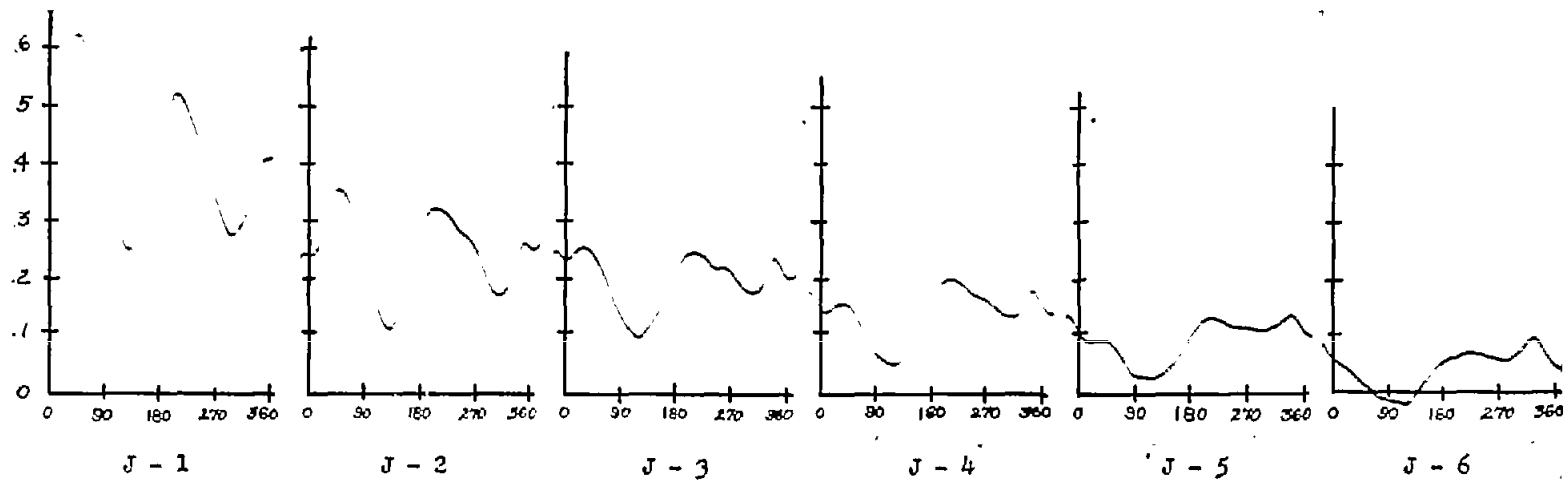


(e) Span station F; $r/R = 0.790$.

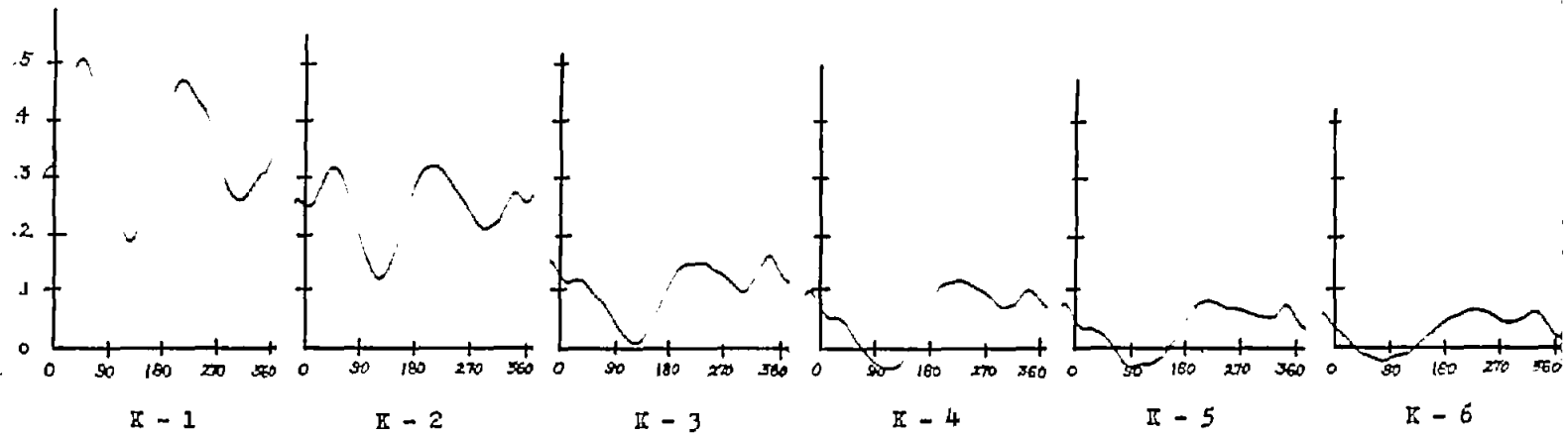


(f) Span station H; $r/R = 0.860$.

Figure 33.- Continued.

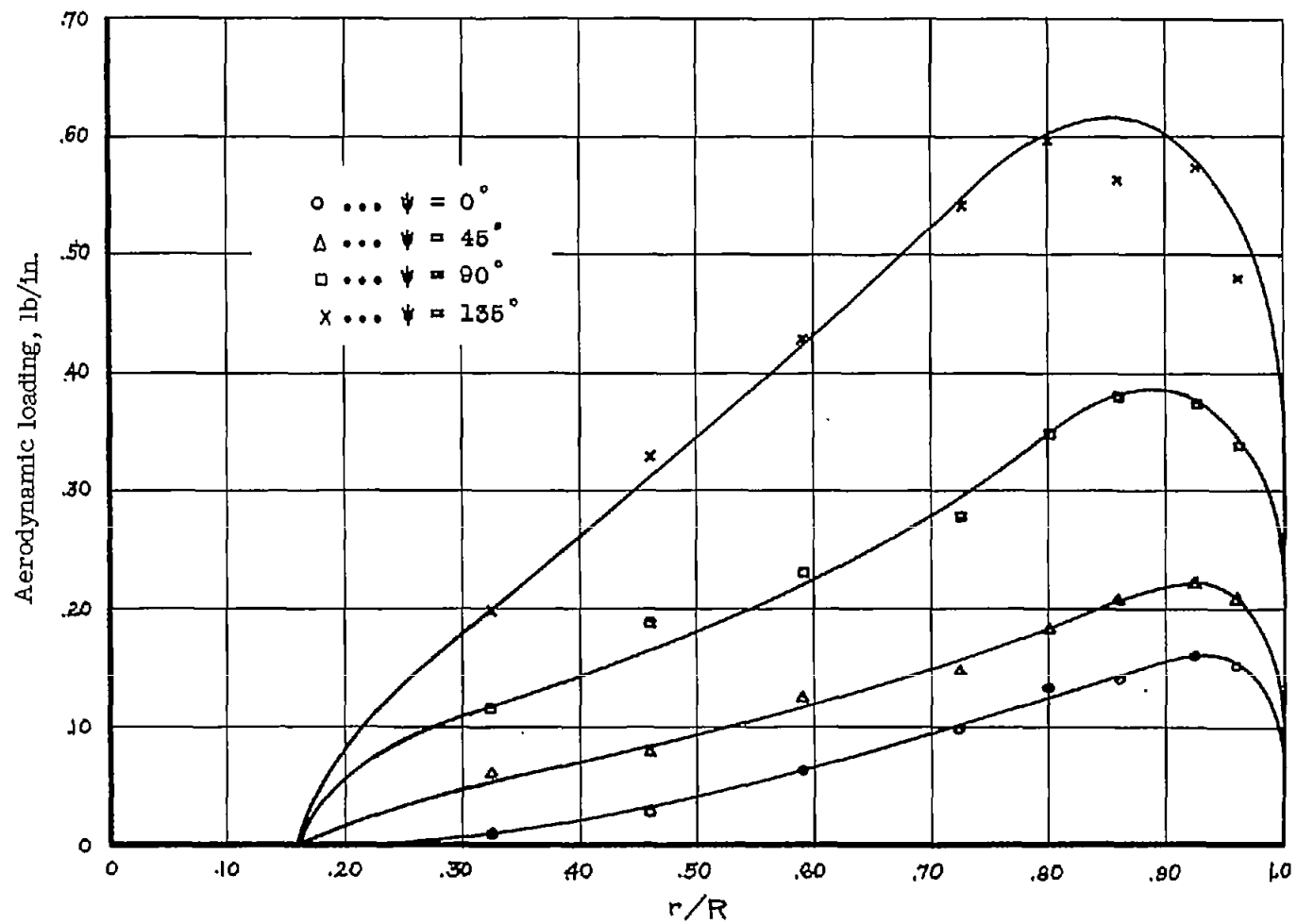


(g) Span station J; $r/R = 0.925$.



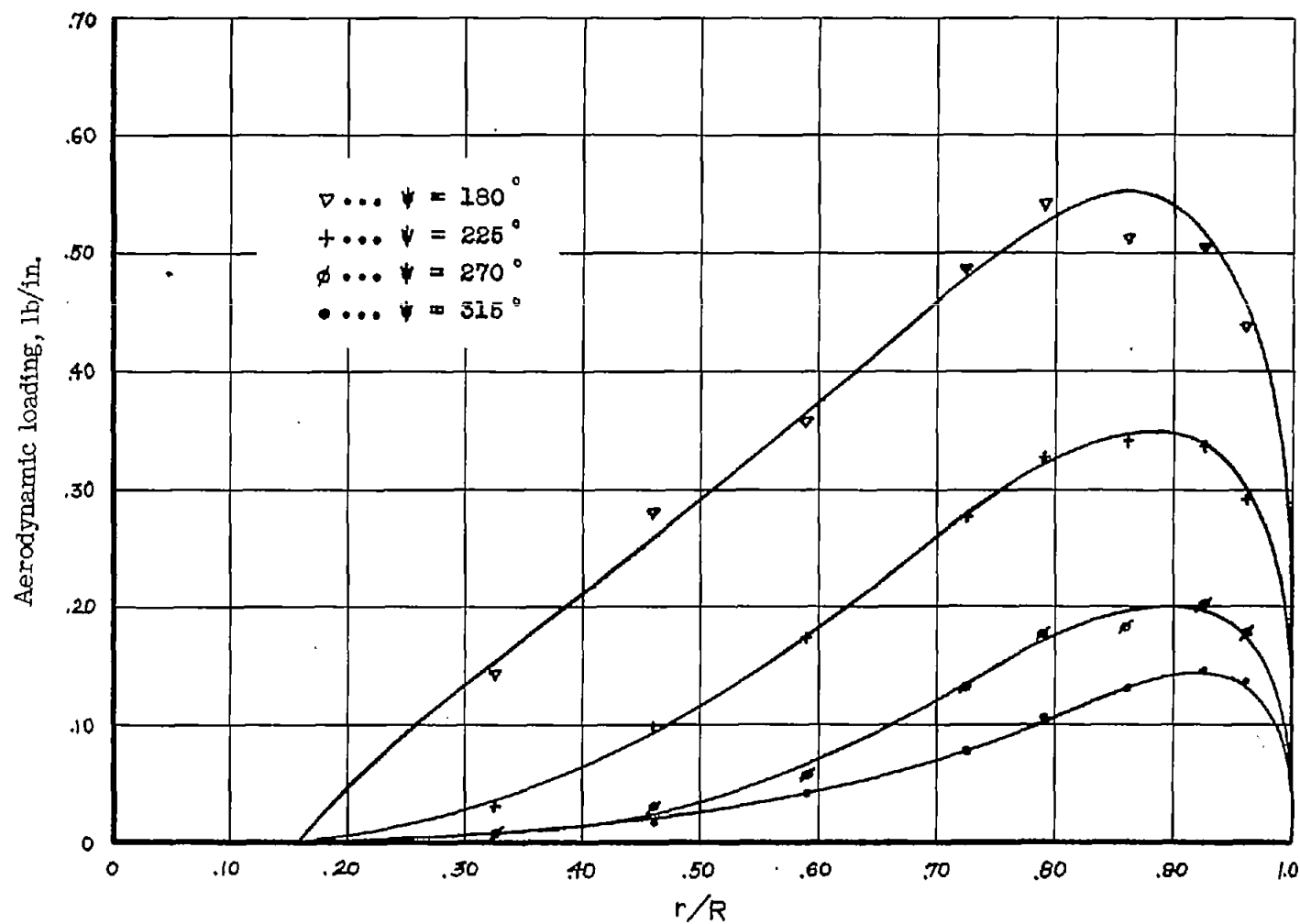
(h) Span station K; $r/R = 0.960$.

Figure 33.- Concluded.



(a) $\psi = 0^\circ$ to 135° .

Figure 34.- Experimental spanwise aerodynamic loading at various azimuths. Profile, NACA 0015; $\mu = 0.30$; $\xi = 0.13$; $A_0 = 8^\circ$; $\alpha = -5^\circ$.



(b) $\psi = 180^\circ$ to 315° .

Figure 34.- Concluded.

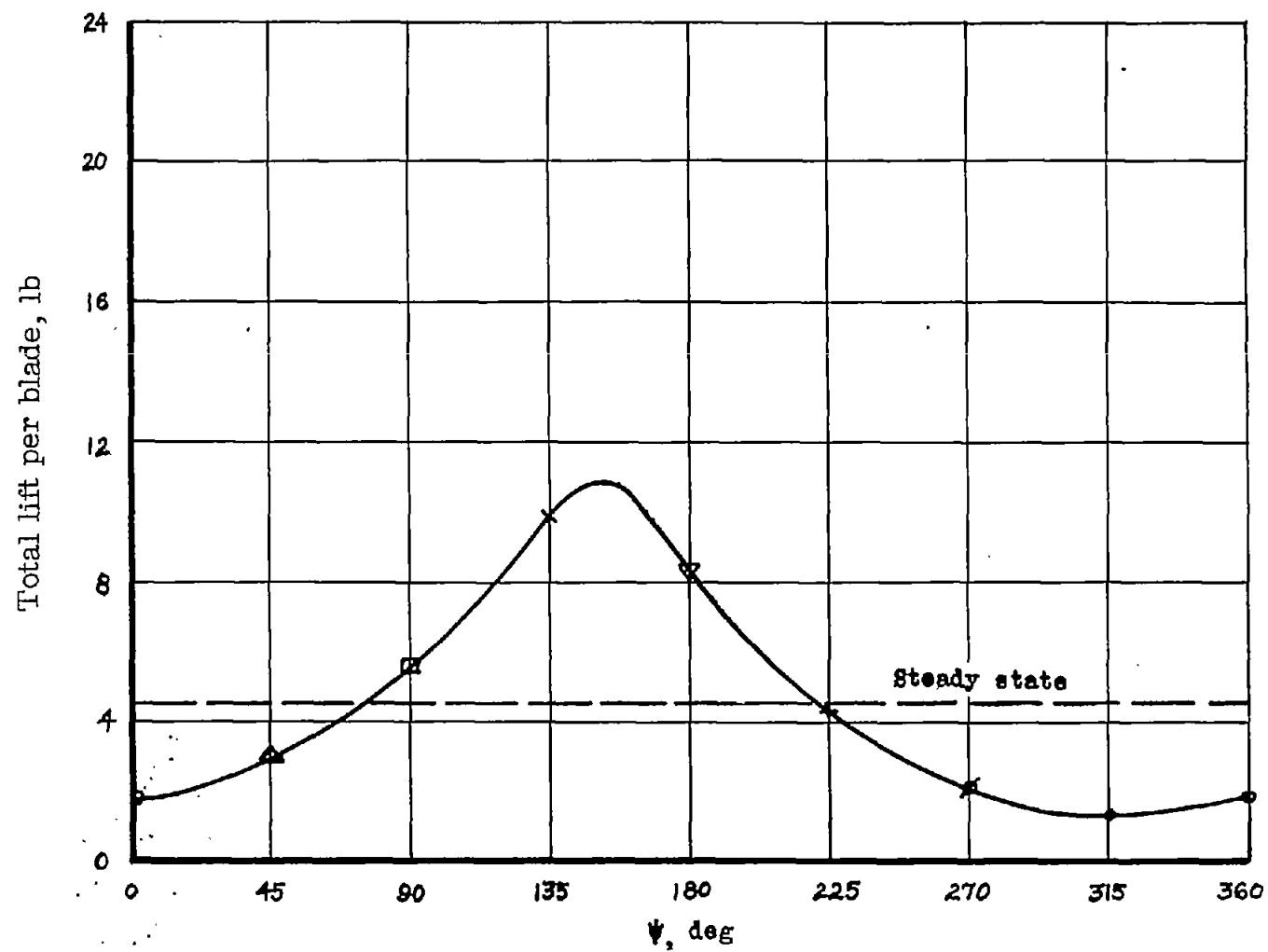


Figure 35.- Variation in total lift per blade. Profile, NACA 0015;
 $\mu = 0.30$; $\xi = 0.13$; $A_0 = 8^\circ$; $\alpha = -5^\circ$.

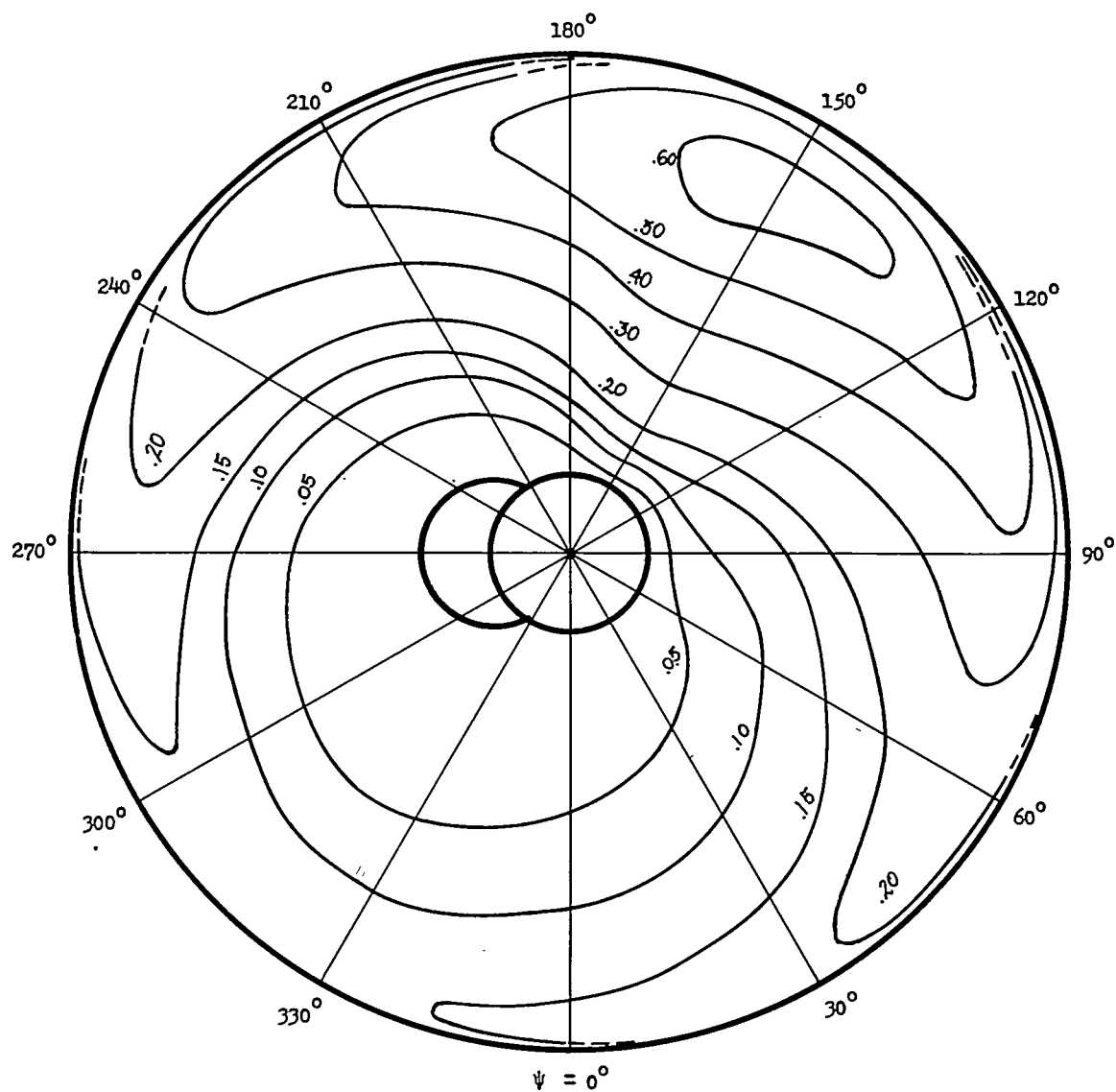


Figure 36.- Curves of constant aerodynamic loading (pounds per inch).

Profile, NACA 0015; $\mu = 0.30$; $\xi = 0.13$; $A_0 = 8^\circ$; $\alpha = -5^\circ$; $C_T/\sigma = 0.070$.

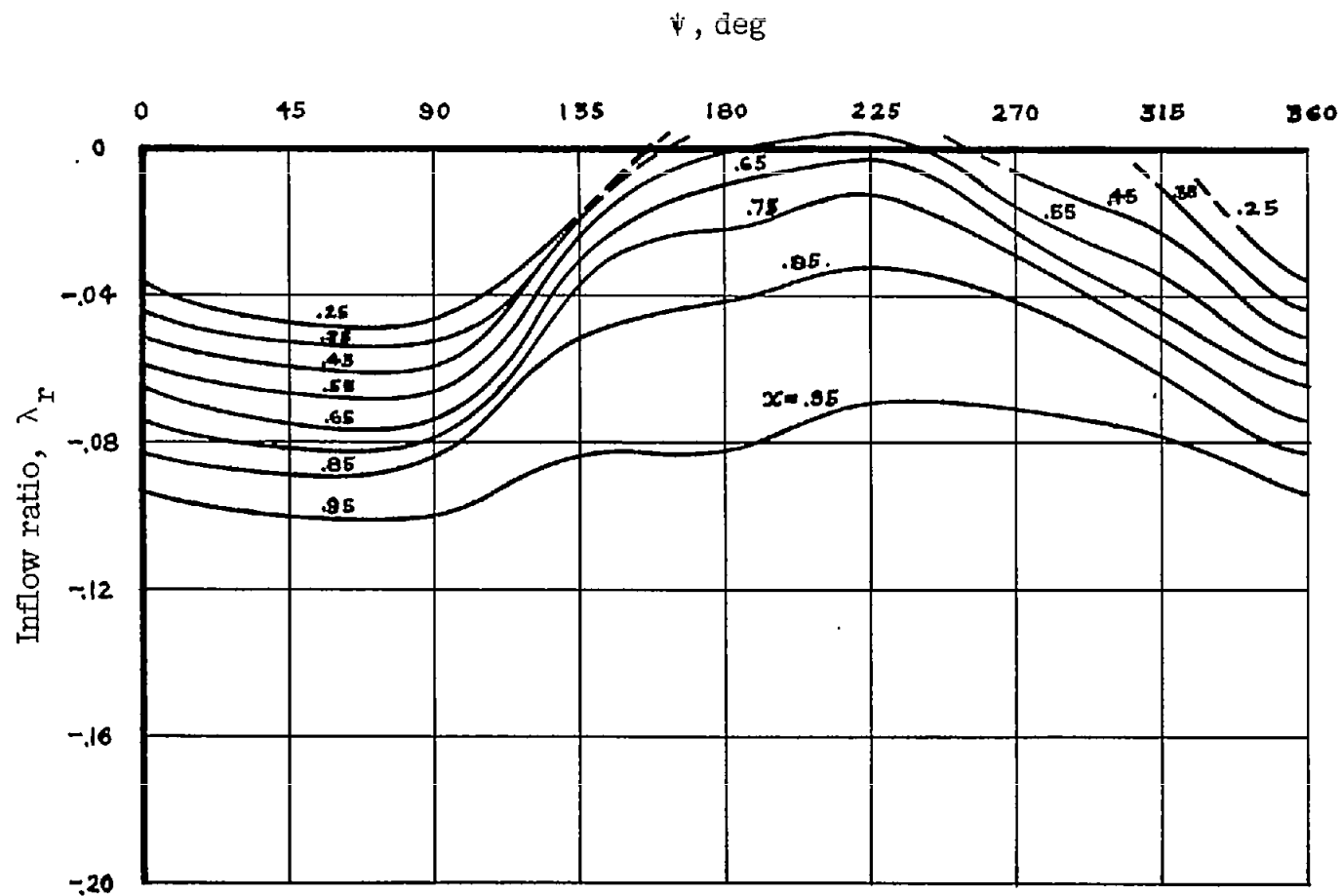


Figure 37.- Inflow distributions from experimental loading and blade-motion data. $\mu = 0.30$; $\xi = 0.13$; $A_0 = 8^\circ$; $\alpha = -5^\circ$; $a = 5.7$; $\mu \sin \alpha = -0.026$. Dashed lines indicate local blade stall.

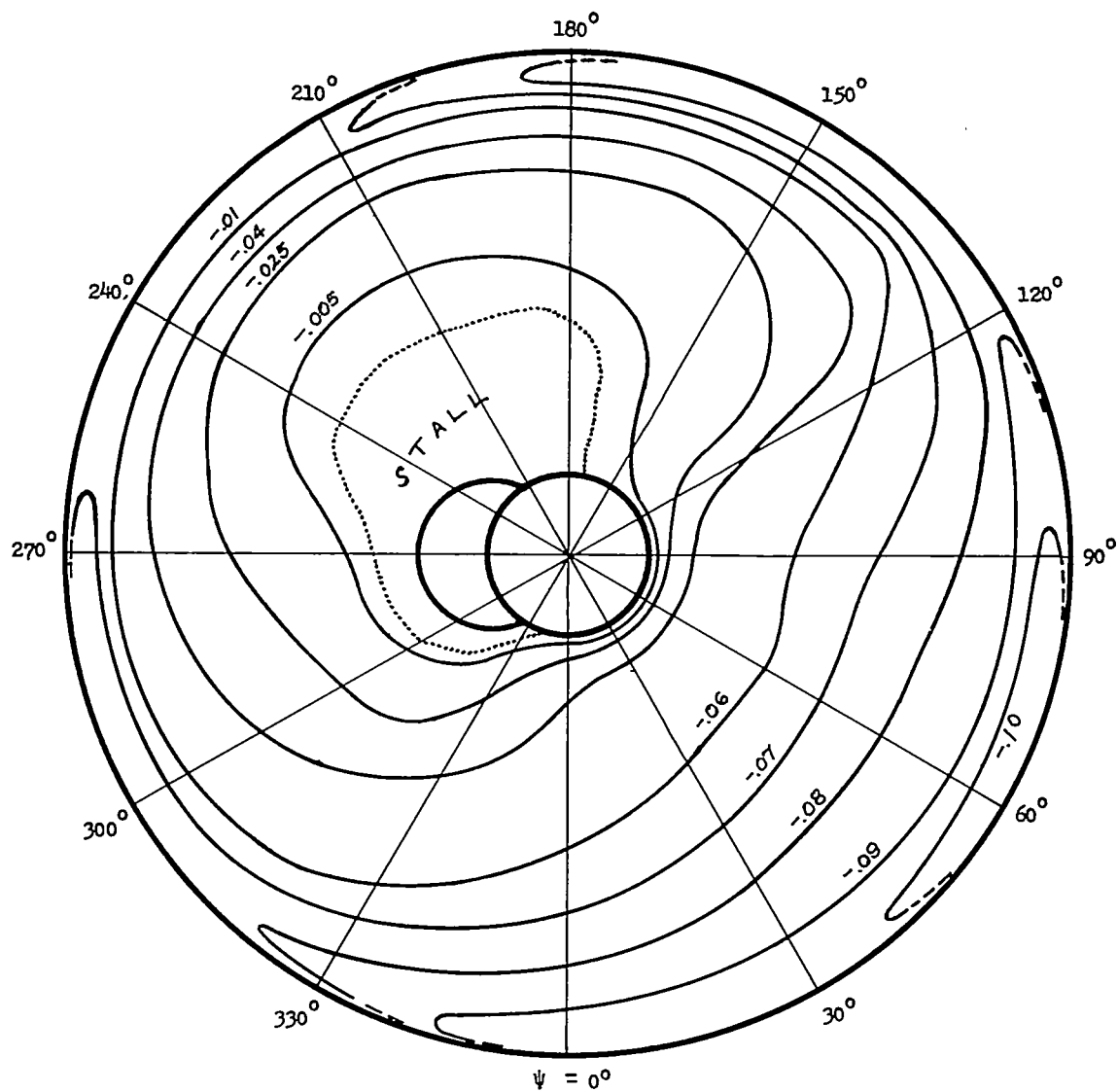
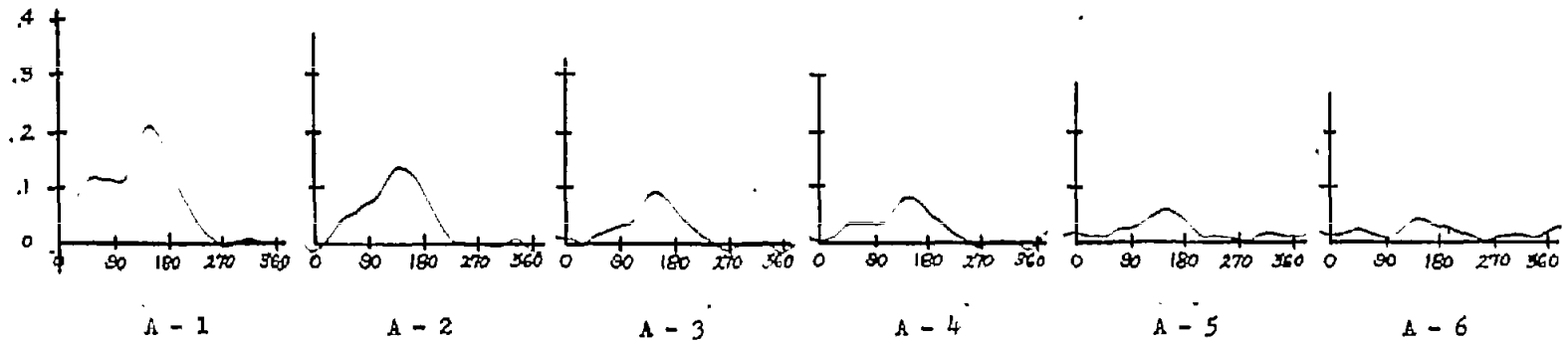
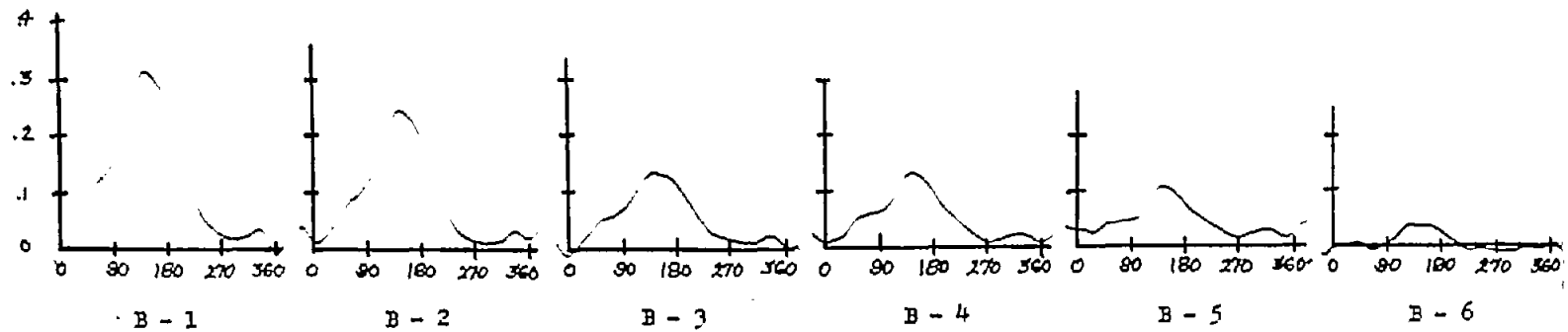


Figure 38.- Curves of constant inflow ratio. Profile, NACA 0015; $\mu = 0.30$; $\xi = 0.13$; $A_0 = 8^\circ$; $\alpha = -5^\circ$; $C_T/\sigma = 0.070$; $\mu \sin \alpha = -0.026$; $\Omega R = 209$ feet per second.



(a) Span station A; $r/R = 0.325$.



(b) Span station B; $r/R = 0.460$.

Figure 39.- Pressure difference in pounds per square inch against azimuth in degrees. Profile, NACA 0015; speed, 800 rpm; $\xi = 0.13$; $\mu = 0.30$; $A_0 = 8^\circ$; $\alpha = -5^\circ$.

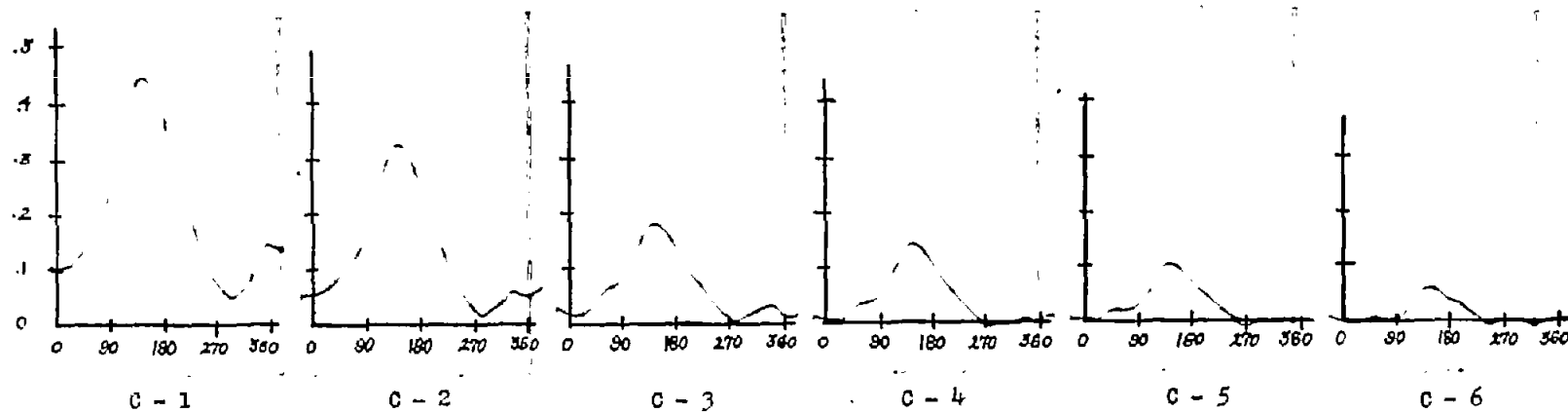
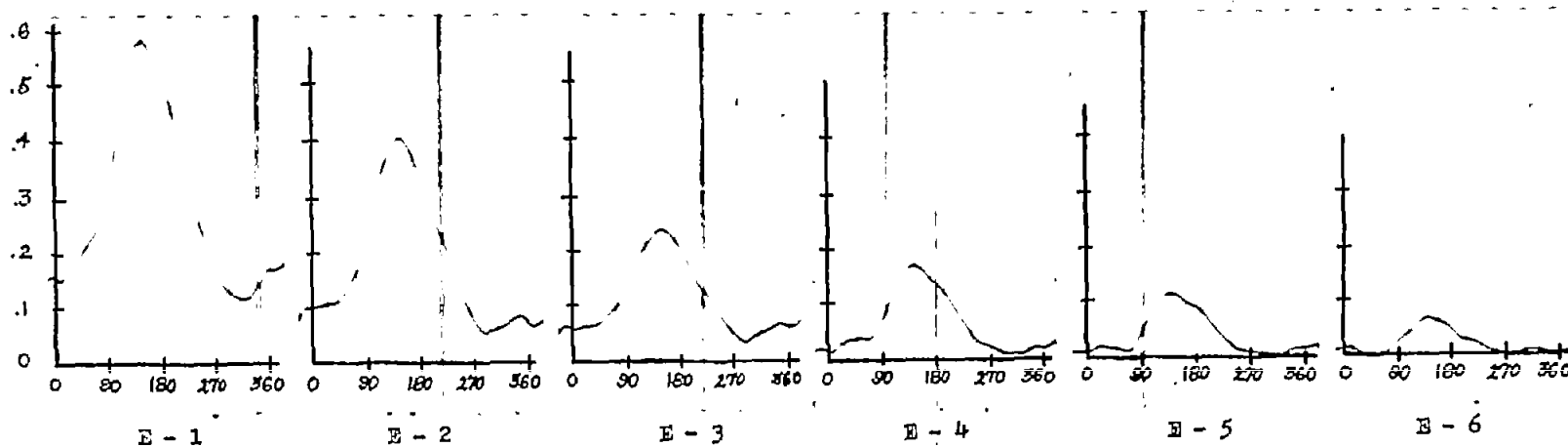
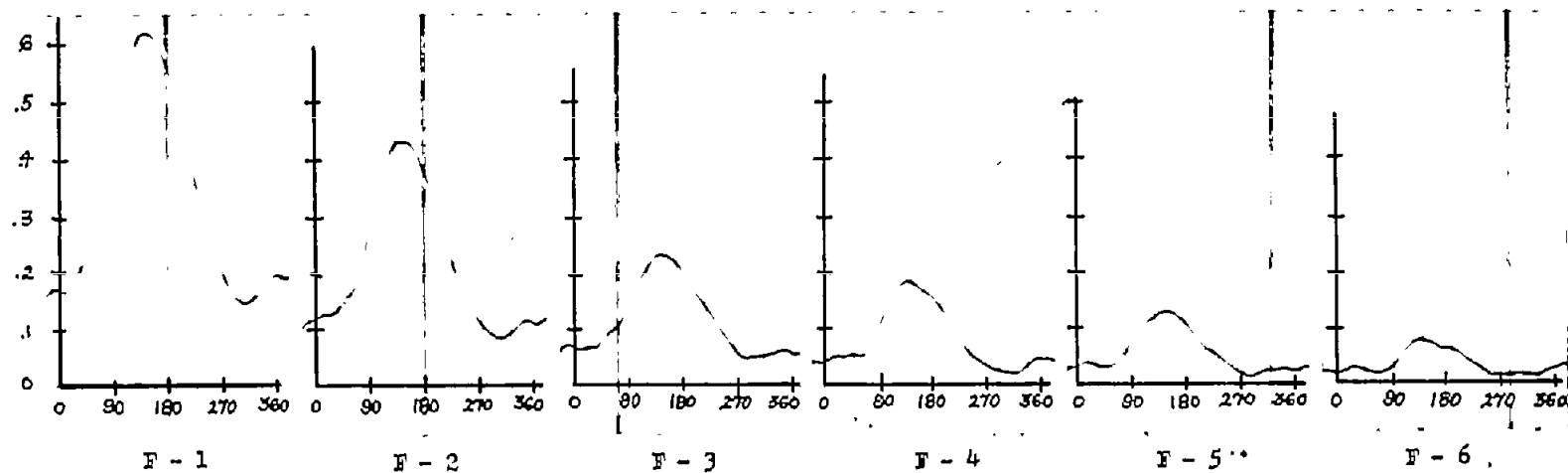
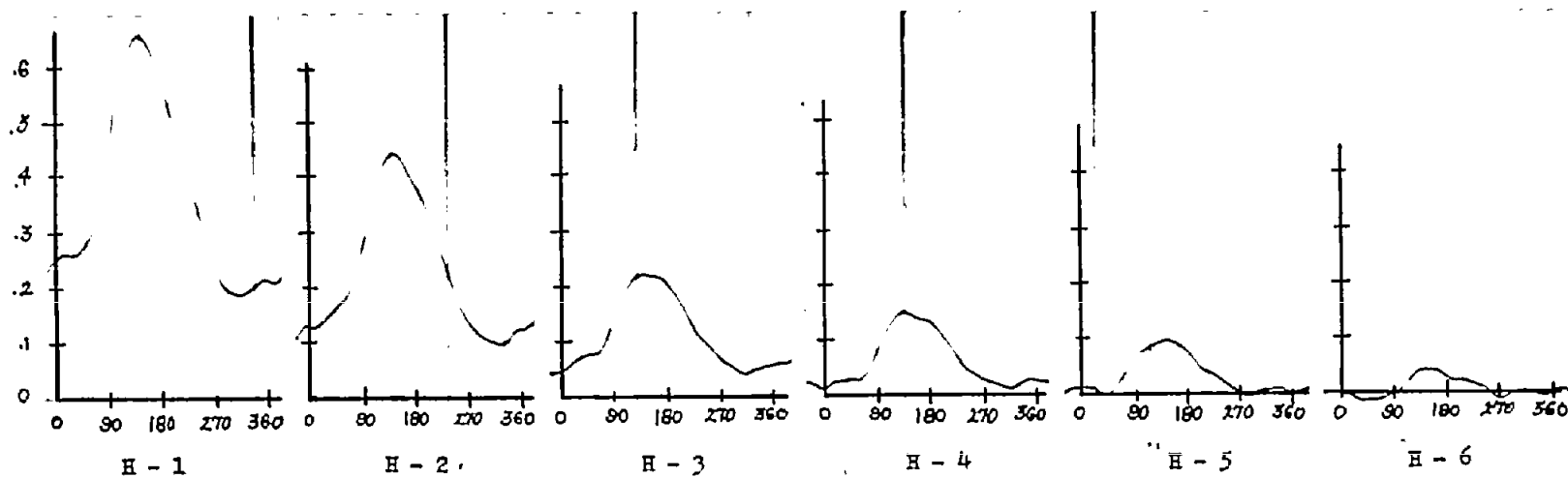
(c) Span station C; $r/R = 0.590$.(d) Span station E; $r/R = 0.725$.

Figure 39.- Continued.

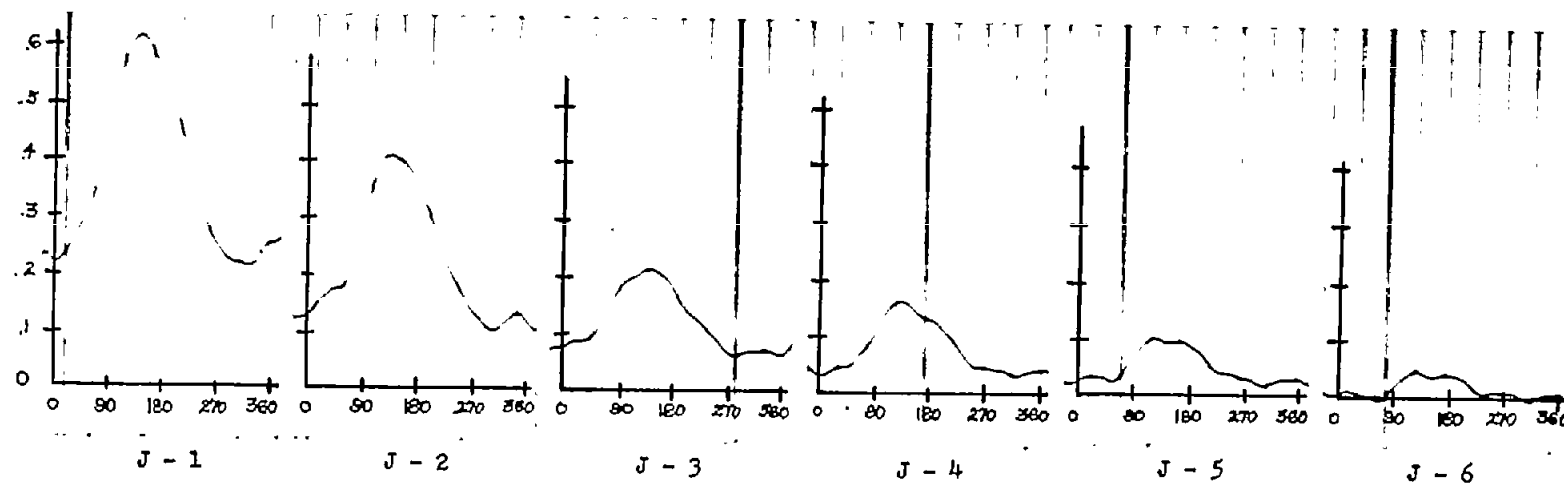


(e) Span station F; $r/R = 0.790$.

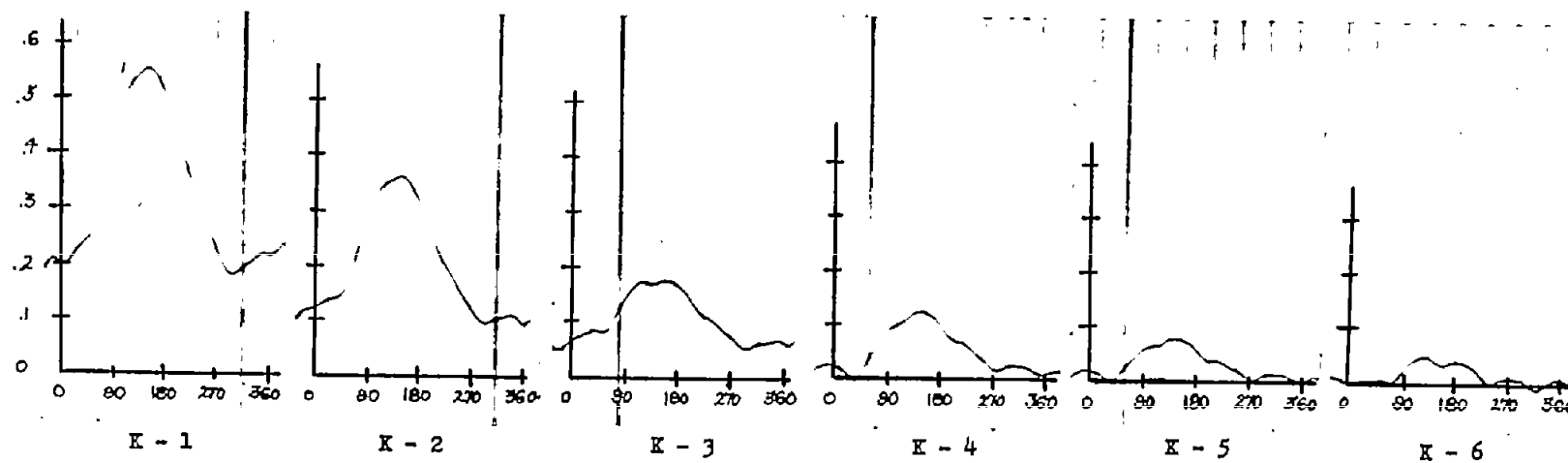


(f) Span station H; $r/R = 0.860$.

Figure 39.- Continued.

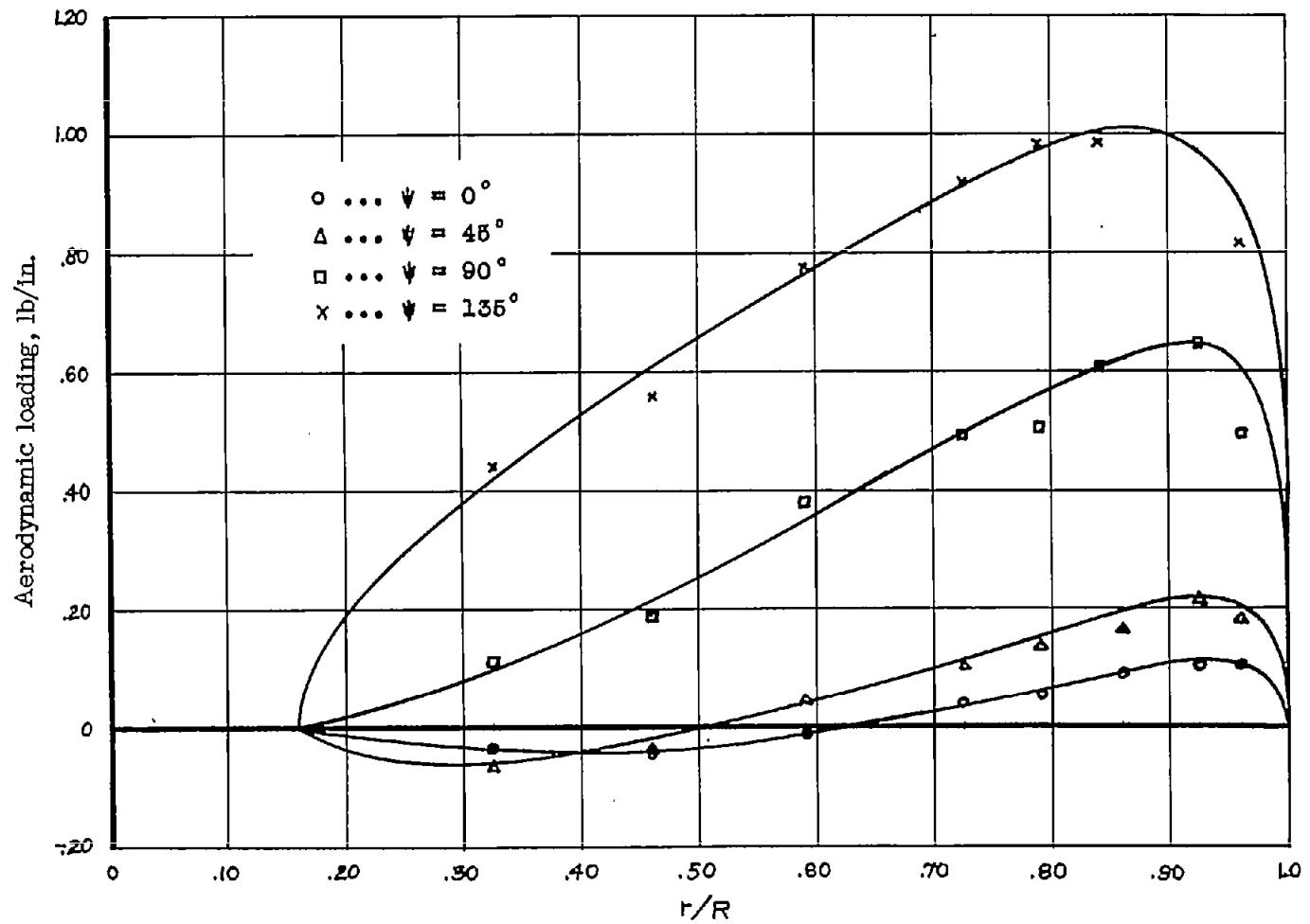


(g) Span station J; $r/R = 0.925$.



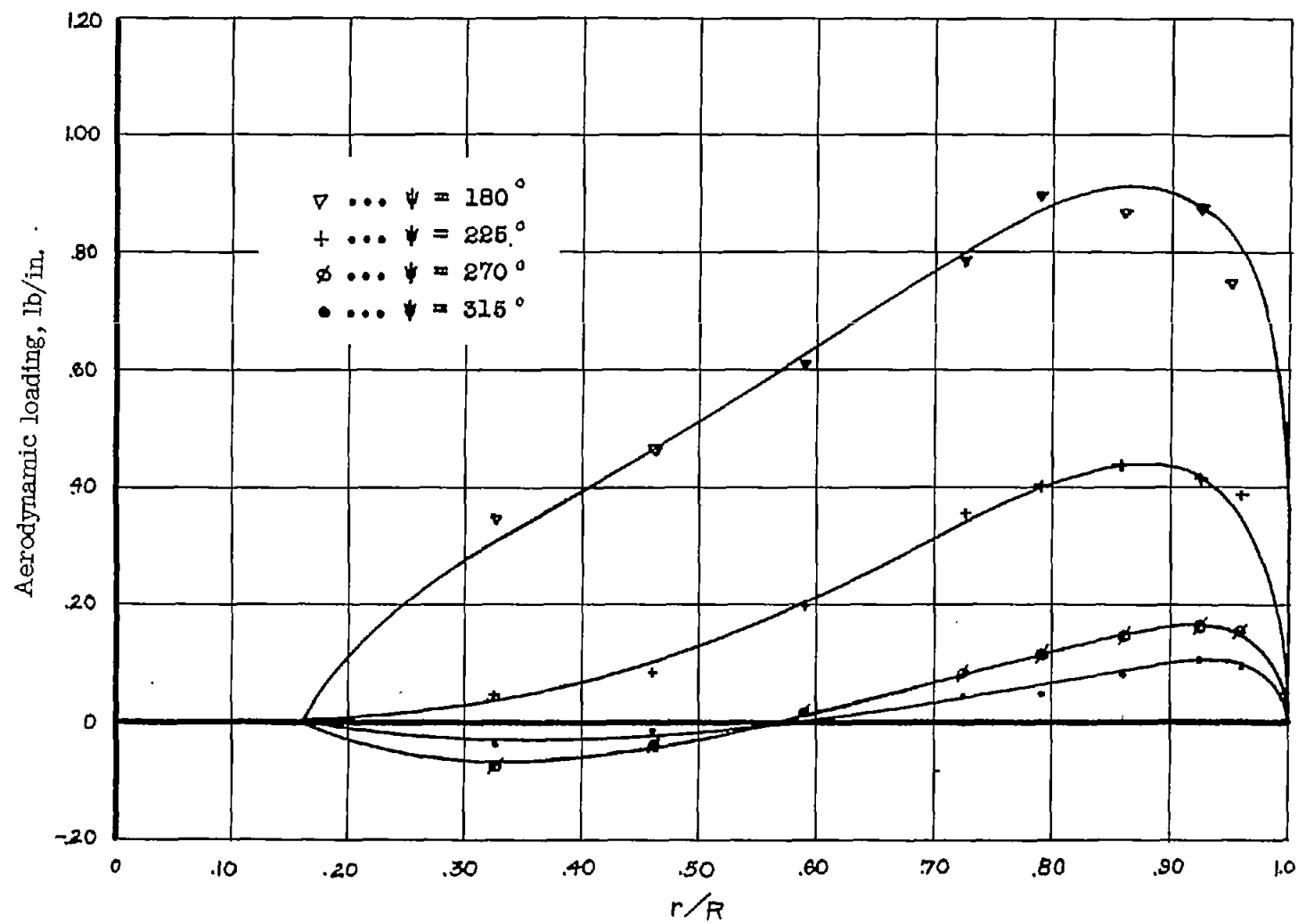
(h) Span station K; $r/R = 0.960$.

Figure 39.- Concluded.



(a) $\psi = 0^\circ$ to 135° .

Figure 40.- Experimental spanwise aerodynamic loading at various azimuths. Profile, NACA 0015;
 $\mu = 0.50$; $\xi = 0.13$; $A_0 = 12^\circ$; $\alpha = -10^\circ$.



(b) $\psi = 180^\circ$ to 315° .

Figure 40.- Concluded.

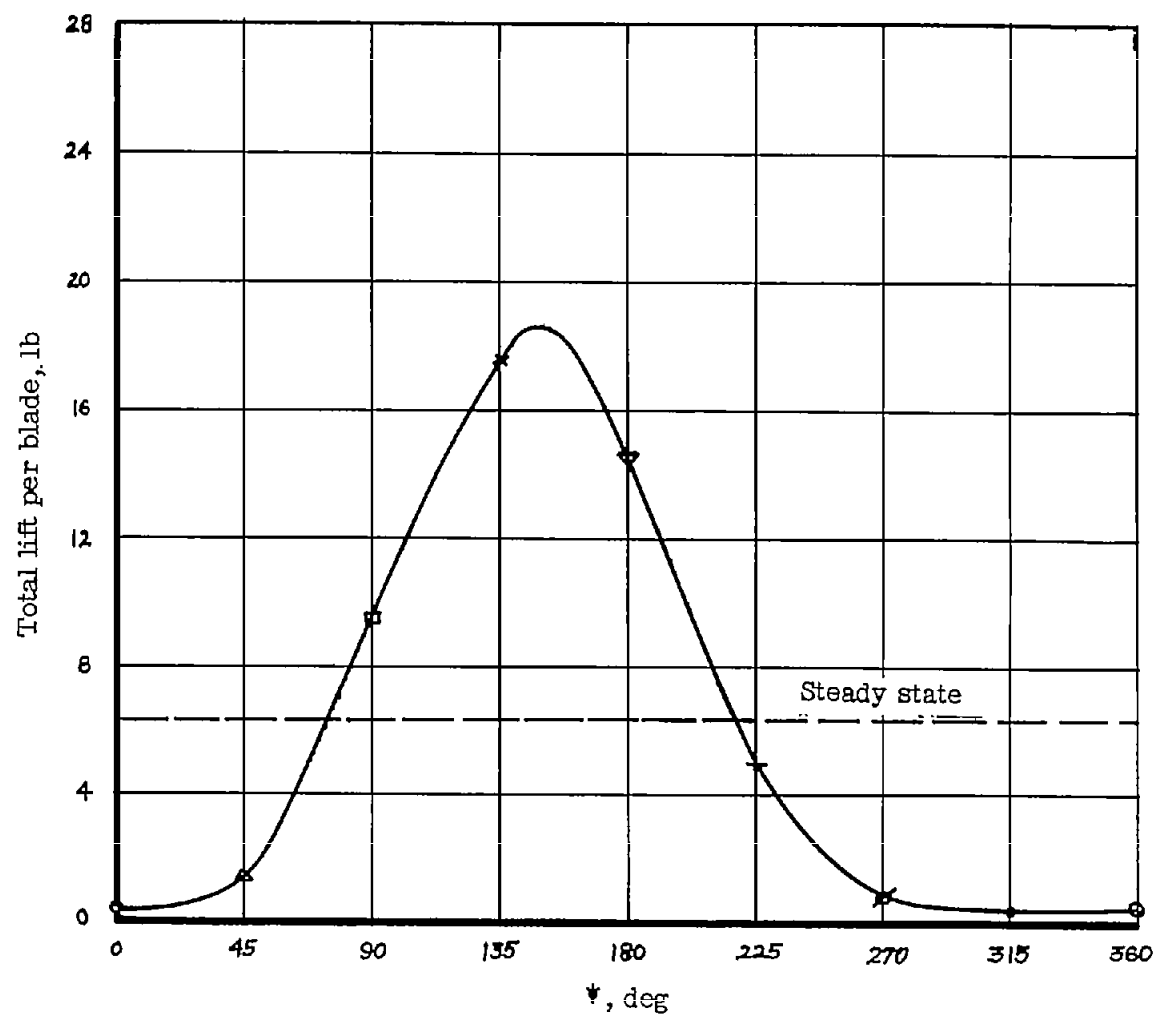


Figure 41.- Variation in total lift per blade. Profile, NACA 0015; $\mu = 0.50$; $\xi = 0.13$; $A_0 = 12^\circ$; $\alpha = -10^\circ$.

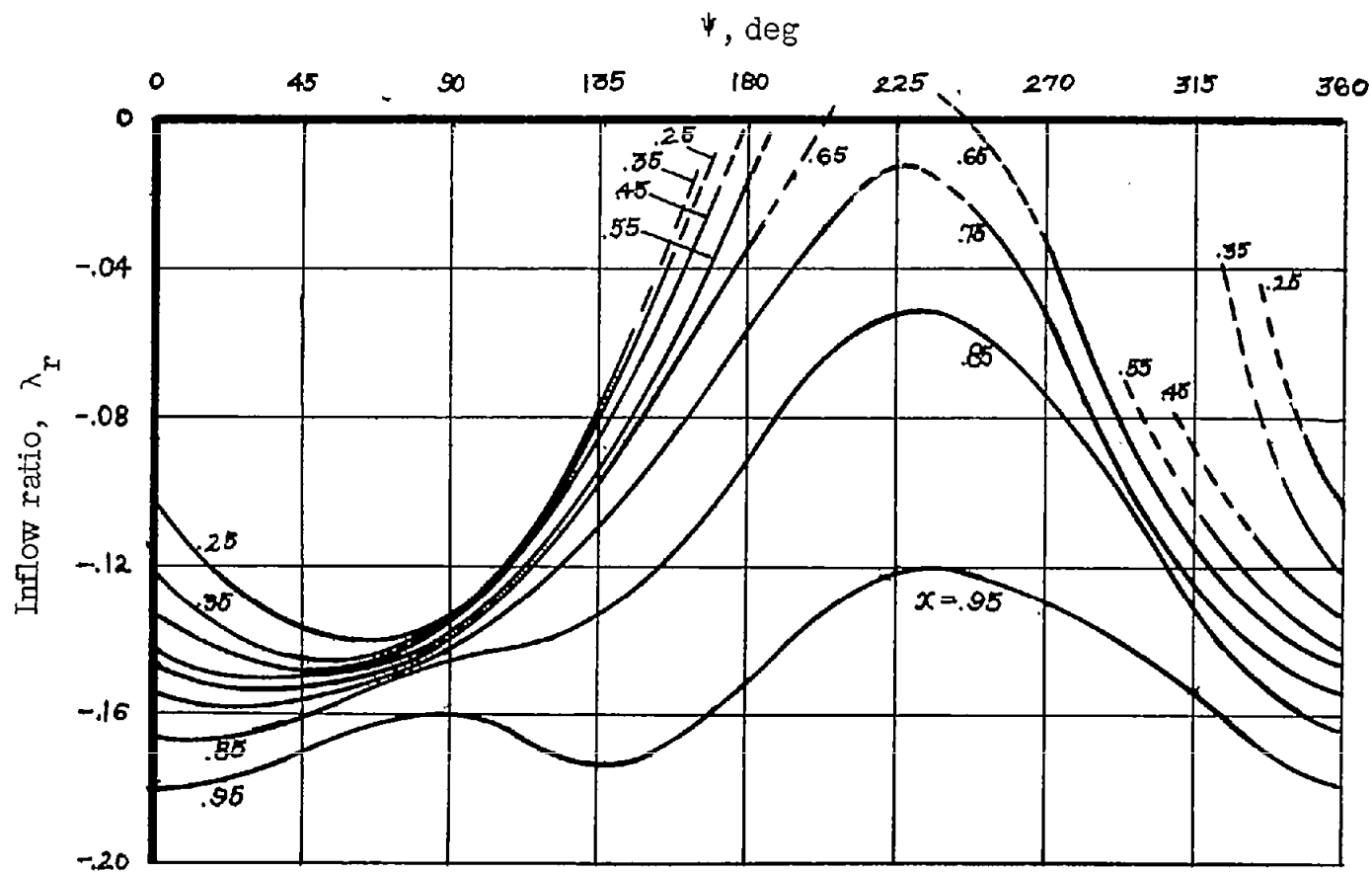
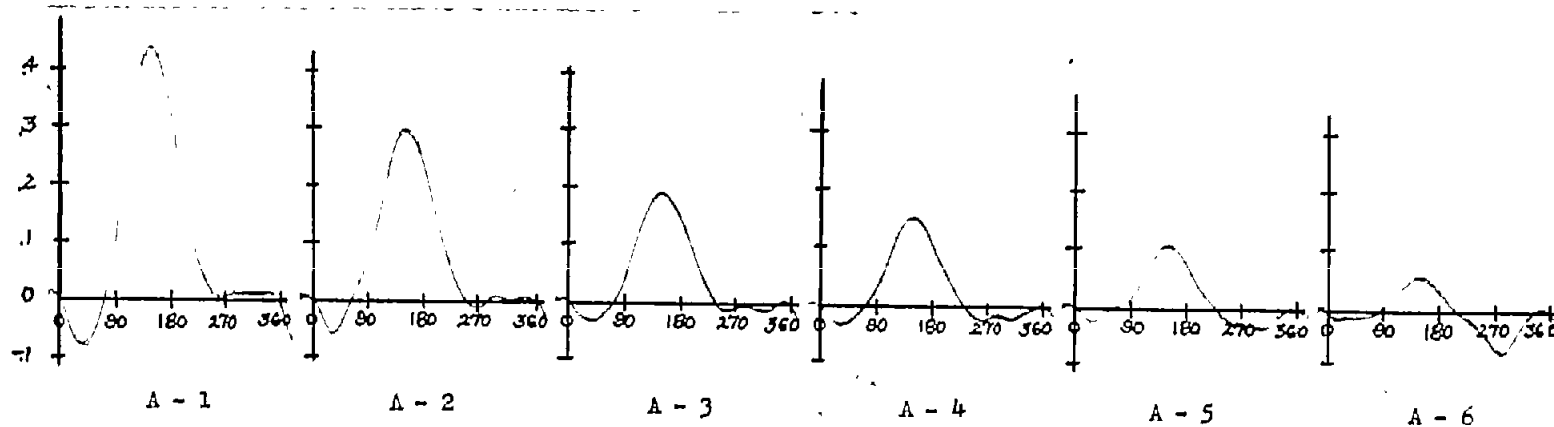
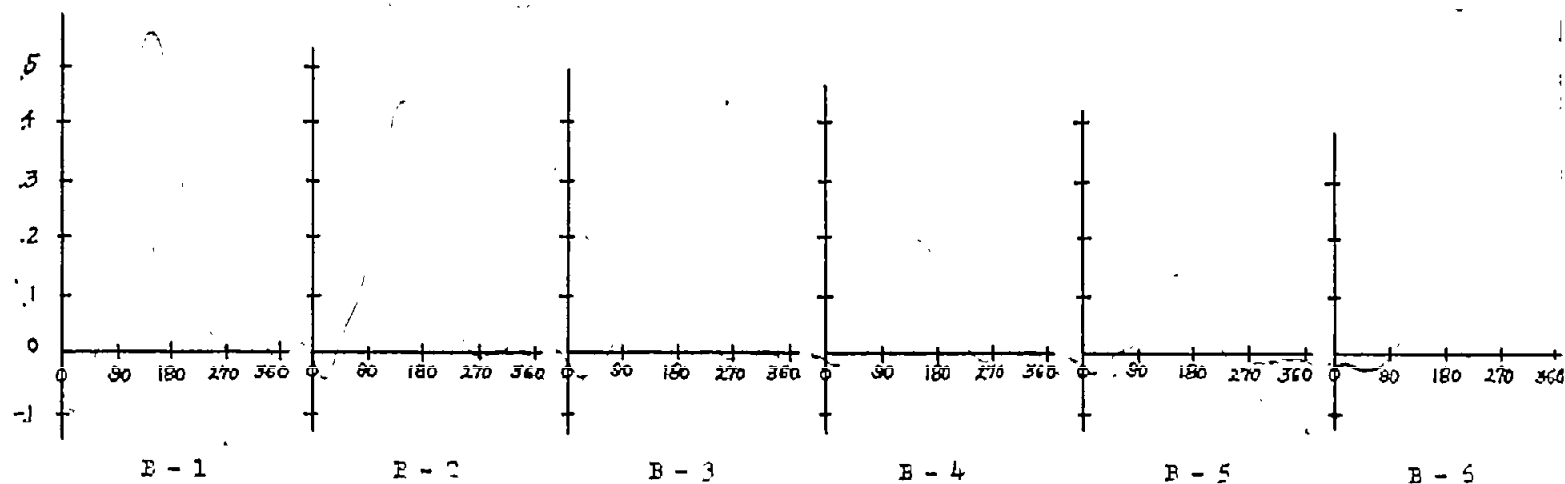


Figure 42.- Inflow distribution from experimental loading and blade-motion data. $\mu = 0.50$; $\xi = 0.13$; $A_0 = 12^\circ$; $\alpha = -10^\circ$; $a = 5.7$; $\mu \sin \alpha = -0.087$. Dashed lines indicate blade stall.

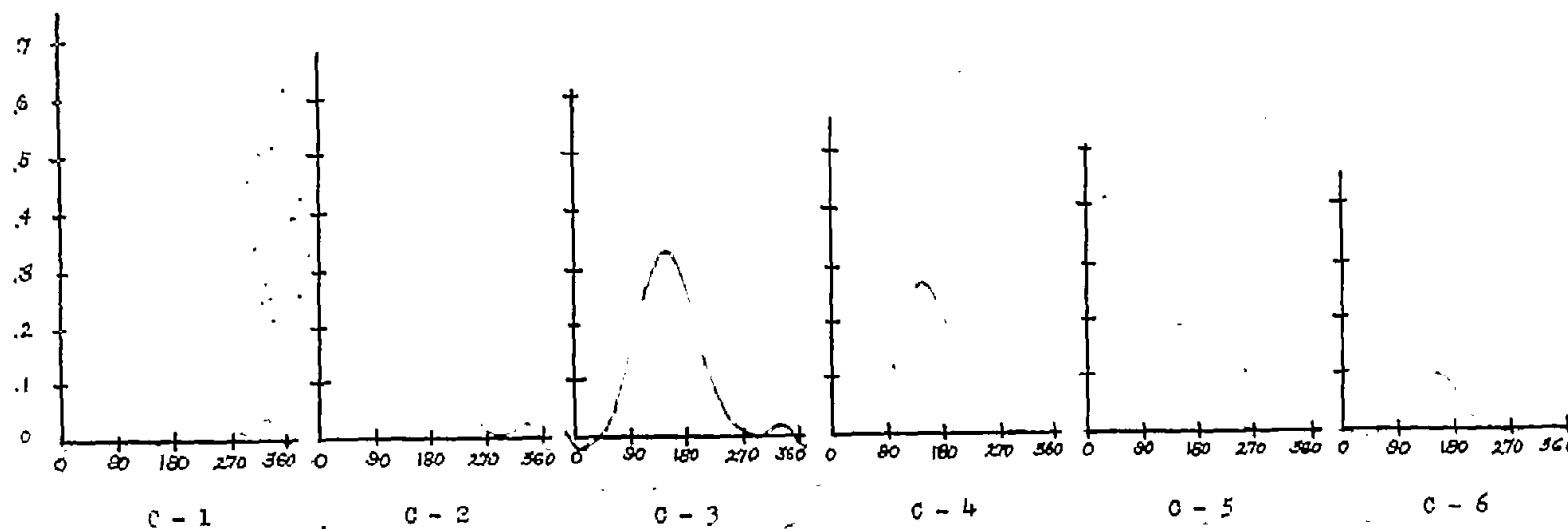


(a) Span station A; $r/R = 0.325$.

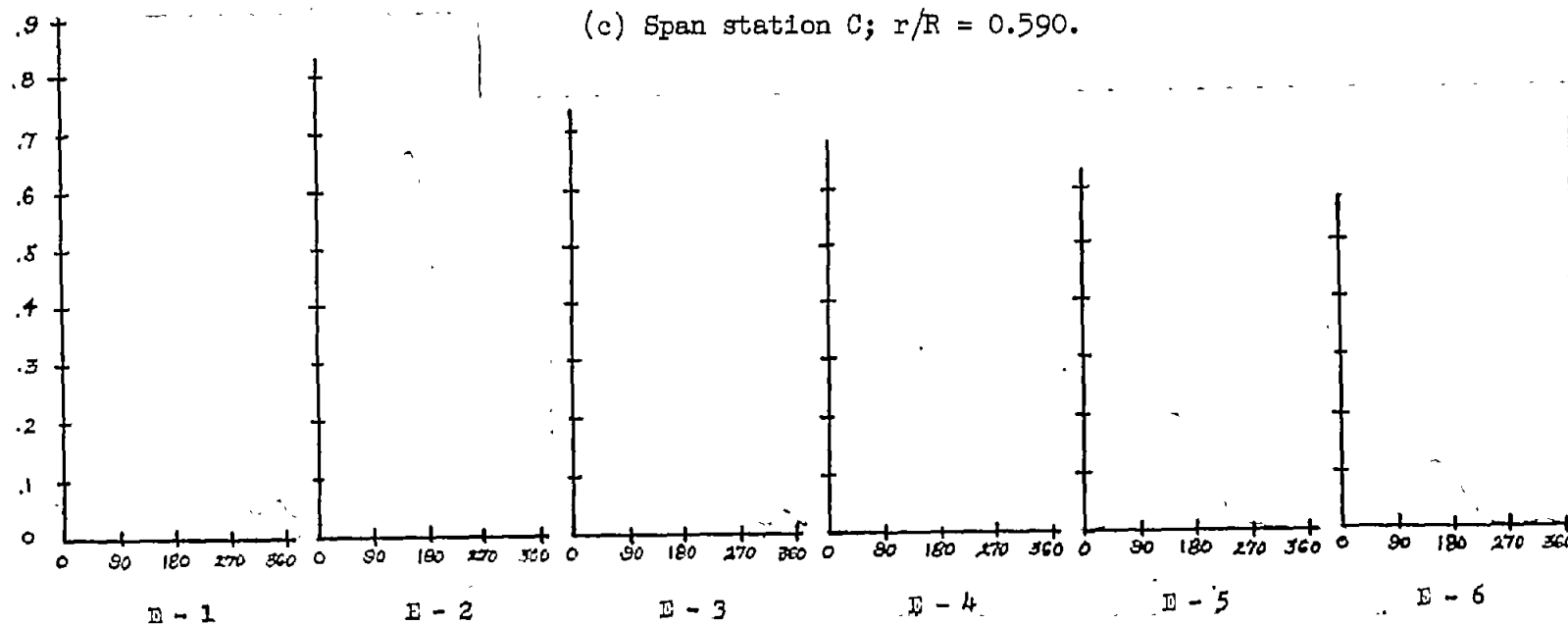


(b) Span station B; $r/R = 0.460$.

Figure 43.- Pressure difference in pounds per square inch against azimuth in degrees. Profile, NACA 0015; speed, 800 rpm; $\xi = 0.13$; $\mu = 0.50$; $A_0 = 12^\circ$; $\alpha = -10^\circ$.

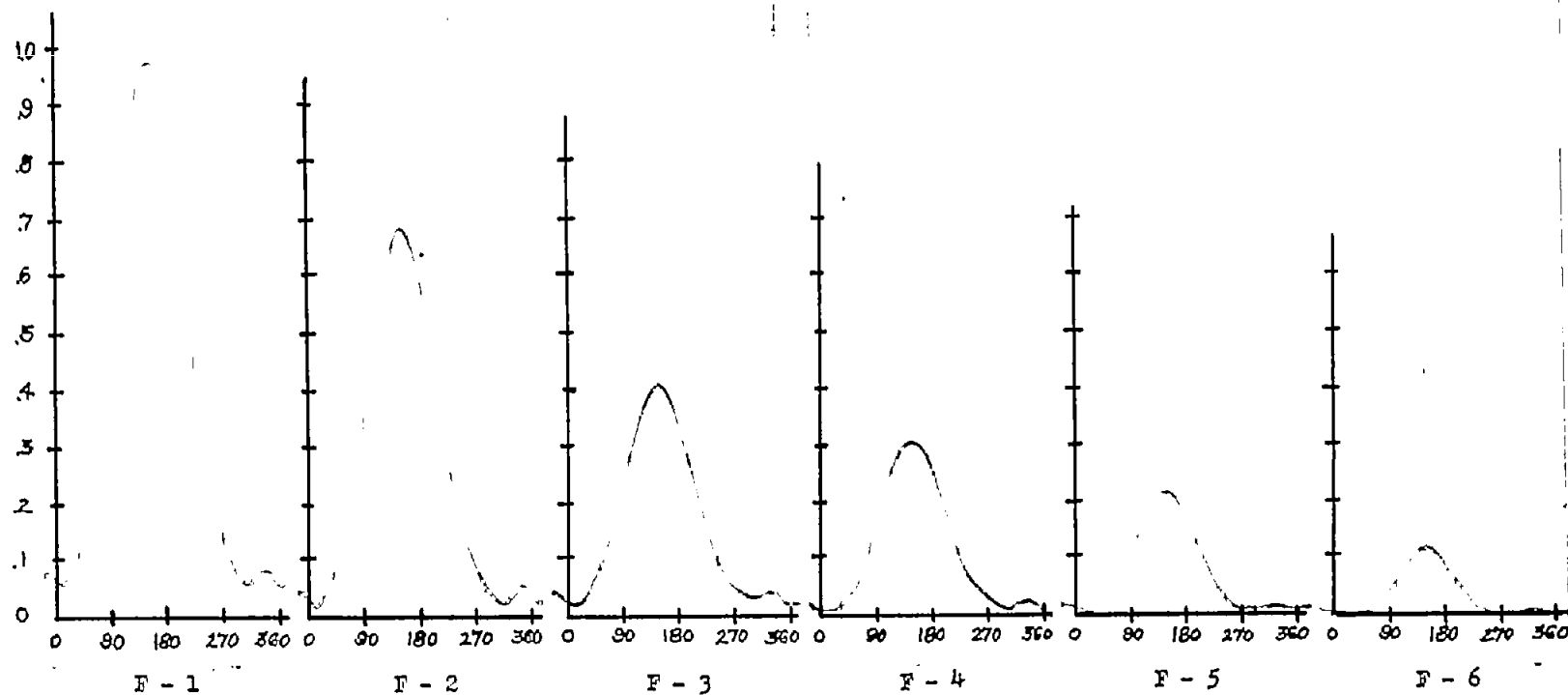


(c) Span station C; $r/R = 0.590$.



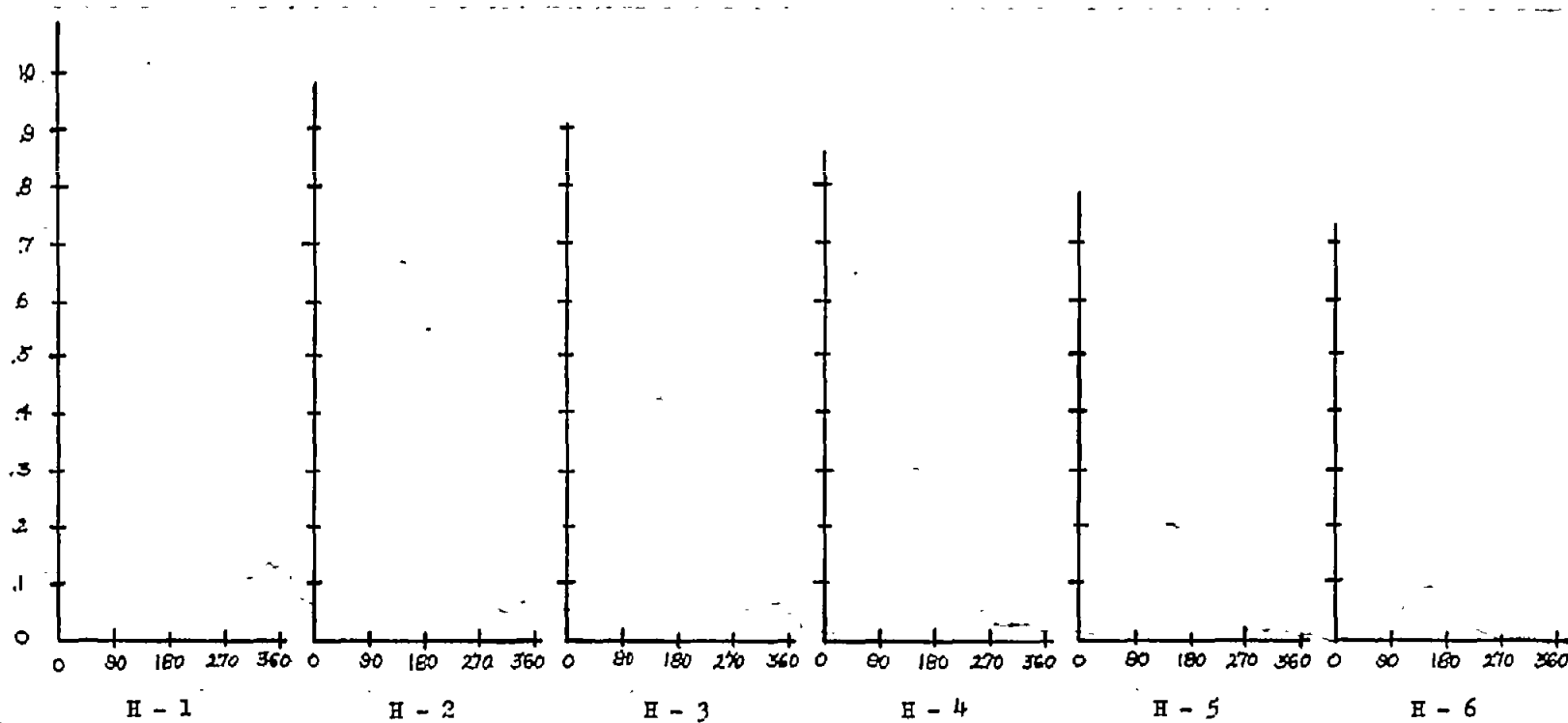
(d) Span station E; $r/R = 0.725$.

Figure 43.- Continued.



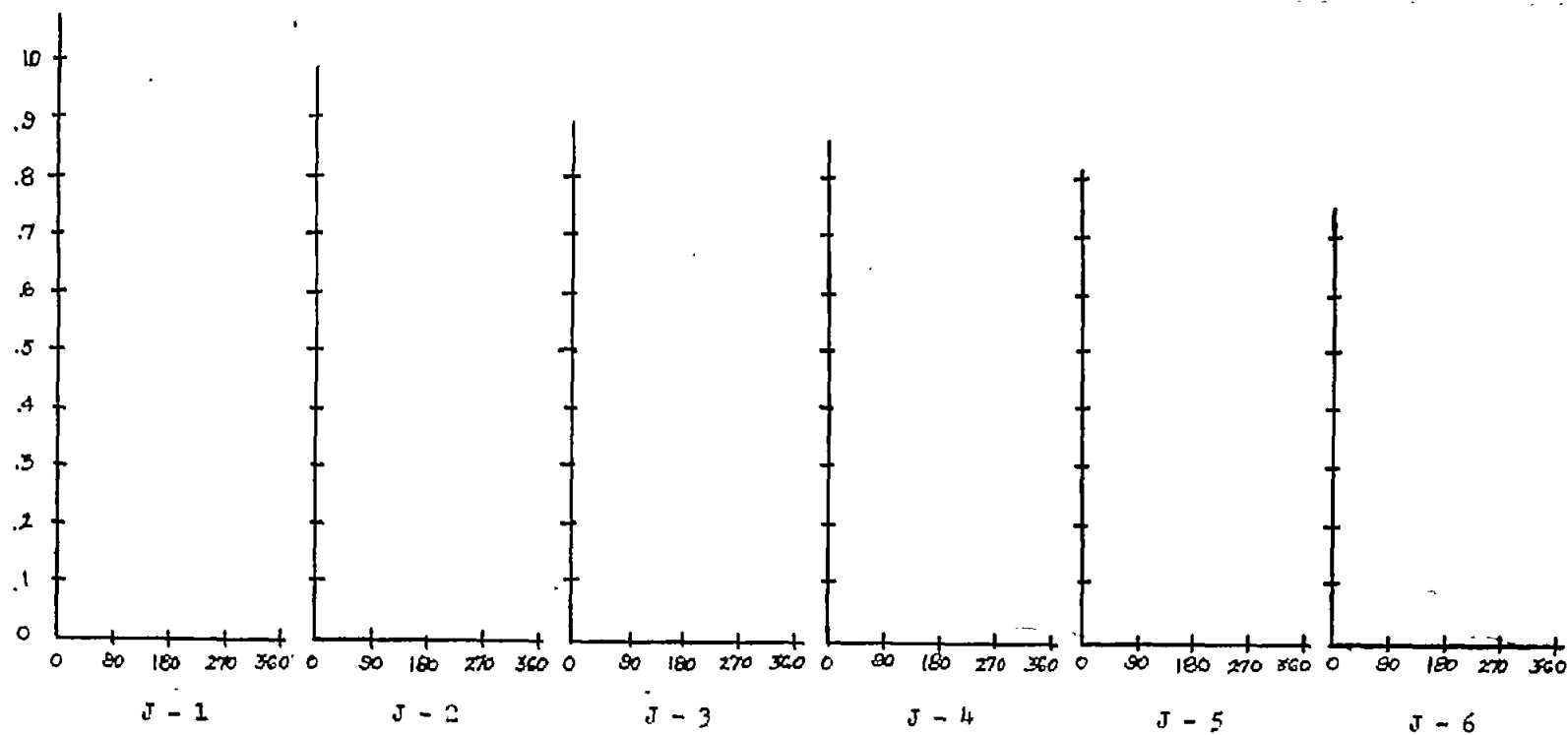
(e) Span station F; $r/R = 0.790$.

Figure 43.- Continued.



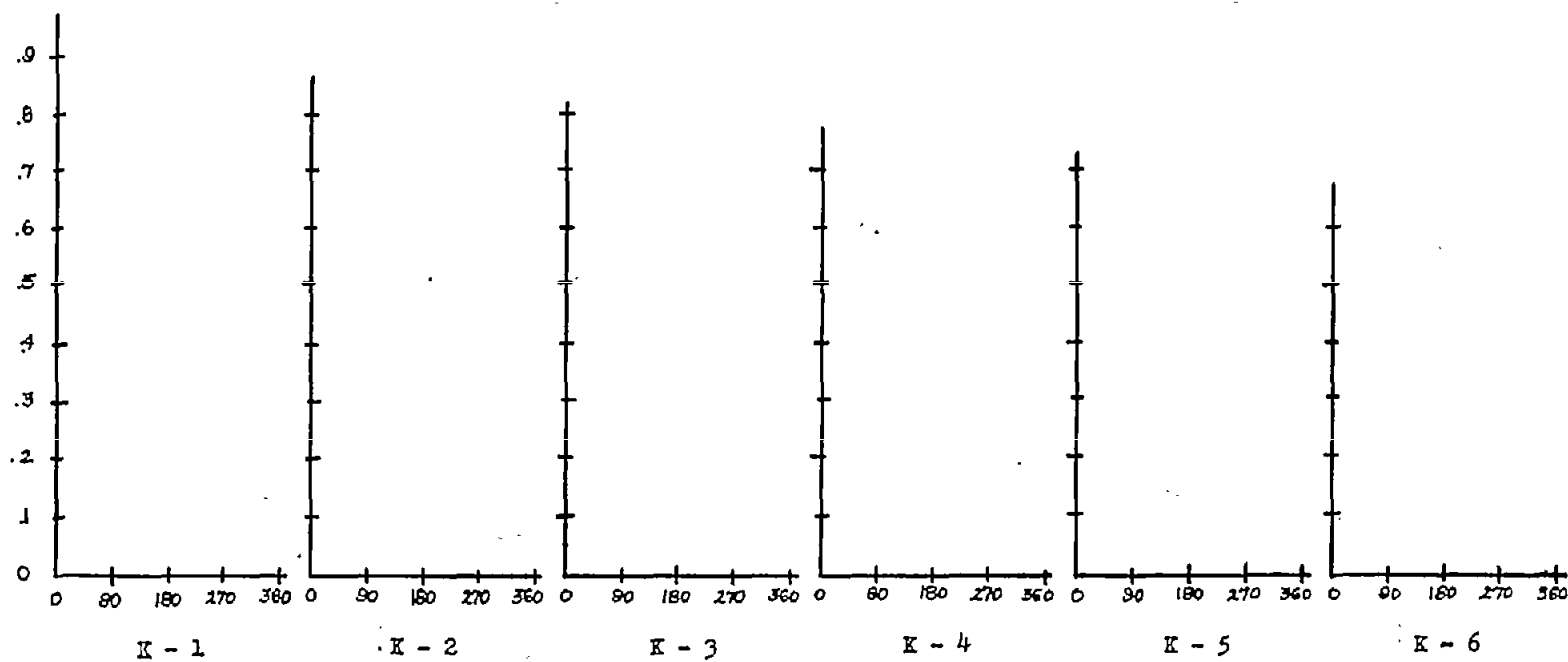
(f) Span station H; $r/R = 0.860$.

Figure 43.- Continued.



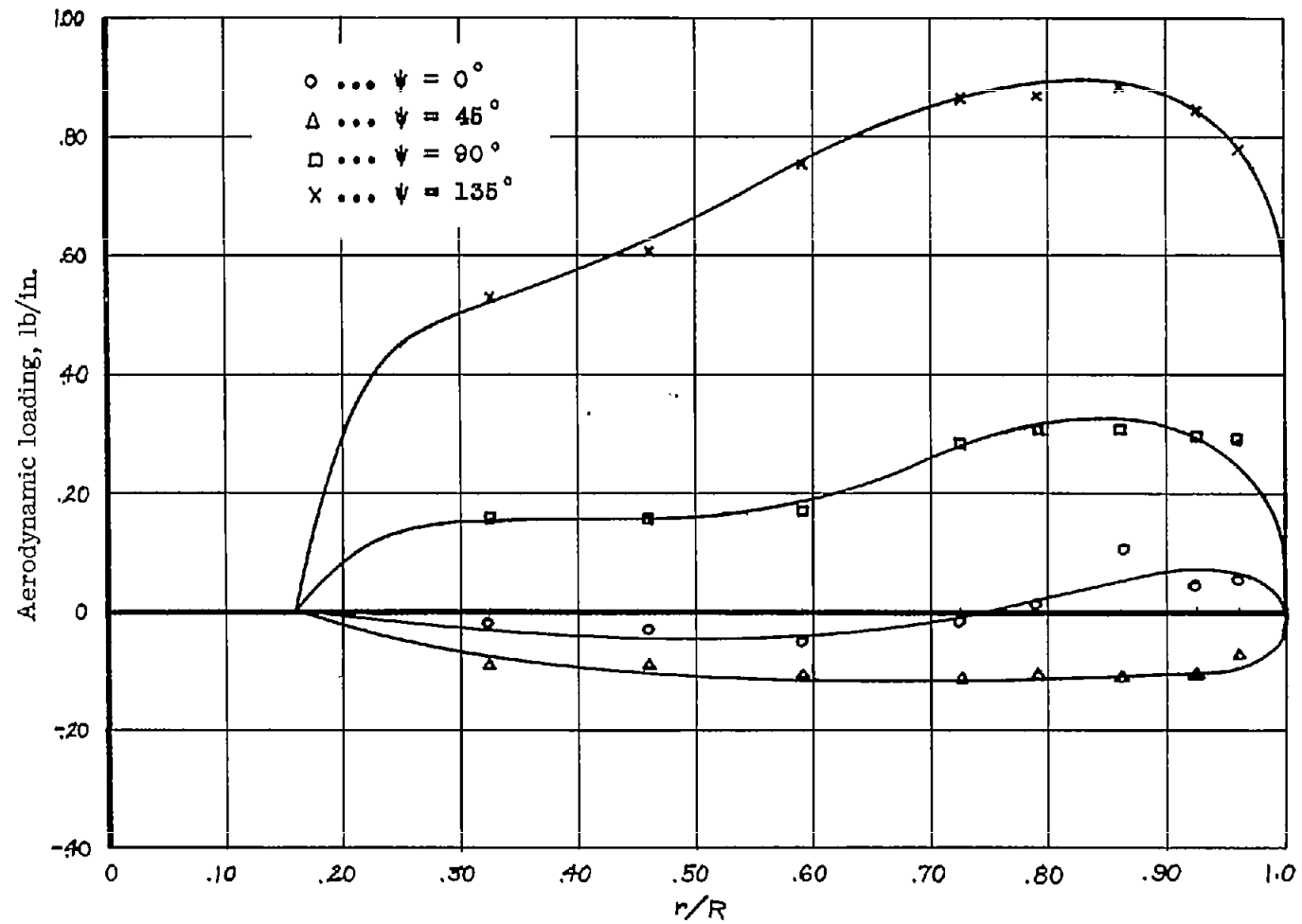
(g) Span station J; $r/R = 0.925$.

Figure 43.- Continued.



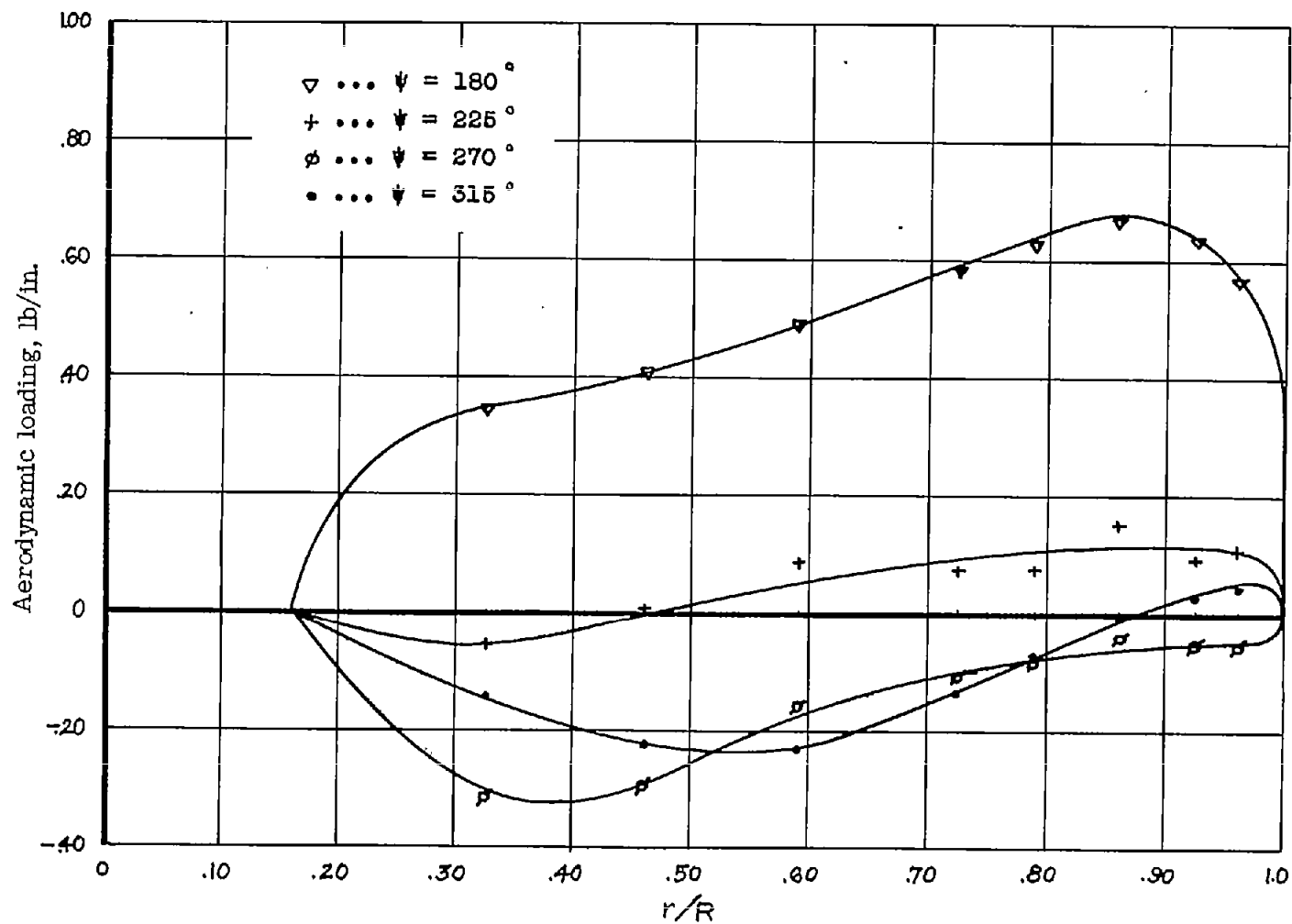
(h) Span station K; $r/R = 0.960$.

Figure 43.- Concluded.



(a) $\psi = 0^\circ$ to 135° .

Figure 44.- Experimental spanwise aerodynamic loading at various azimuths. Profile, NACA 0015;
 $\mu = 1.0$; $\xi = 0.13$; $A_0 = 17^\circ$; $\alpha = -15^\circ$.



(b) $\psi = 180^\circ$ to 315° .

Figure 44.- Concluded.

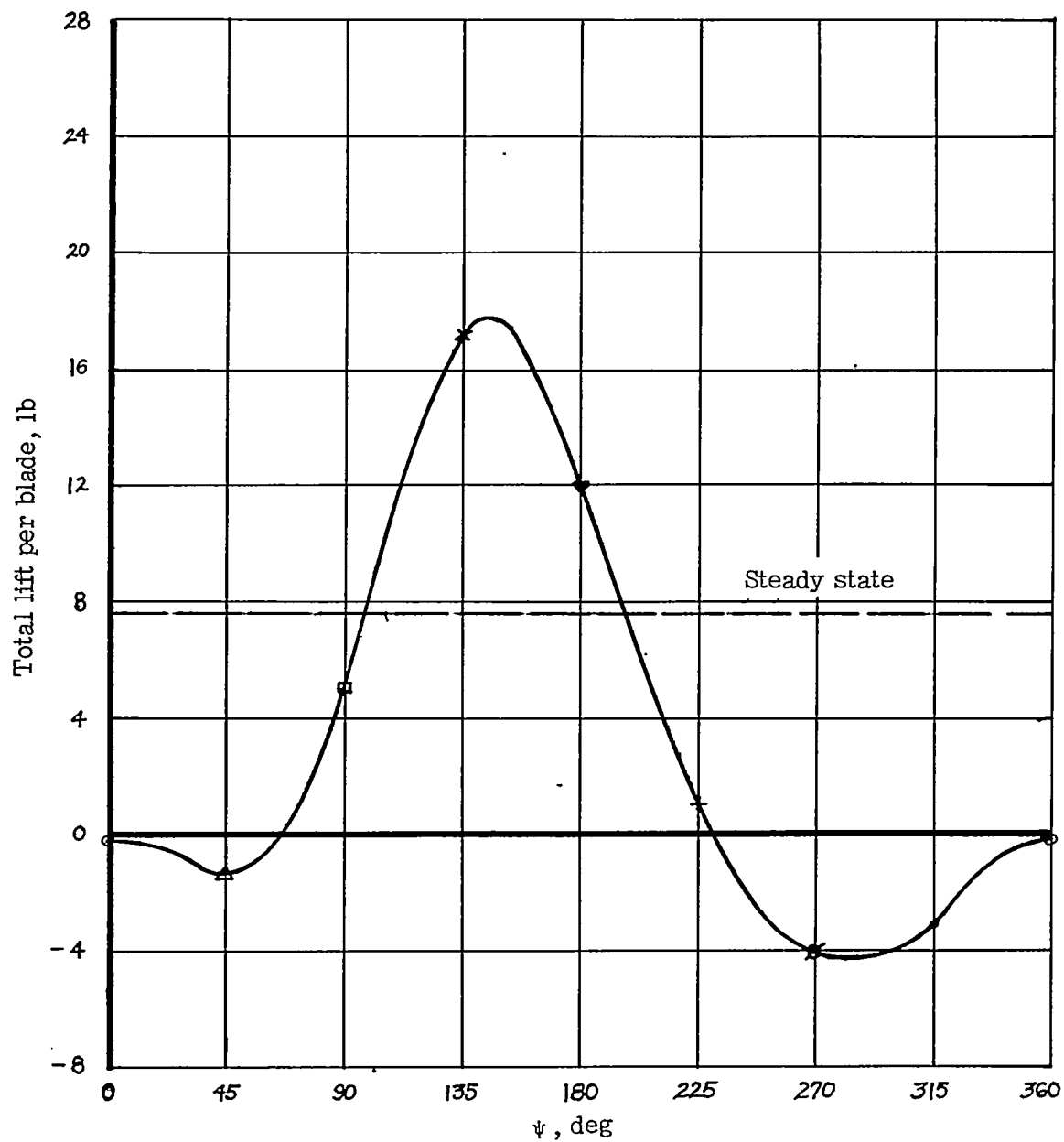


Figure 45.- Variation in total lift per blade. Profile, NACA 0015; $\mu = 1.0$; $\xi = 0.13$; $A_0 = 17^\circ$; $\alpha = -15^\circ$.

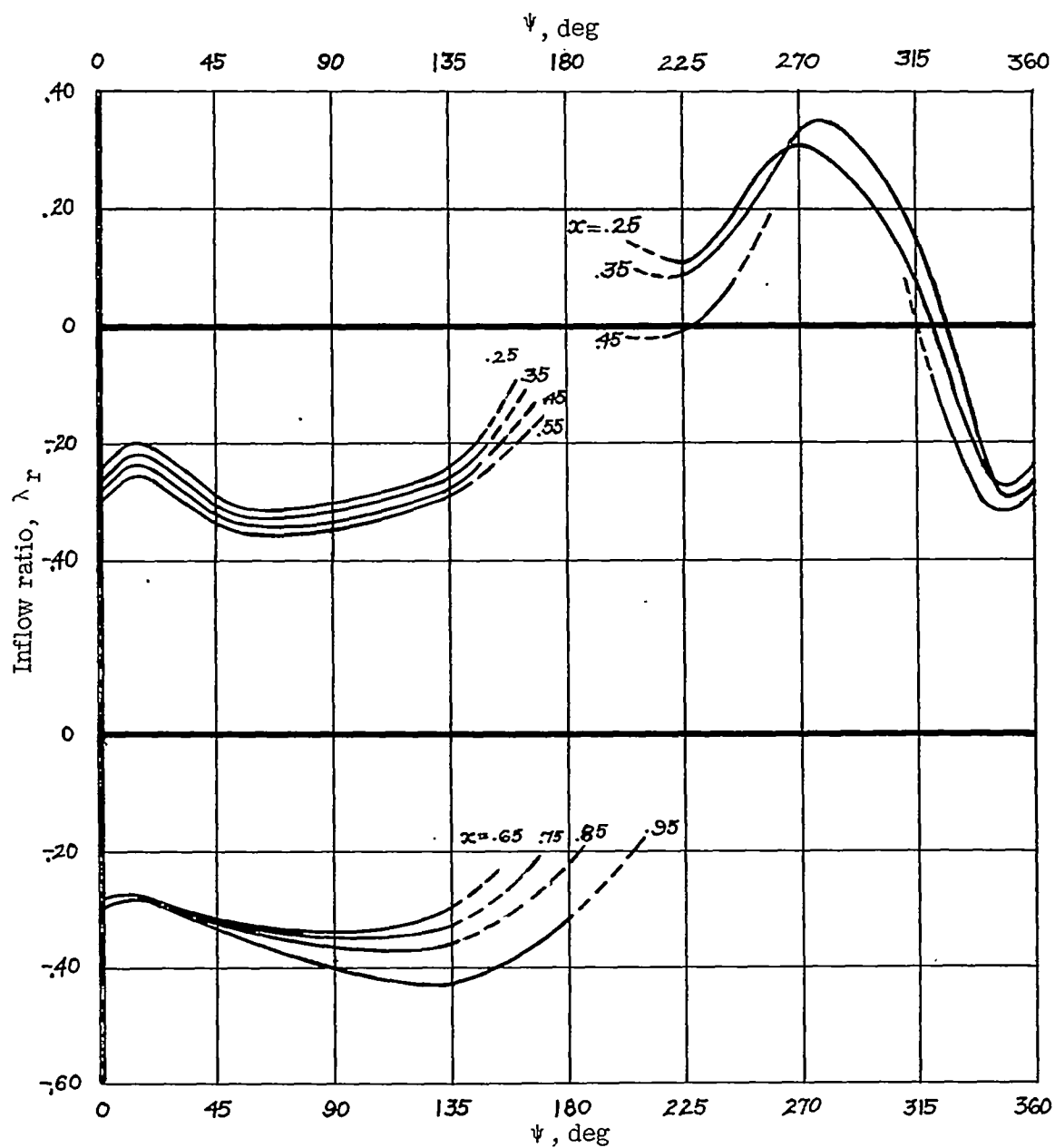
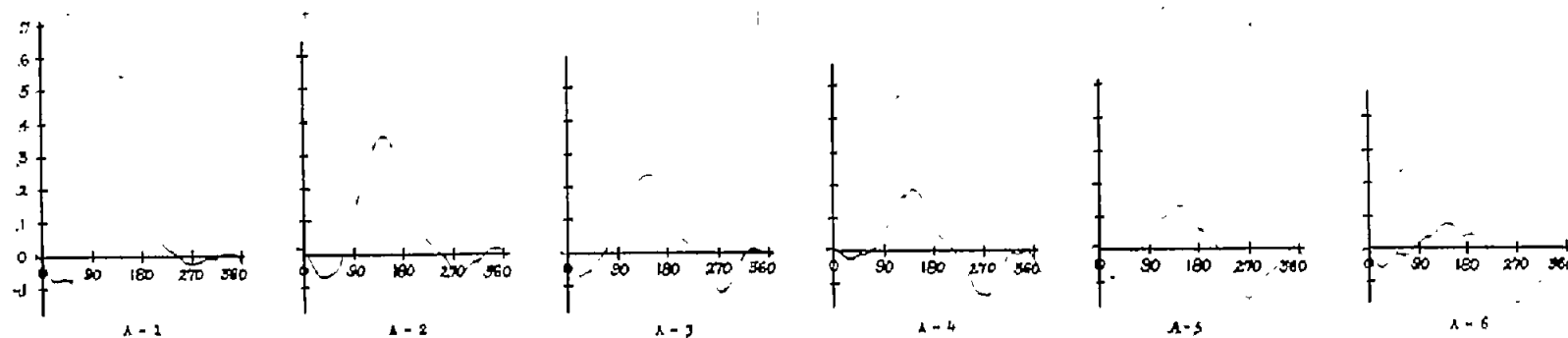
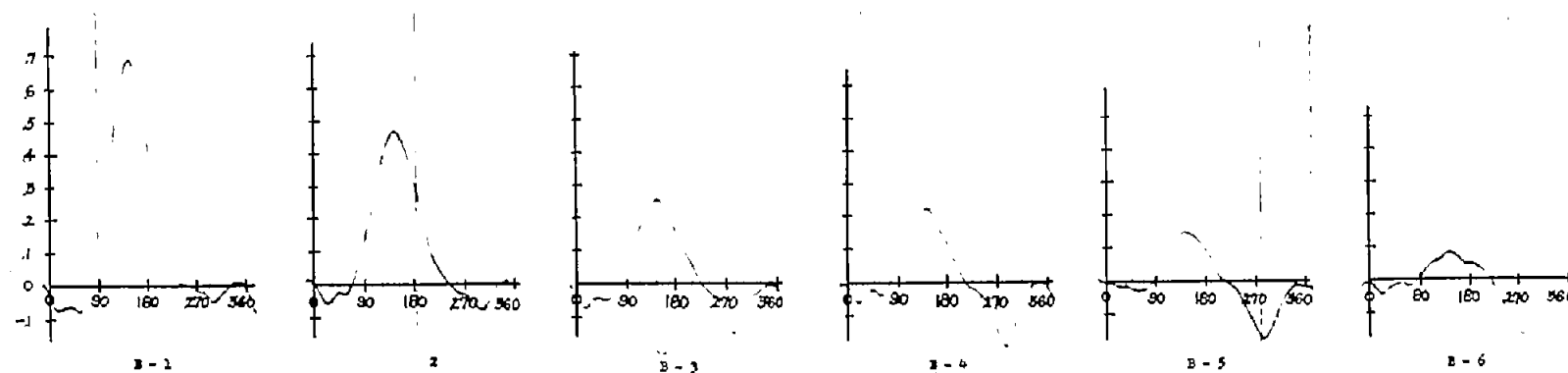


Figure 46.- Inflow distribution from experimental loading and blade-motion data. $\mu = 1.0$; $\xi = 0.13$; $A_0 = 17^\circ$; $\alpha = -15^\circ$; $a = 5.7$; $\mu \sin \alpha = -0.259$.



(a) Span station A; $r/R = 0.325$.



(b) Span station B; $r/R = 0.460$.

Figure 47.- Pressure difference in pounds per square inch against azimuth in degrees. Profile, NACA 0015; speed, 500 rpm; $\xi = 0.13$; $\mu = 1.0$; $A_0 = 17^\circ$; $\alpha = -15^\circ$.

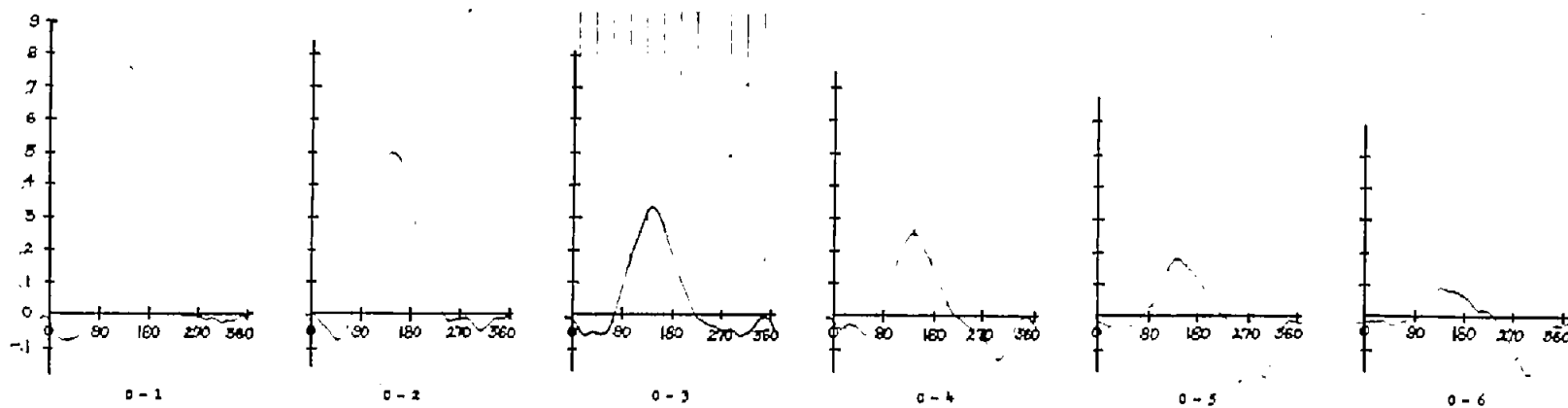
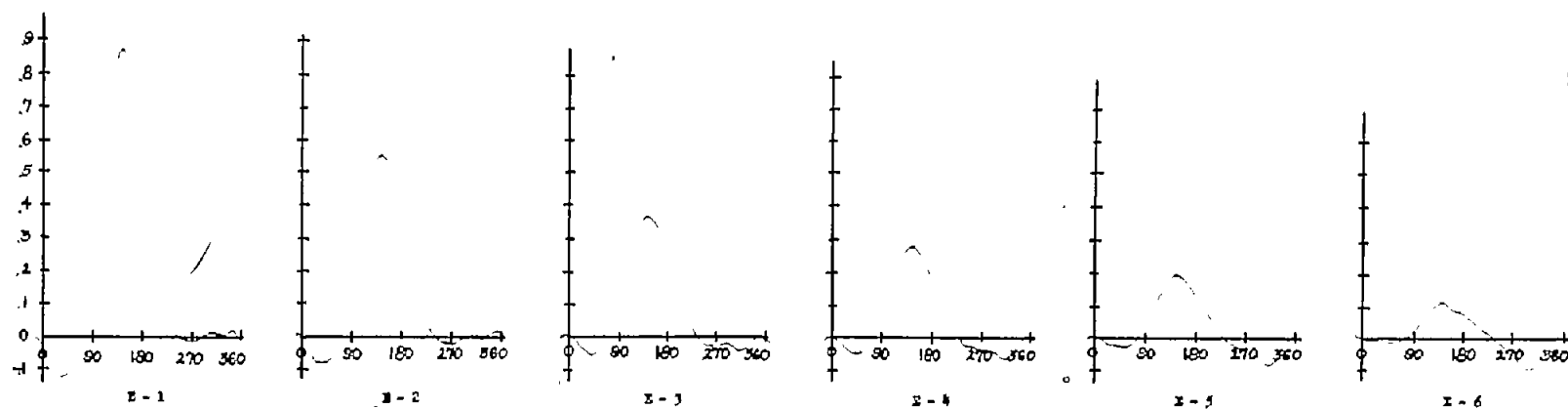
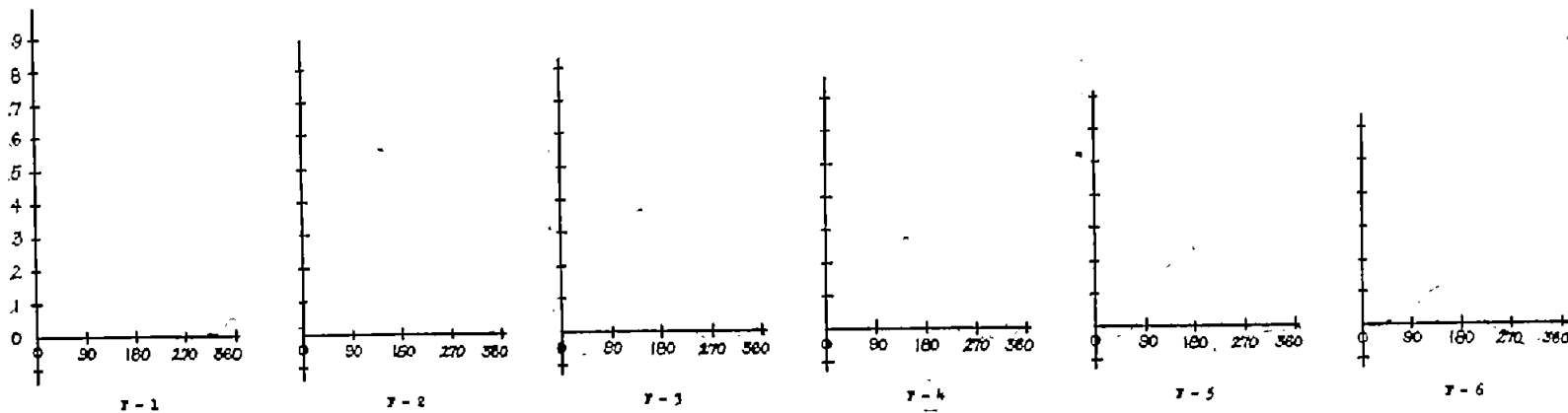
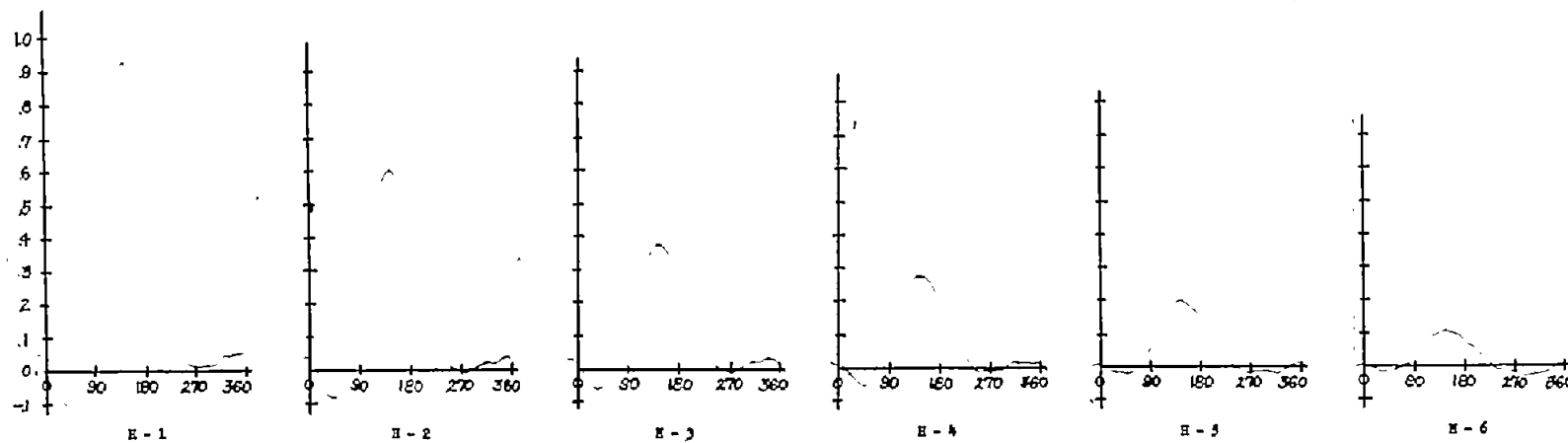
(c) Span station C; $r/R = 0.590$.(d) Span station E; $r/R = 0.725$.

Figure 47.- Continued.

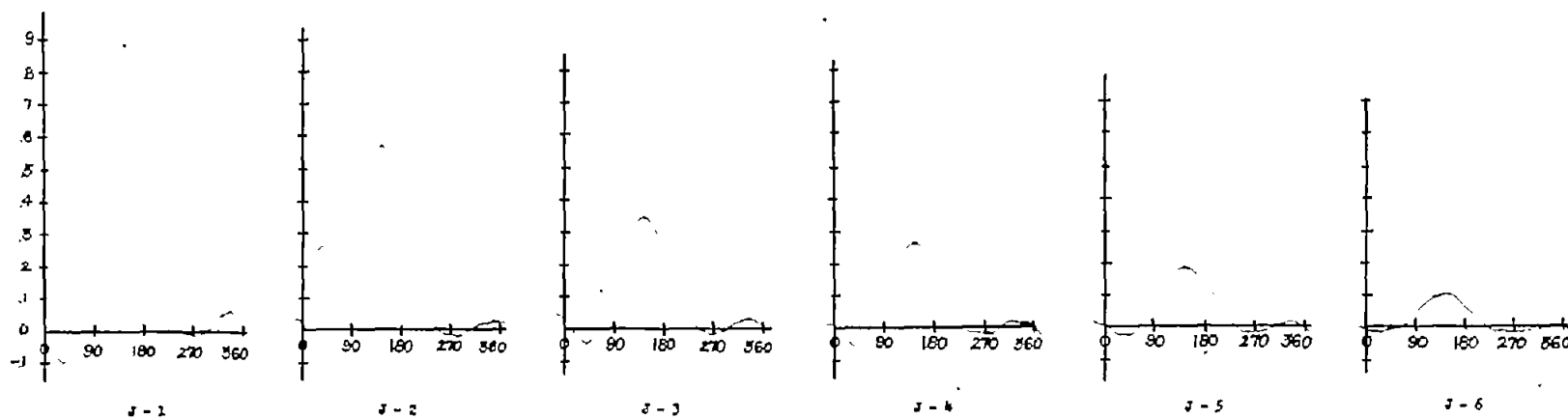


(e) Span station F; $r/R = 0.790$.

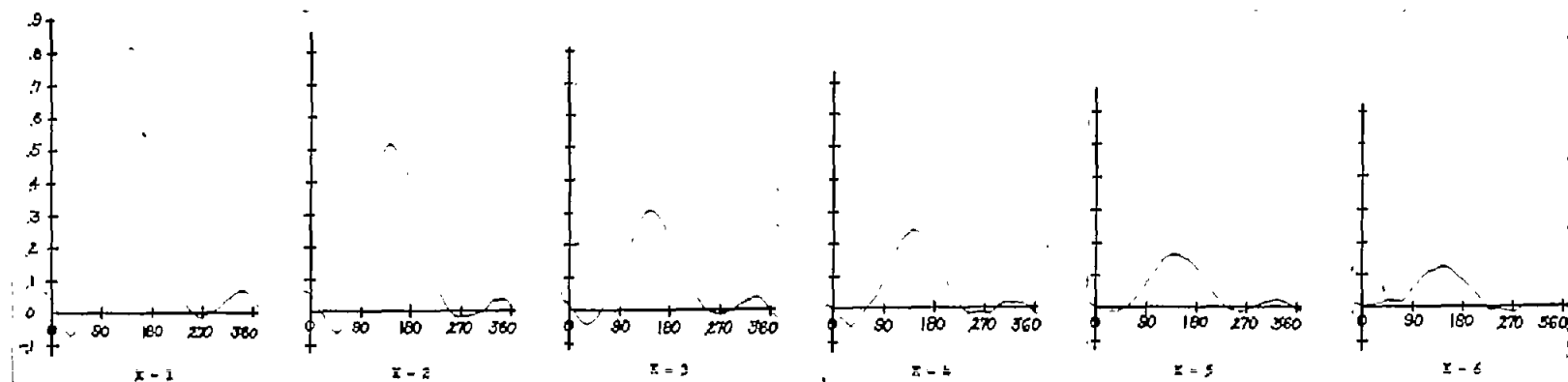


(f) Span station H; $r/R = 0.860$.

Figure 47.- Continued.

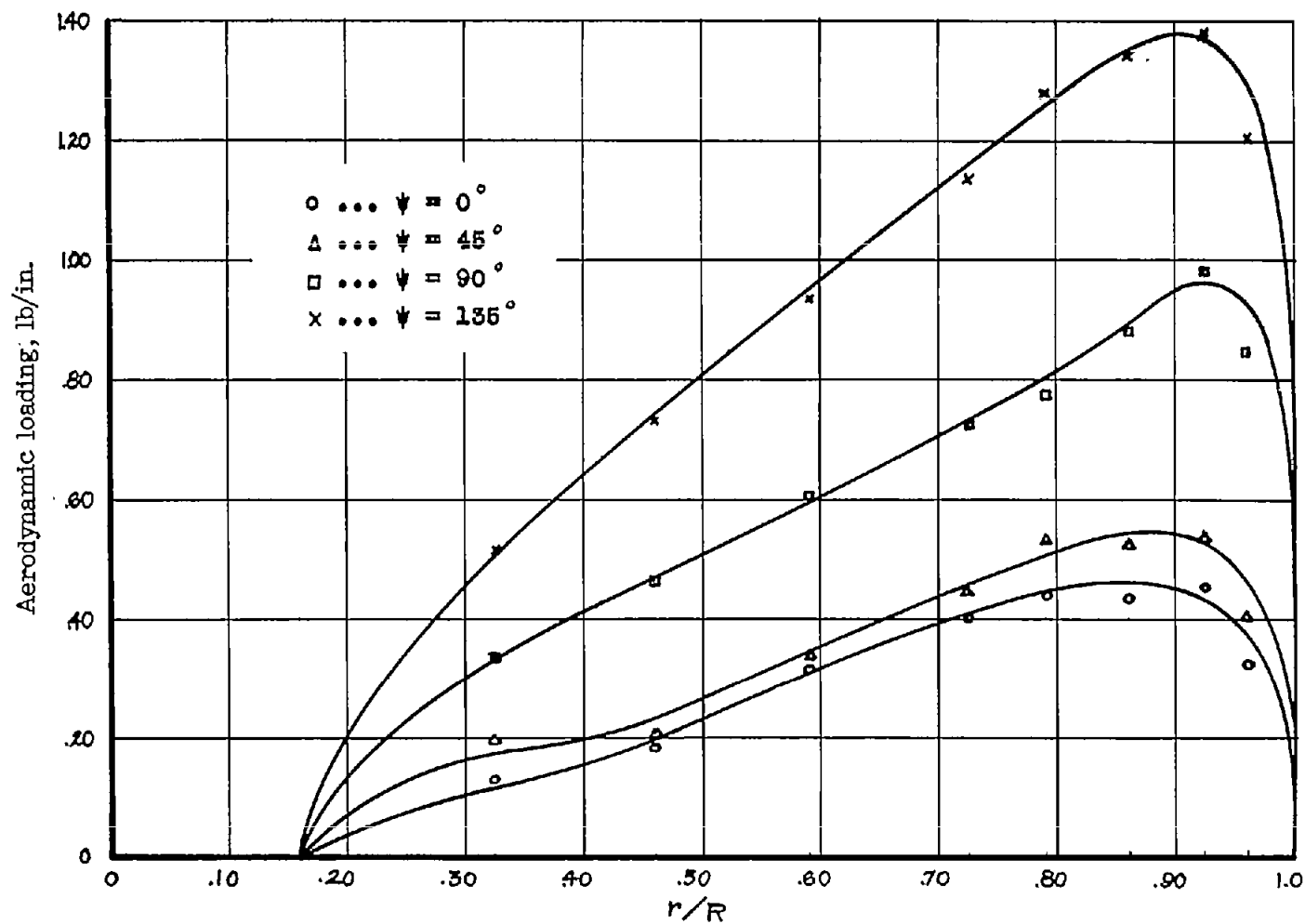


(g) Span station J; $r/R = 0.925$.



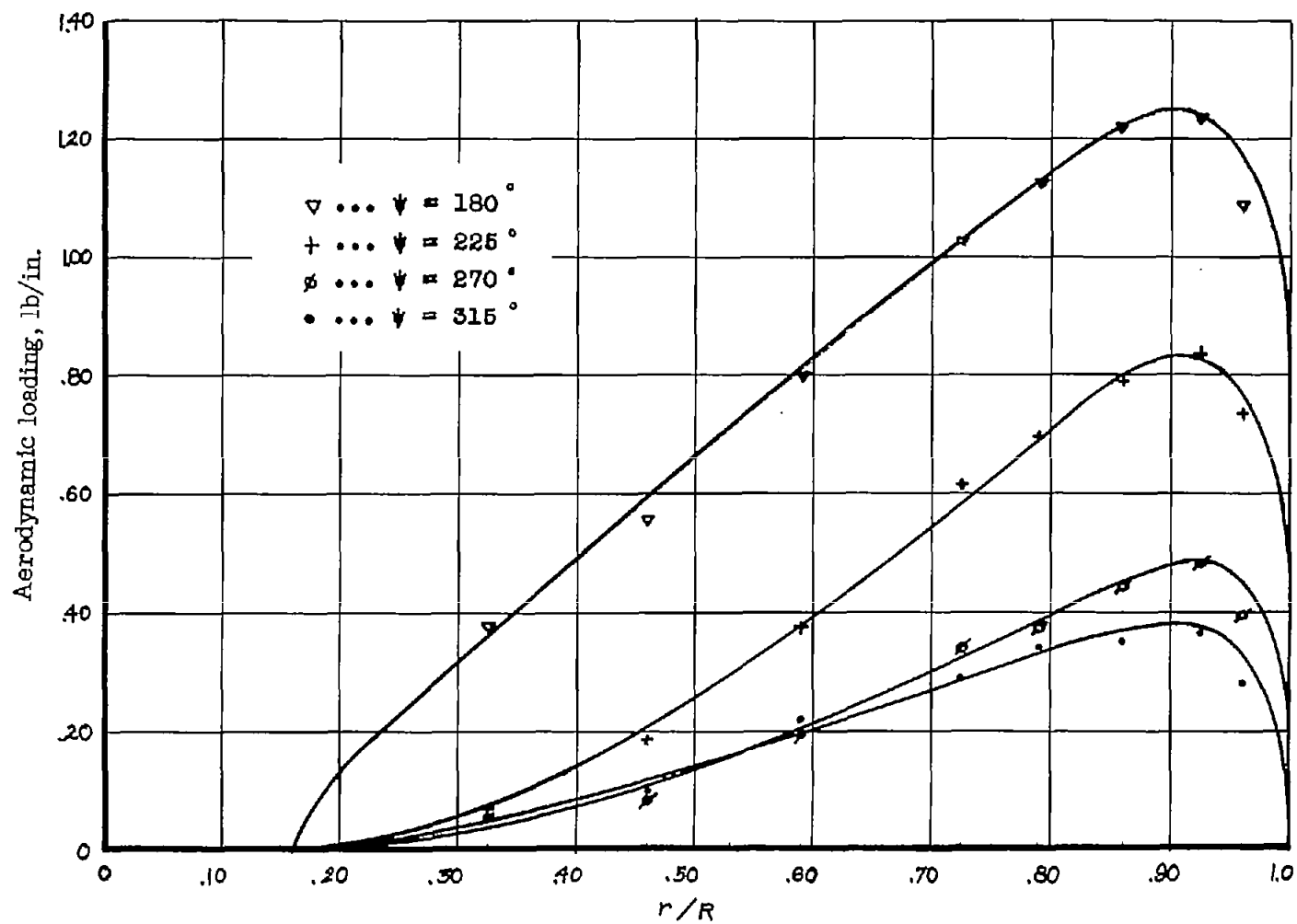
(h) Span station K; $r/R = 0.960$.

Figure 47.- Concluded.



(a) $\psi = 0^\circ$ to 135° .

Figure 48.- Experimental spanwise aerodynamic loading at various azimuths. Profile, NACA 0015; $\mu = 0.30$; $\xi = 0.13$; $A_0 = 15^\circ$; $\alpha = 0^\circ$.



(b) $\psi = 180^\circ$ to 315° .

Figure 48.- Concluded.

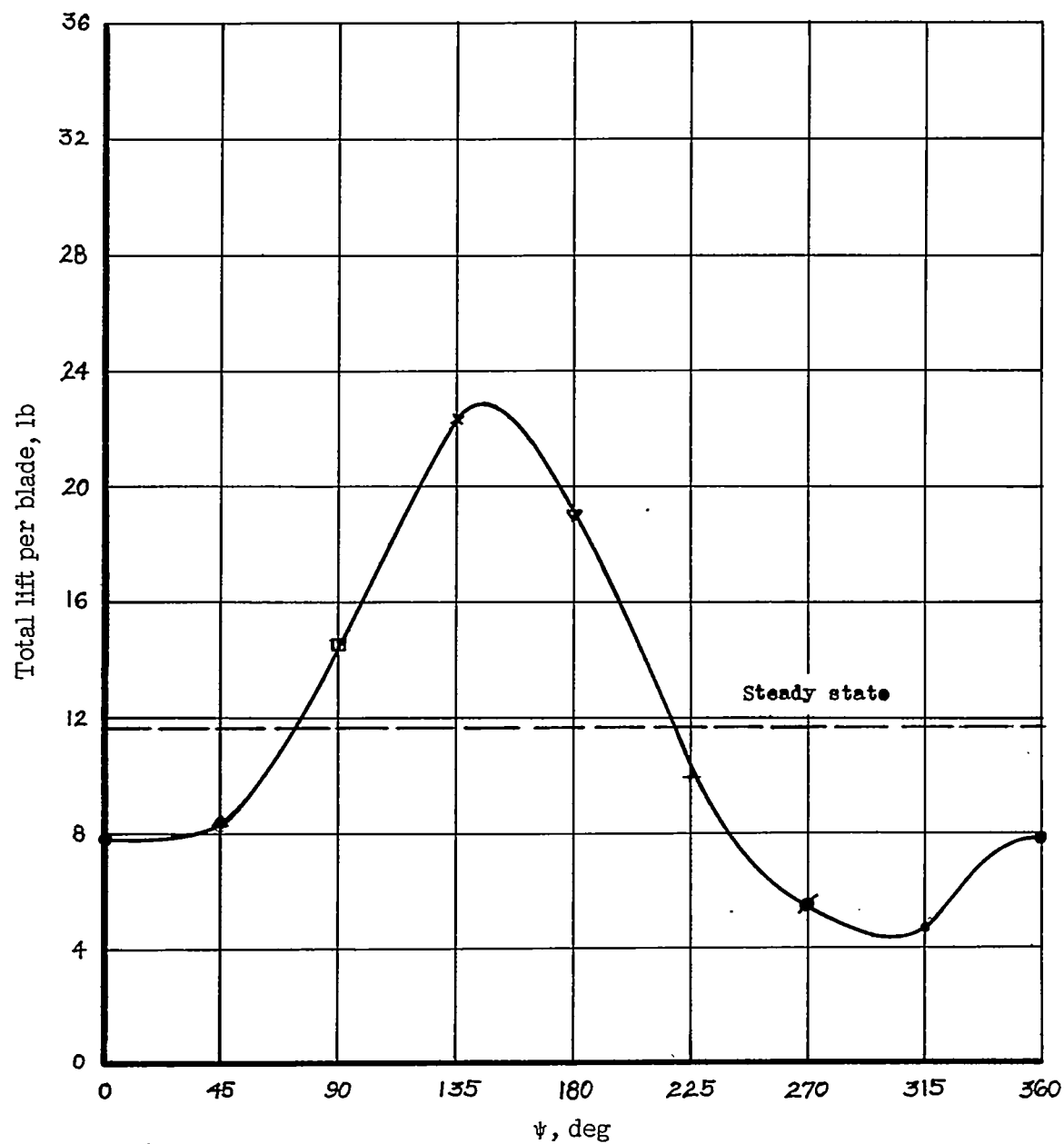


Figure 49.- Variation in total lift per blade. Profile, NACA 0015; $\mu = 0.30$; $\xi = 0.13$; $A_0 = 15^\circ$; $\alpha = 0^\circ$.

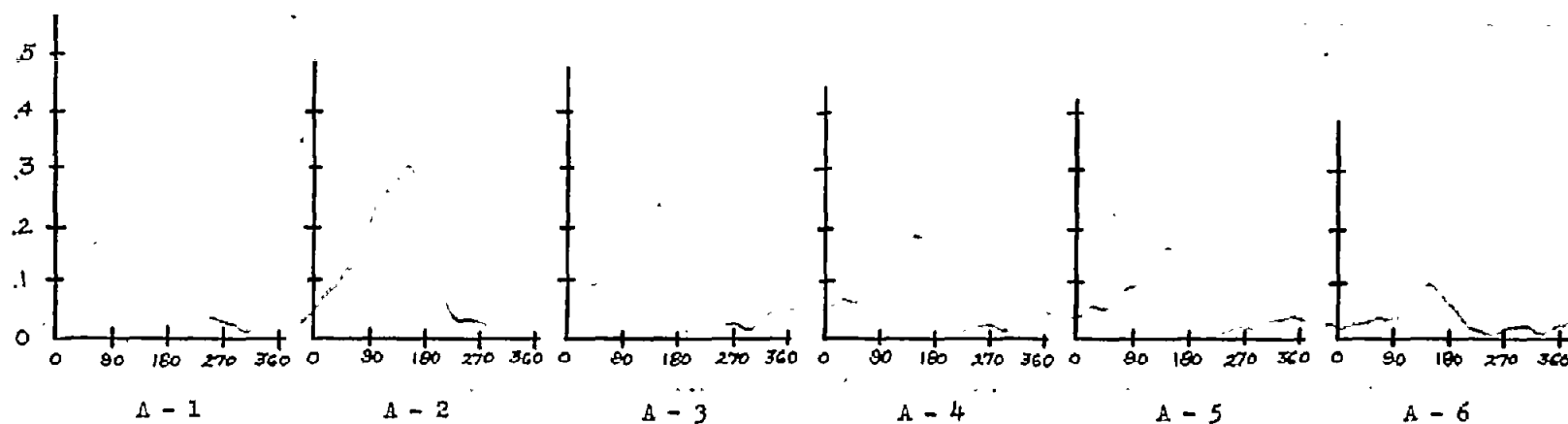
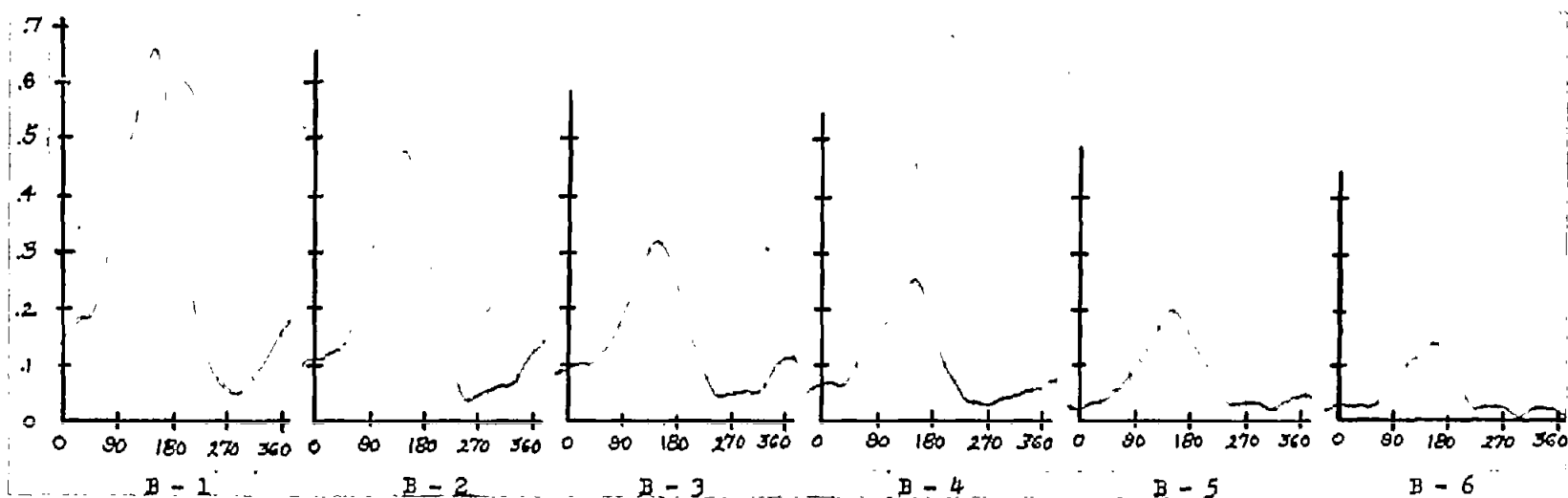
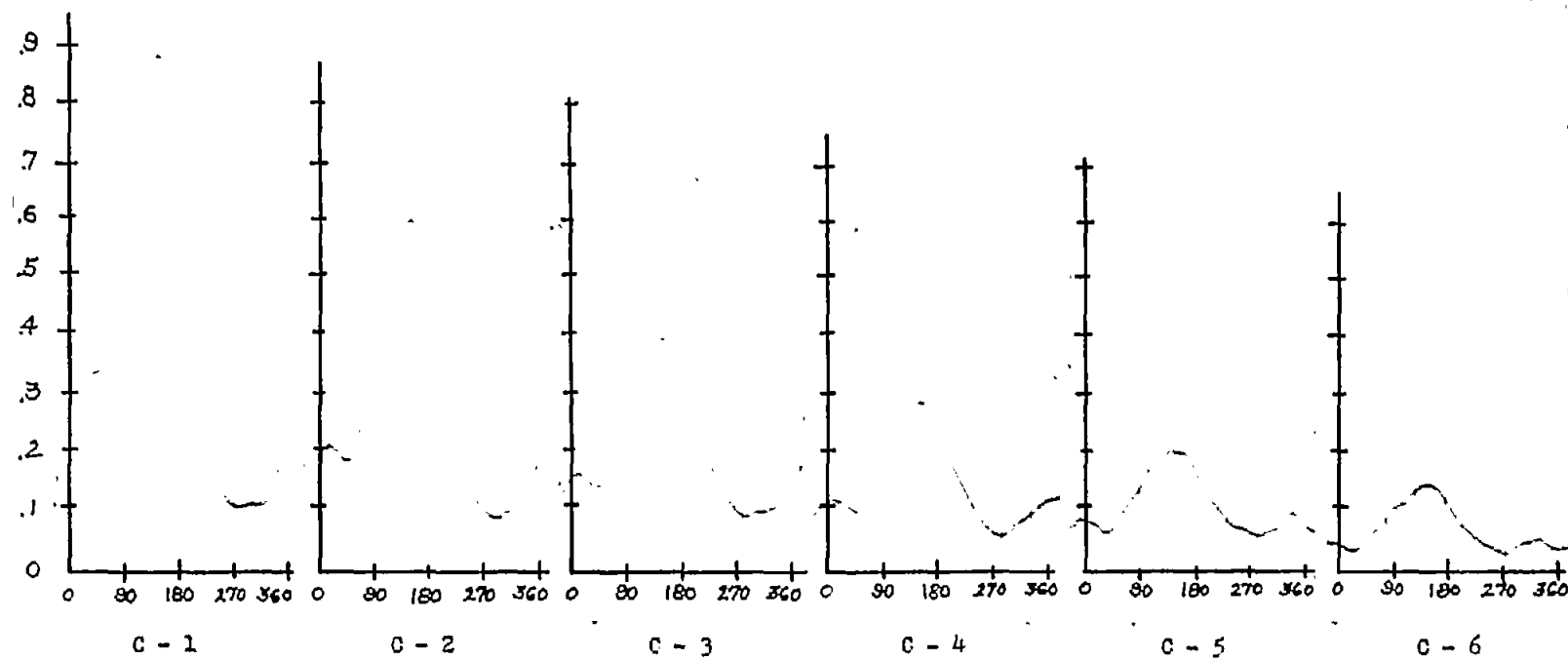
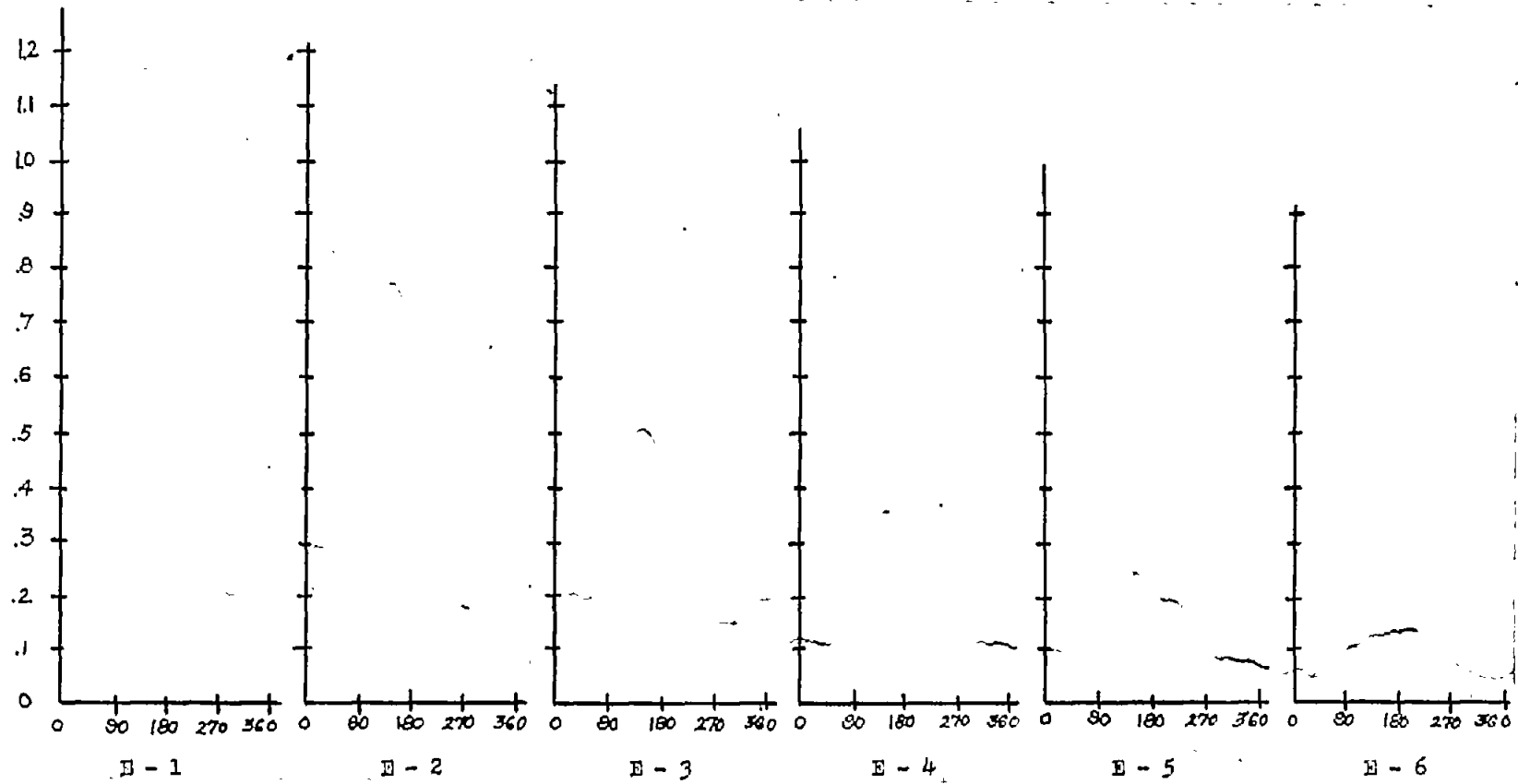
(a) Span station A; $r/R = 0.325$.(b) Span station B; $r/R = 0.460$.

Figure 50.- Pressure difference in pounds per square inch against azimuth in degrees. Profile, NACA 0015; speed, 800 rpm; $\xi = 0.13$; $\mu = 0.30$; $A_0 = 15^\circ$; $\alpha = 0^\circ$.



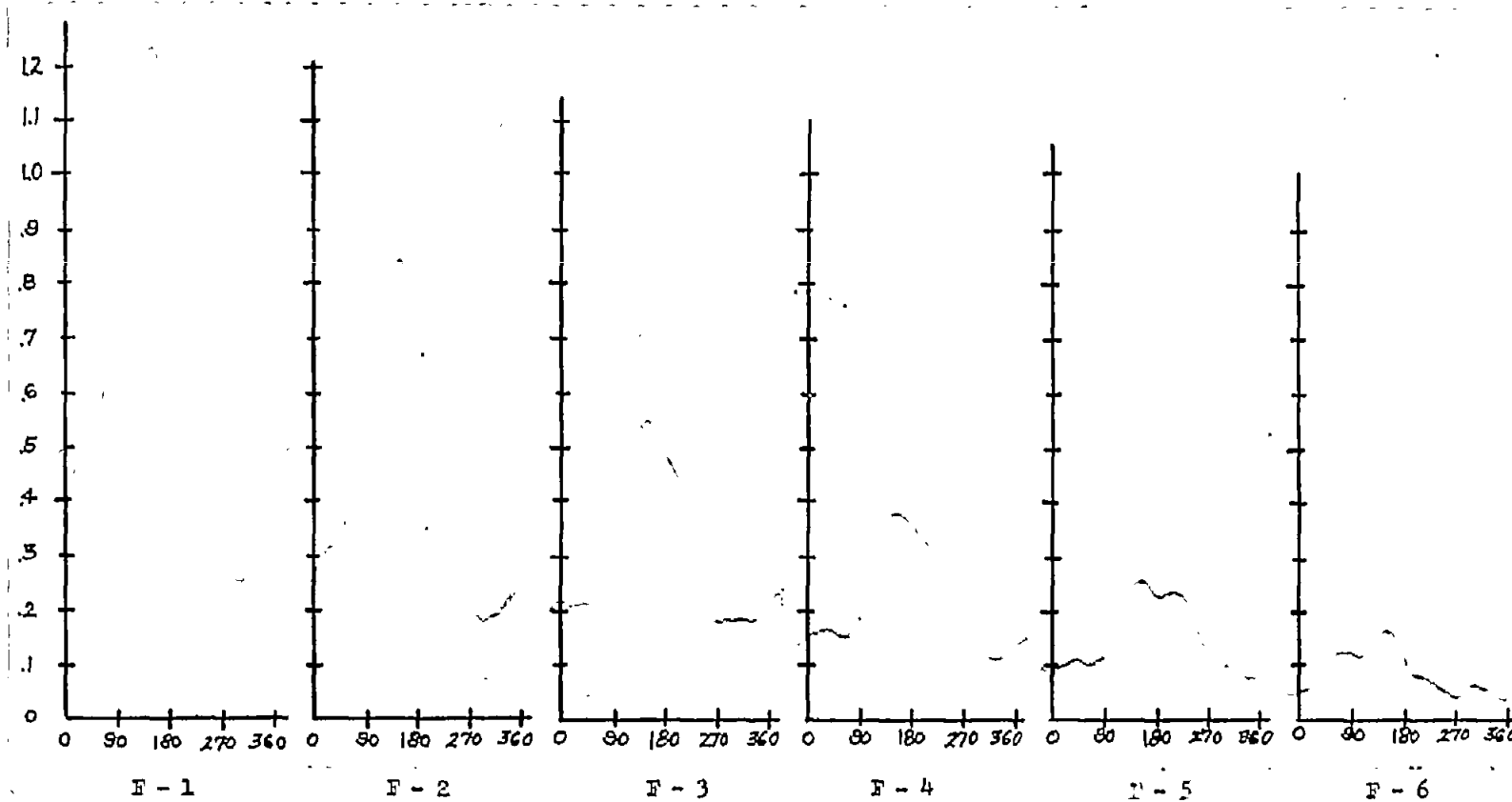
(c) Span station C; $r/R = 0.590$.

Figure 50.- Continued.



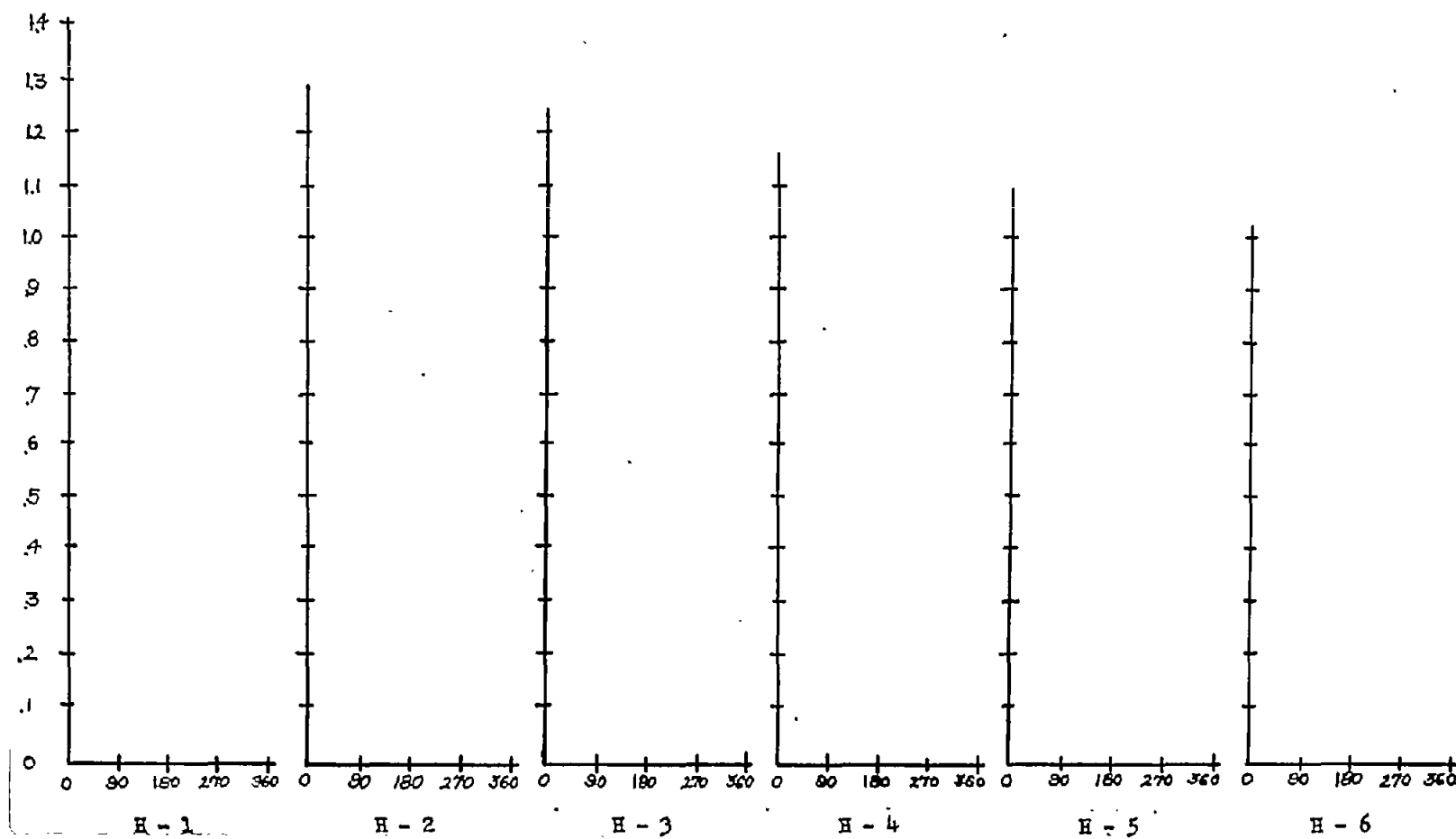
(d) Span station E; $r/R = 0.725$.

Figure 50.- Continued.



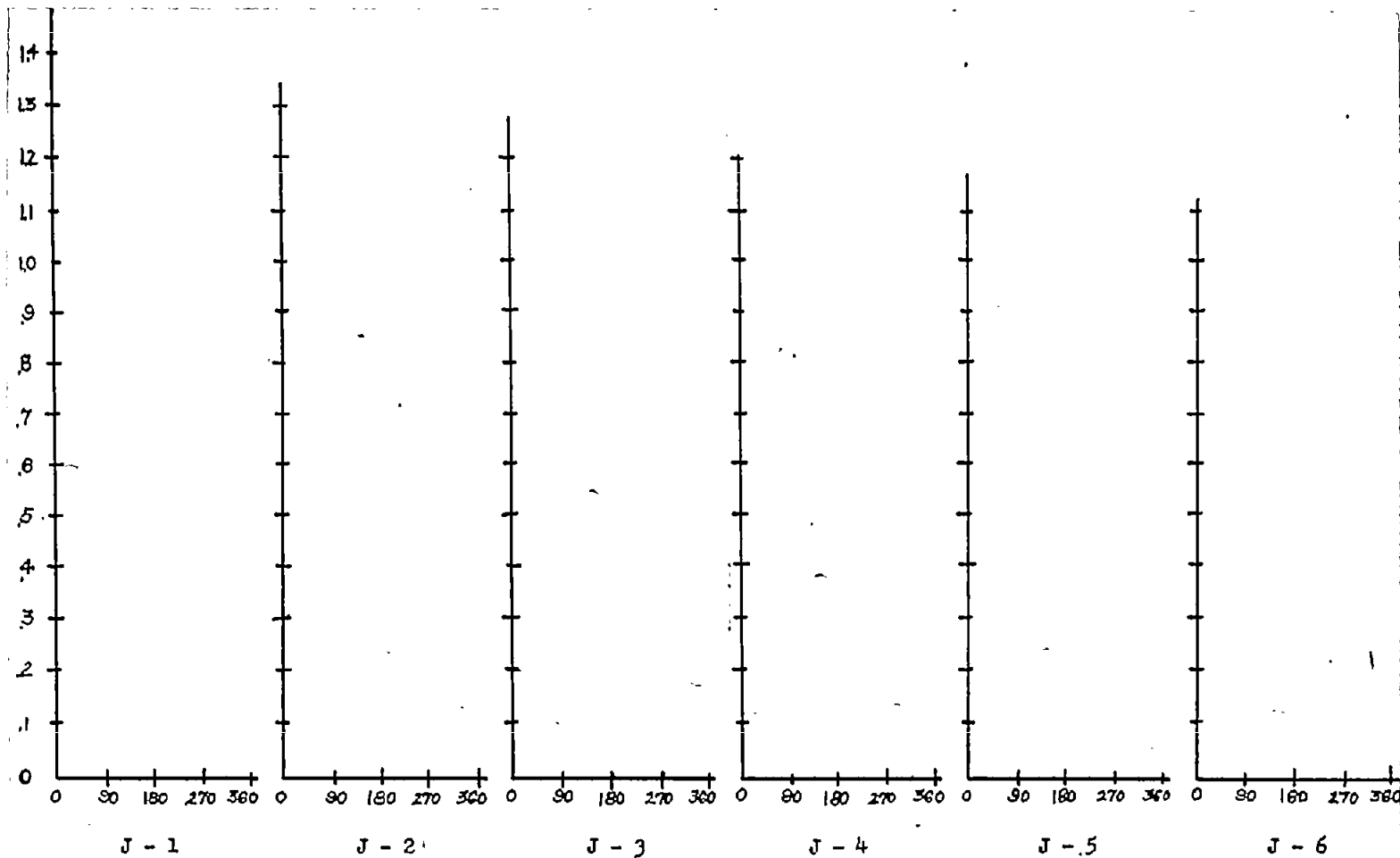
(e) Span station F; $r/R = 0.790$.

Figure 50.- Continued.



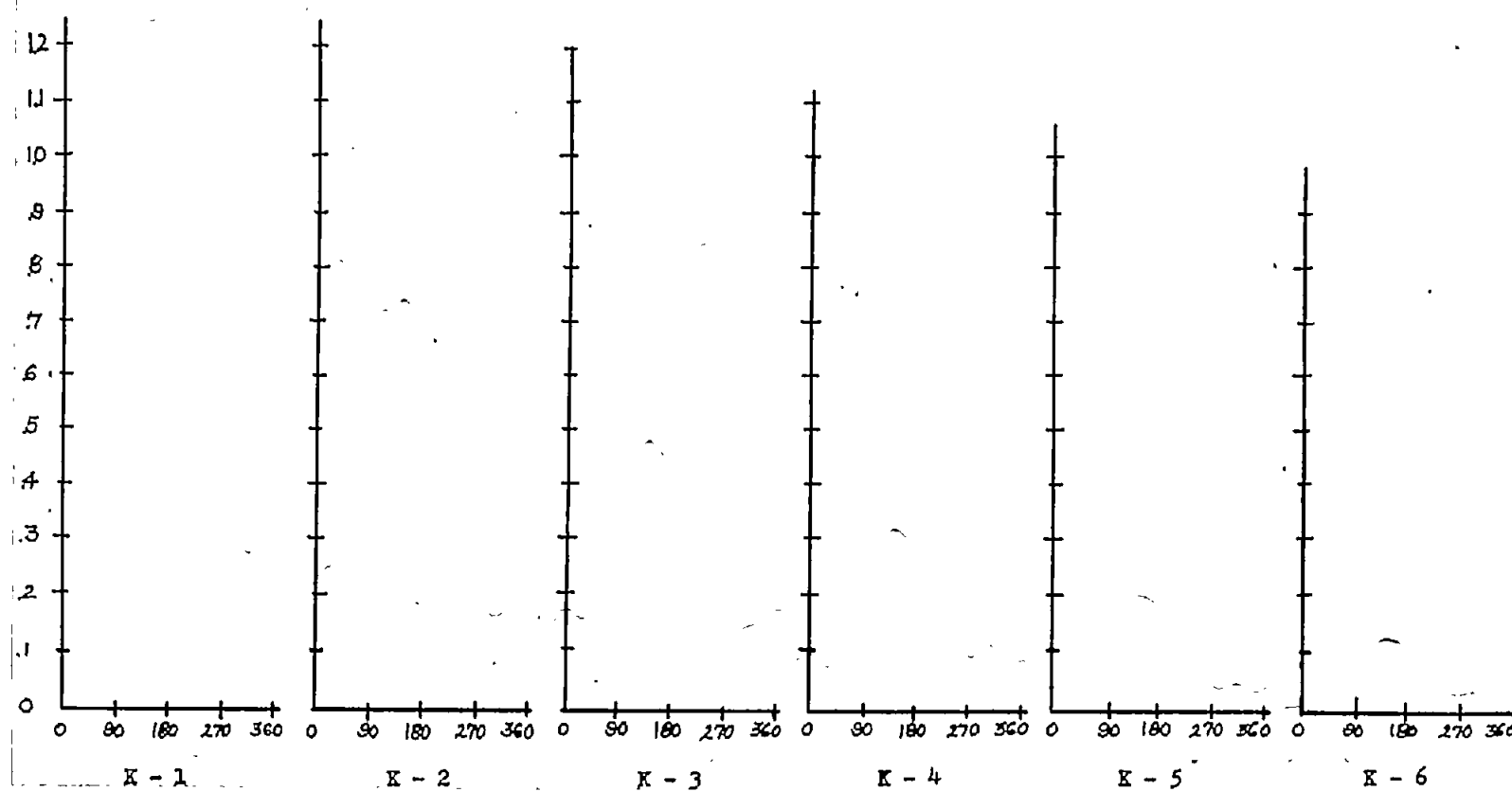
(f) Span station H; $r/R = 0.860$.

Figure 50.- Continued.



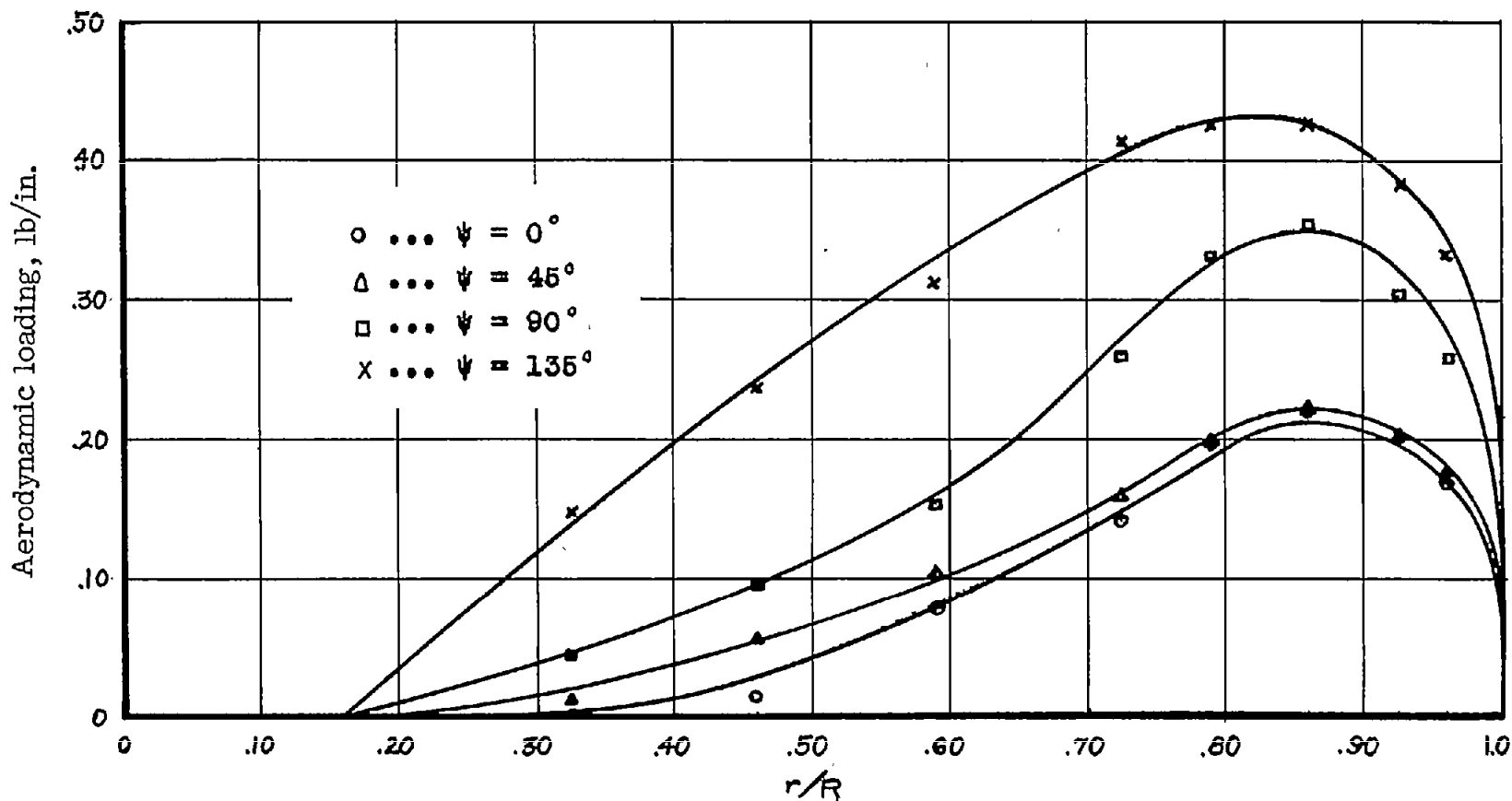
(g) Span station J; $r/R = 0.925$.

Figure 50.- Continued.



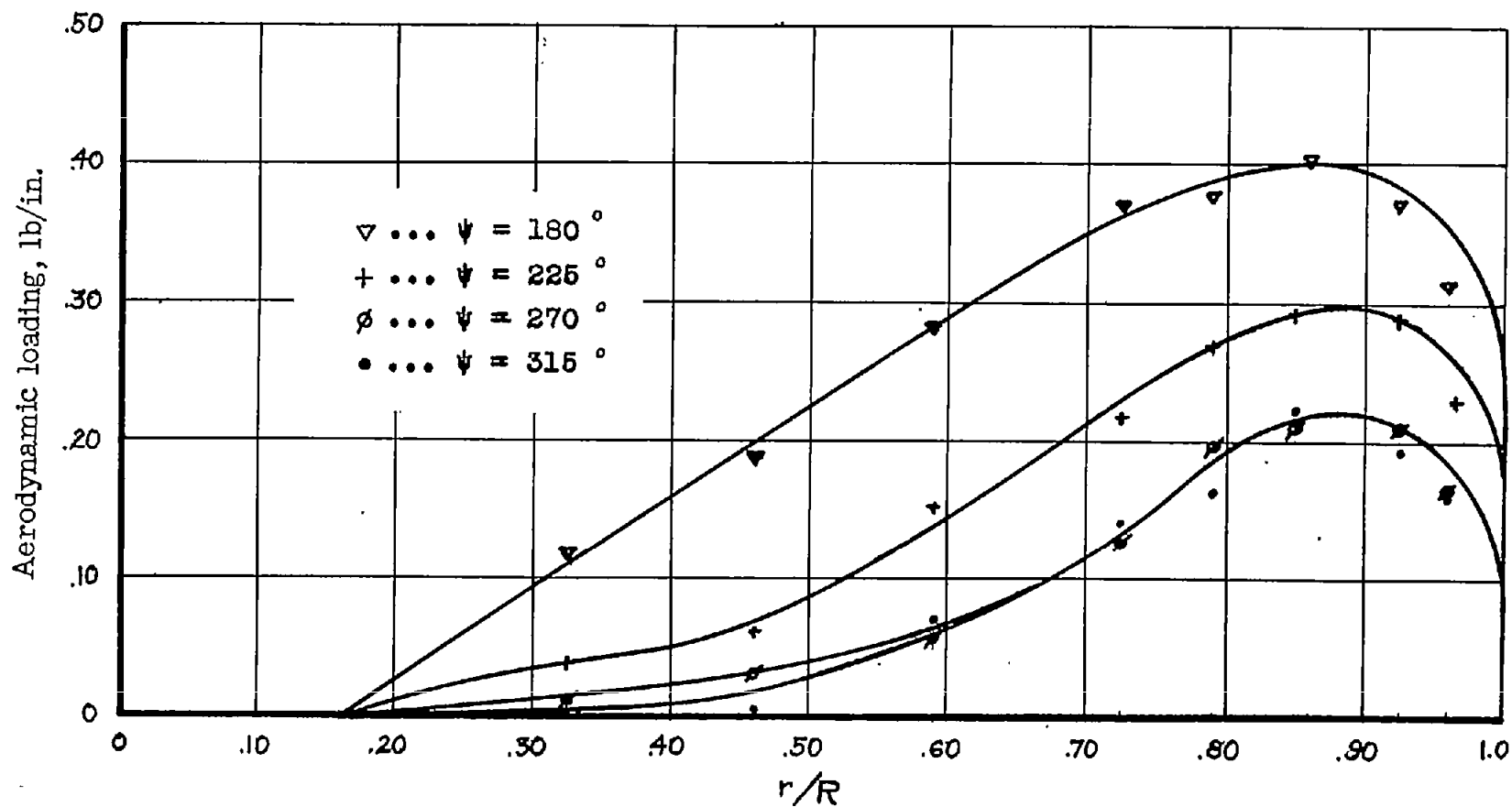
(h) Span station K; $r/R = 0.960$.

Figure 50.- Concluded.



(a) $\psi = 0^\circ$ to 135° .

Figure 51.- Experimental spanwise aerodynamic loading at various azimuths. Profile, NACA 0015;
 $\mu = 0.30$; $\xi = 0.13$; $A_0 = 8^\circ$; $B_1 = 3^\circ$; $\alpha = -8^\circ$.



(b) $\psi = 180^\circ$ to 315° .

Figure 51.- Concluded.

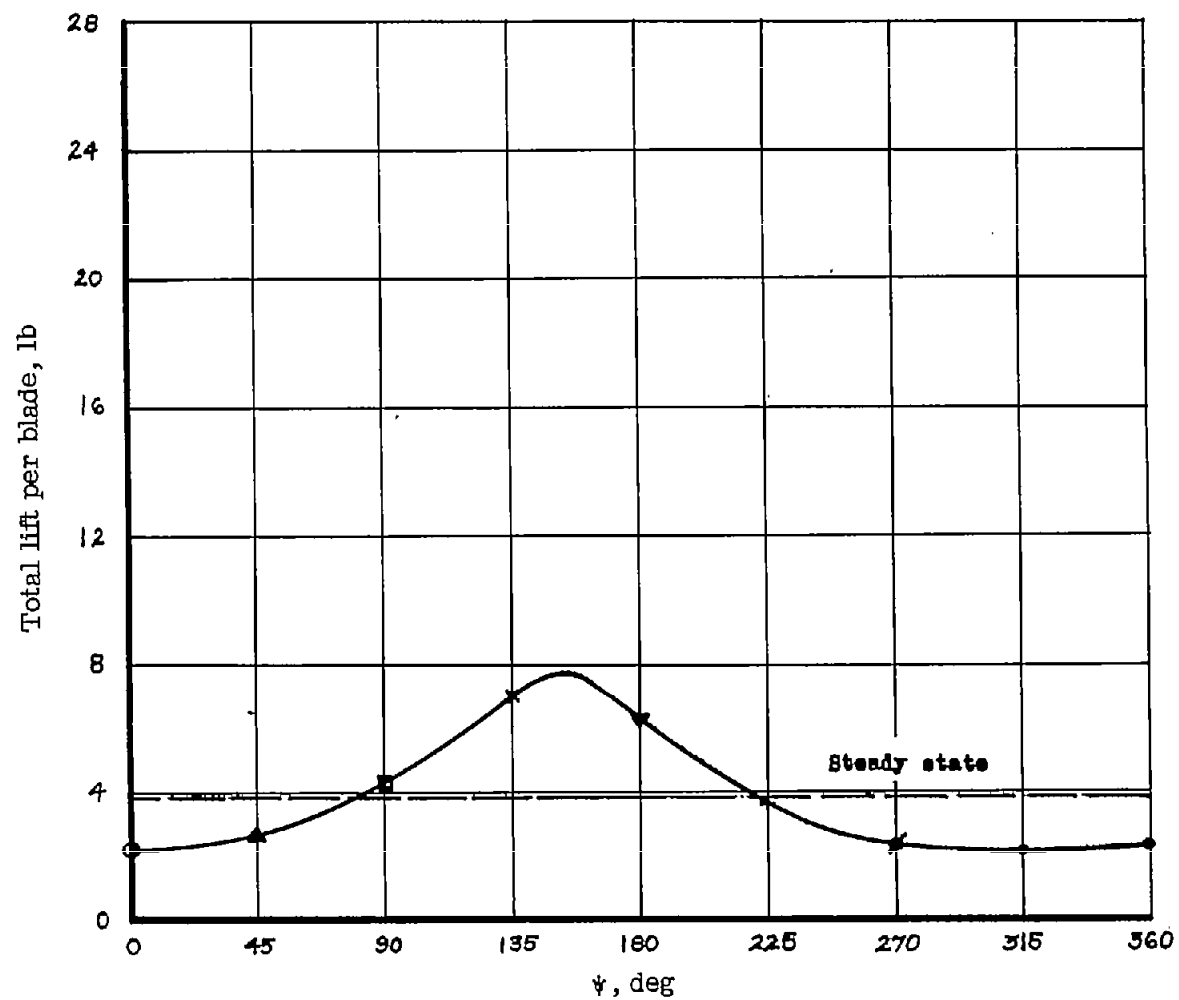


Figure 52.- Variation in total lift per blade. Profile, NACA 0015; $\mu = 0.30$; $\xi = 0.13$; $A_0 = 8^\circ$; $B_1 = 3^\circ$; $\alpha = -8^\circ$.

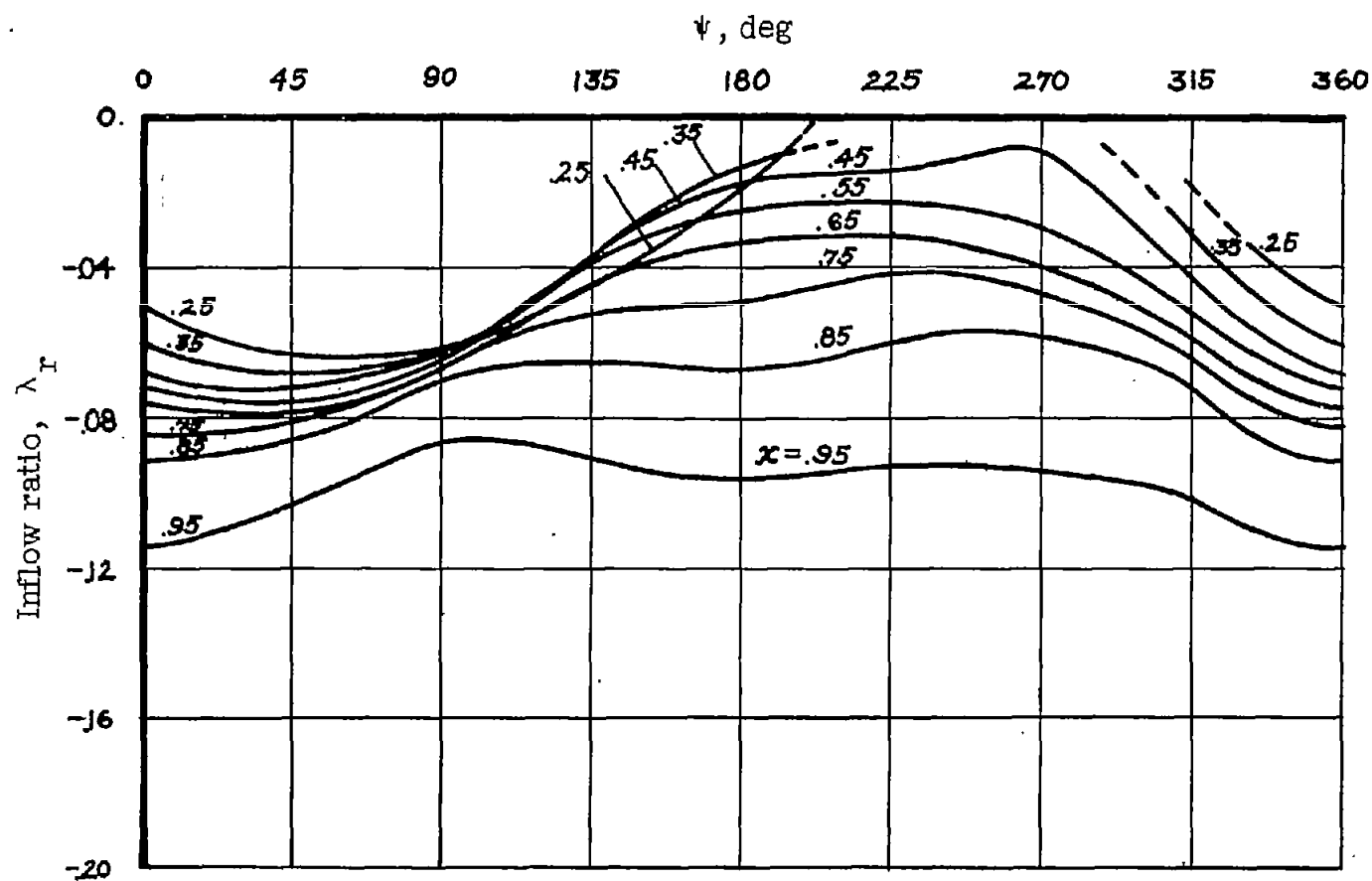
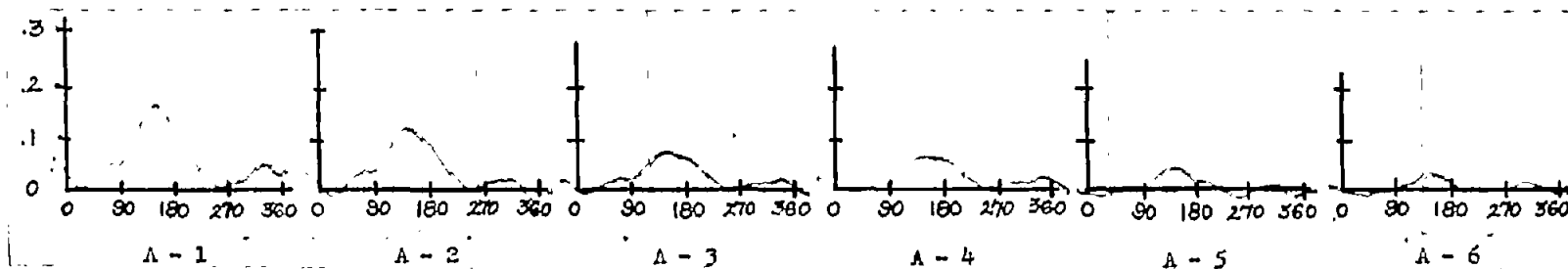
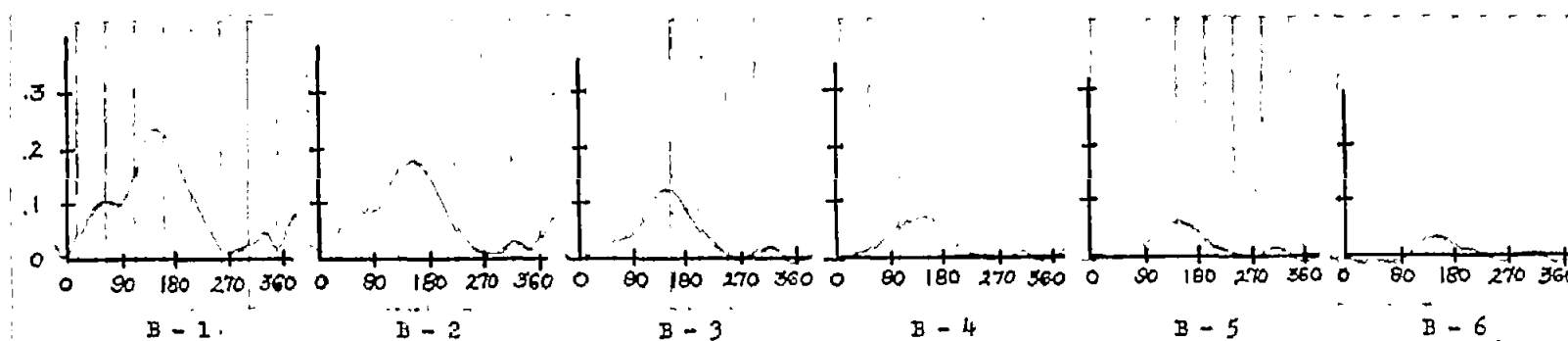


Figure 53.- Inflow distribution from experimental loading and blade-motion data. $\mu = 0.30$; $\xi = 0.13$; $A_0 = 8^\circ$; $B_1 = 3^\circ$; $\alpha = -8^\circ$; $a = 5.7$; $\mu \sin \alpha = -0.026$. Dashed line indicates blade stall.

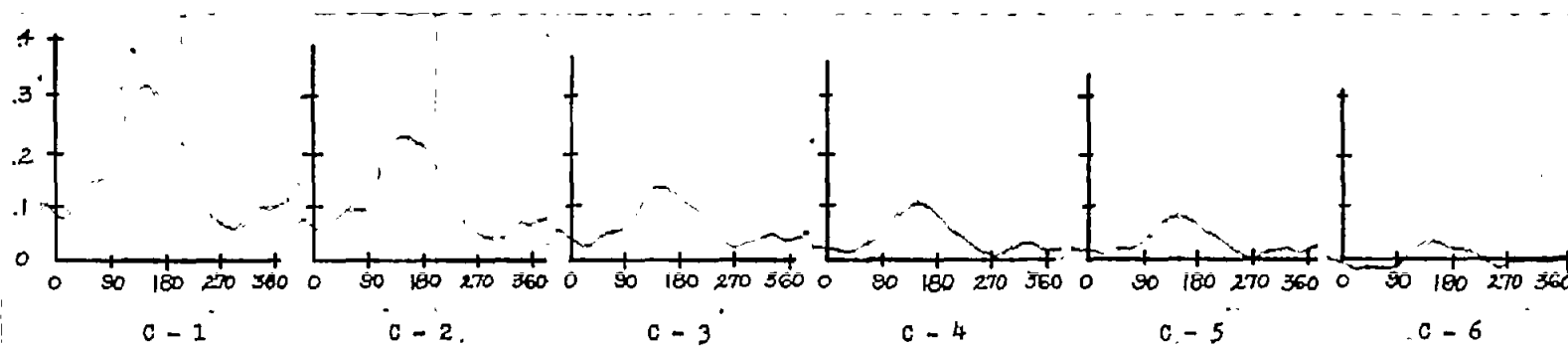


(a) Span station A; $r/R = 0.325$.

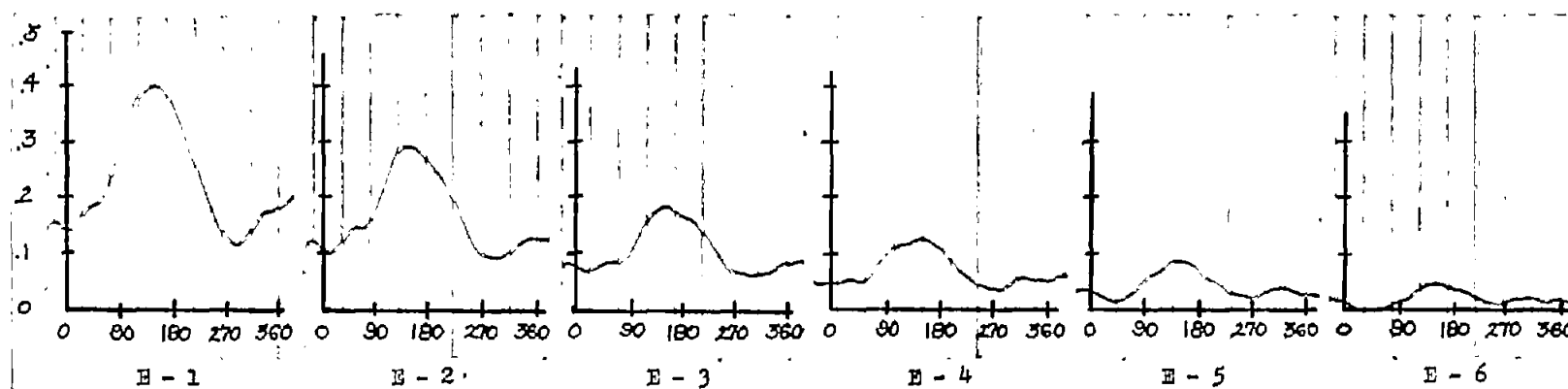


(b) Span station B; $r/R = 0.460$.

Figure 54.- Pressure difference in pounds per square inch against azimuth in degrees. Profile, NACA 0015; speed, 800 rpm; $\xi = 0.13$; $\mu = 0.30$; $A_0 = 8^\circ$; $B_1 = 3^\circ$; $\alpha = -8^\circ$.

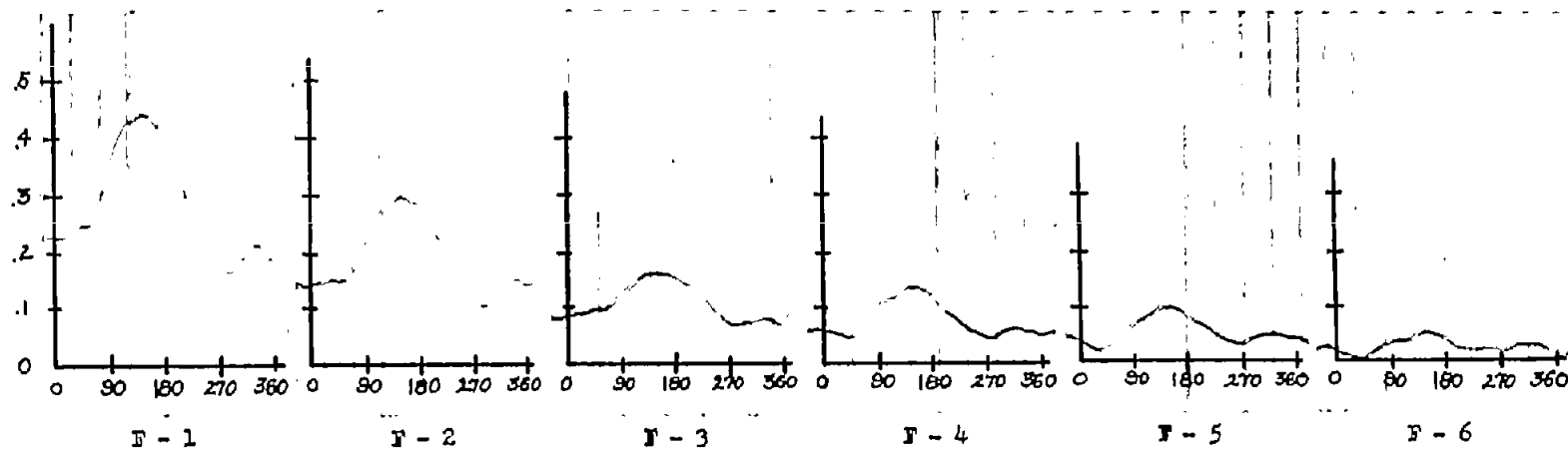


(c) Span station C; $r/R = 0.590$.

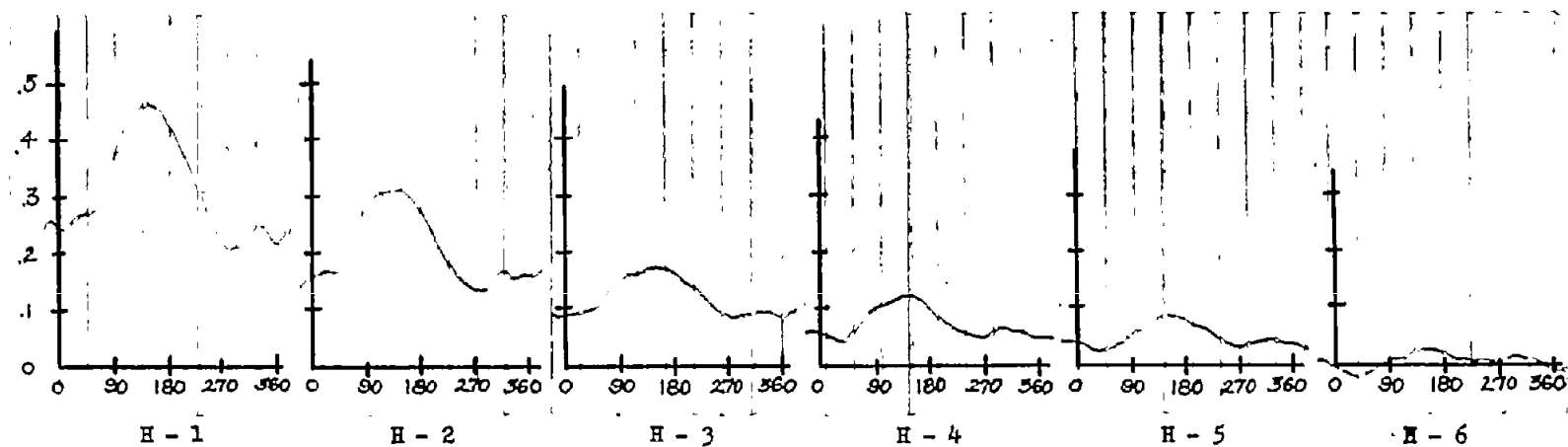


(d) Span station E; $r/R = 0.725$.

Figure 54.- Continued.

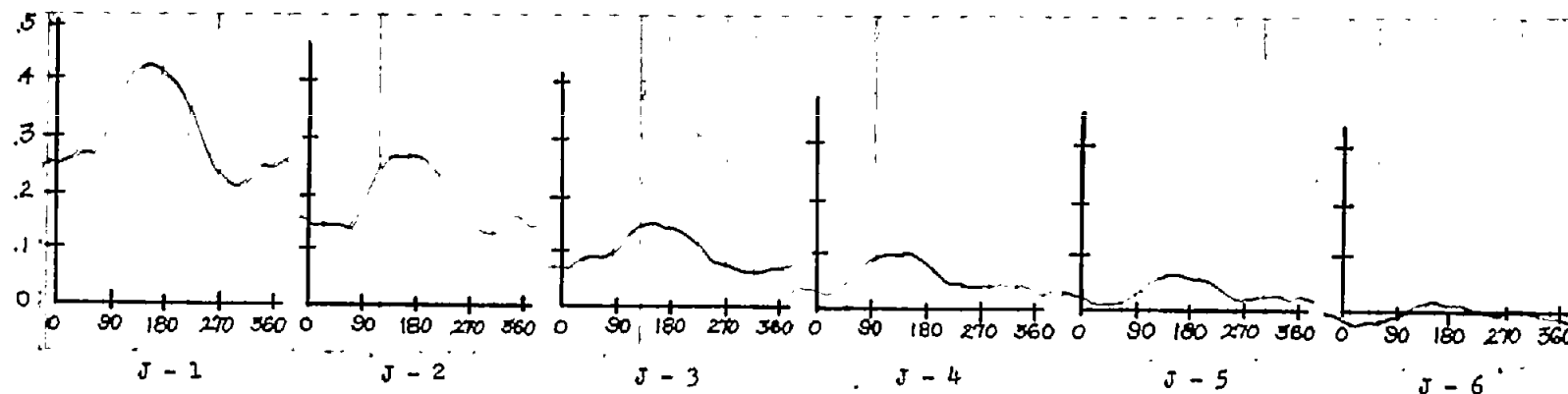


(e) Span station F; $r/R = 0.790$.

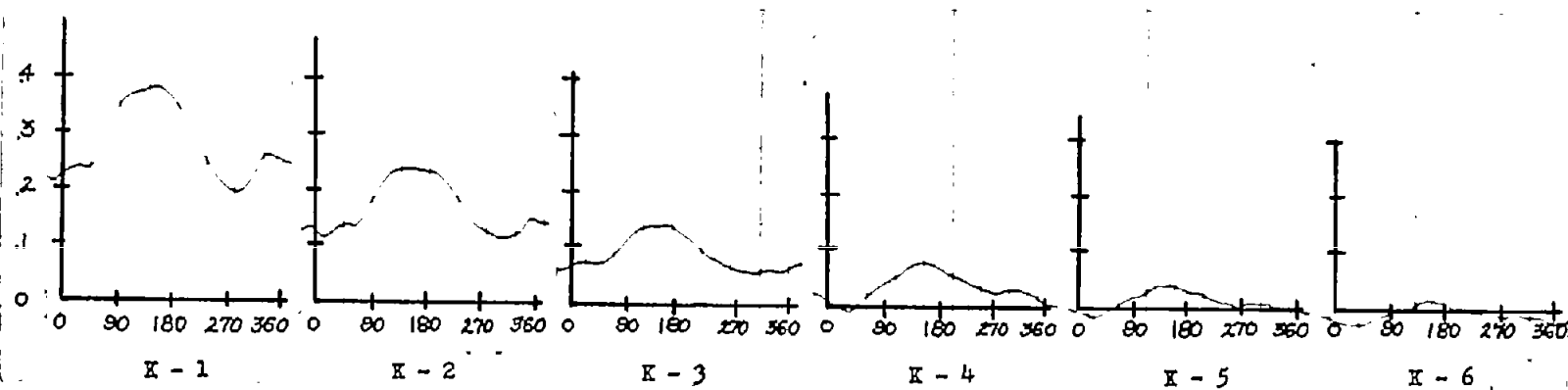


(f) Span station H; $r/R = 0.860$.

Figure 54.- Continued.



(g) Span station J; $r/R = 0.925$.



(h) Span station K; $r/R = 0.960$.

Figure 54.- Concluded.

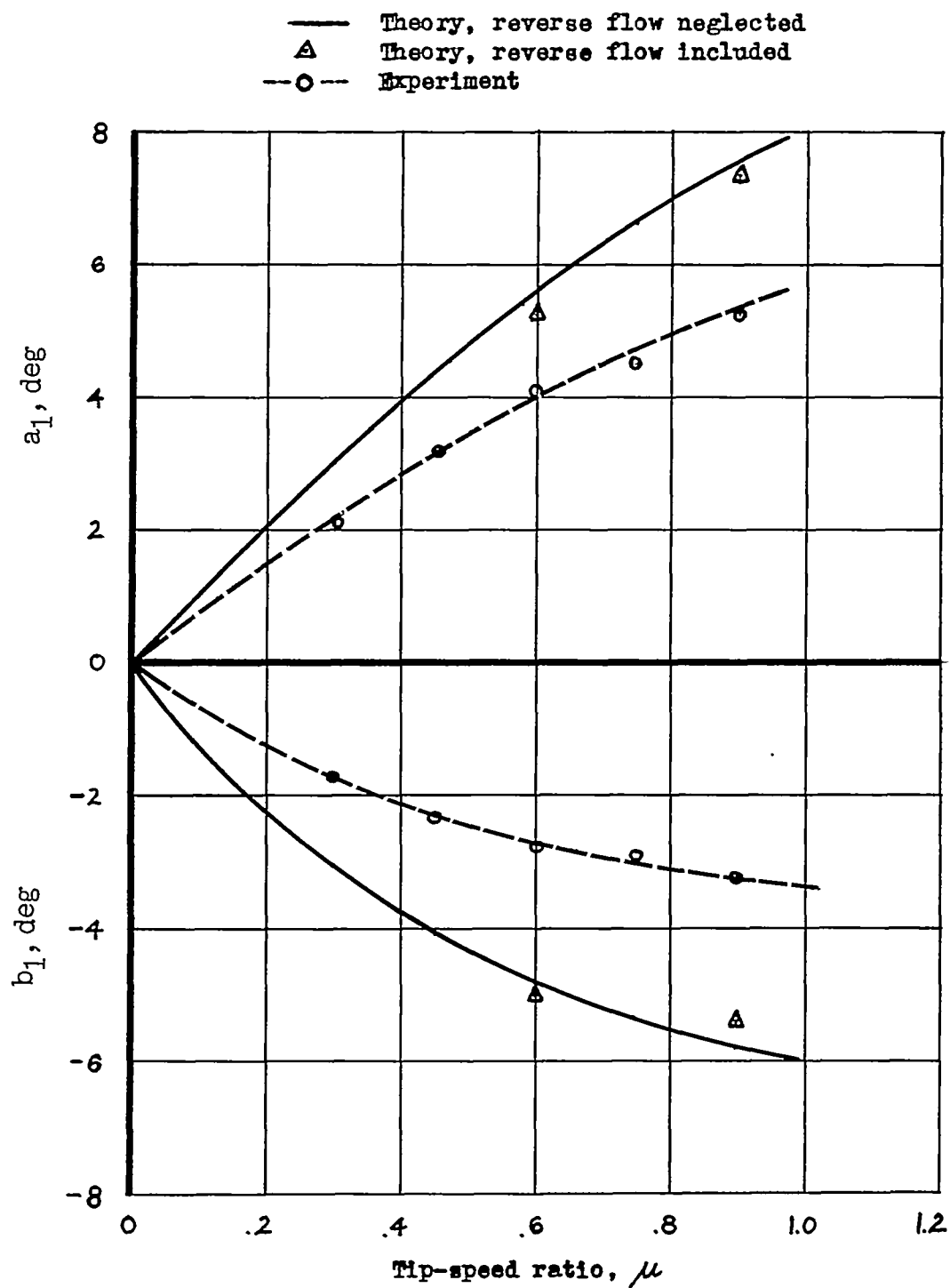


Figure 55.- Comparison of theoretical and experimental values of blade flapping coefficients. $\xi = 0.20$; $\gamma = 4$; $A_0 = 8^\circ$; $C_T/\sigma = 0.10$.

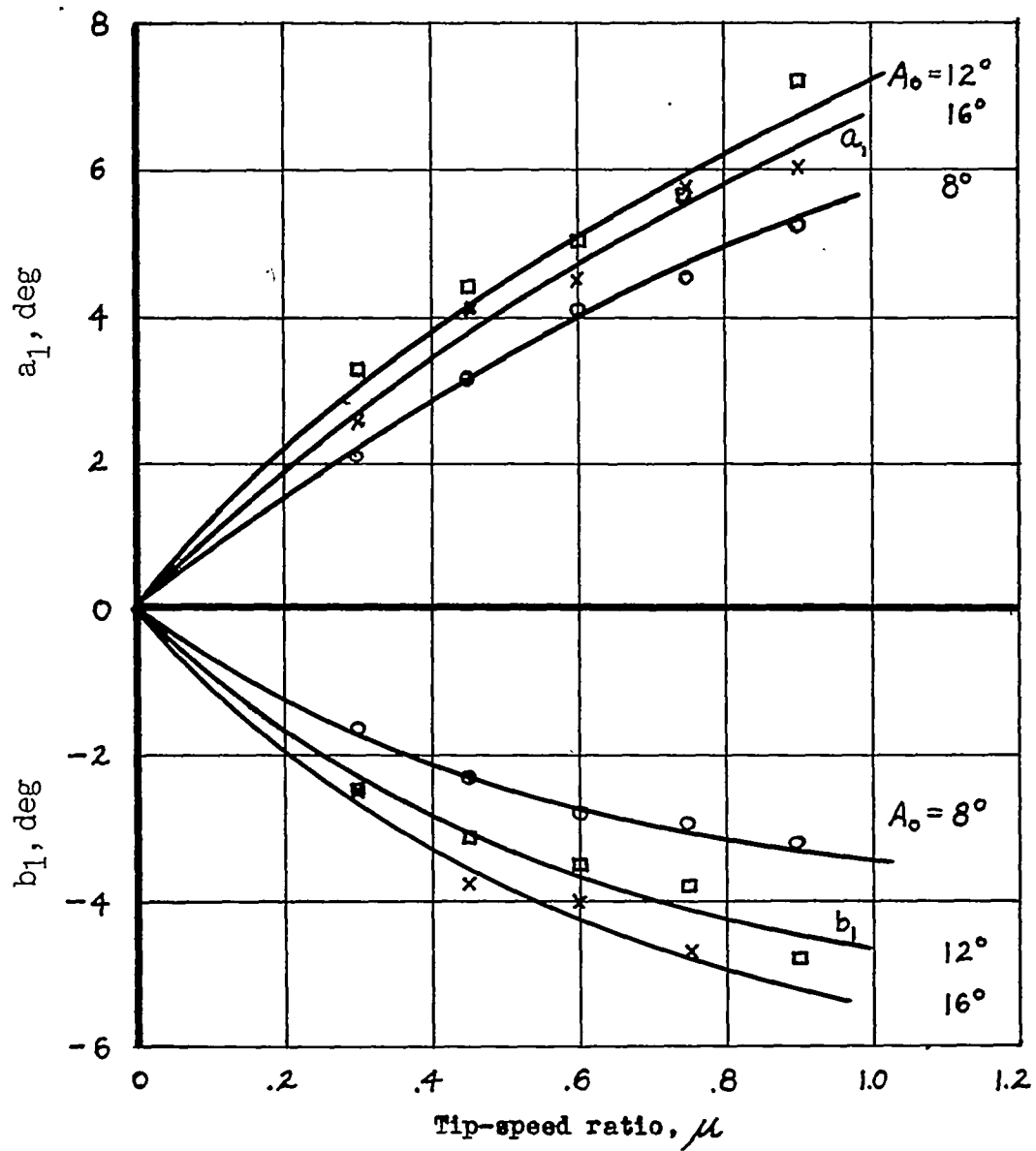


Figure 56.-- Experimental values of blade flapping coefficients for various blade pitch settings. $\xi = 0.20$; $\gamma = 4$; $C_T/\sigma = 0.10$.

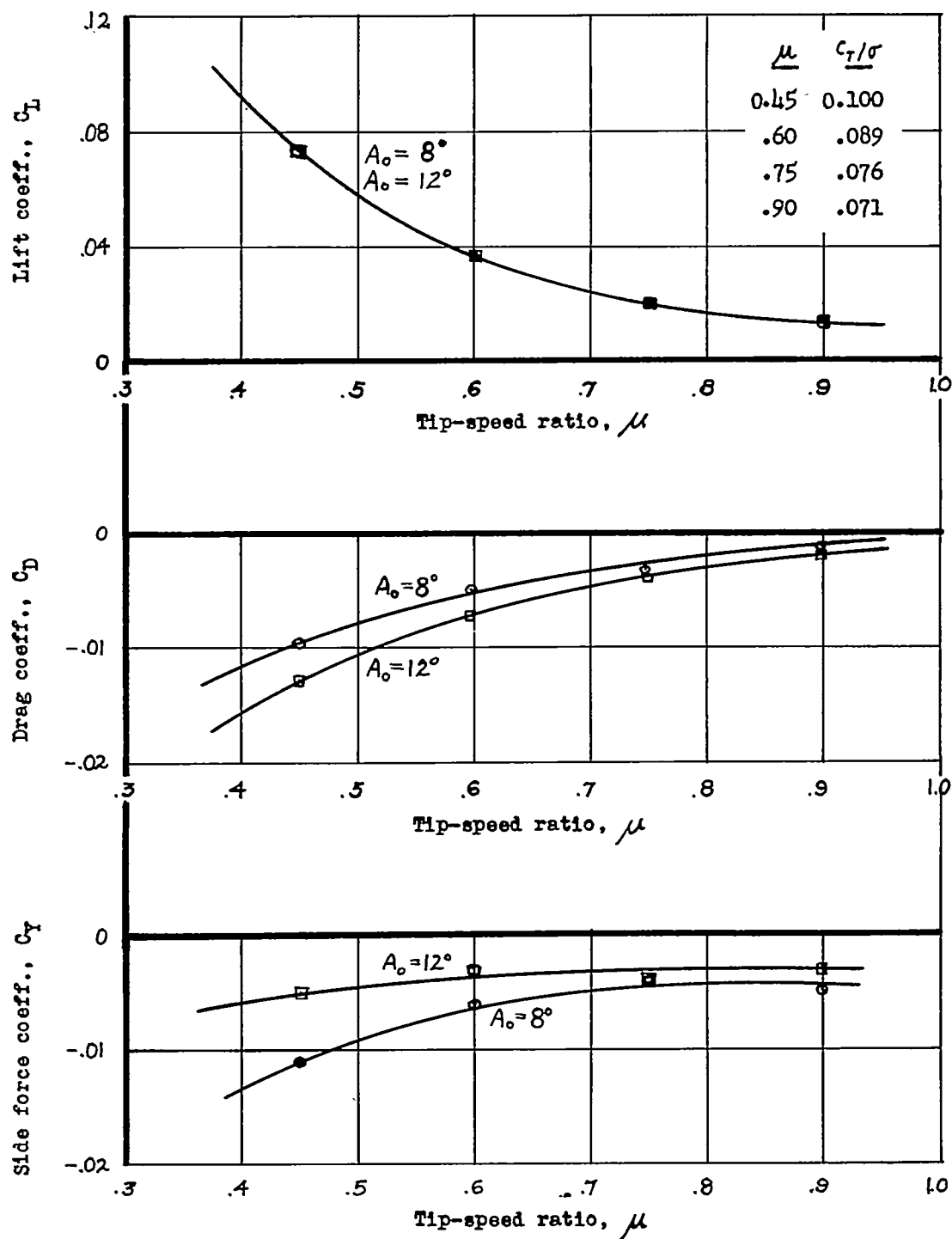


Figure 57.- Experimental values of the three force components at various advance ratios. $\gamma = 4$; $\xi = 0.20$; $\sigma = 0.073$; $R = 2.19$ feet; speed, 600 rpm.

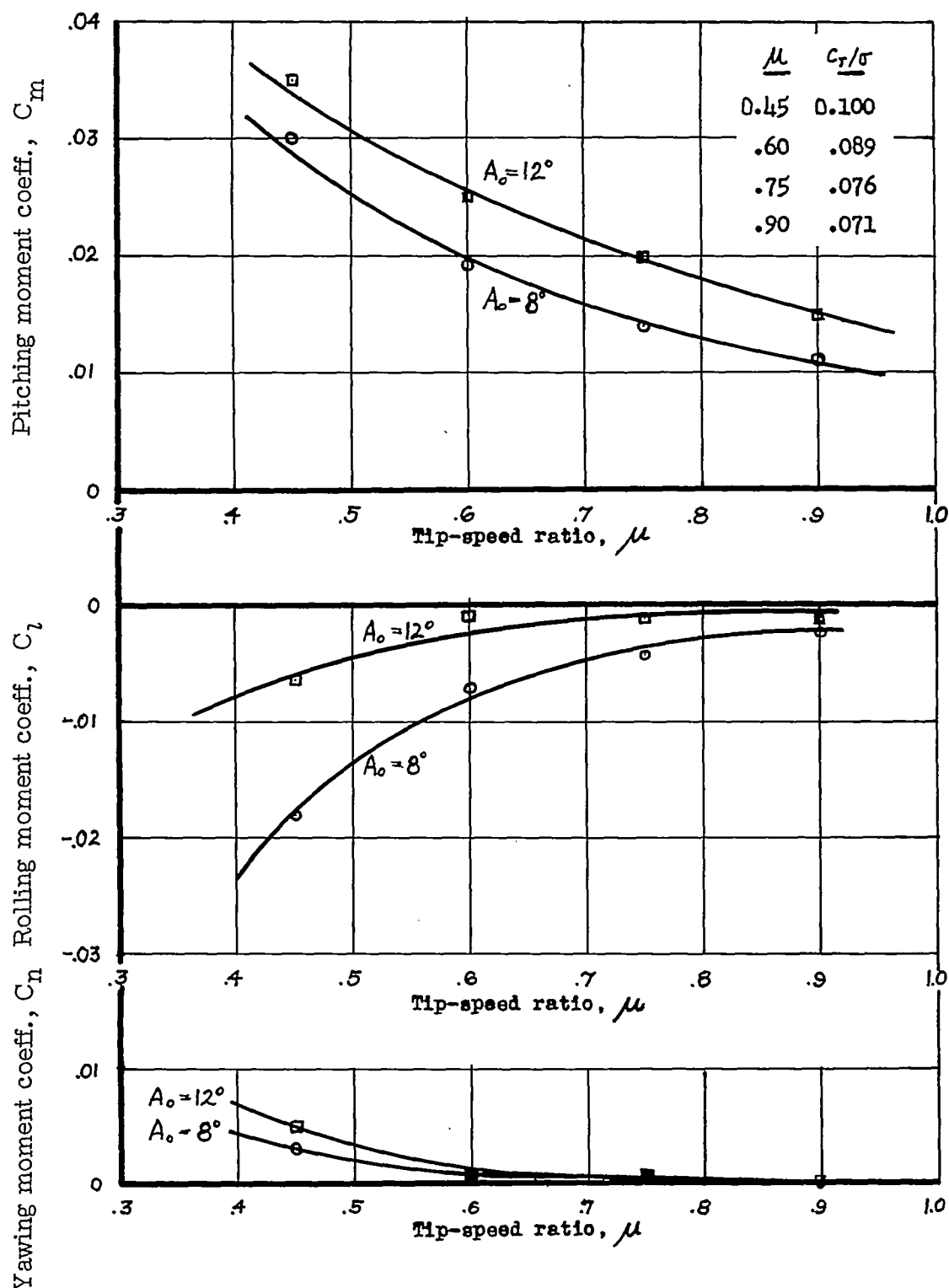


Figure 58.- Experimental values of the three moment components at various advance ratios. $\gamma = 4$; $\xi = 0.20$; $\sigma = 0.073$; $R = 2.19$ feet; speed, 600 rpm.

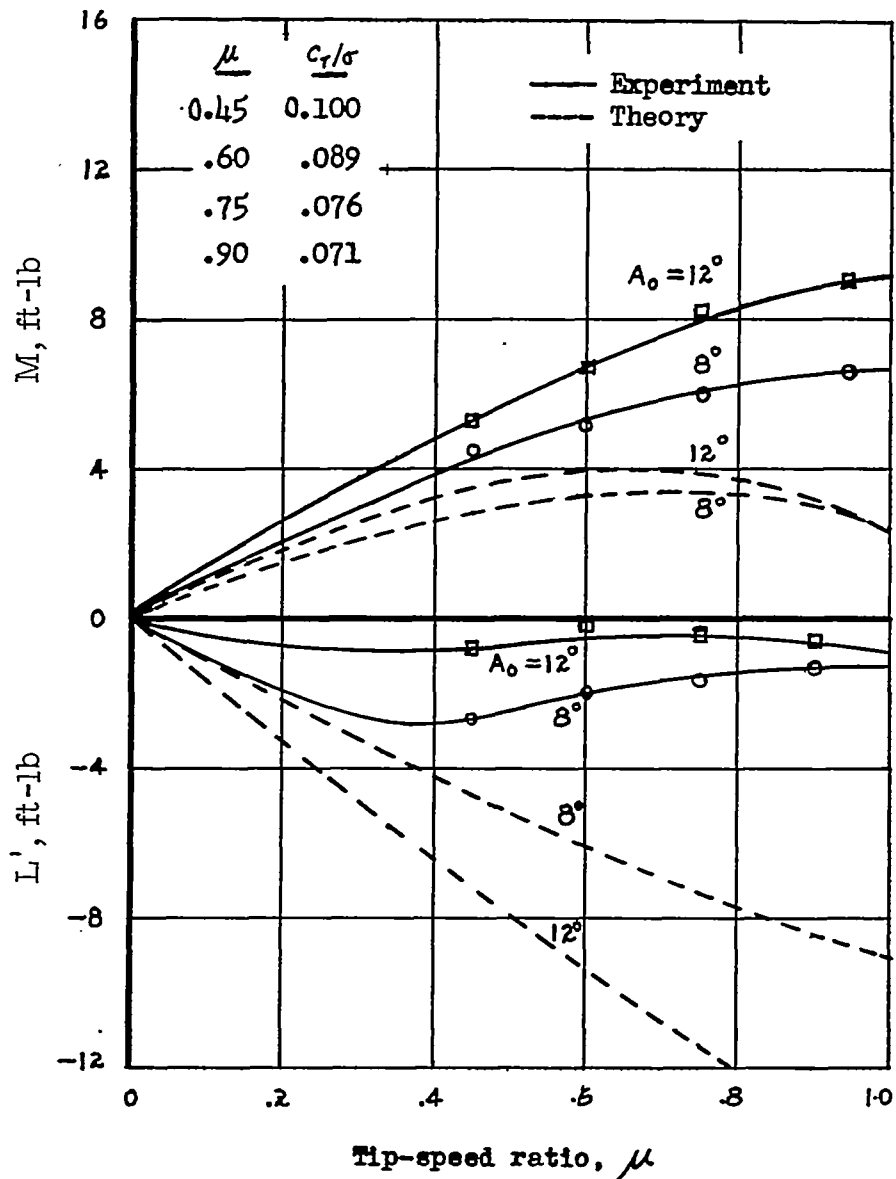


Figure 59.- Comparison of experimental and theoretical moment components.
 $\gamma = 4$; $\xi = 0.20$; $\sigma = 0.073$; $R = 2.19$ feet; speed, 600 rpm.

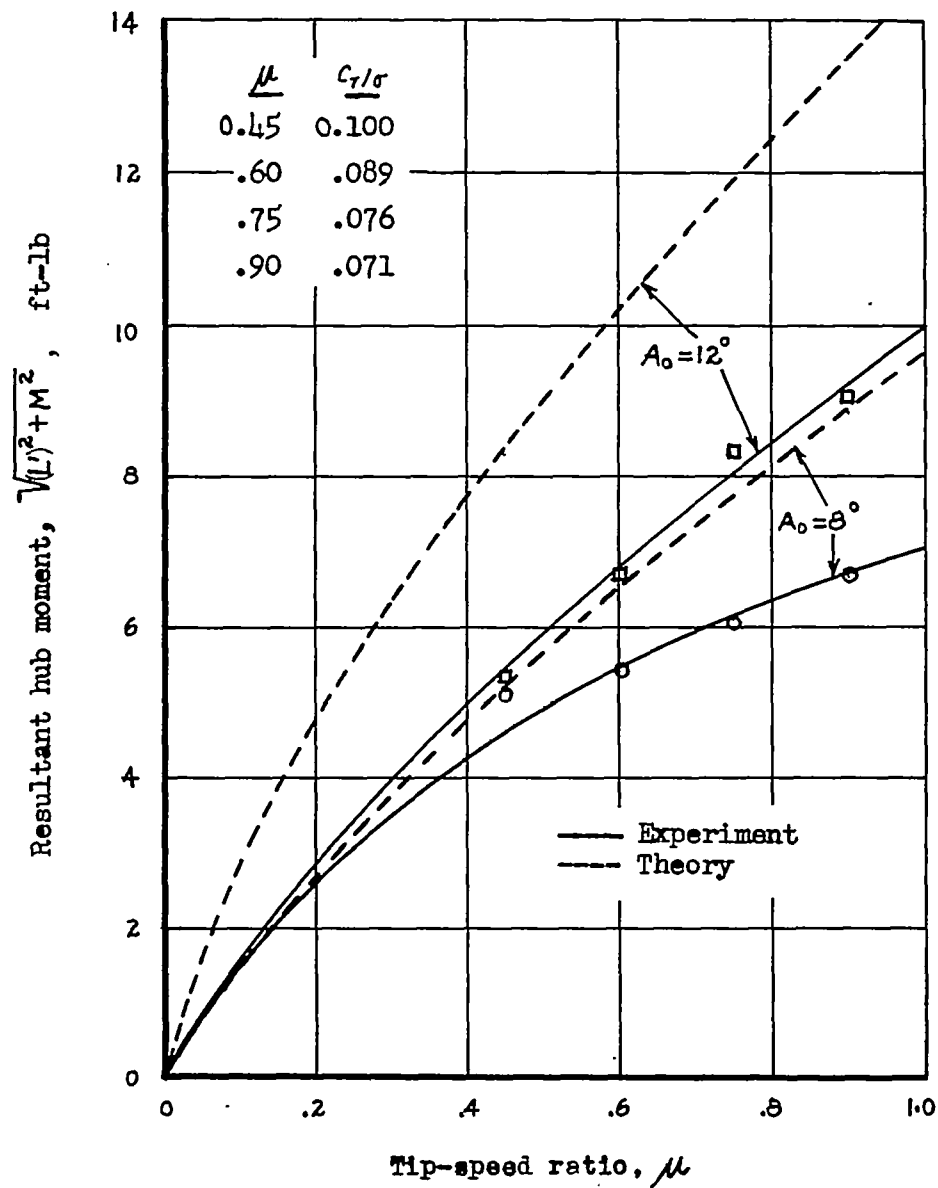
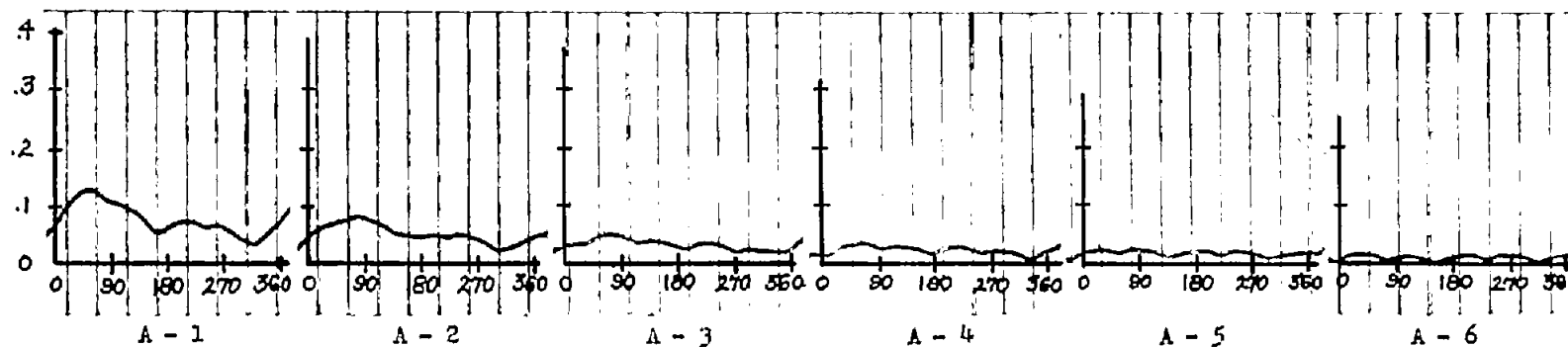
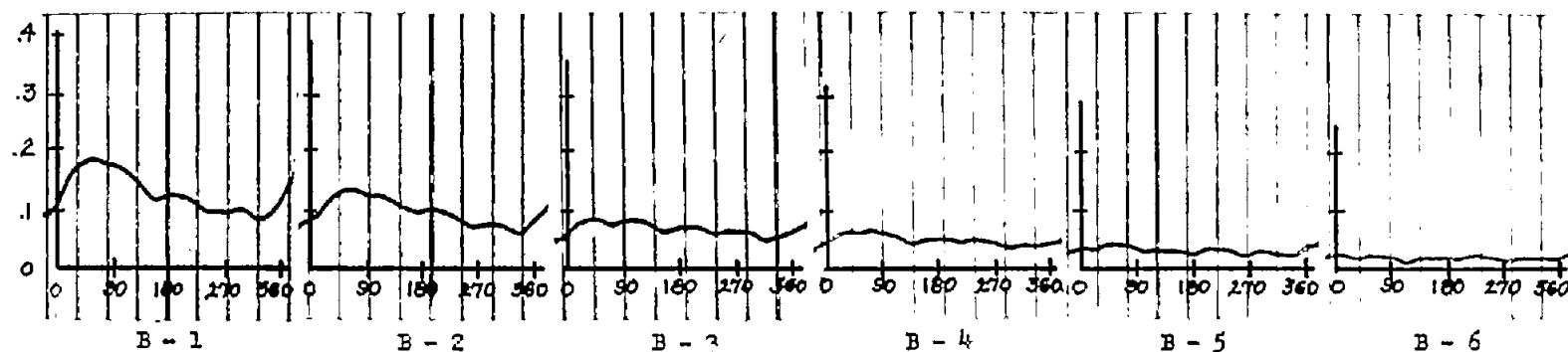


Figure 60.- Comparison of experimental and theoretical resultant hub moments. $\gamma = 4$; $\xi = 0.20$; $\sigma = 0.073$; $R = 2.19$ feet; speed, 600 rpm.

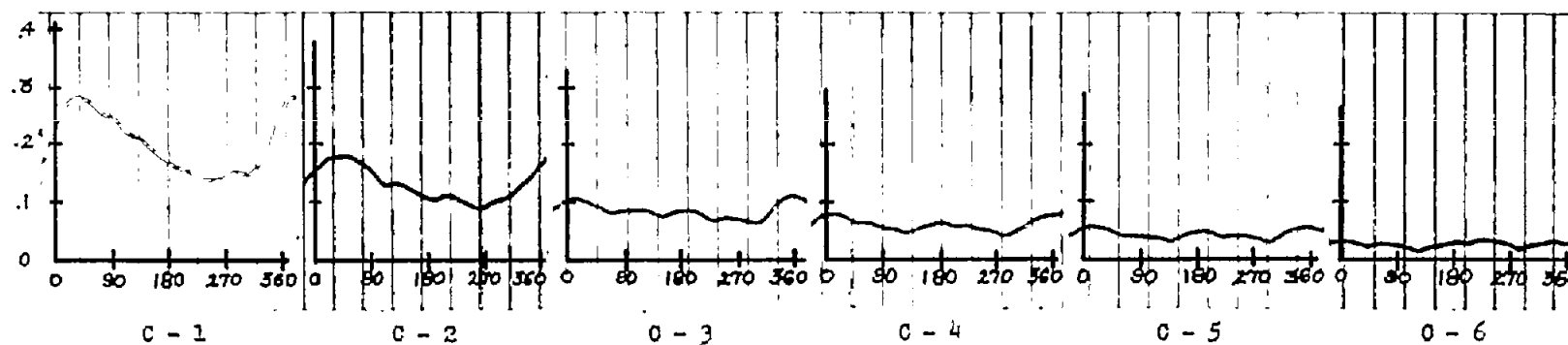


(a) Span station A; $r/R = 0.325$.

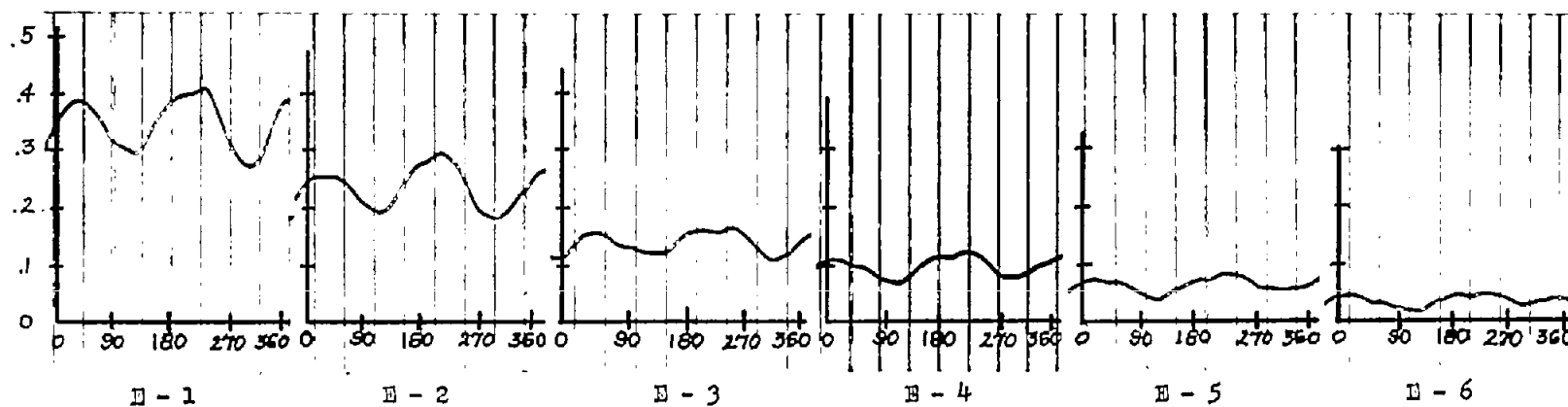


(b) Span station B; $r/R = 0.460$.

Figure 61.- Pressure difference in pounds per square inch against azimuth in degrees. Profile, NACA 0015; speed, 800 rpm; $\xi = 0$; $\mu = 0.10$; $A_0 = 8^\circ$; $\alpha = 0^\circ$.

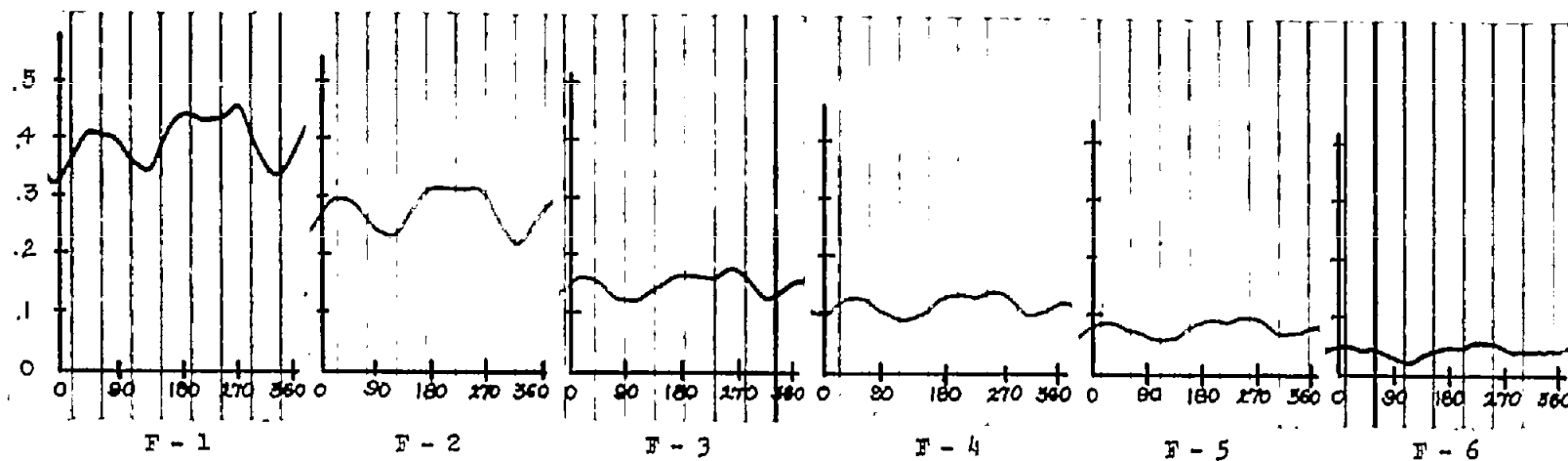


(c) Span station C; $r/R = 0.590$.

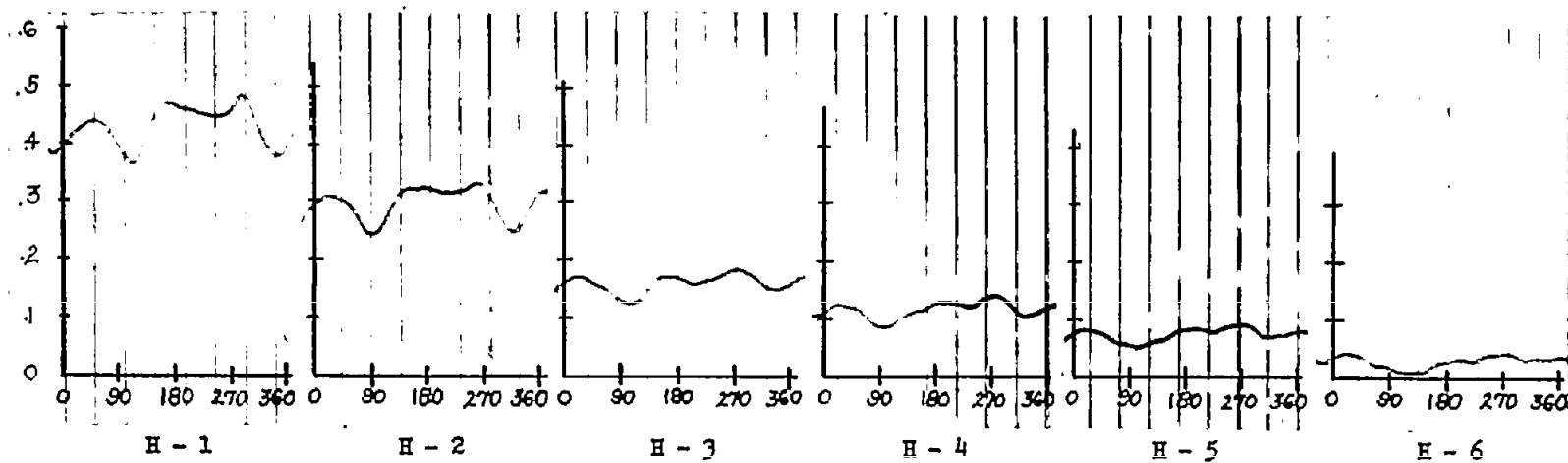


(d) Span station E; $r/R = 0.725$.

Figure 61.- Continued.

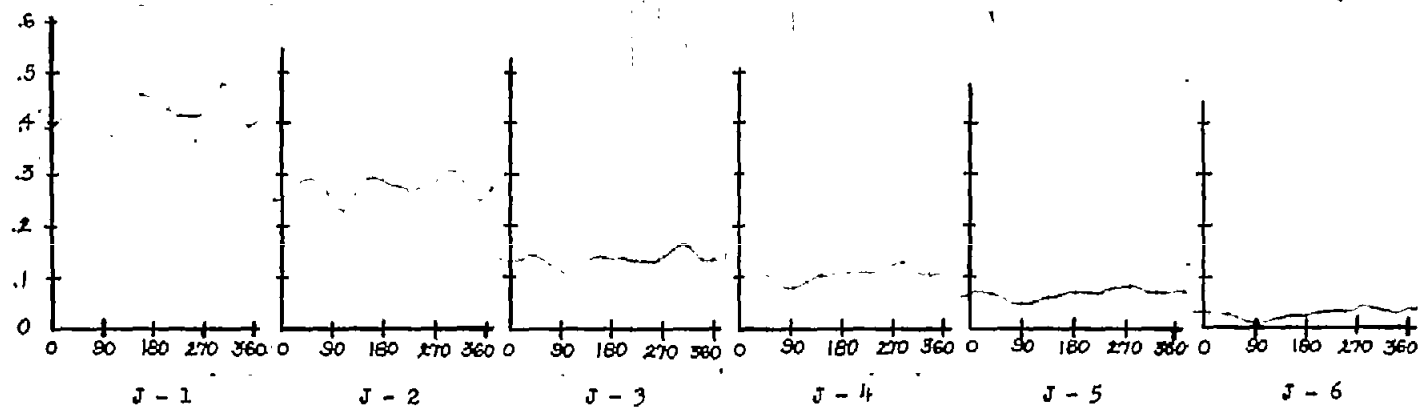


(e) Span station F; $r/R = 0.790$.

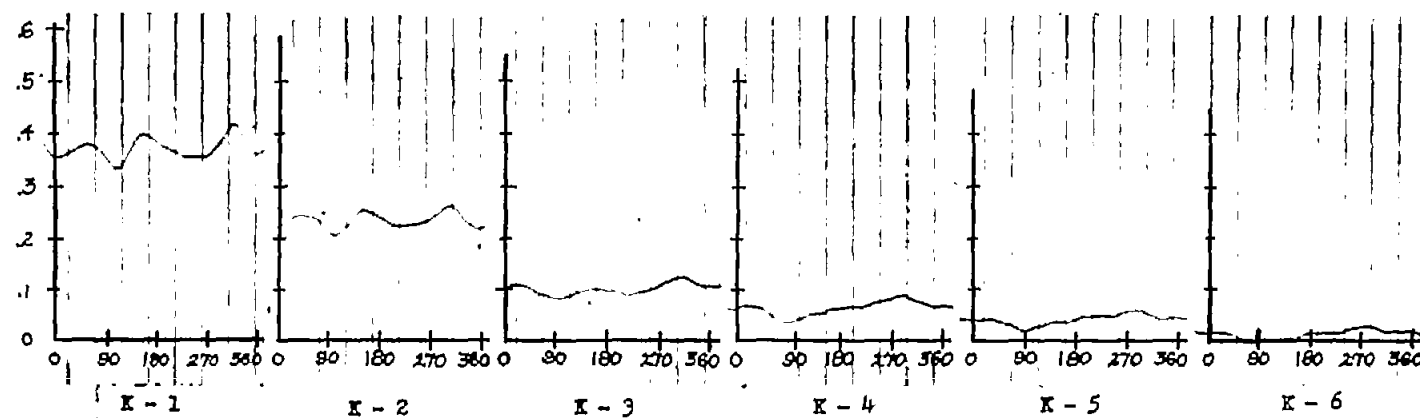


(f) Span station H; $r/R = 0.860$.

Figure 61.- Continued.

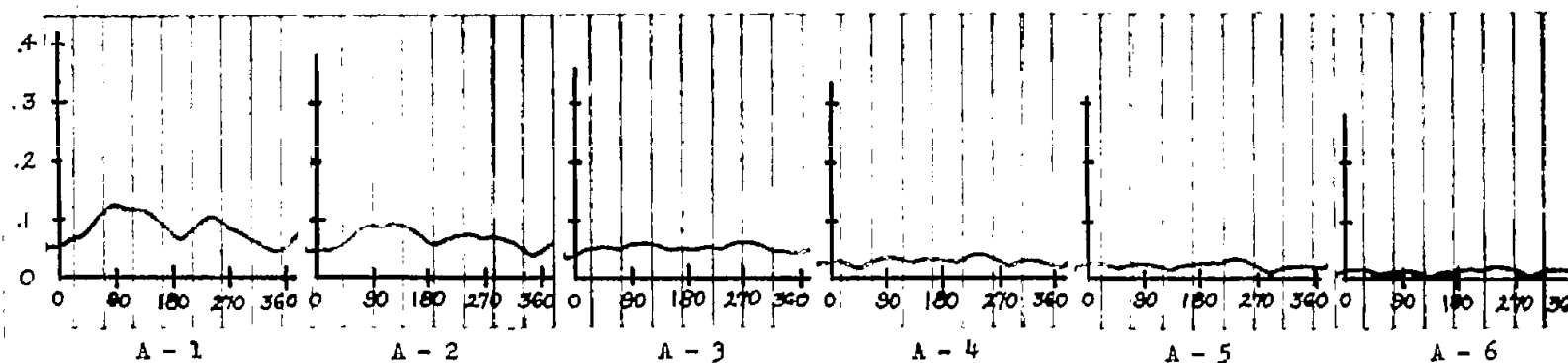


(g) Span station J; $r/R = 0.925$.

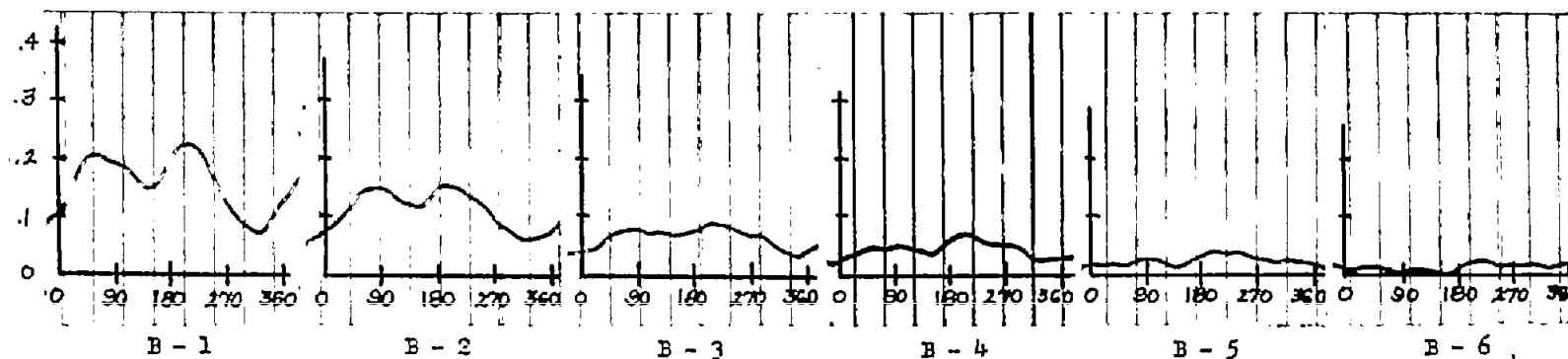


(h) Span station K; $r/R = 0.960$.

Figure 61.- Concluded.

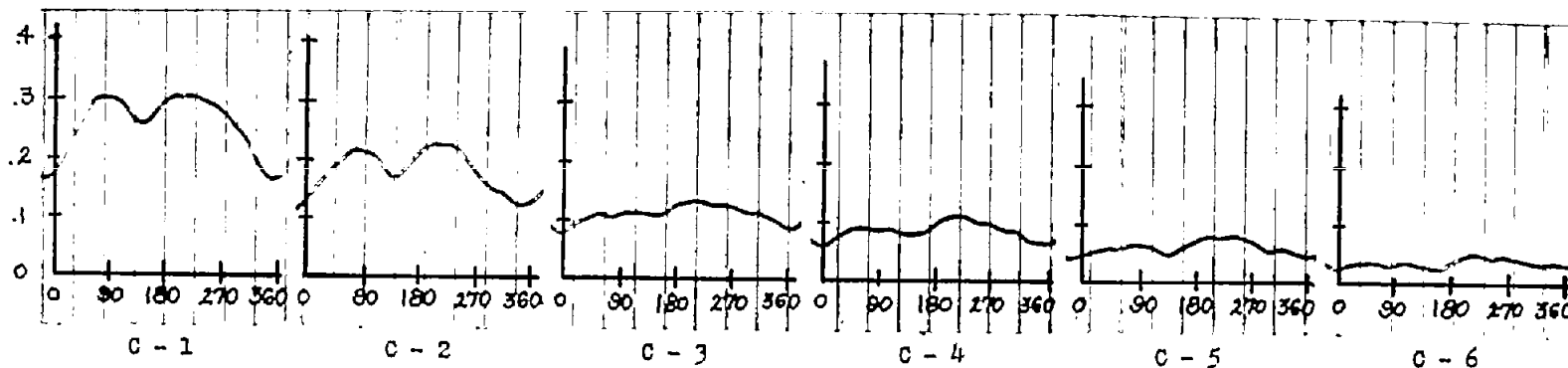


(a) Span station A; $r/R = 0.325$.

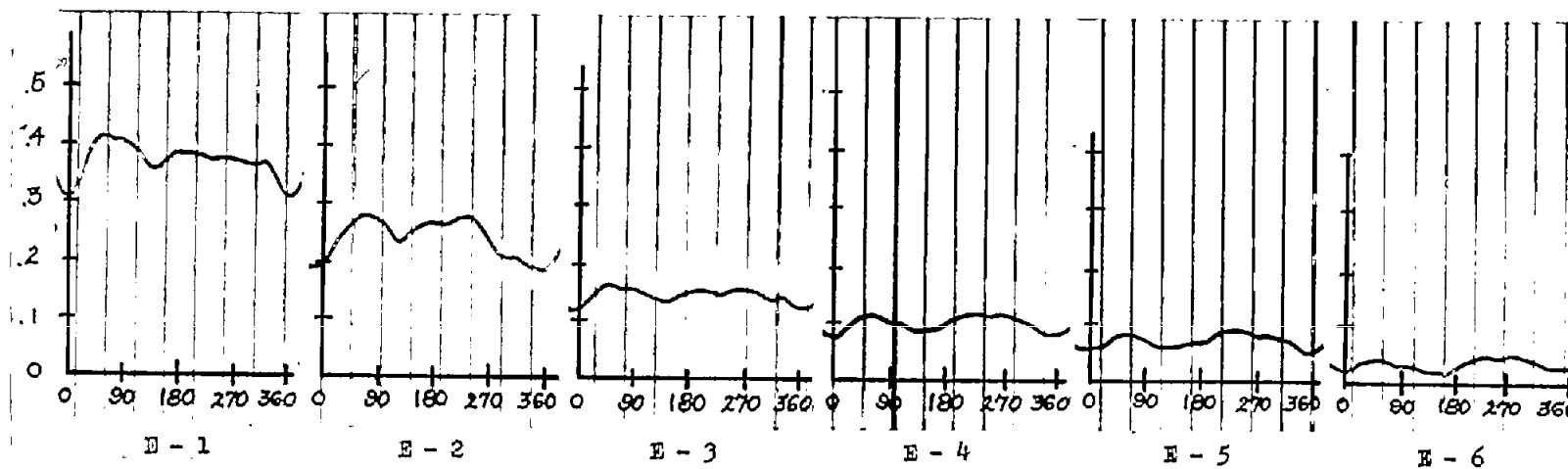


(b) Span station B; $r/R = 0.460$.

Figure 62.- Pressure difference in pounds per square inch against azimuth in degrees. Profile, NACA 0015; speed, 800 rpm; $\xi = 0$; $\mu = 0.20$; $A_0 = 8^\circ$; $\alpha = 0^\circ$.

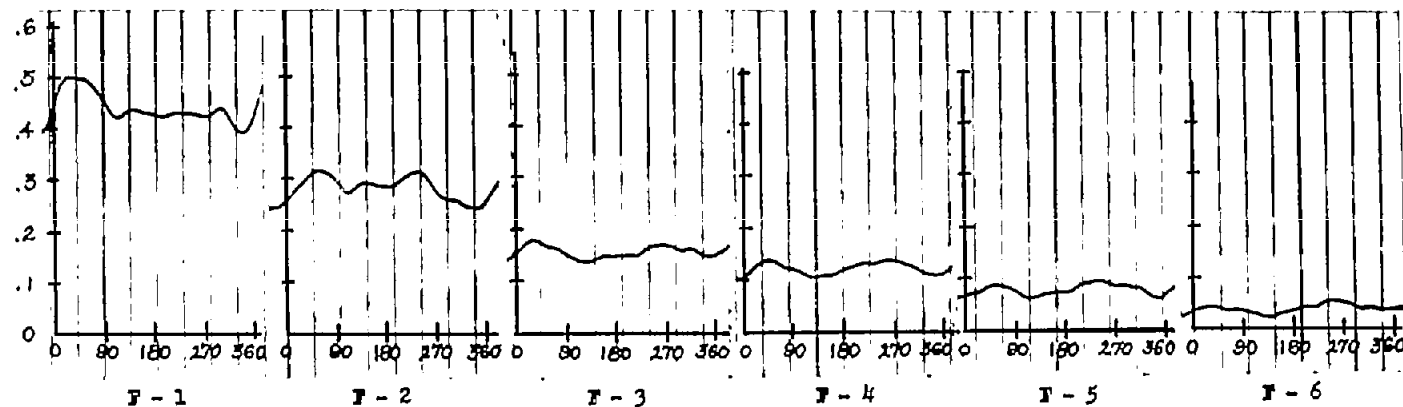


(c) Span station C; $r/R = 0.590$.

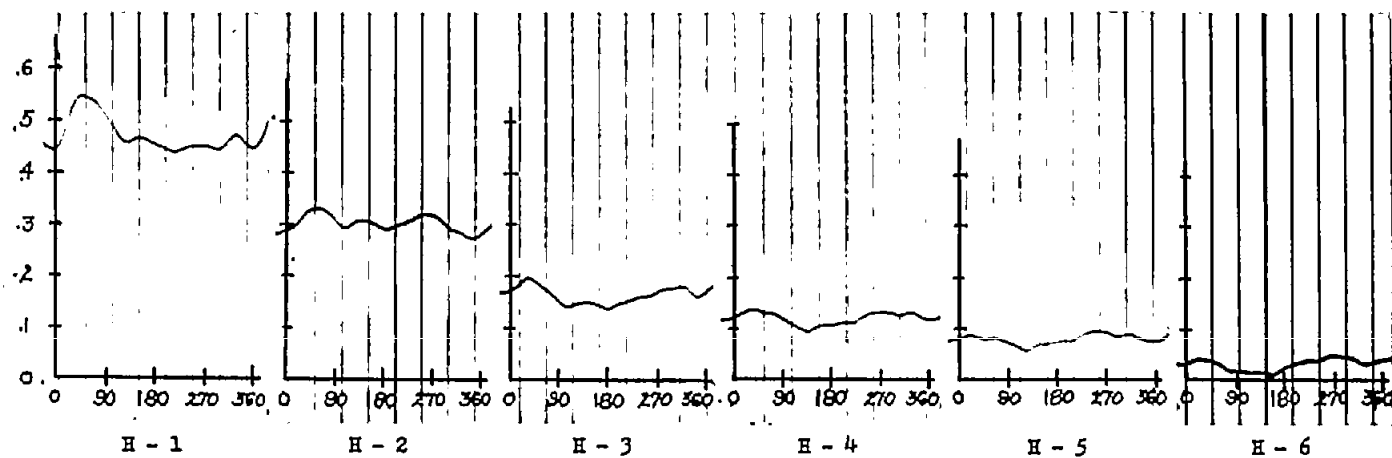


(d) Span station E; $r/R = 0.725$.

Figure 62.- Continued.

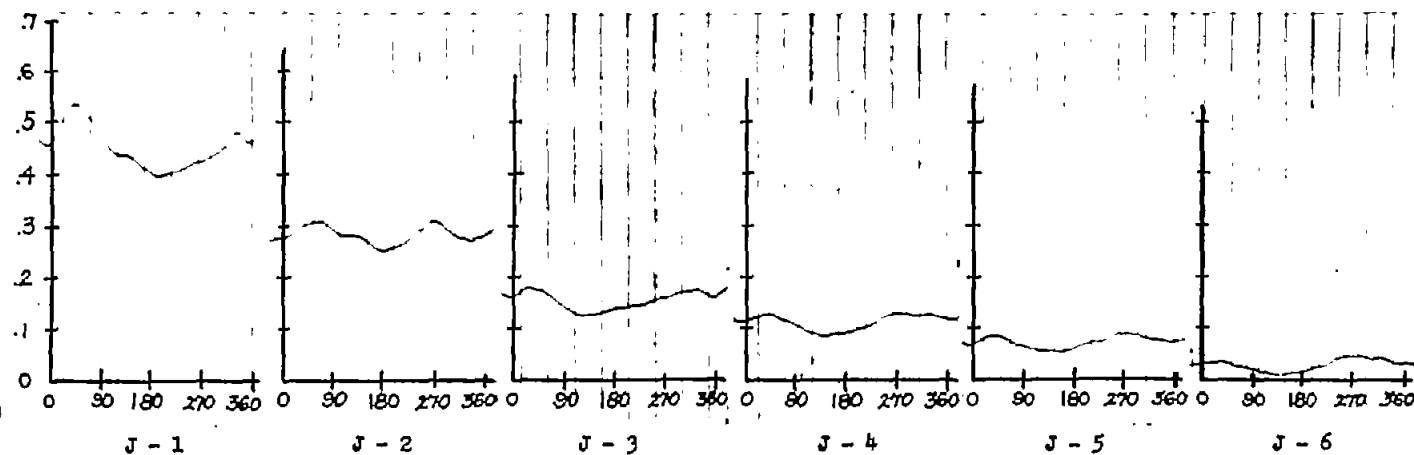


(e) Span station F; $r/R = 0.790$.

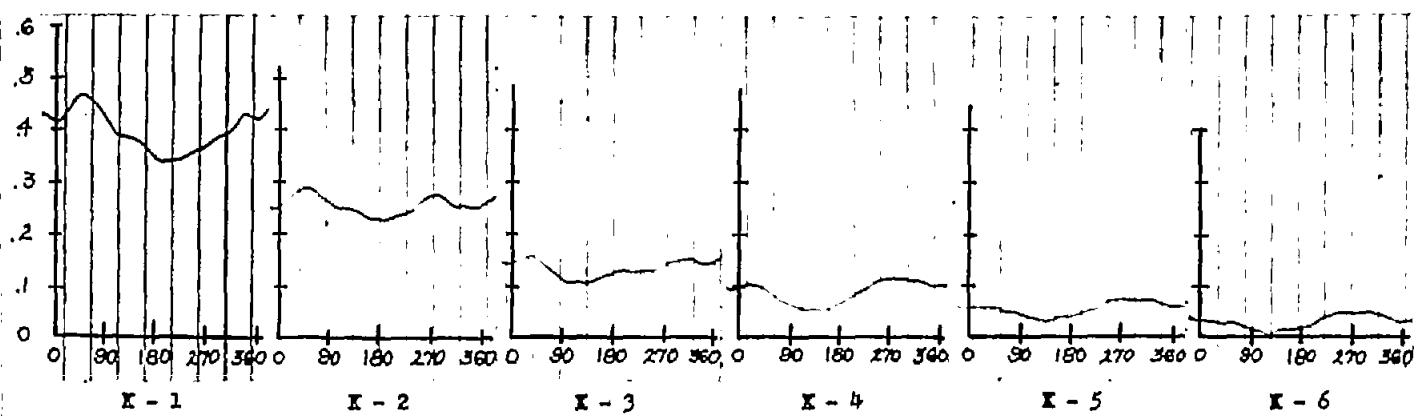


(f) Span station H; $r/R = 0.860$.

Figure 62.- Continued.

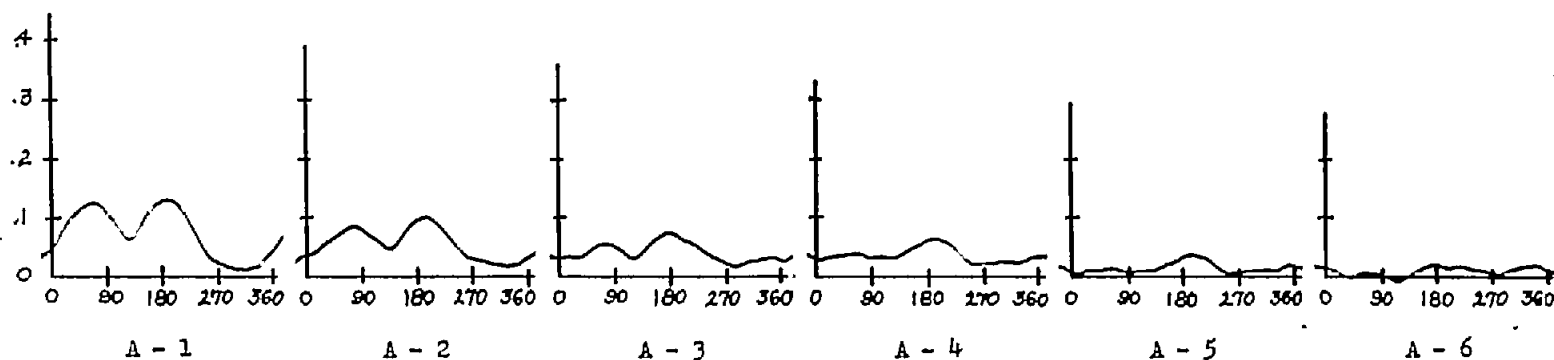


(g) Span station J; $r/R = 0.925$.

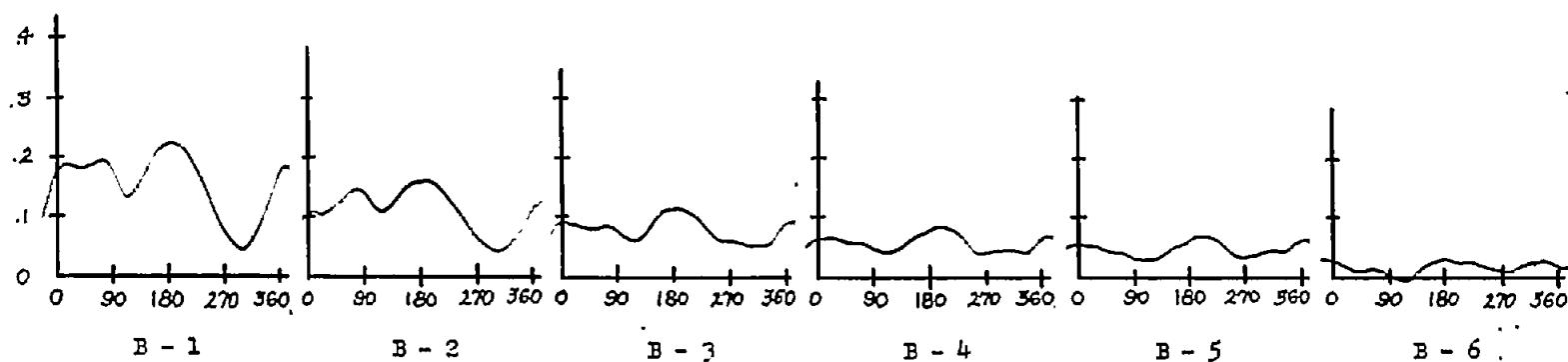


(h) Span station K; $r/R = 0.960$.

Figure 62.- Concluded.

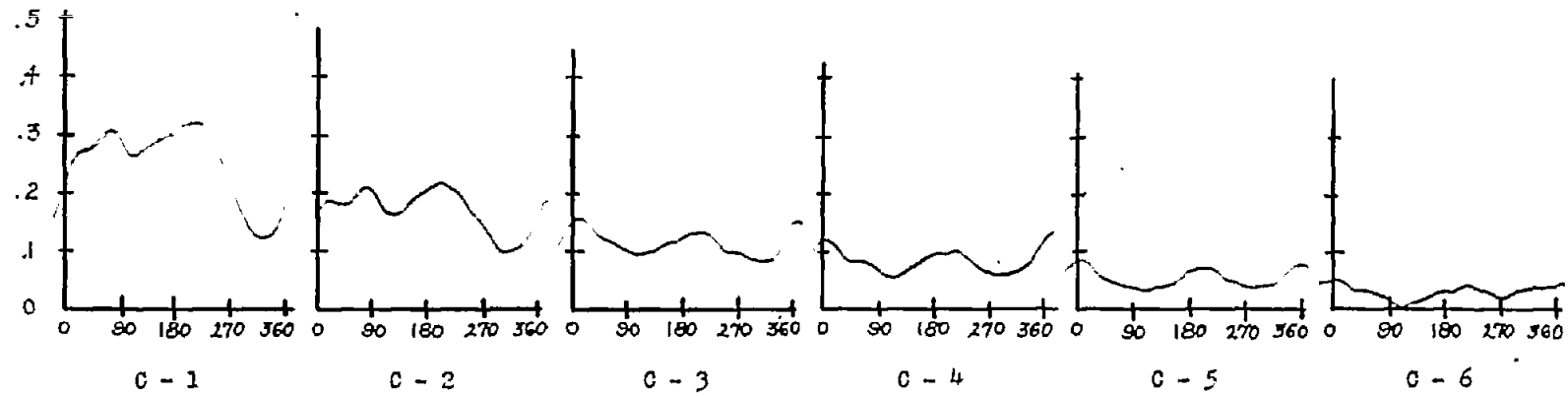


(a) Span station A; $r/R = 0.325$.

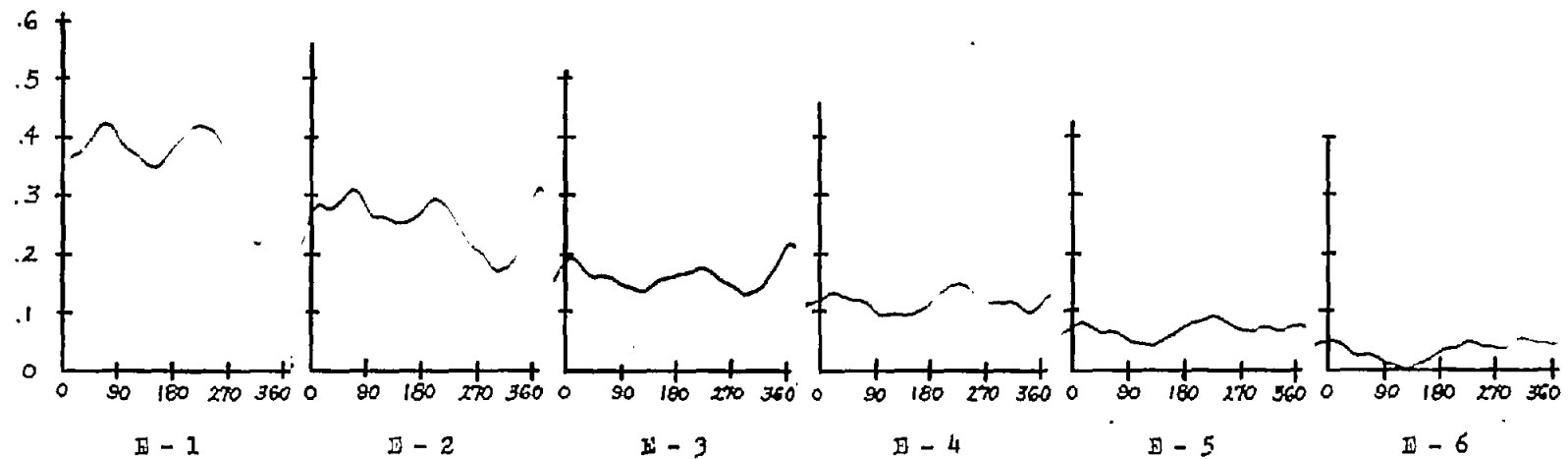


(b) Span station B; $r/R = 0.460$.

Figure 63.- Pressure difference in pounds per square inch against azimuth in degrees. Profile, NACA 0015; speed, 800 rpm; $\xi = 0$; $\mu = 0.30$; $A_0 = 12^\circ$; $\alpha = -10^\circ$.

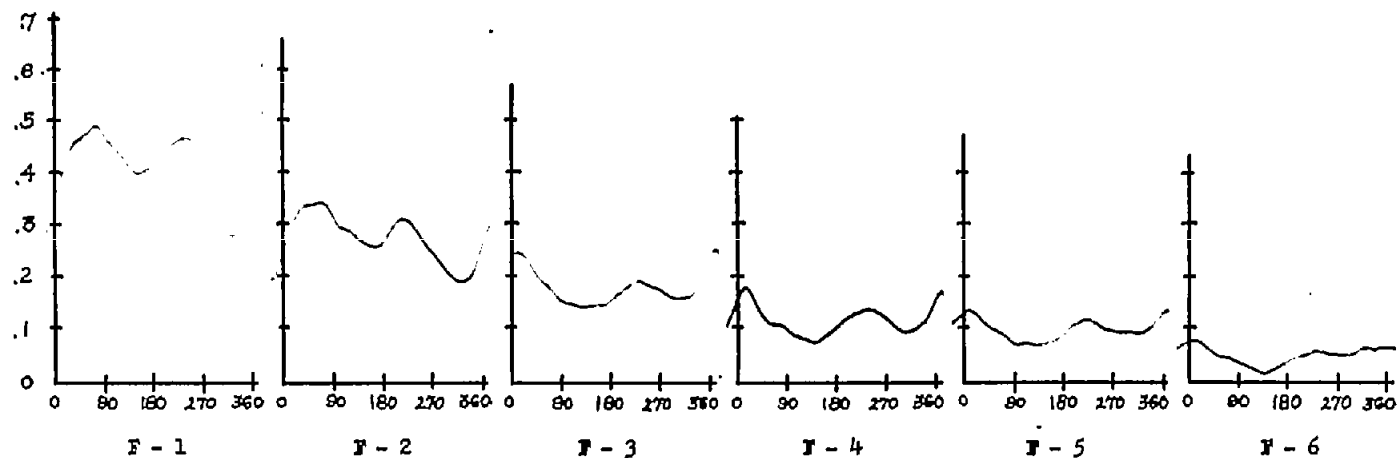


(c) Span station C; $r/R = 0.590$.

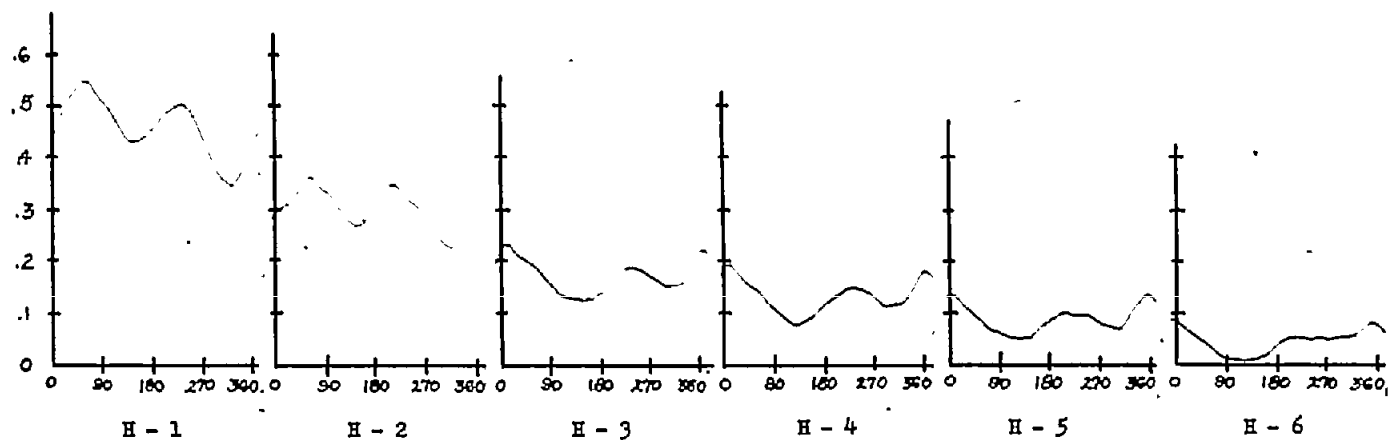


(d) Span station E; $r/R = 0.725$.

Figure 63.- Continued.

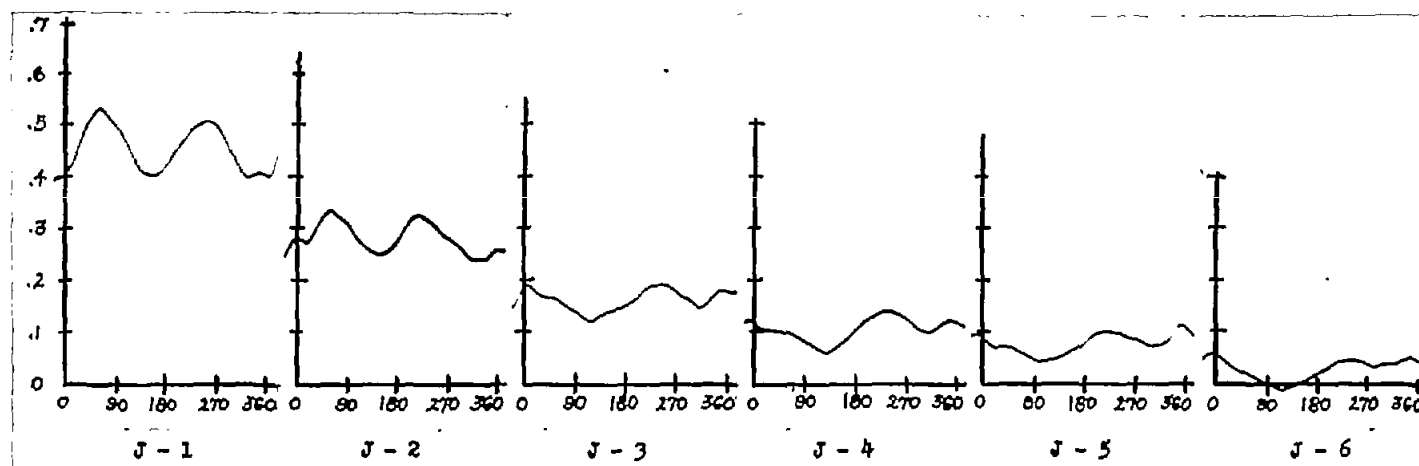


(e) Span station F; $r/R = 0.790$.

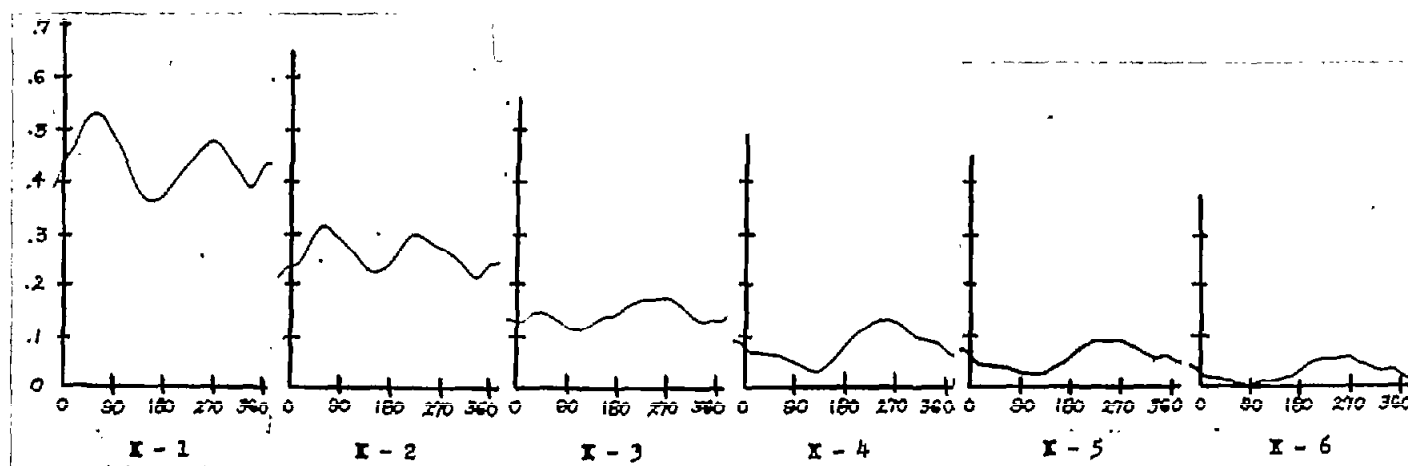


(f) Span station H; $r/R = 0.860$.

Figure 63.- Continued.

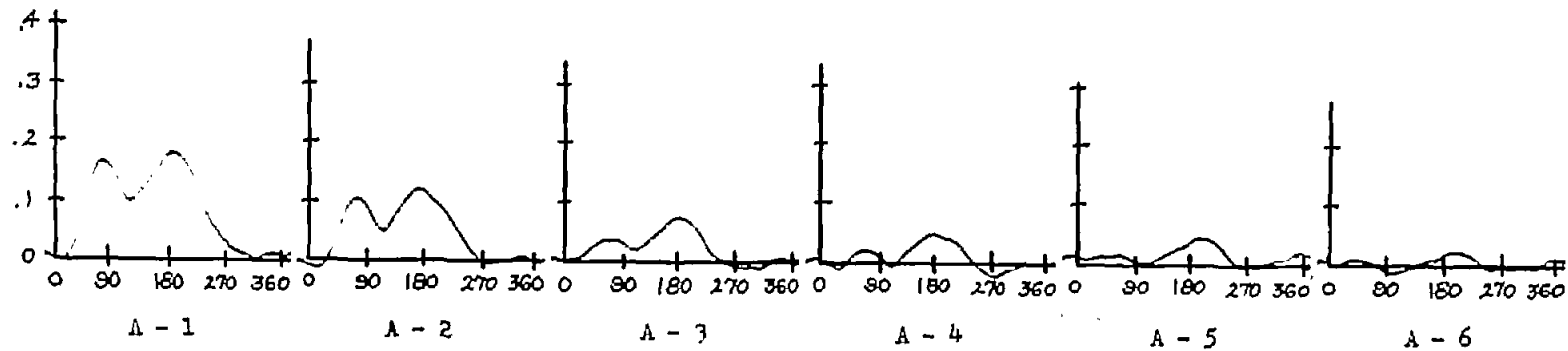


(g) Span station J; $r/R = 0.925$.

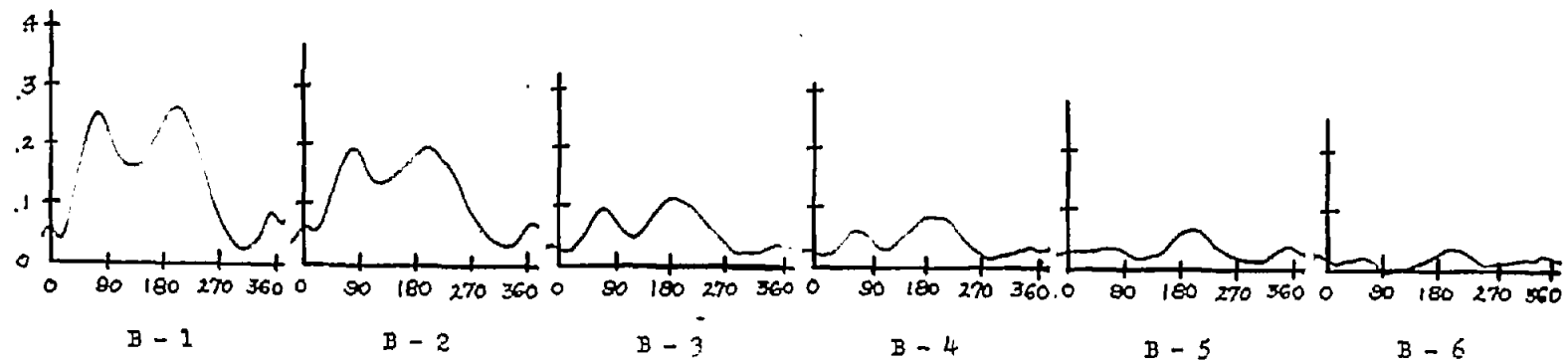


(h) Span station K; $r/R = 0.960$.

Figure 63.- Concluded.

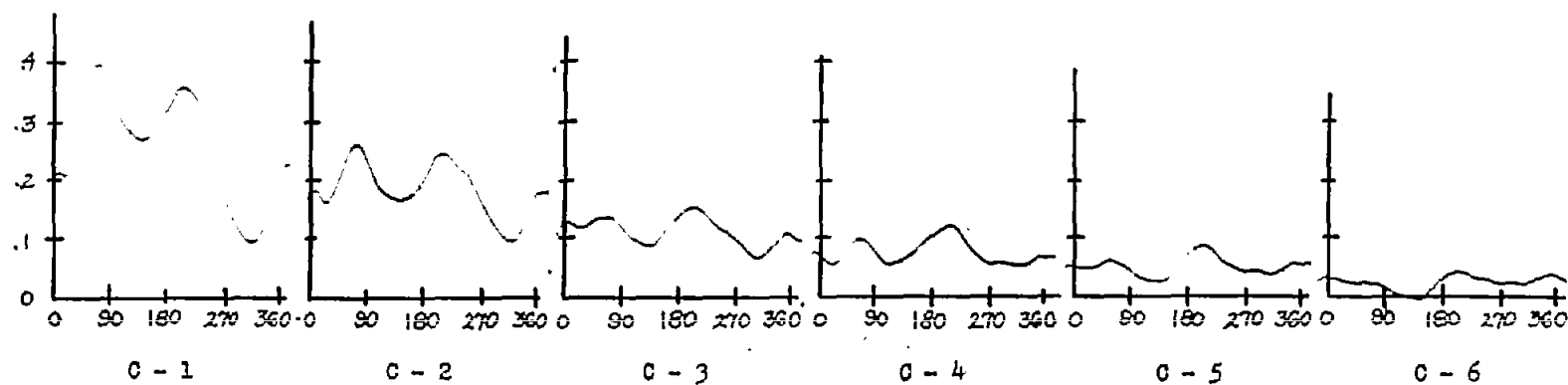


(a) Span station A; $r/R = 0.325$.

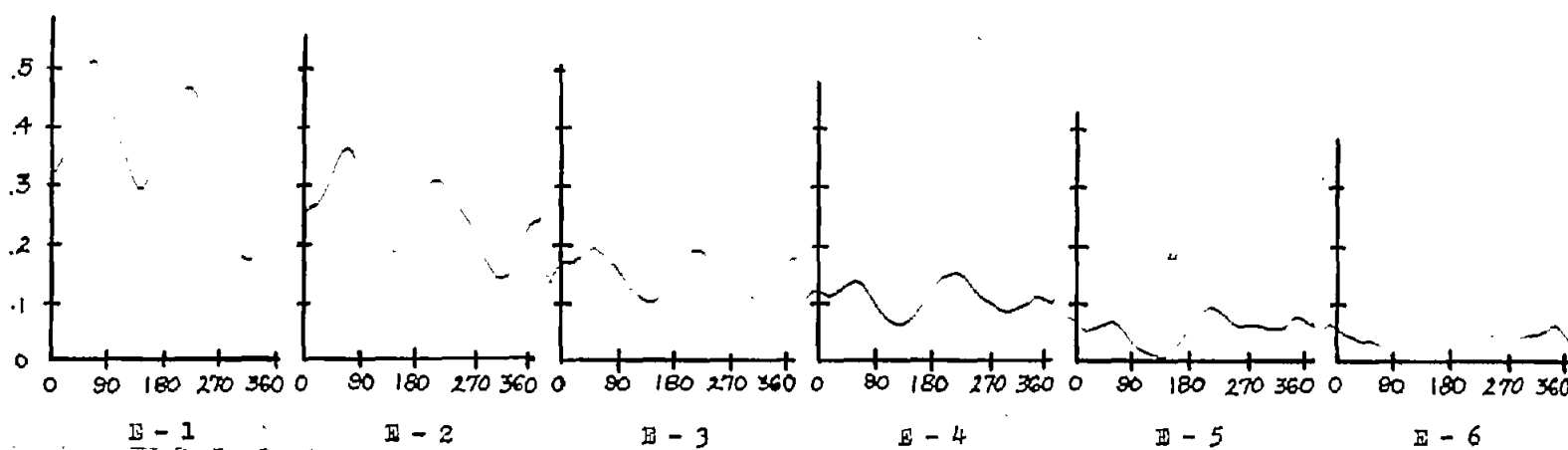


(b) Span station B; $r/R = 0.460$.

Figure 64.- Pressure difference in pounds per square inch against azimuth in degrees. Profile, NACA 0015; speed, 800 rpm; $\xi = 0$; $\mu = 0.40$; $A_0 = 12^\circ$; $\alpha = -10^\circ$.

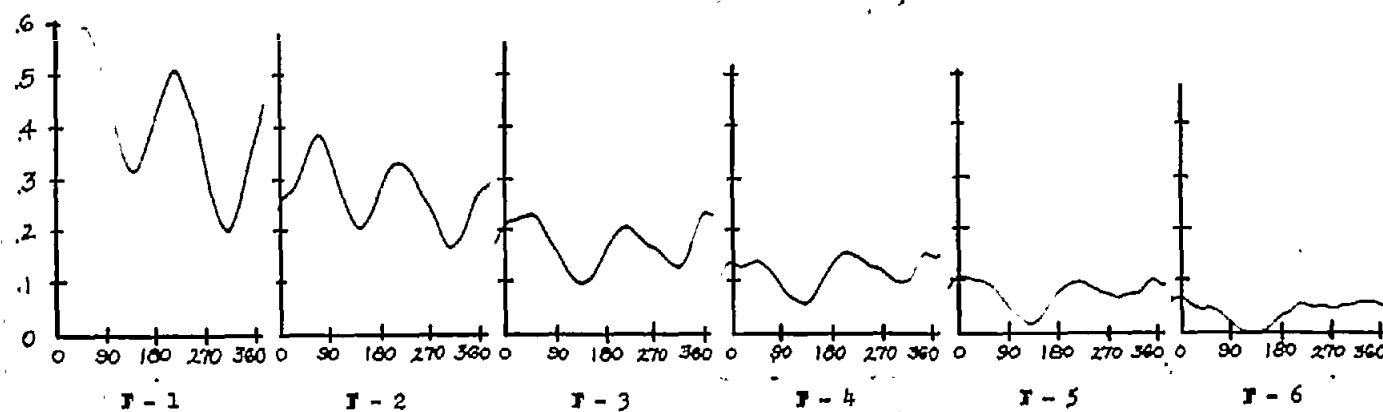


(c) Span station C; $r/R = 0.590$.

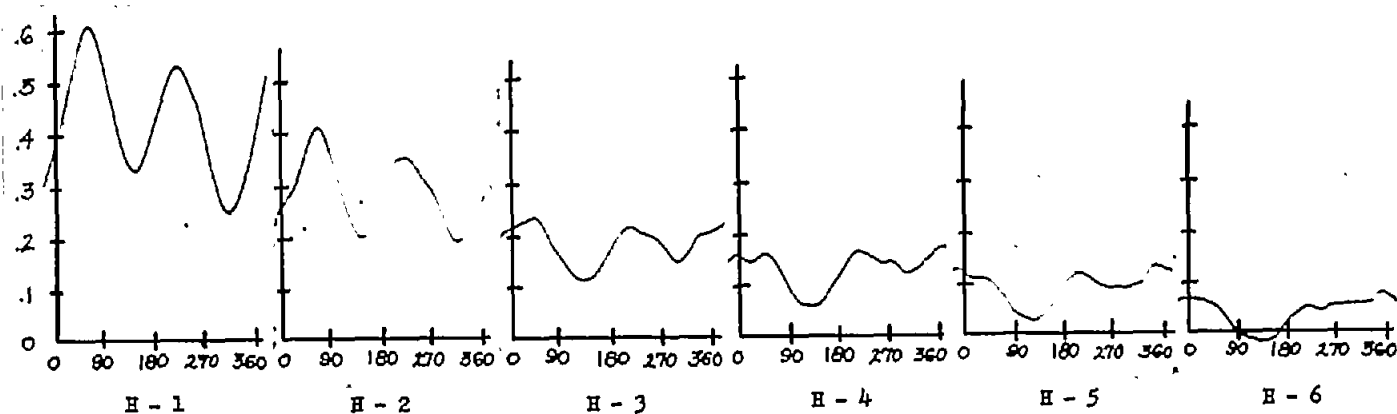


(d) Span station E; $r/R = 0.725$.

Figure 64.- Continued.

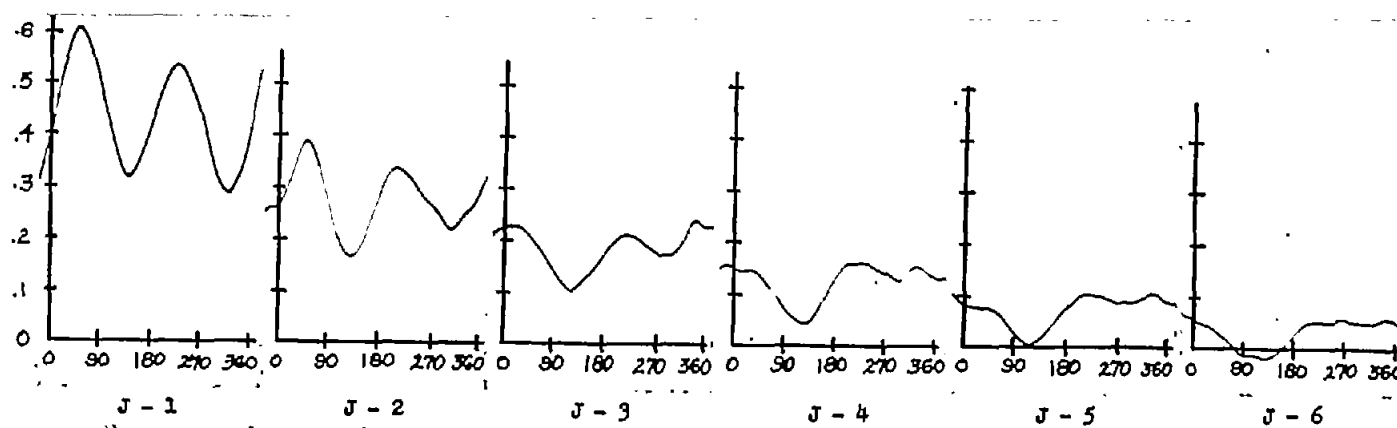


(e) Span station F; $r/R = 0.790$.

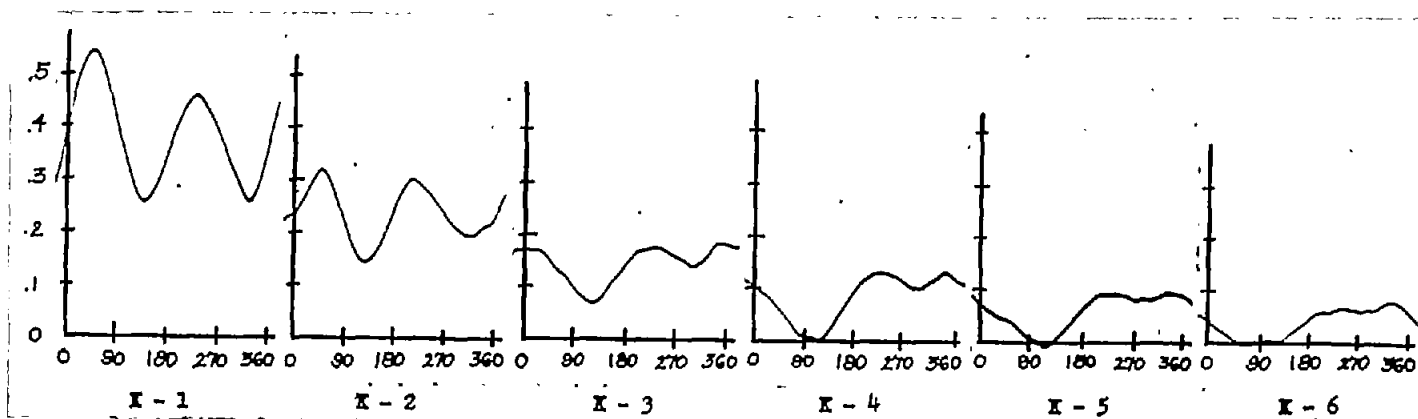


(f) Span station H; $r/R = 0.860$.

Figure 64.- Continued.

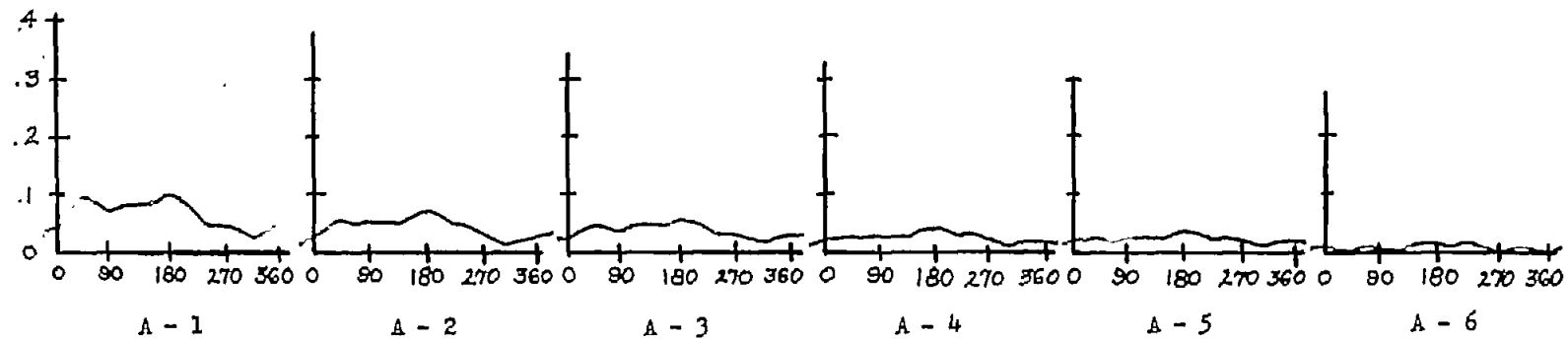


(g) Span station J; $r/R = 0.925$.



(h) Span station K; $r/R = 0.960$.

Figure 64.- Concluded.

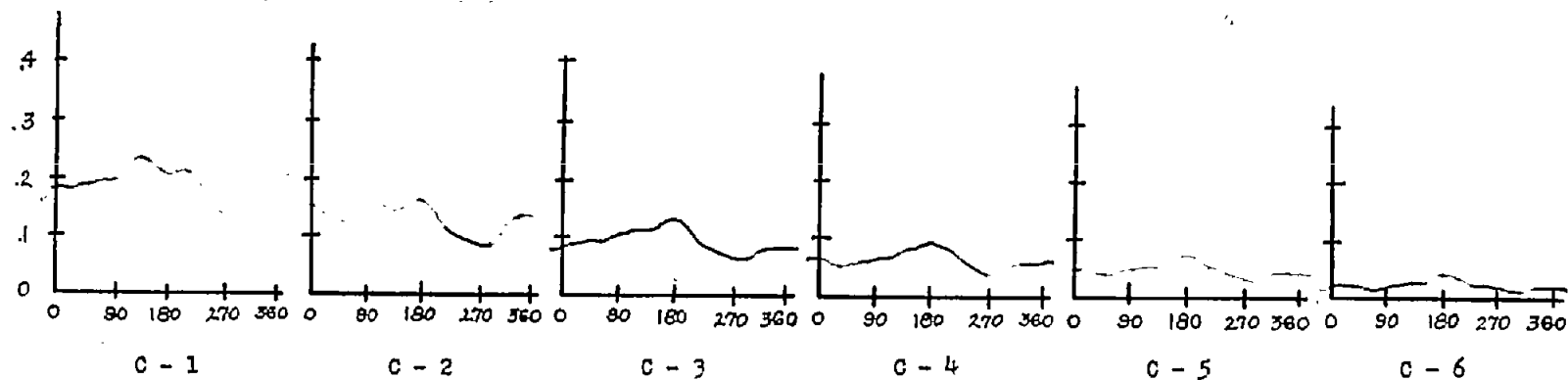


(a) Span station A; $r/R = 0.325$.

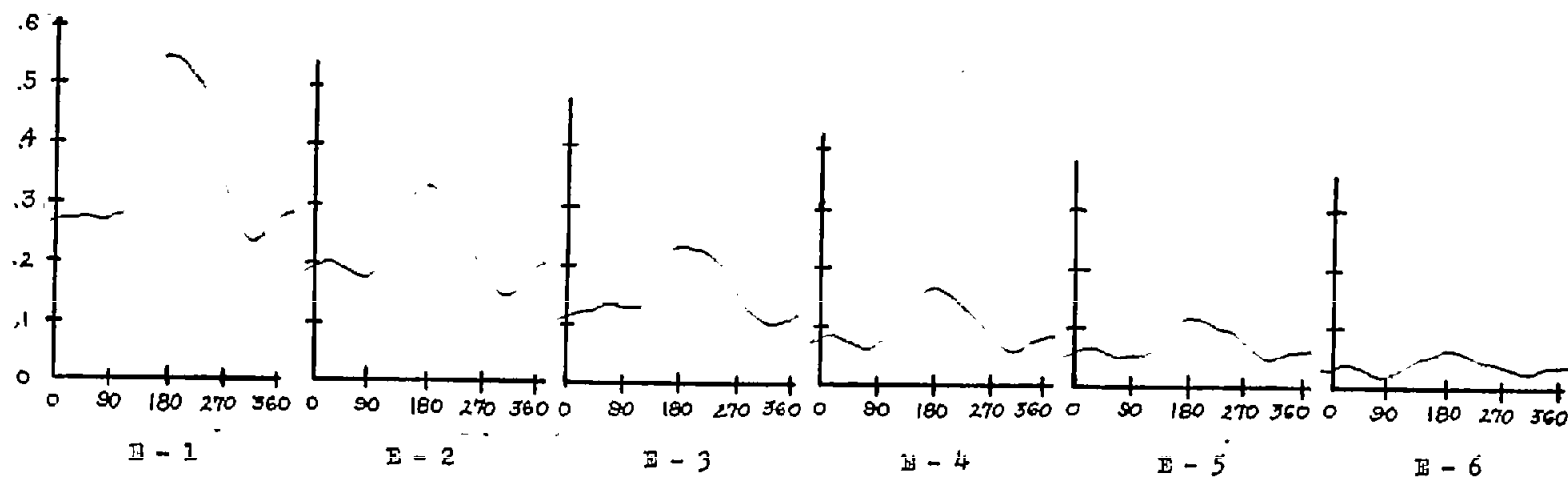


(b) Span station B; $r/R = 0.460$.

Figure 65.- Pressure difference in pounds per square inch against azimuth in degrees. Profile, NACA 0015; speed, 800 rpm; $\xi = 0.13$; $\mu = 0.10$; $A_0 = 8^\circ$; $\alpha = 0^\circ$.

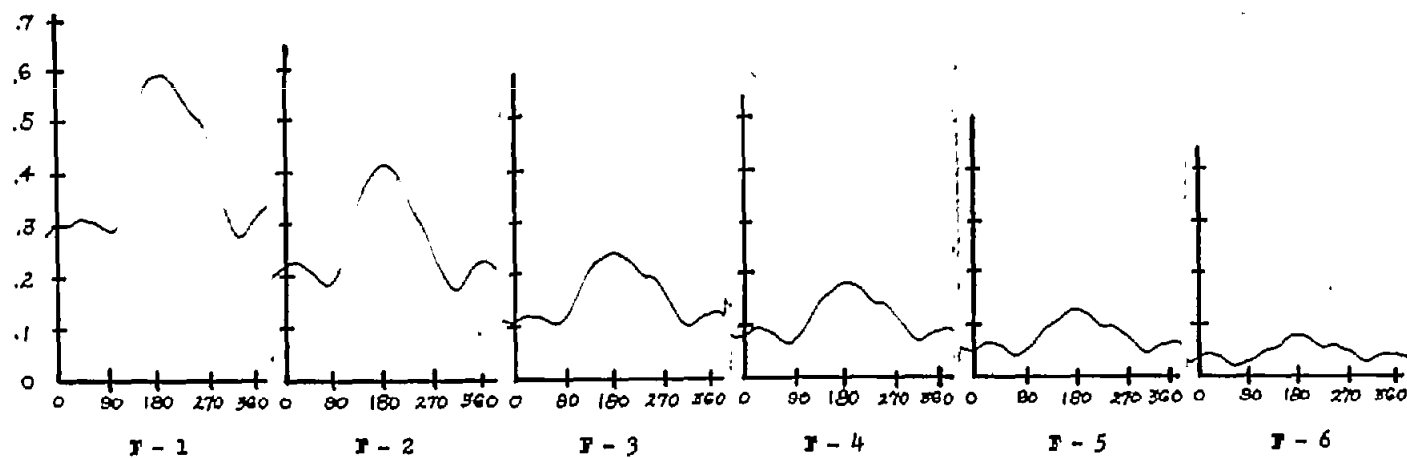


(c) Span station C; $r/R = 0.590$.

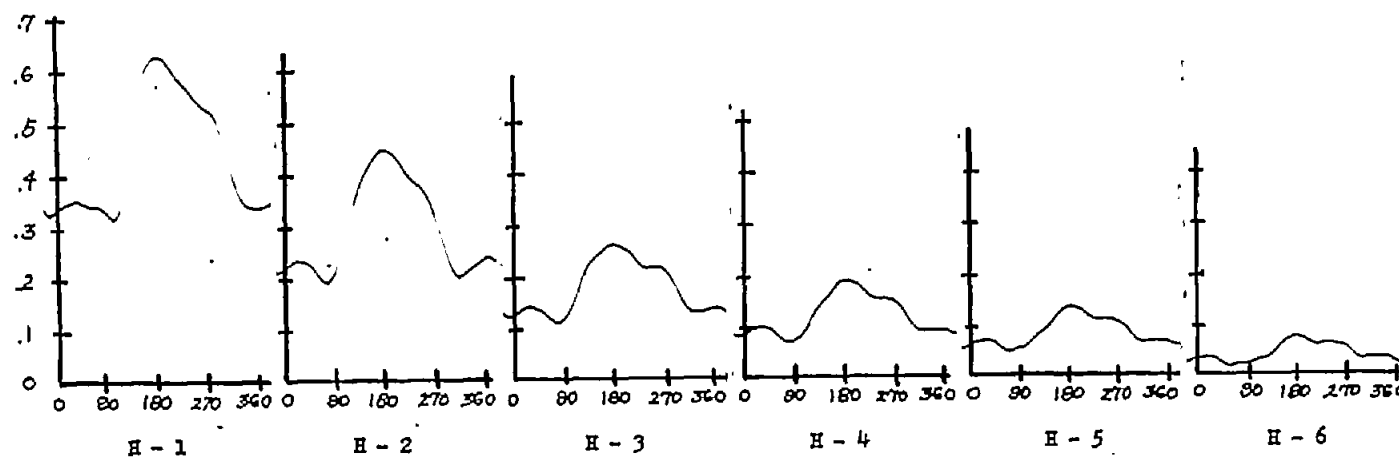


(d) Span station E; $r/R = 0.725$.

Figure 65.- Continued.

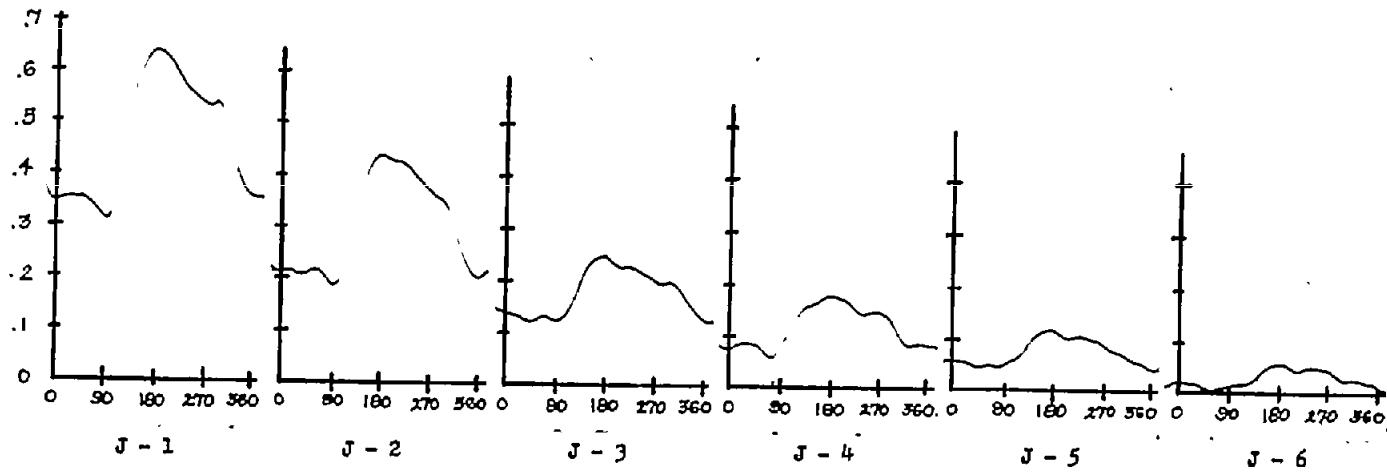


(e) Span station F; $r/R = 0.790$.

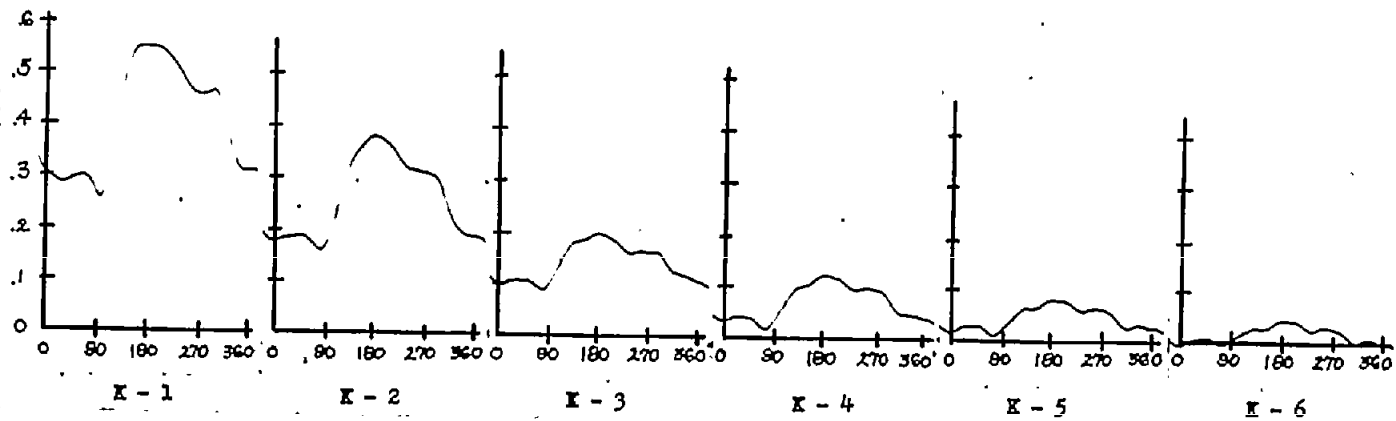


(f) Span station H; $r/R = 0.860$.

Figure 65.- Continued.

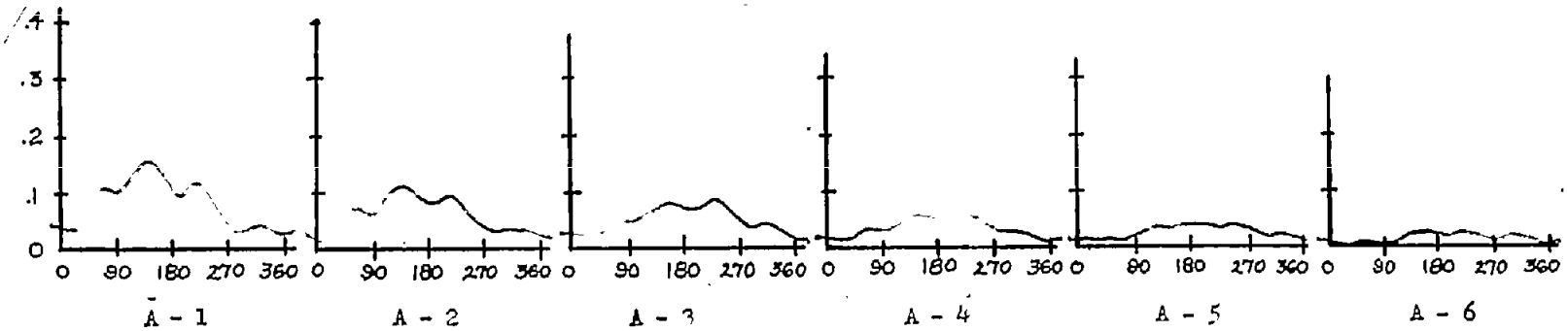


(g) Span station J; $r/R = 0.925$.

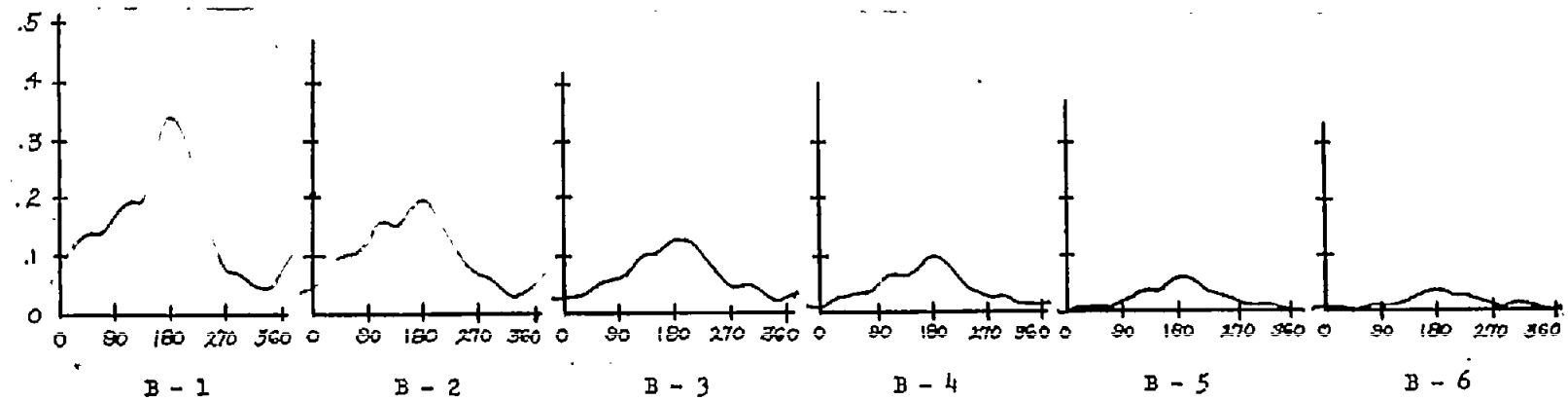


(h) Span station K; $r/R = 0.960$.

Figure 65.- Concluded.

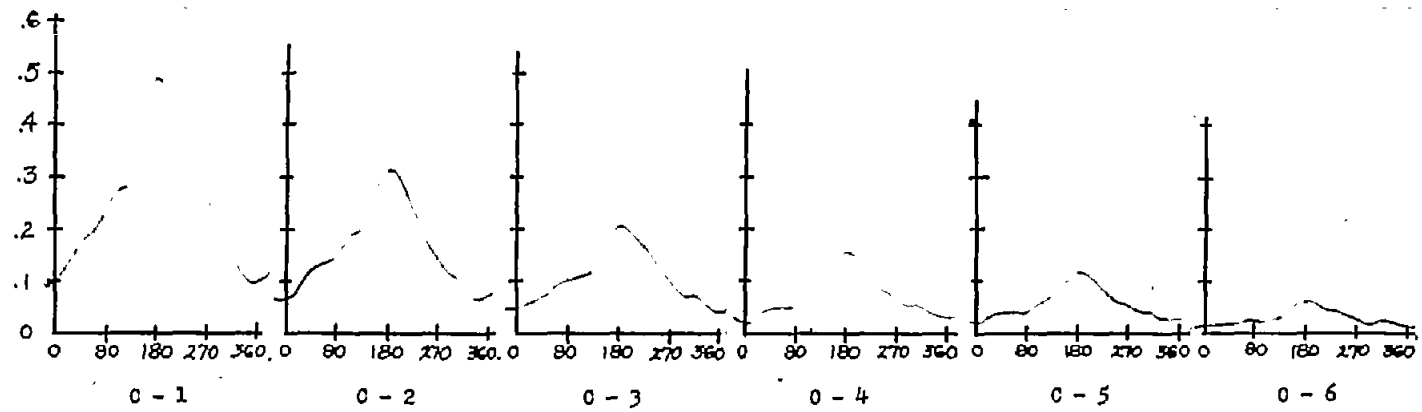


(a) Span station A; $r/R = 0.325$.

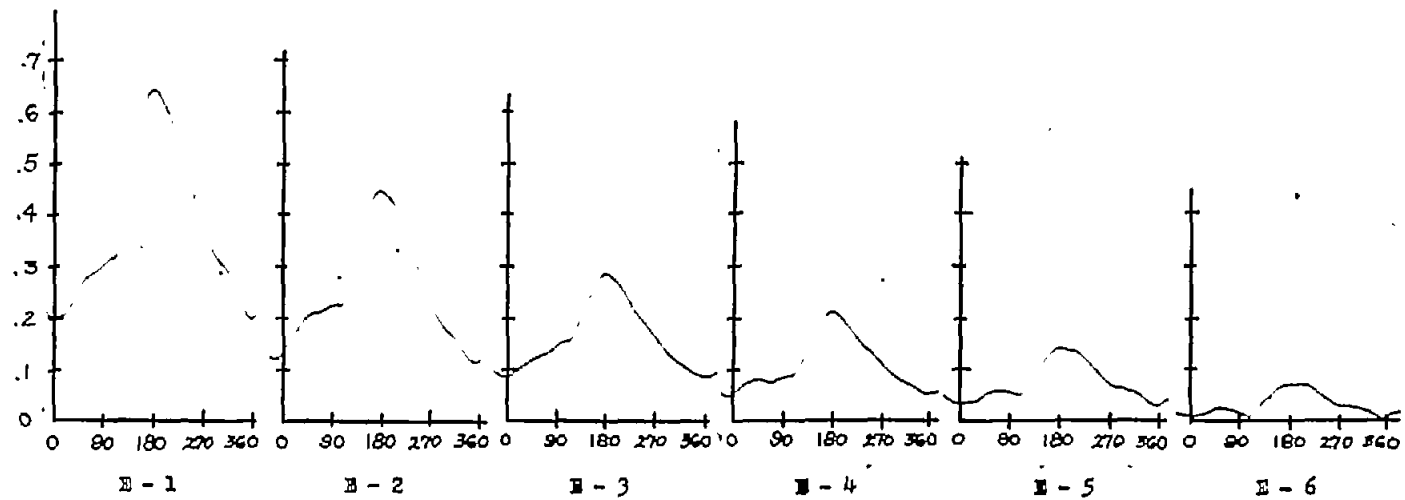


(b) Span station B; $r/R = 0.460$.

Figure 66.- Pressure difference in pounds per square inch against azimuth in degrees. Profile, NACA 0015; speed, 800 rpm; $\xi = 0.13$; $\mu = 0.20$; $A_0 = 8^\circ$; $\alpha = 0^\circ$.

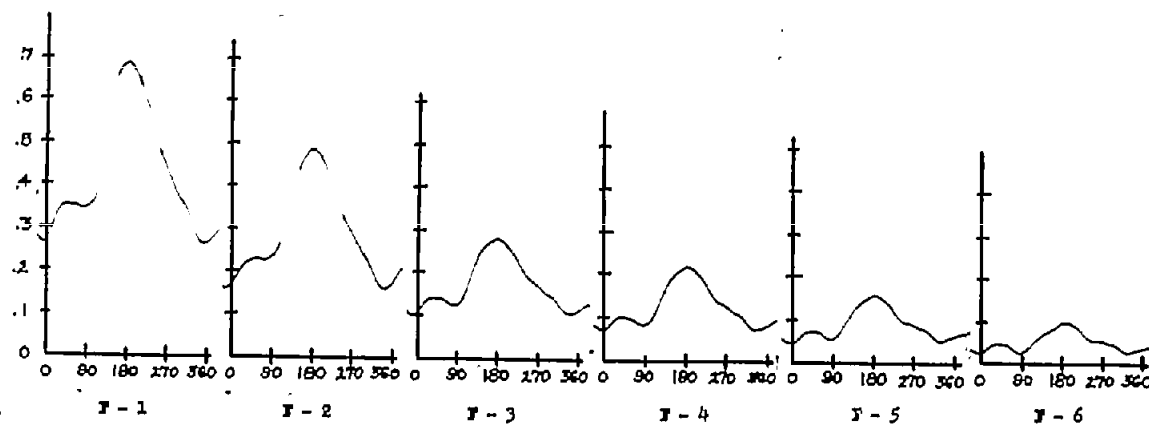


(c) Span station C; $r/R = 0.590$.

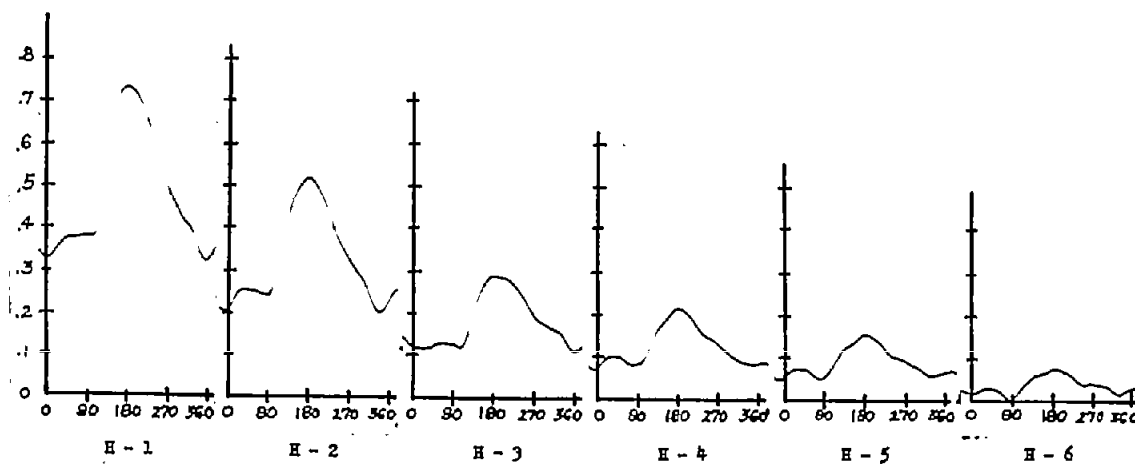


(d) Span station E; $r/R = 0.725$.

Figure 66.- Continued.

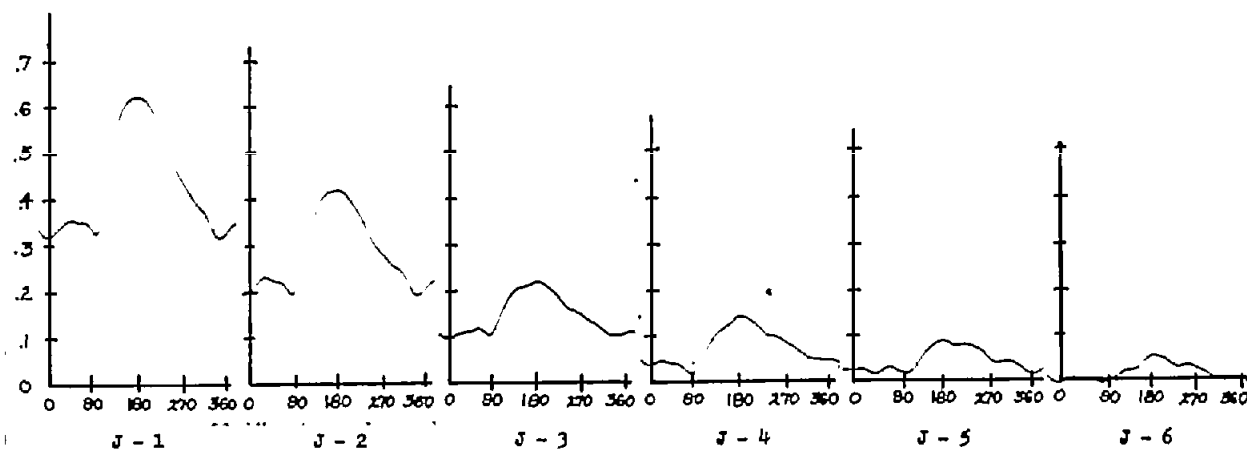


(e) Span station F; $r/R = 0.790$.

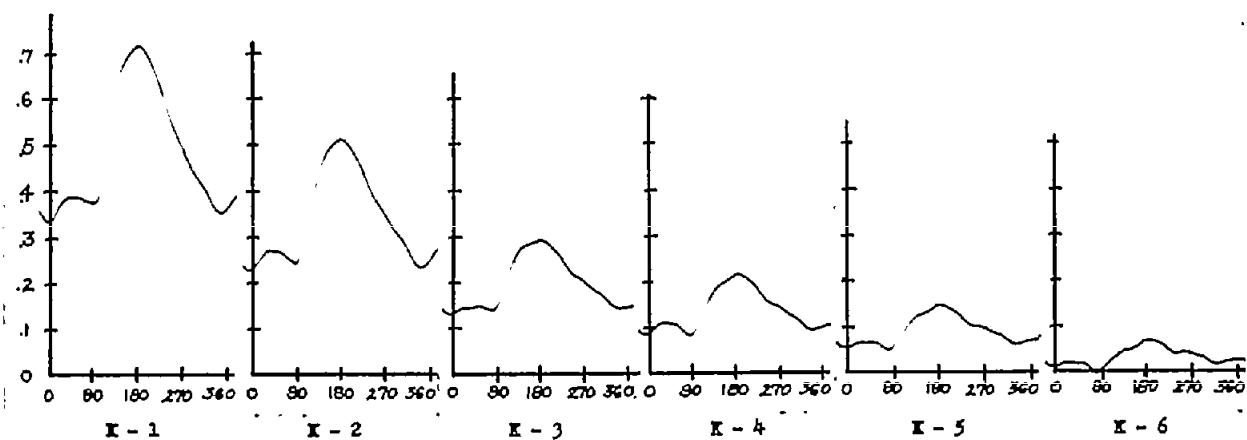


(f) Span station H; $r/R = 0.860$.

Figure 66.- Continued.

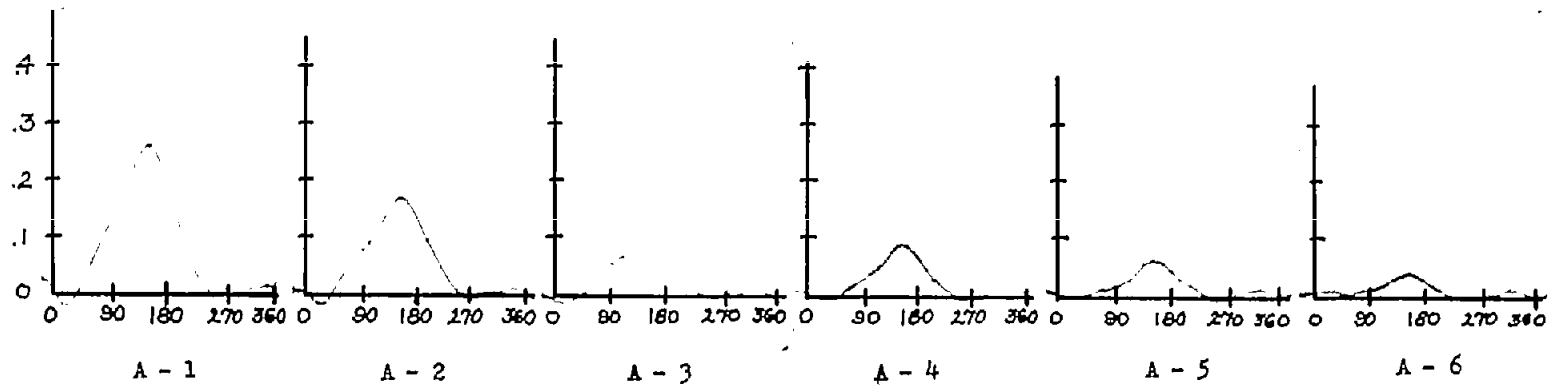


(g) Span station J; $r/R = 0.925$.

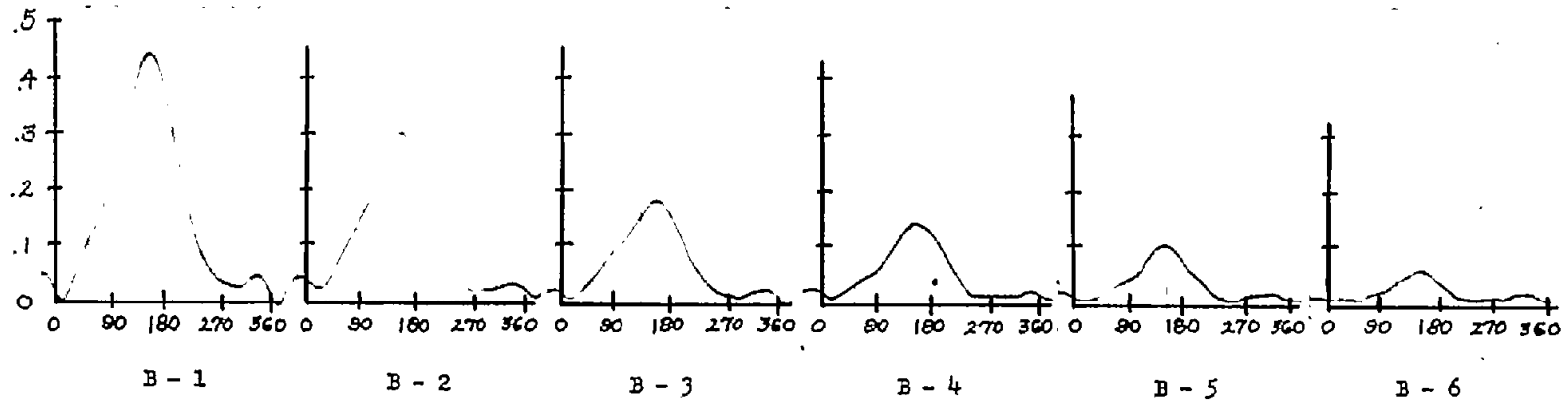


(h) Span station K; $r/R = 0.960$.

Figure 66.- Concluded.

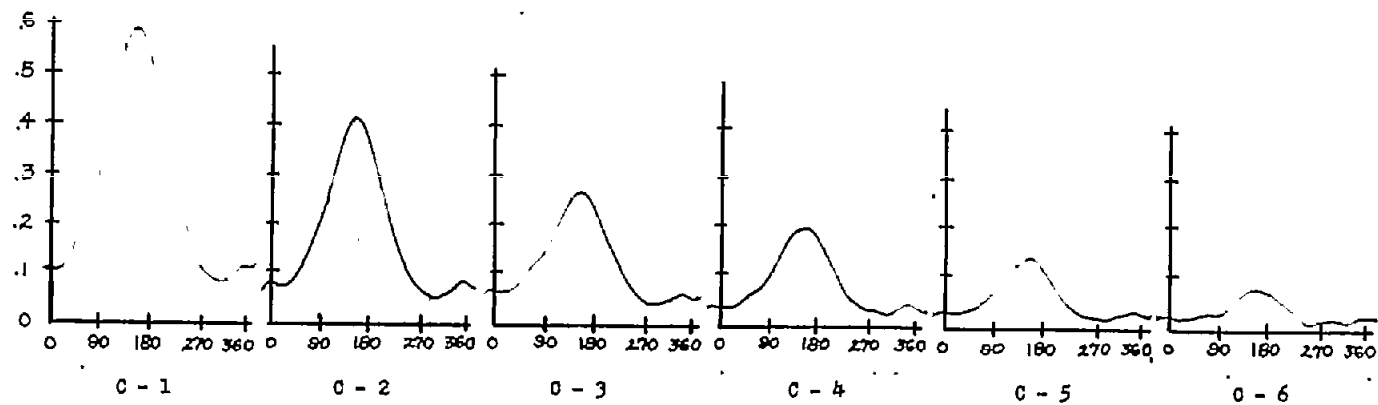


(a) Span station A; $r/R = 0.325$.

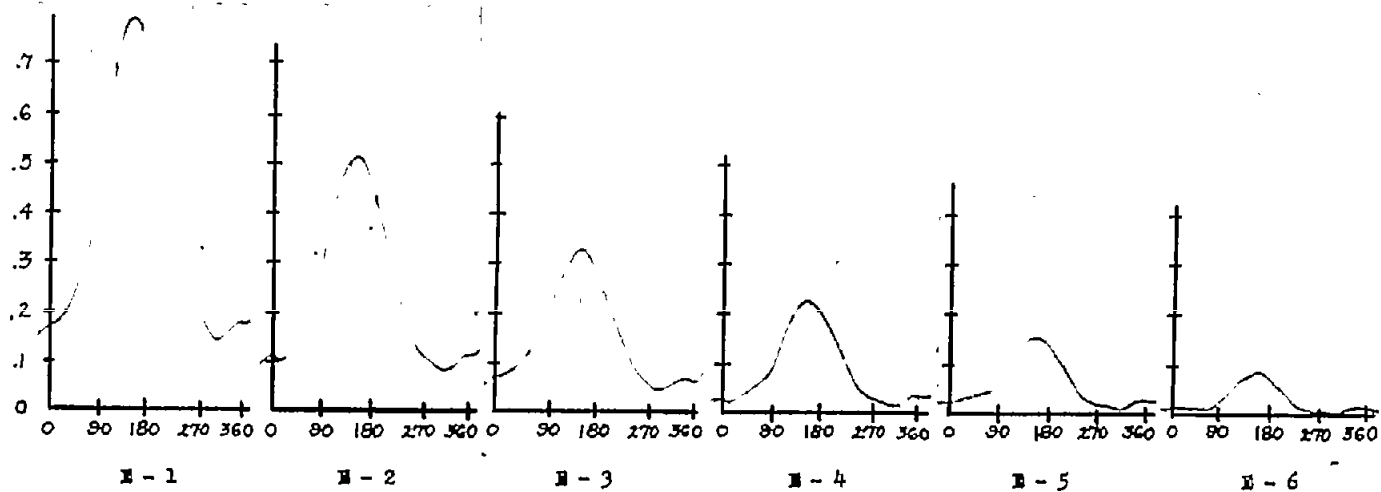


(b) Span station B; $r/R = 0.460$.

Figure 67.- Pressure difference in pounds per square inch against azimuth in degrees. Profile, NACA 0015; speed, 800 rpm; $\xi = 0.13$; $\mu = 0.30$; $A_0 = 12^\circ$; $\alpha = -10^\circ$.

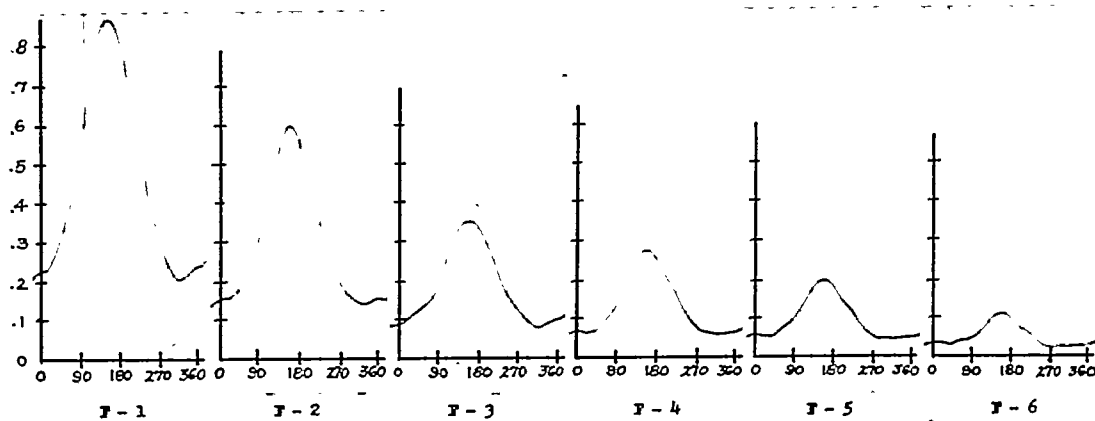


(c) Span station C; $r/R = 0.590$.

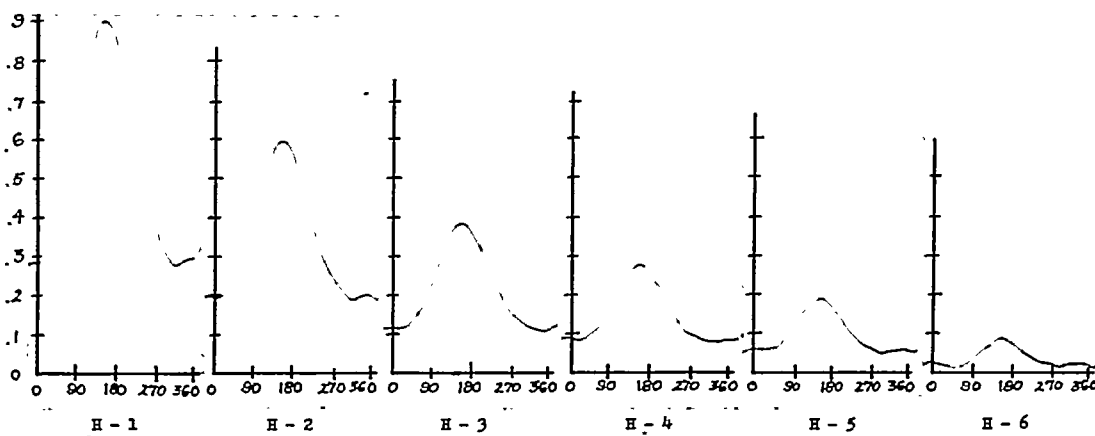


(d) Span station E; $r/R = 0.725$.

Figure 67.- Continued.

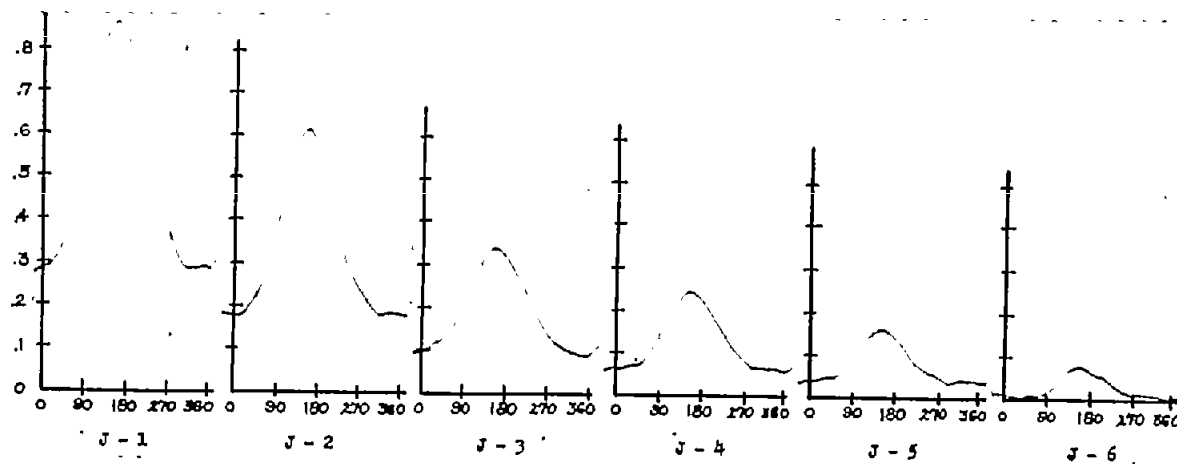


(e) Span station F; $r/R = 0.790$.

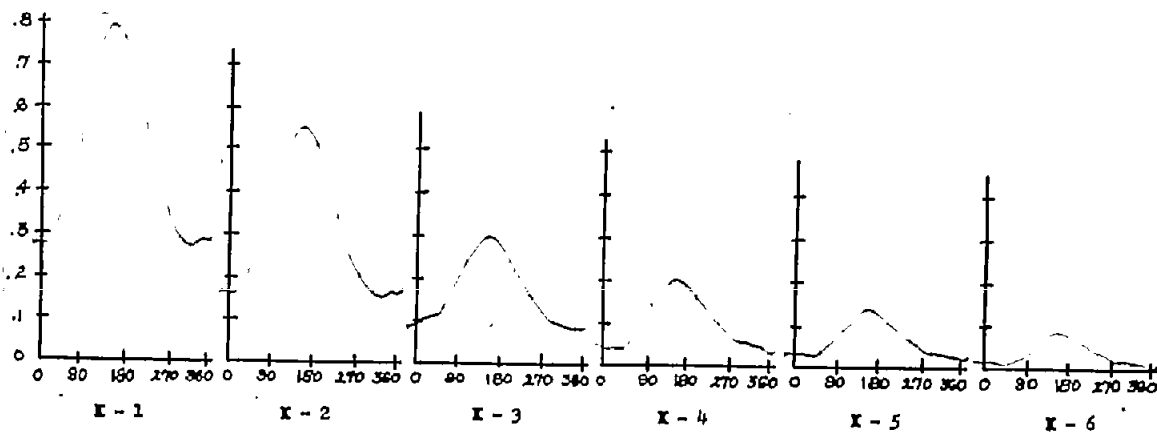


(f) Span station H; $r/R = 0.860$.

Figure 67.- Continued.

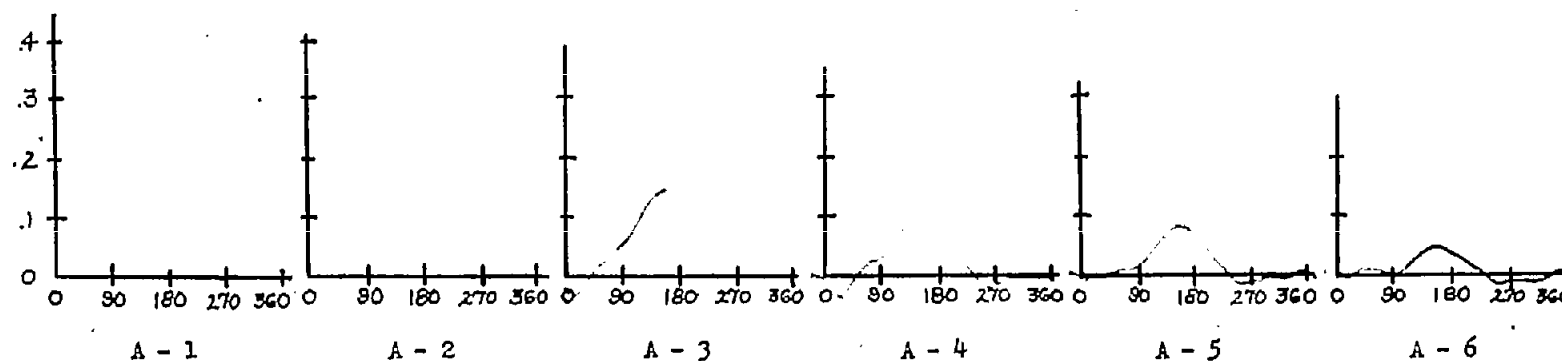


(g) Span station J; $r/R = 0.925$.

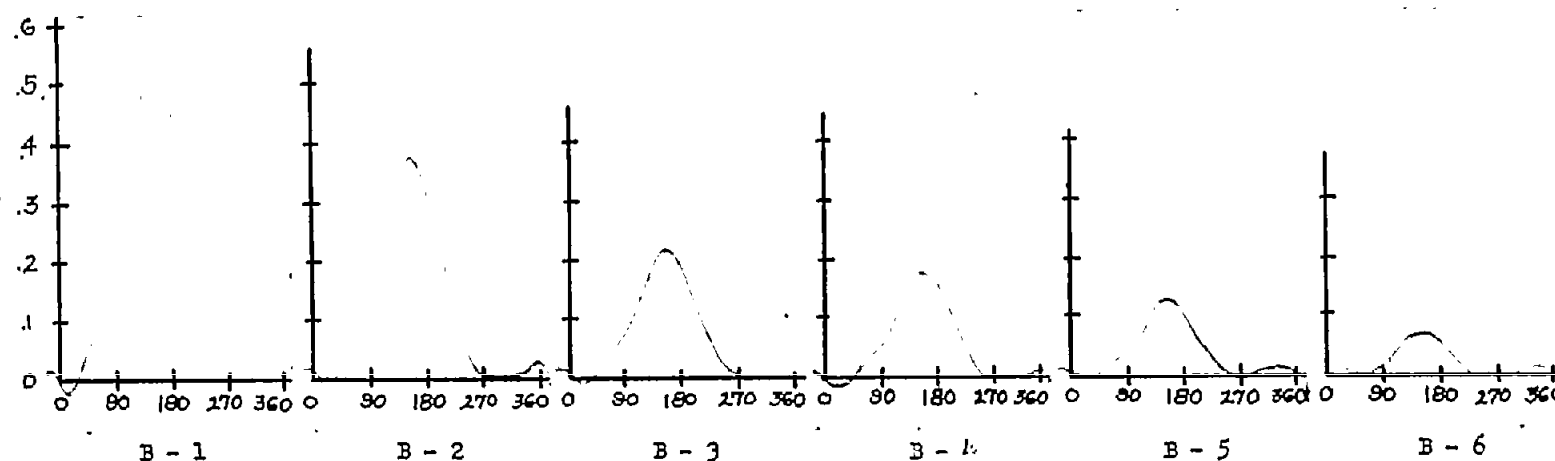


(h) Span station K; $r/R = 0.960$.

Figure 67.- Concluded.

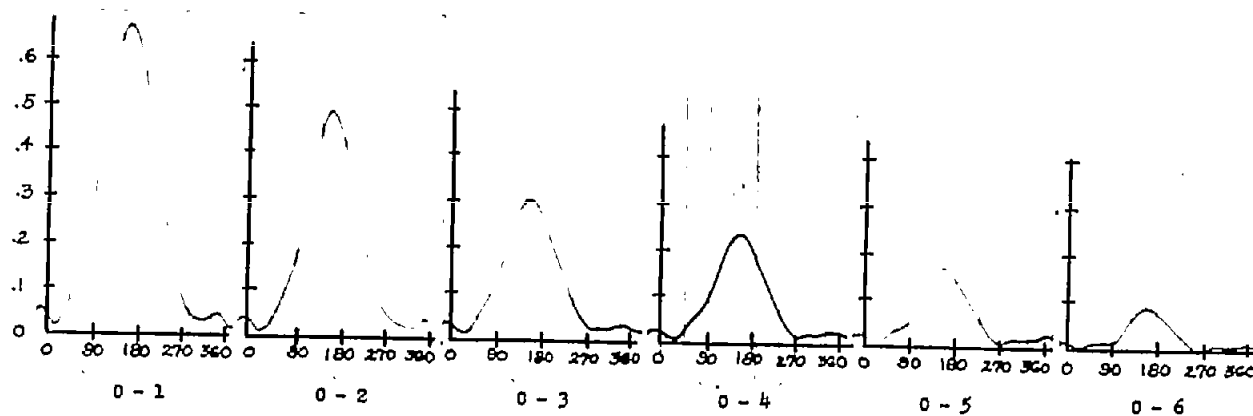


(a) Span station A; $r/R = 0.325$.

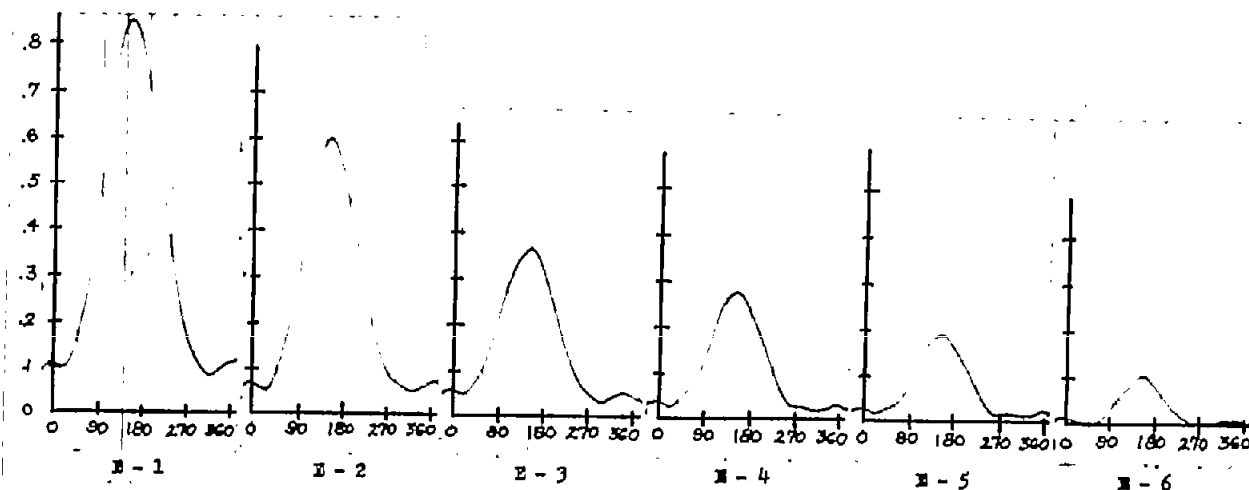


(b) Span station B; $r/R = 0.460$.

Figure 68.- Pressure difference in pounds per square inch against azimuth in degrees. Profile, NACA 0015; speed, 800 rpm; $\xi = 0.13$; $\mu = 0.40$; $A_0 = 12^\circ$; $\alpha = -10^\circ$.

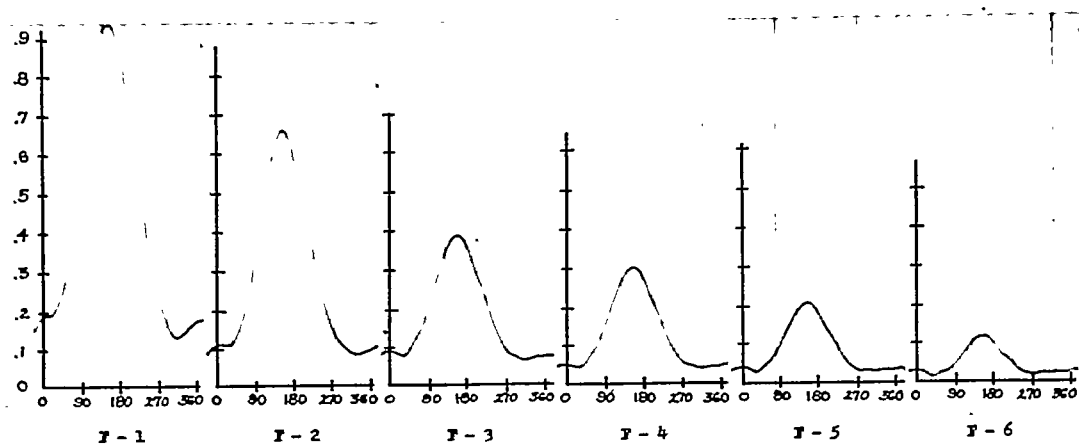


(c) Span station C; $r/R = 0.590$.

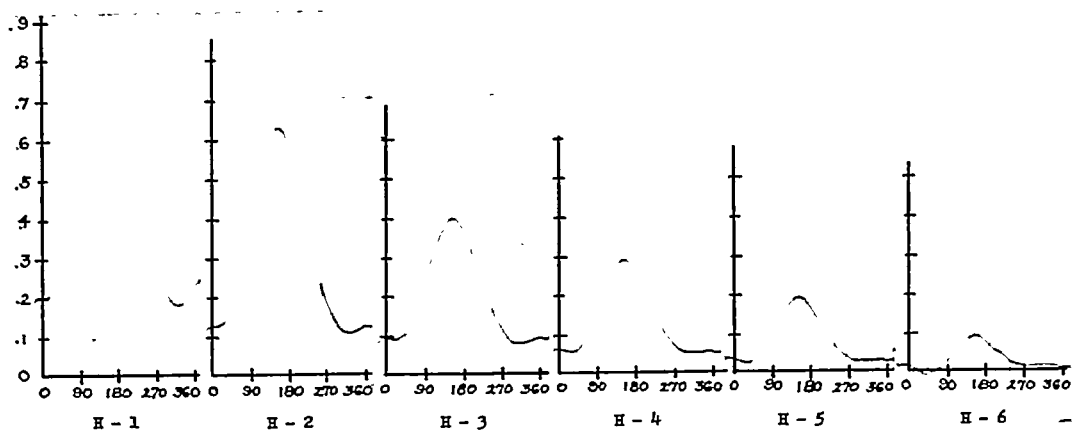


(d) Span station E; $r/R = 0.725$.

Figure 68.- Continued.

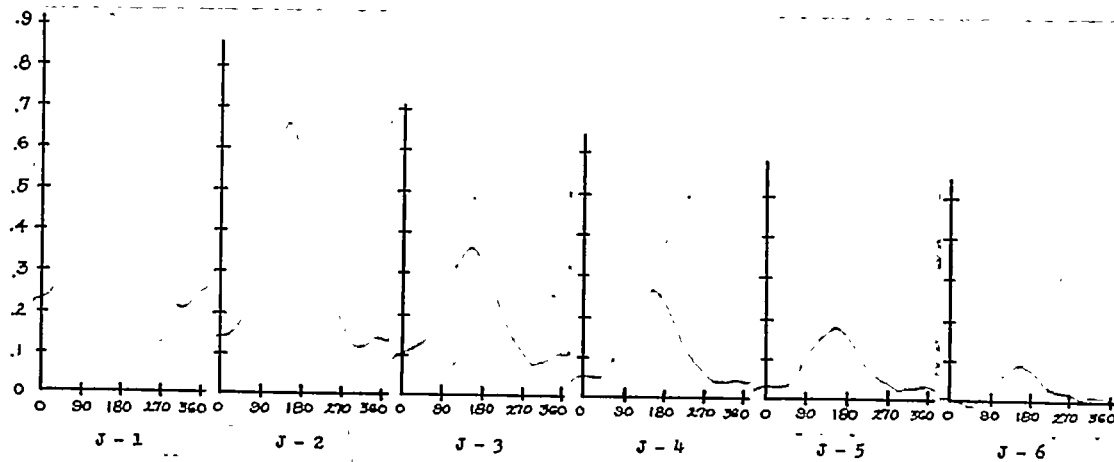


(e) Span station F; $r/R = 0.790$.

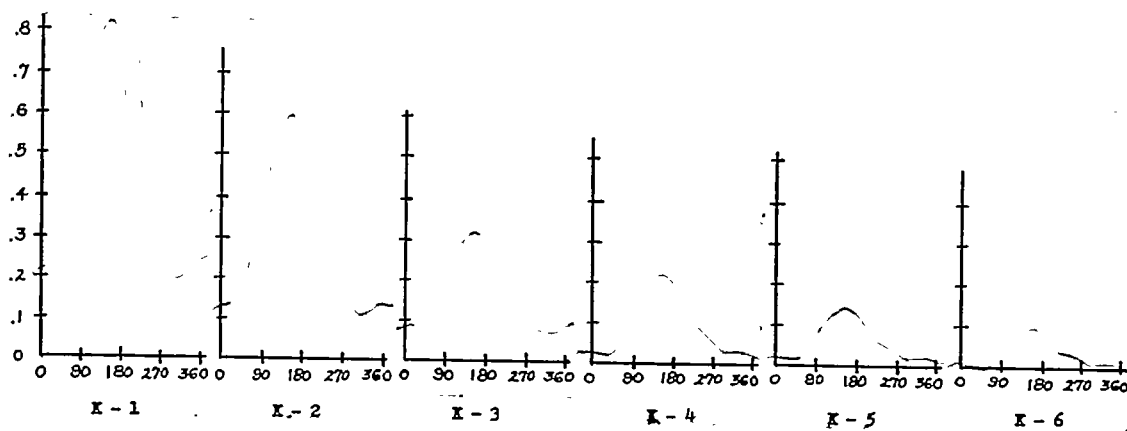


(f) Span station H; $r/R = 0.860$.

Figure 68.- Continued.

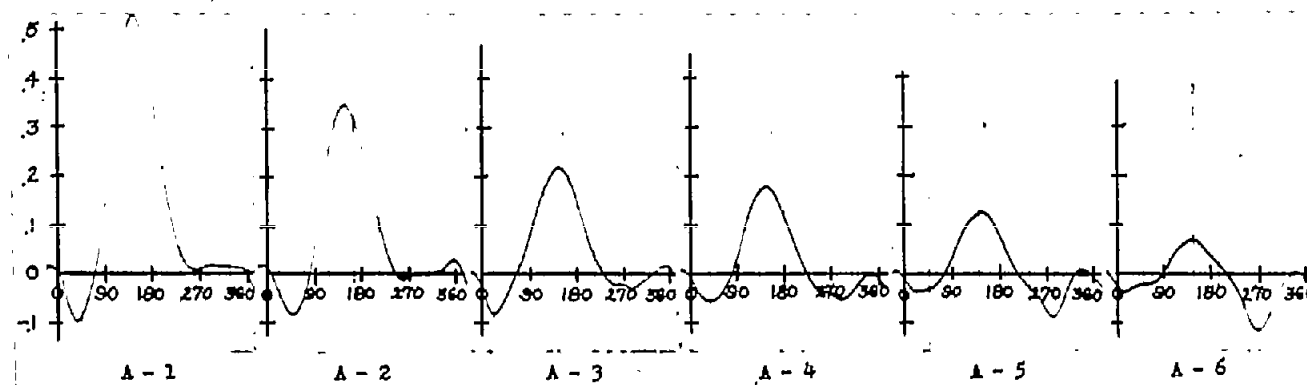


(g) Span station J; $r/R = 0.925$.

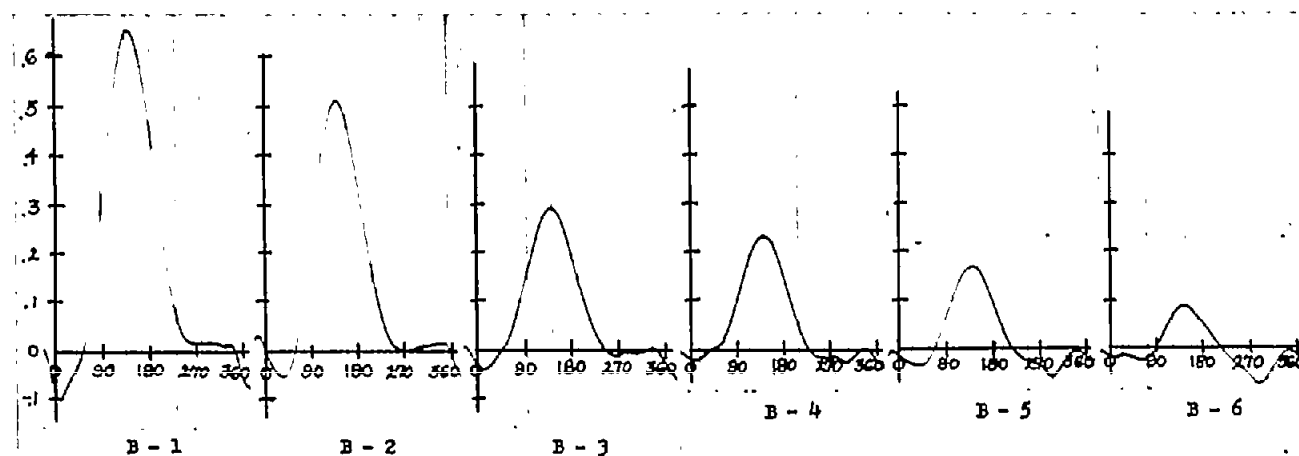


(h) Span station K; $r/R = 0.960$.

Figure 68.- Concluded.

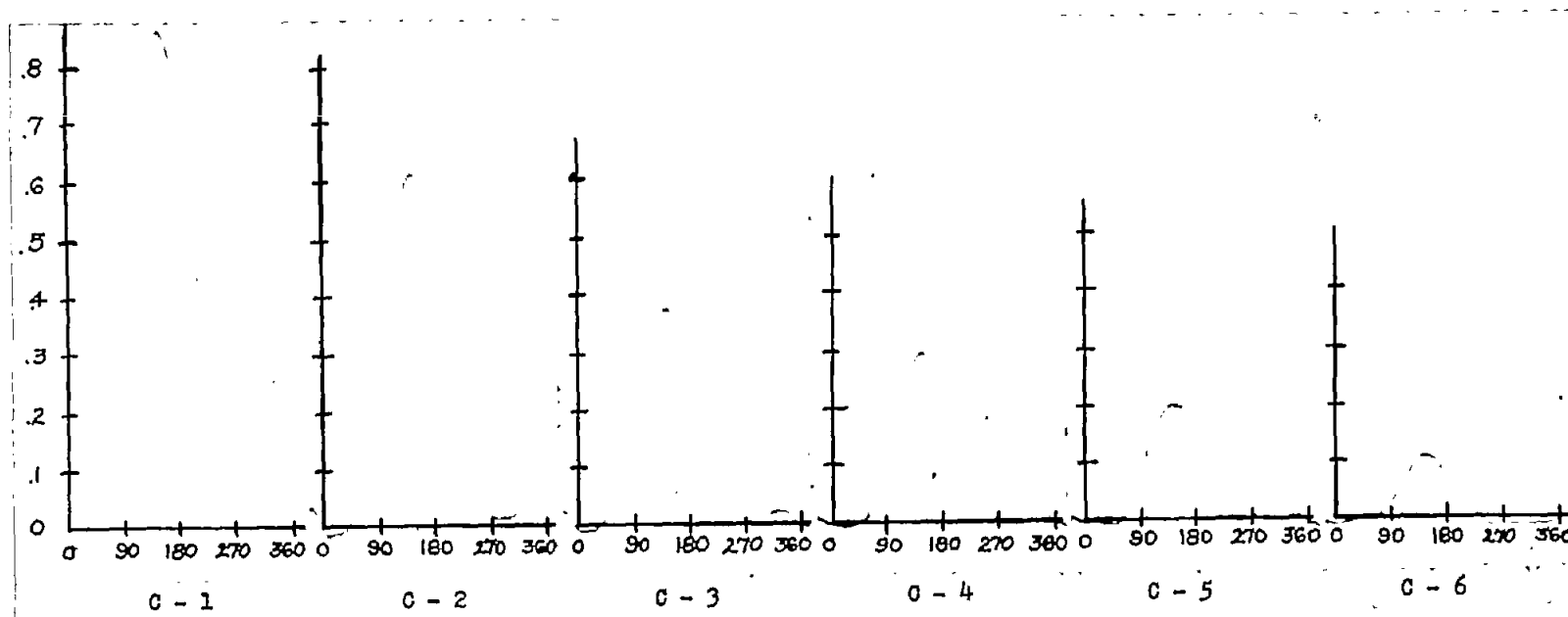


(a) Span station A; $r/R = 0.325$.



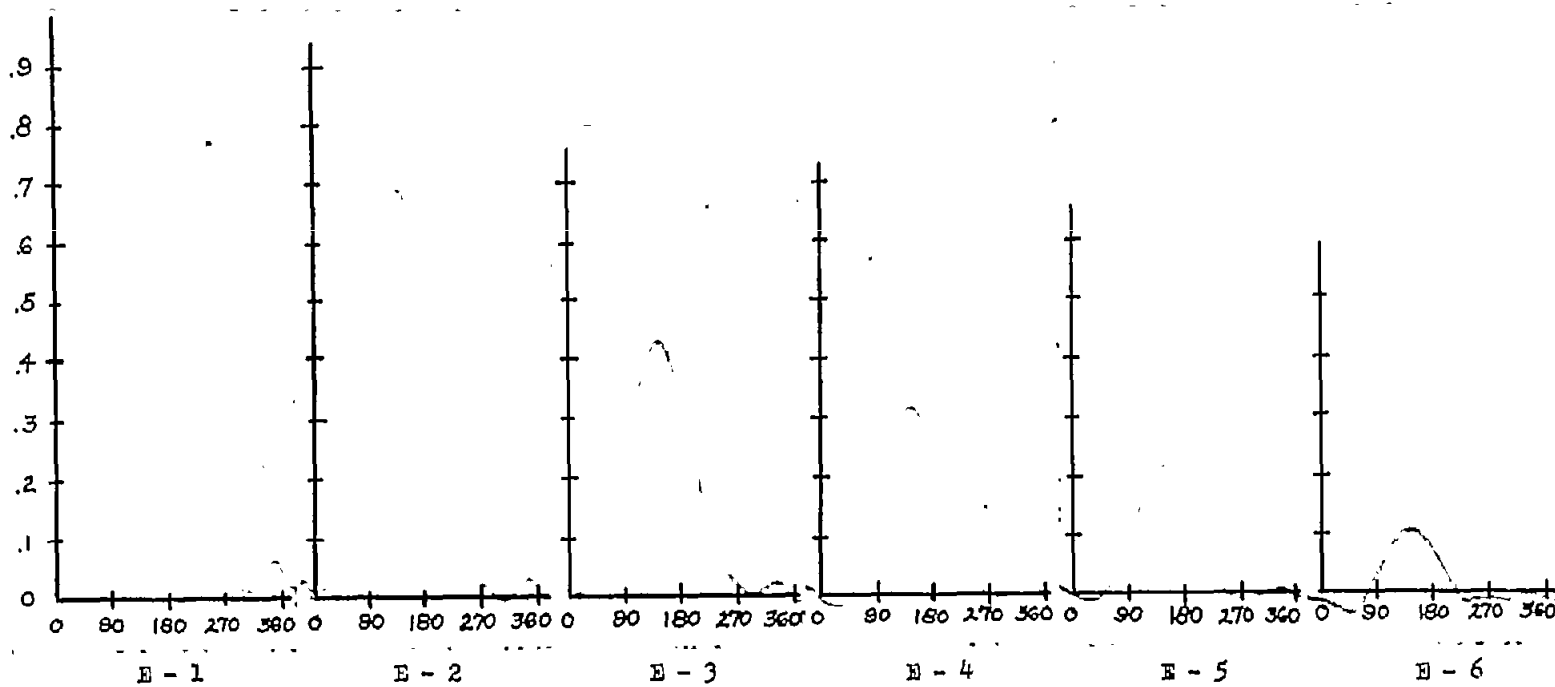
(b) Span station B; $r/R = 0.460$.

Figure 69.- Pressure difference in pounds per square inch against azimuth in degrees. Profile, NACA 0015; speed, 800 rpm; $\xi = 0.13$; $\mu = 0.60$; $A_0 = 12^\circ$; $\alpha = -10^\circ$.



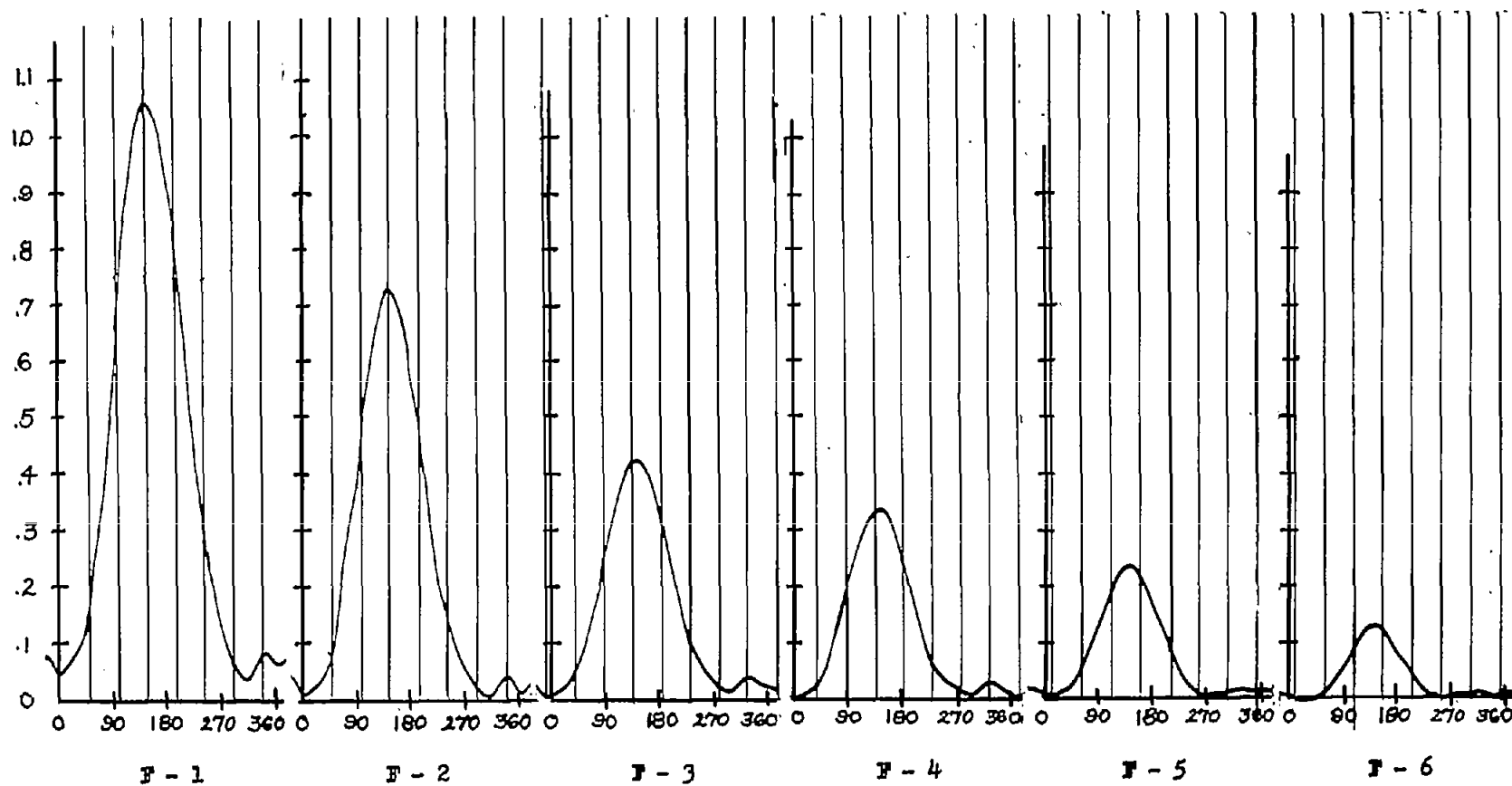
(c) Span station C; $r/R = 0.590$.

Figure 69.- Continued.



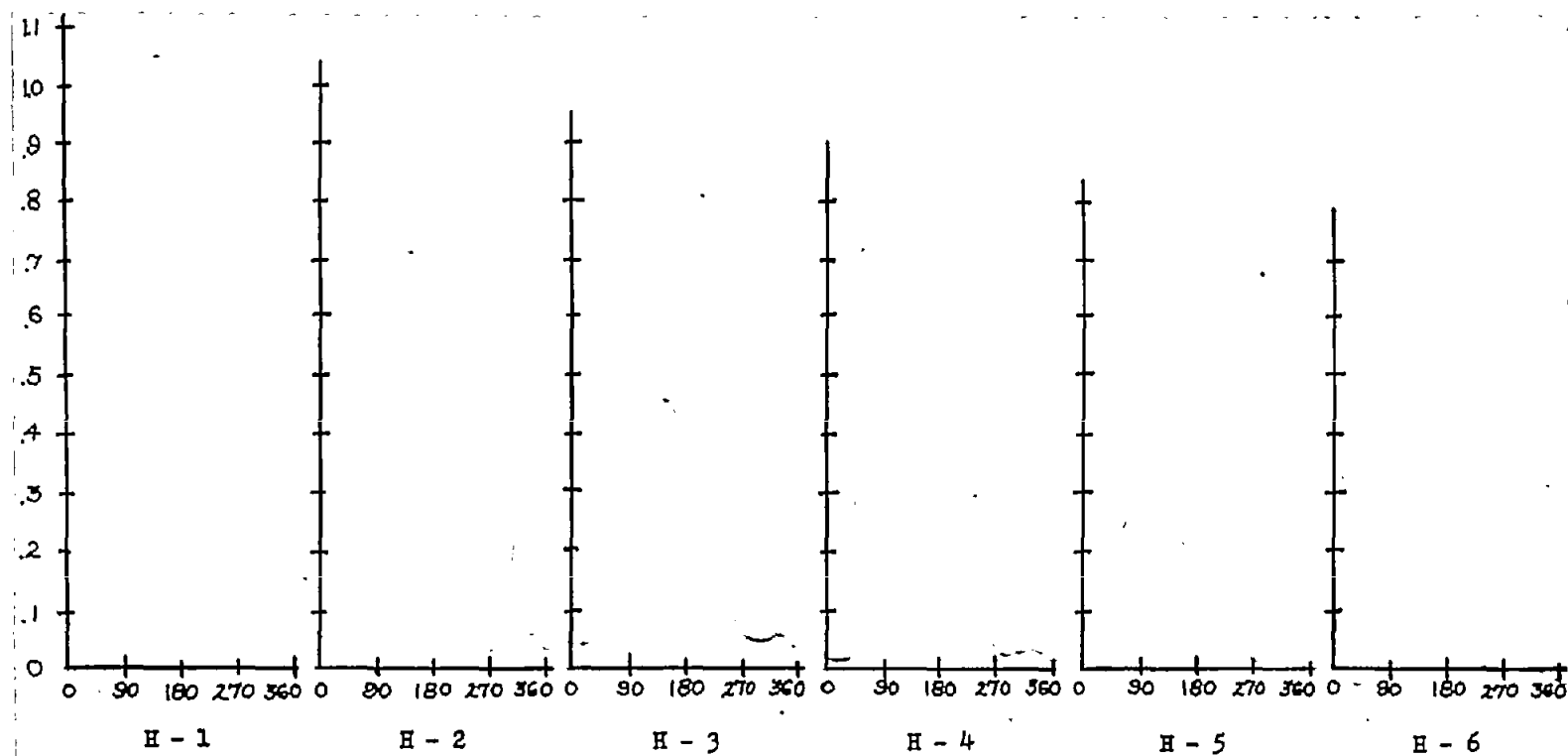
(d) Span station E; $r/R = 0.725$.

Figure 69.- Continued.



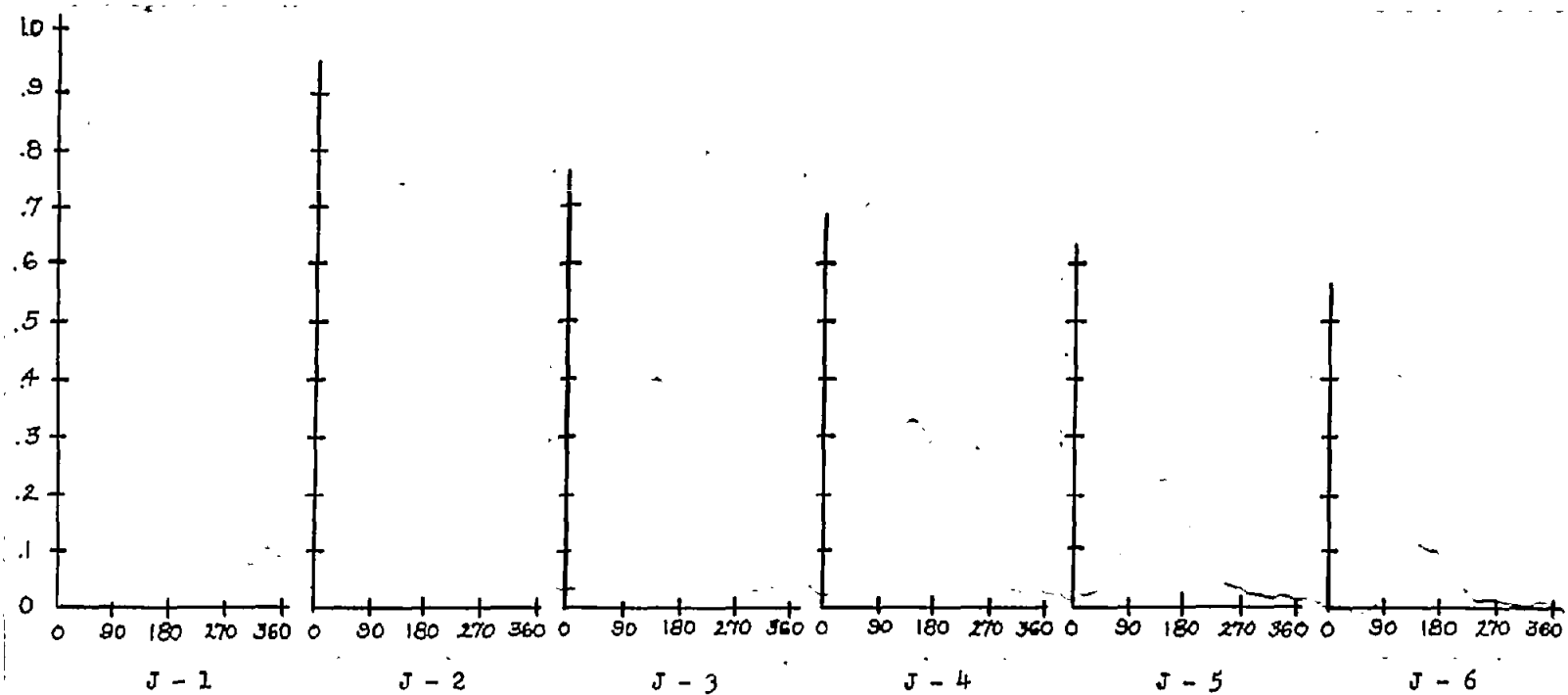
(e) Span station F; $r/R = 0.790$.

Figure 69.- Continued.



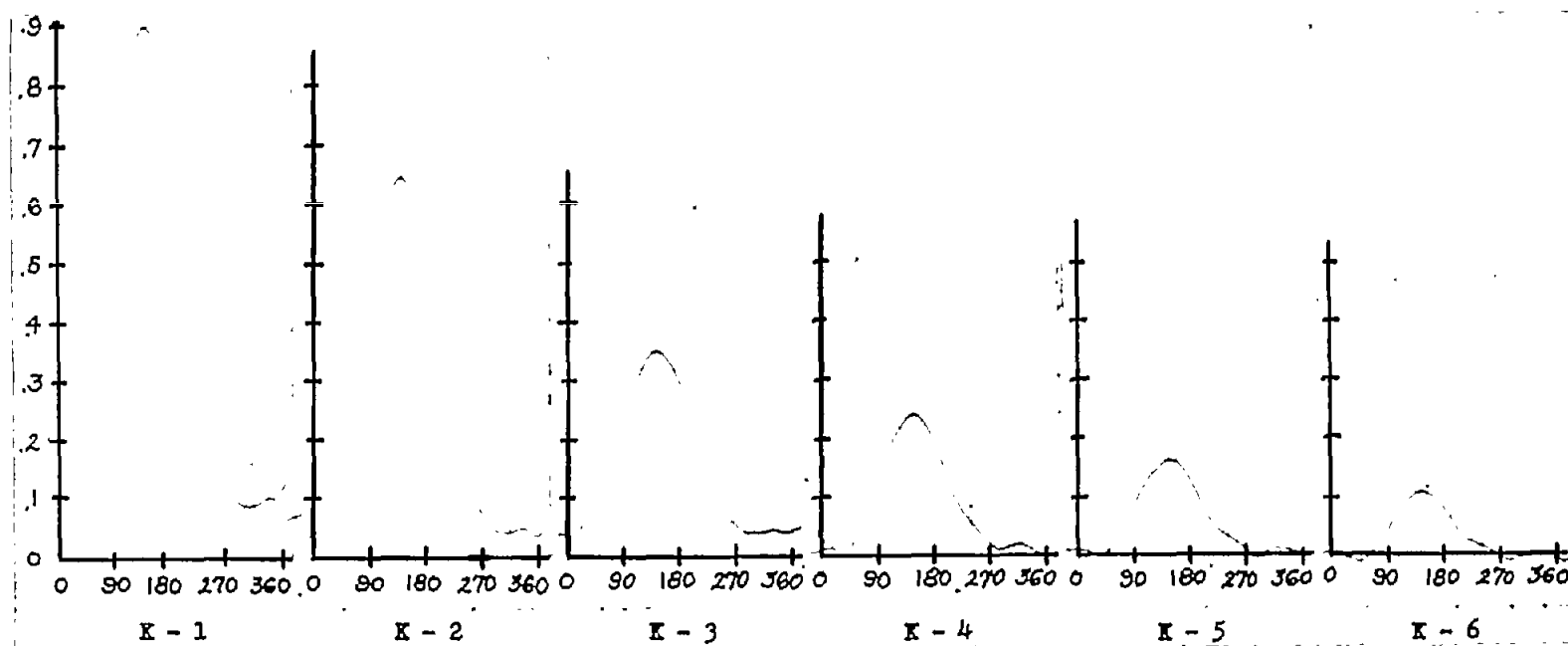
(f) Span station H; $r/R = 0.860$.

Figure 69.- Continued.



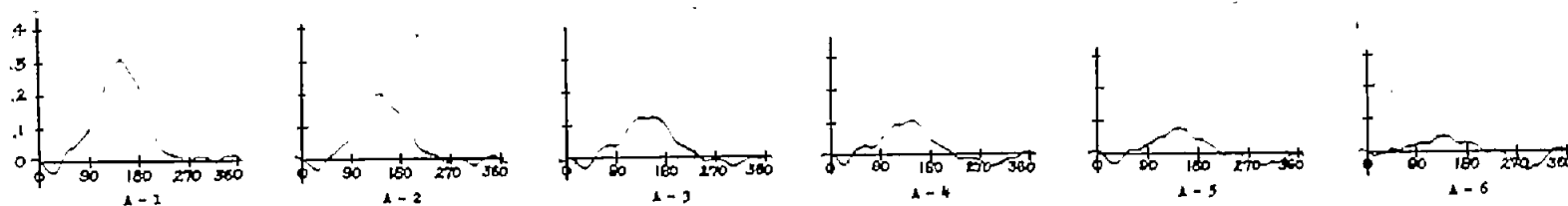
(g) Span station J ; $r/R = 0.925$.

Figure 69.- Continued.

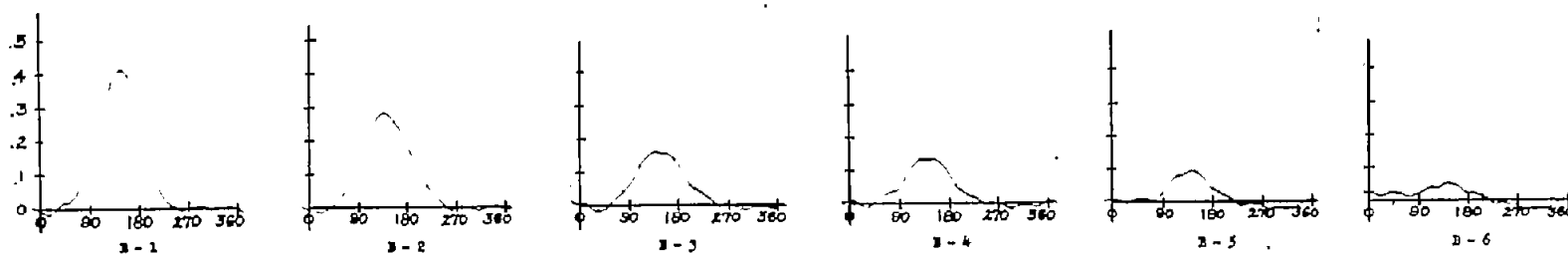


(h) Span station K; $r/R = 0.960$.

Figure 69.- Concluded.

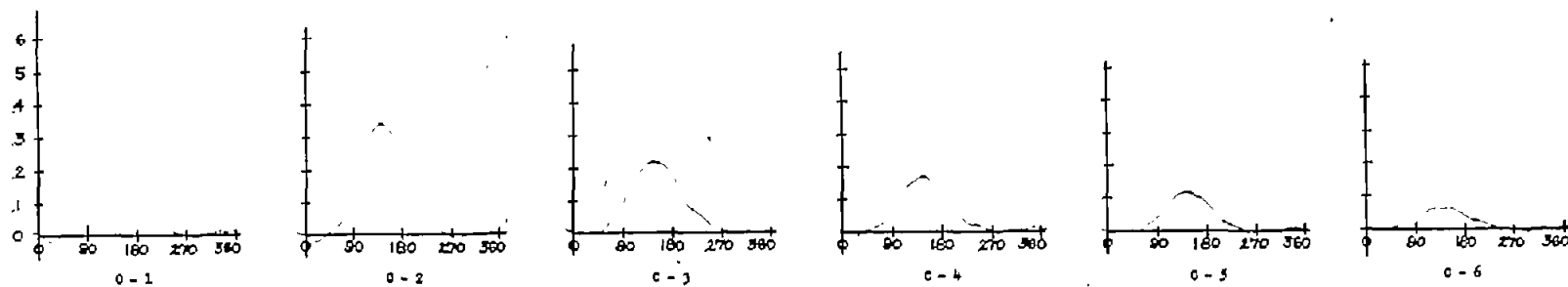


(a) Span station A; $r/R = 0.325$.

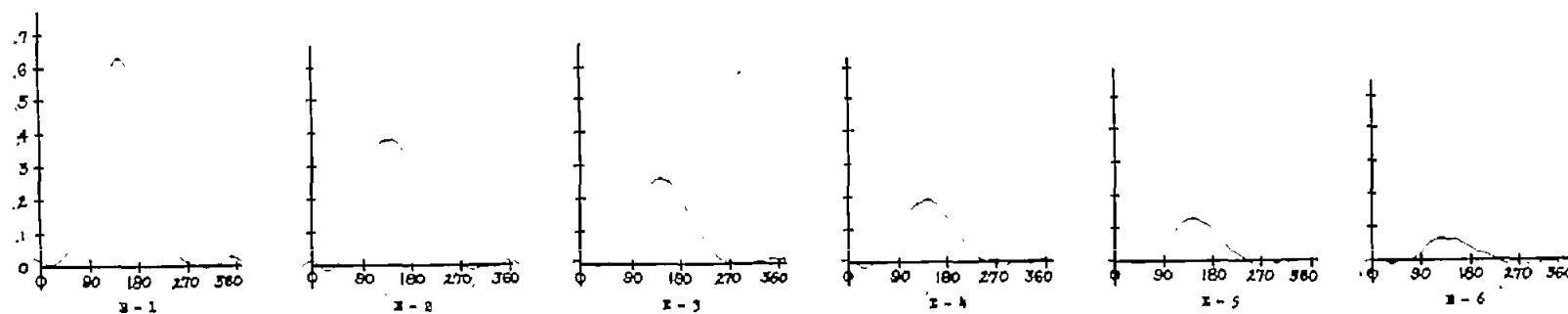


(b) Span station B; $r/R = 0.460$.

Figure 70.- Pressure difference in pounds per square inch against azimuth in degrees. Profile, NACA 0015; speed, 500 rpm; $\xi = 0.13$; $\mu = 0.60$; $A_0 = 17$; $\alpha = -15^\circ$.

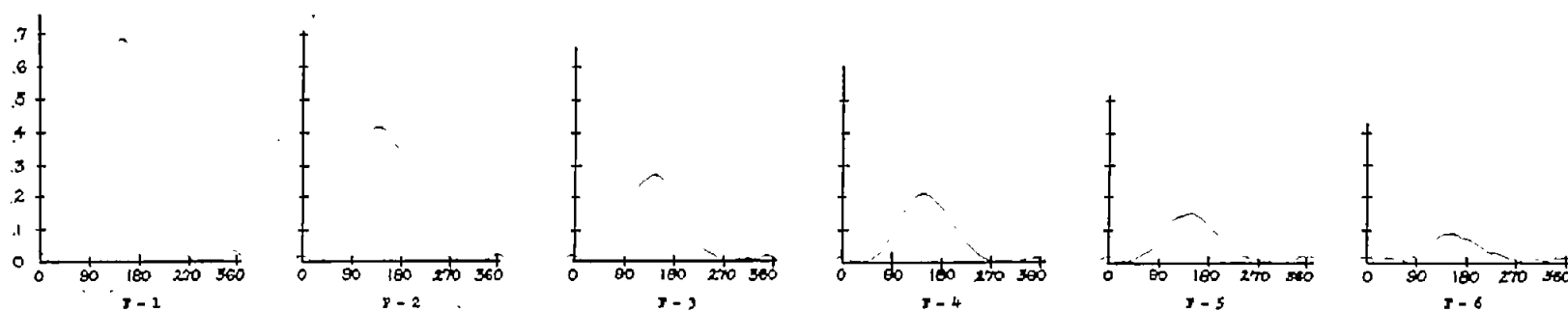


(c) Span station C; $r/R = 0.590$.

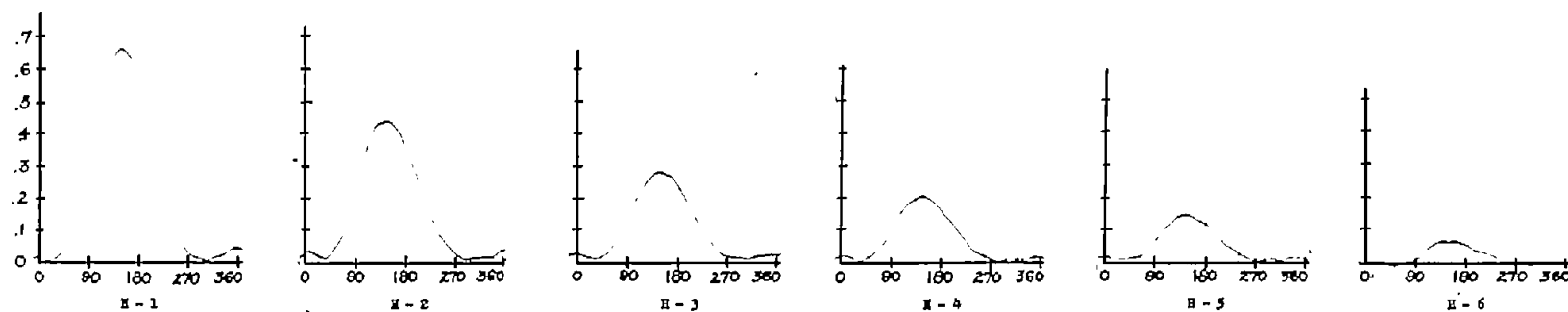


(d) Span station E; $r/R = 0.725$.

Figure 70.- Continued.

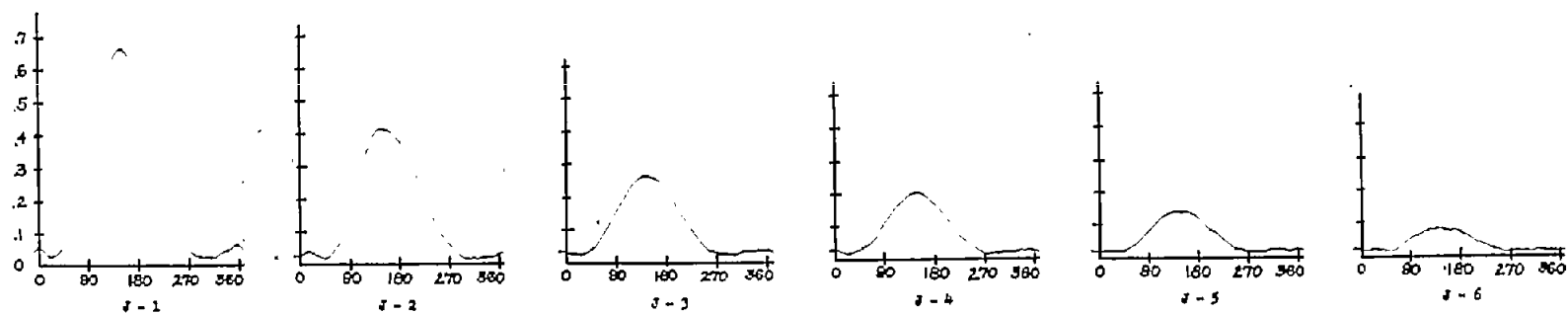


(e) Span station F; $r/R = 0.790$.

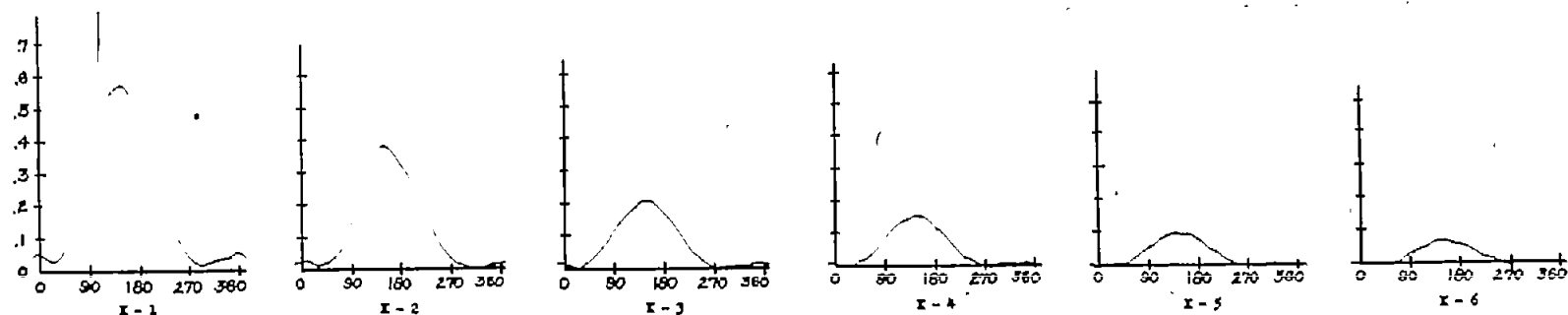


(f) Span station H; $r/R = 0.860$.

Figure 70.- Continued.

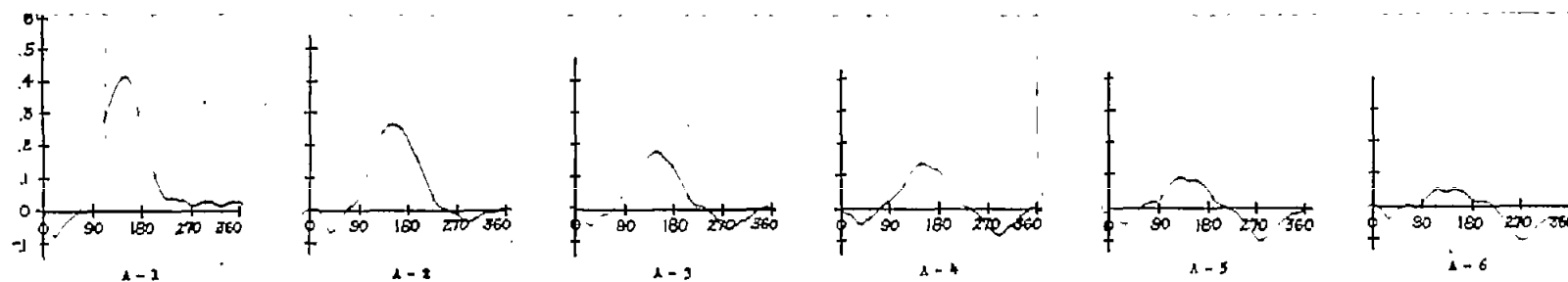


(g) Span station J; $r/R = 0.925$.

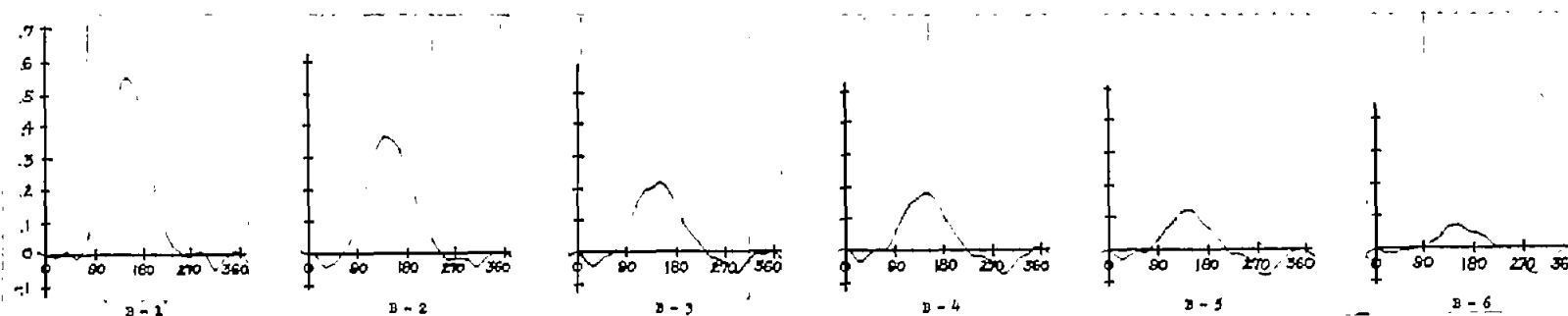


(h) Span station K; $r/R = 0.960$.

Figure 70.- Concluded.

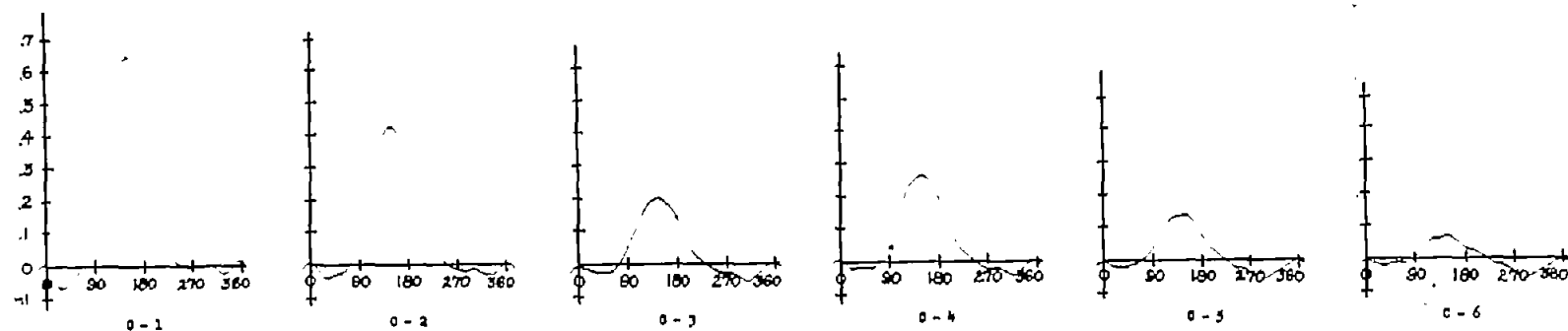


(a) Span station A; $r/R = 0.325$.

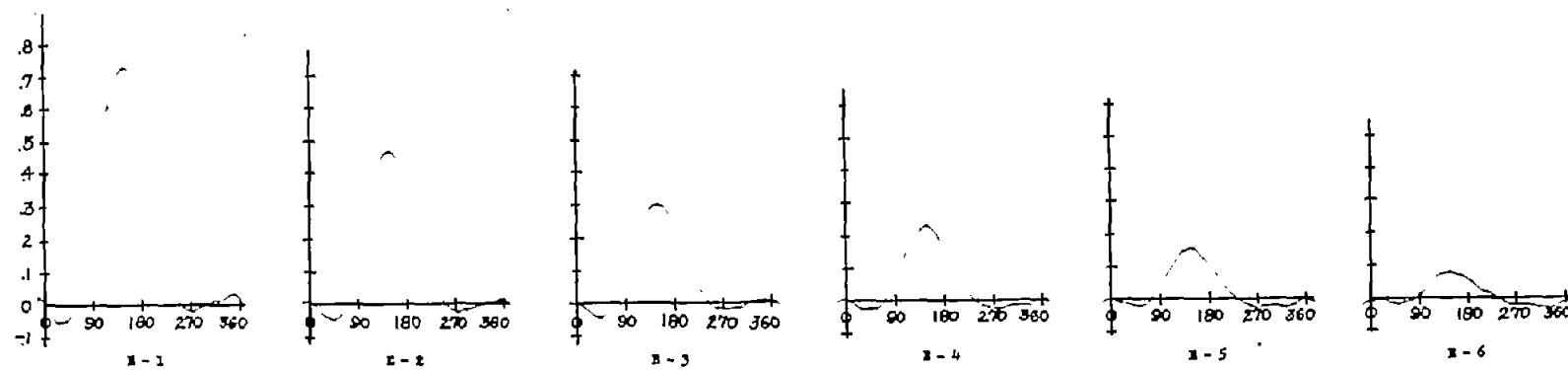


(b) Span station B; $r/R = 0.460$.

Figure 71.- Pressure difference in pounds per square inch against azimuth in degrees. Profile, NACA 0015; speed, 500 rpm; $\xi = 0.13$; $\mu = 0.80$; $A_0 = 17$; $\alpha = -15^\circ$.

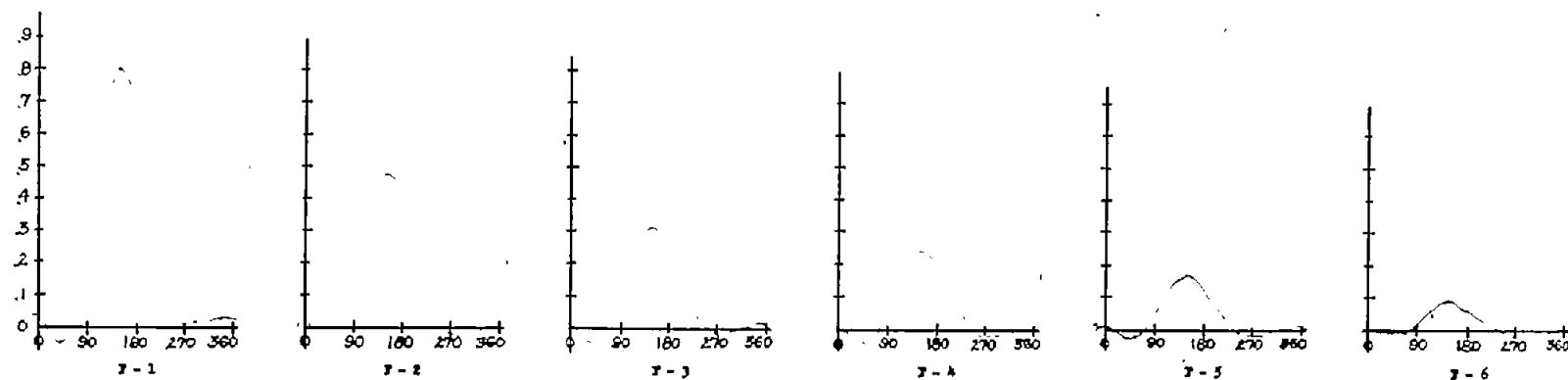


(c) Span station C; $r/R = 0.590$.

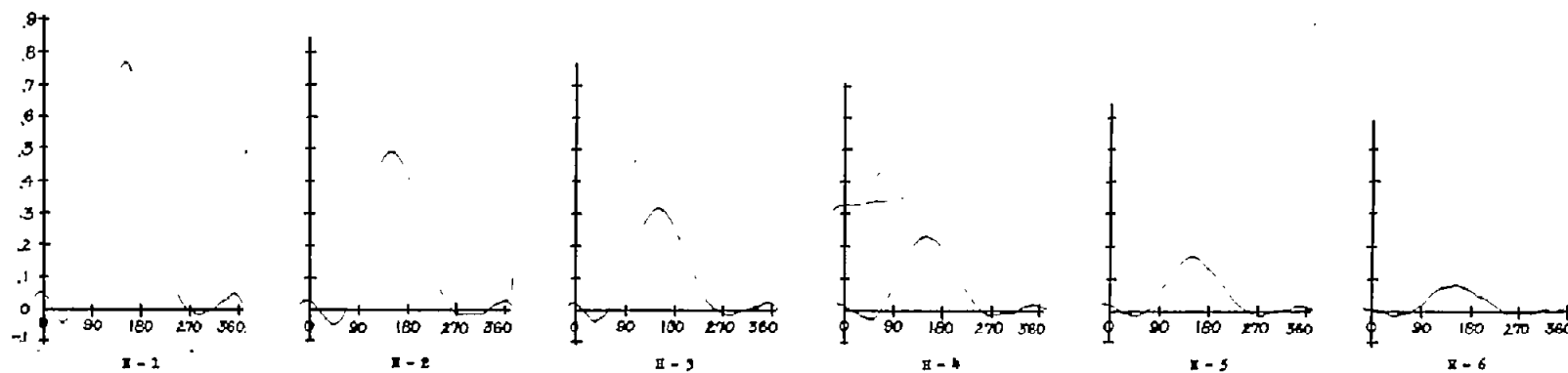


(d) Span station E; $r/R = 0.725$.

Figure 71.- Continued.

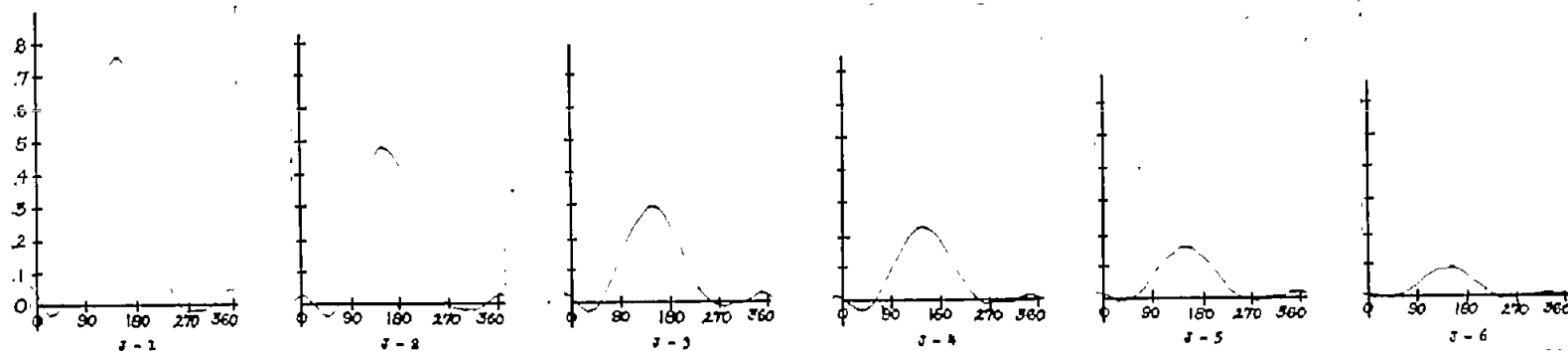


(e) Span station F; $r/R = 0.790$.

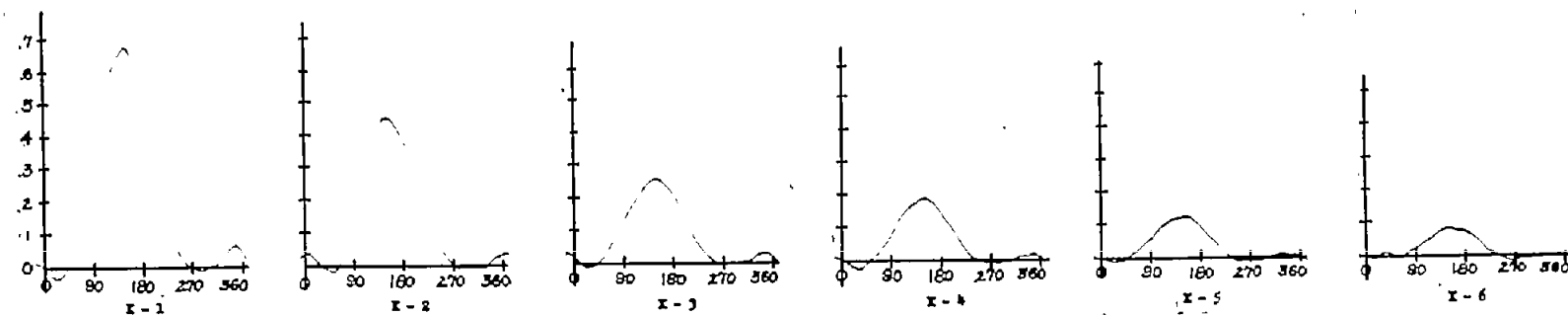


(f) Span station H; $r/R = 0.860$.

Figure 71.- Continued.



(g) Span station J; $r/R = 0.925$.



(h) Span station K; $r/R = 0.960$.

Figure 71.- Concluded.